ELECTRON SPIN POLARIZATION PRESERVATION IN THE ELECTRON-ION COLLIDER

A Dissertation

Presented to the Faculty of the Graduate School

of Cornell University

in Partial Fulfillment of the Requirements for the Degree of

Doctor of Philosophy

by

Matthew George Signorelli

December 2025

ELECTRON SPIN POLARIZATION PRESERVATION IN THE ELECTRON-ION COLLIDER

Matthew George Signorelli, Ph.D.

Cornell University 2025

We present various works aimed at maximizing polarization in the Electron Storage Ring (ESR) of the soon-to-be-built Electron-Ion Collider (EIC), and describe in detail the polarization properties of the ESR throughout its design evolution. Most significantly, we present a novel method called "Best Adjustment Groups for ELectron Spin" (BAGELS) that achieves simultaneous control of the polarization, orbit, and optics in electron storage rings by use of special vertical orbit bumps constructed via dimensionality reduction. Using BAGELS, we nearly double the asymptotic polarization in a 1-interaction point (IP) ESR lattice, and more than triple it in a 2-IP lattice. We also use BAGELS to construct knobs that can be used for global coupling correction, and knobs that generate vertical emittance for beam size matching, all while having minimal impacts on the polarization and orbit/optics. Furthermore, we present *SciBmad*, a new, modular, differentiable, and high performance accelerator physics software that can be used easily in Python or Julia. SciBmad's symplectic integrators, which include spin, are universally polymorphic, forwards-/backwards-/Taylor-differentiable, and CPU/GPU parallelizable. Also included are a high-order automatic differentiation library, and routines for doing perturbation theory with nonlinear (possibly damped) Hamiltonian maps using Lie algebraic methods. SciBmad's machine learning-enabled ecosystem aims to be a powerful tool for modern particle accelerator design and simulation.

BIOGRAPHICAL SKETCH

Matthew G. Signorelli was born in 1999 and grew up in Toms River, New Jersey. He graduated from Toms River High School North in 2017, and pursued undergraduate studies in engineering and computer science at Rutgers University. During a summer 2019 undergraduate internship at Brookhaven National Laboratory, he discovered accelerator physics and immediately fell in love with the field. In May 2021, Matthew earned his B.S. in Mechanical Engineering, with a concentration in Aerospace Engineering and minors in Computer Science and Physics. That summer, he began his research in electron polarization, and arrived in Ithaca, New York in August 2021 to pursue a Ph.D. in Physics at Cornell University. To this day, Matthew yearns to return to New Jersey, and holds the impractical dream of building a linear accelerator up and down the Jersey Shore solely so he can live and work there.

To my Dad, my brother Joe, and perfect dogs Coco and Simba

ACKNOWLEDGEMENTS

First and foremost, I thank my Dad, for always being there for me no matter what, and being the most stable and secure source of support for me. I'm very lucky to have you as my dad. I also thank my twin brother Joe, for also always being there and being someone I could talk to about pretty much anything. I must also acknowledge Coco and Simba, my Dad's two perfect dogs, for all the happiness and love they have brought to our lives.

I'm deeply grateful for all of my closest friends that I've met at Cornell, in particular Chloe Cho, Joseph Grassi, Chad Mowers, and Liana Shpani. From our night walks, camping trips, gorge swimming, everything, you guys have made Ithaca so much fun and are truly an amazing support. It's been so nice learning and growing with you since we started here, and I'm very lucky to have you all in my life.

I also have to thank the SRF group for providing the Newman lab 4th floor lounge. Daily lunches there with everyone, including Thomas Oseroff and Gabriel Gaitan, always made coming into work not only fun, but also humbling as my ping-pong abilities were regularly put to shame.

Finally, thanks to Yi Wu, for being a truly genuine friend, for showing me around Switzerland and the mountains, and for always sending me perfect, sometimes crazy, dog pictures.

Now onto the more-professional acknowledgements. I give my deepest thanks to my advisor Georg Hoffstaetter de Torquat, for being an amazing mentor, teacher, and advisor. I remember before I joined the group I talked to a previous graduate of Georg's, who told me that Georg is great because "he will find out exactly what you don't know, and make sure you learn it". I couldn't agree more with this statement. Georg has been quintessential in helping me learn

and grow as a scientist and professional throughout graduate school. His pizza is also pretty good, and with my New Jersey standards, that says a lot. I really could not have asked for a better PhD advisor.

Next I thank David Sagan, for his simulation code Bmad. The work and methods developed in this dissertation would not have been possible without Bmad.

Thanks to Jorg Kewisch, for first introducing me to accelerator physics at my undergraduate BNL internship, and for being an amazing mentor and friend.

Thanks to the entire Electron-Ion Collider team that I've worked with closely throughout my Ph.D. program, in particular Christoph Montag, Daniel Marx, Vadim Ptitsyn, and J. Scott Berg, among many others. It has been a pleasure working with you all, and I'm excited to continue our work together in the future. I'm honored to have had the opportunity to contribute to such a significant project.

Thanks to Desmond P. Barber for ensuring that I received a proper education in spin dynamics from the very beginning of my graduate program.

I give major thanks to Etienne Forest, for his significant time and patience in teaching me a most general, self-consistent, and widely-applicable approach to accelerator physics. His work and contributions have guided many aspects of our new SciBmad accelerator physics software. My hope is that this dissertation provides another useful piece of literature introducing such methods.

Thanks to Laurent Deniau, for all of his time spent teaching me how his powerful Generalised Truncated Power Series Algebra library works, and our many invigorating conversations about accelerator physics software. His work has also inspired parts of the SciBmad implementation.

Finally, I thank all the developers and contributors of our new SciBmad soft-

ware. Especially, I acknowledge fellow group member Joe Devlin, for implementing and testing all of the symplectic orbital and spin integrators, and for many enlightening discussions.

All work supported in part by Brookhaven Science Associates, LLC under Contract No. DE-SC0012704 with the U.S. Department of Energy.

CONTENTS

LIST OF TABLES

LIST OF FIGURES

CHAPTER 1

INTRODUCTION

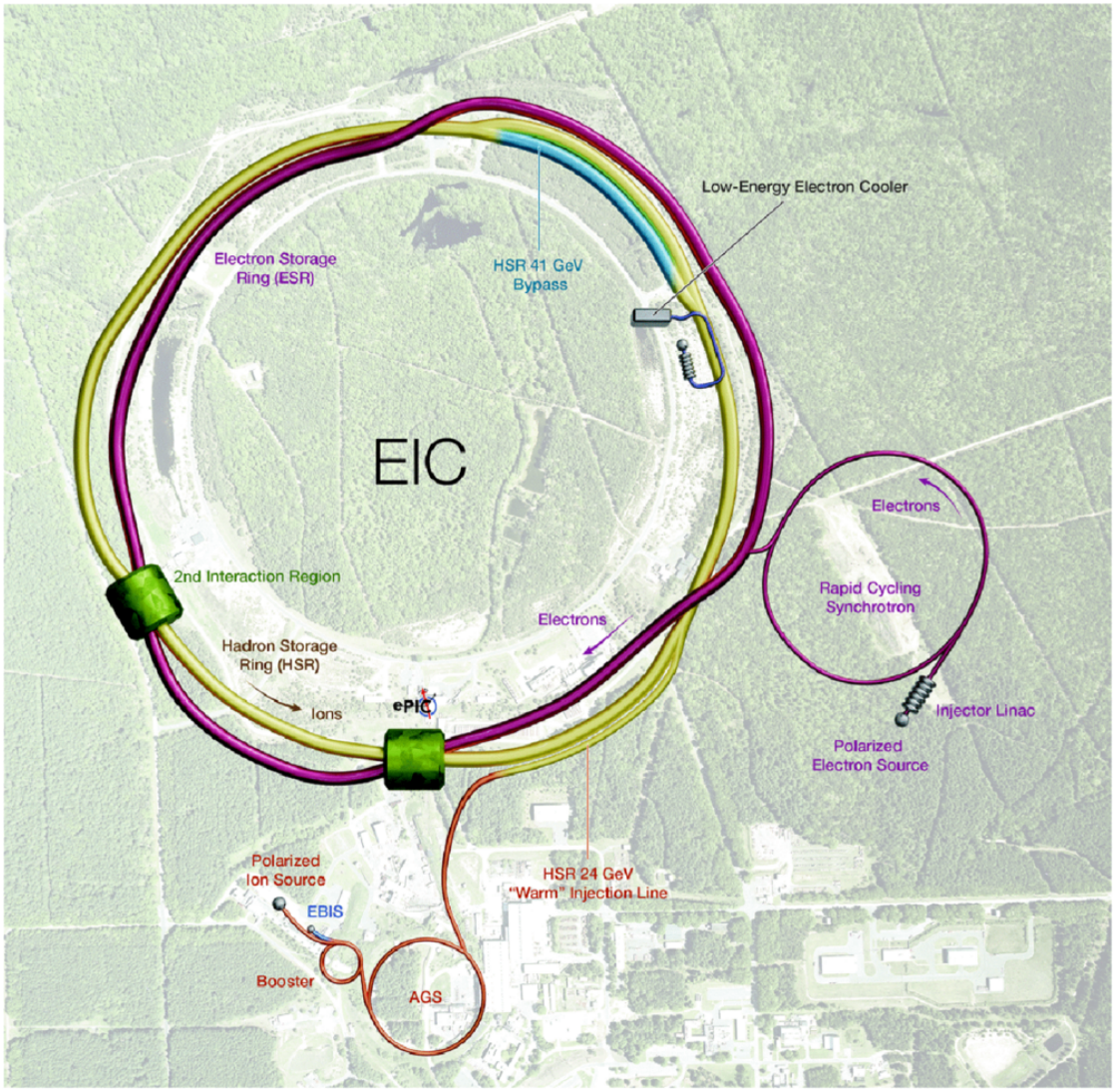

Figure 1.1: Conceptual schematic of the Electron-Ion Collider.

Spin-polarized particle colliders provide one of the best probes of the internal structures of fundamental particles and their interactions, and remain one of the most important tools in high energy physics. The Hadron-Elektron-RingAnlage (HERA) collider at DESY, which operated between 1992-2007, col-

lided protons with spin-polarized electrons or positrons, providing valuable high energy physics results, including excellent experimental agreement of the electro-weak interaction spin dependence with standard model predictions [79]. Now, the Electron-Ion Collider (EIC) soon to be built at Brookhaven National Laboratory will push the frontier even further, being the first circular collider of longitudinally-spin-polarized electrons with longitudinally-spin-polarized light-ions for a wide range of selected center-of-mass energies [74]. Data from such collisions in the EIC will answer important questions about the origin of proton spin, among others.

Maintaining high spin polarization throughout storage for sufficiently long amounts of time is essential to achieving optimal physics data. The Electron Storage Ring (ESR) of the EIC, shown in Fig. 1.1, aims to provide longitudinally-polarized electron bunches at each of roughly 5, 10, and 18 GeV in both a 1- and 2-colliding interaction point (IP) configuration. A time-averaged polarization of at least 70% is required to achieve the goals of the EIC [74]. Meeting this requirement, while also simultaneously satisfying all of the other requirements of the ESR, in particular a beam size match at the interaction point for maximum luminosity, proves to be a significant challenge.

In this dissertation, we describe in detail how we overcame this challenge. The dissertation is organized as follows: Chapter 2 introduces important concepts from classical mechanics and the basic theory of accelerator physics, using Lie methods. Chapter 3 describes the theory of spin dynamics in particle accelerators, the invariant spin field, electron bunch polarization evolution in storage rings, first-order spin-orbit motion, traditional methods used to minimize radiative depolarization, and computational methods. In Chapter 4, we discuss

in detail the ESR of the EIC, its spin rotator and valid configurations for longitudinal polarization at the IPs, best polarization figures-of-merit for the ESR, the conditions for a strong synchro-beta spin match, and the evolution of the different ESR lattice versions. Chapter 5 studies a problematic nonlinear resonance that led to changes in the working point of the ESR. Chapter 6 shows an attempt to achieve higher polarization in the 18 GeV case via a "partial" longitudinal spin match across both interaction regions, where a reasonable improvement to the 2-IP lattice is achieved. Our polarization work then culminates in Chapter 7, where a novel, best solution to simultaneously optimize the polarization, orbit, and optics is developed and applied with significant success in simulations. The method, which we call "Best Adjustment Groups for ELectron Spin" (BAGELS), utilizes dimensionality reduction to construct a minimal number of special vertical orbit bumps that achieve the simultaneous control. Using BAGELS, the asymptotic polarization is nearly doubled in the 18 GeV 1-IP lattice, and more than tripled in the 18 GeV 2-IP lattice. BAGELS is also used to construct knobs that can be used for global coupling correction, and knobs that generate vertical emittance for beam size matching, all while having minimal impacts on the polarization and orbit/optics. Next, Chapter 8 shares some significant polarization findings from simulations including a weak-strong beam-beam interaction model. Specifically, nonlinearities from the beam-beam interaction appear to substantially reduce polarization, and the cause is correlated to the beam-beam interaction tune spread and second-order effects in the rest of the ring. Ideas to further investigate and resolve the effect are also proposed. Finally, Chapter 9 introduces SciBmad, a new, fully differentiable, CPU/GPU-parallelized, modular, and machine learning-enabled accelerator physics software ecosystem providing powerful tools for modern accelerator design and simulation.

CHAPTER 2

BACKGROUND

In this chapter we review important concepts in classical mechanics, with a significant amount of material taken directly from [41, 30, 32, 51, 73, 24, 26, 25, 13].

2.1 Review of Classical Mechanics

Lagrangian mechanics is a formulation of classical mechanics where equations of motion for generalized coordinates of a body can be derived easily. One first formulates the Lagrangian as a function of some generalized position and velocity $\mathcal{L}(\boldsymbol{q}(t), \dot{\boldsymbol{q}}(t), t)$, which in many cases is just $T - V$ where T is the kinetic energy and V is the potential energy. Then the path taken will be that which extremizes the *action*, defined as

$$S = \int_{t_0}^{t_1} \mathcal{L}(\boldsymbol{q}(t), \dot{\boldsymbol{q}}(t), t)\, dt\,, \tag{2.1}$$

where the endpoints are kept fixed - that is, changes to the action δS do not vary $\boldsymbol{q}(t_0)$ and $\boldsymbol{q}(t_1)$. We use variational calculus to determine the conditions where the action is extremized,

$$\begin{aligned}
\delta S &= \int_{t_0}^{t_1} \mathcal{L}(\boldsymbol{q} + \delta\boldsymbol{q}, \dot{\boldsymbol{q}} + \delta\dot{\boldsymbol{q}}, t) - \mathcal{L}(\boldsymbol{q}(t), \dot{\boldsymbol{q}}(t), t)\, dt \\
&= \int_{t_0}^{t_1} \left(\frac{\partial \mathcal{L}}{\partial \boldsymbol{q}} \cdot \delta\boldsymbol{q} + \frac{\partial \mathcal{L}}{\partial \dot{\boldsymbol{q}}} \cdot \delta\dot{\boldsymbol{q}} \right) dt \\
&= \int_{t_0}^{t_1} \text{`}\frac{\partial \mathcal{L}}{\partial \boldsymbol{q}} \cdot \delta\boldsymbol{q}\, dt + \underbrace{\left[\frac{\partial \mathcal{L}}{\partial \dot{\boldsymbol{q}}} \cdot \delta\boldsymbol{q} \right]_{t_0}^{t_1}}_{=0} - \int_{t_0}^{t_1} \left(\frac{d}{dt} \frac{\partial \mathcal{L}}{\partial \dot{\boldsymbol{q}}} \right) \cdot \delta\boldsymbol{q}\, dt \\
&= \int_{t_0}^{t_1} \left(\frac{\partial \mathcal{L}}{\partial \boldsymbol{q}} - \frac{d}{dt} \frac{\partial \mathcal{L}}{\partial \dot{\boldsymbol{q}}} \right) \cdot \delta\boldsymbol{q}\, dt\,,
\end{aligned} \tag{2.2}$$

where we use the fixed endpoints condition so that $\delta\boldsymbol{q}(t_0) = \delta\boldsymbol{q}(t_1) = \boldsymbol{0}$. It is clear now that δS is equal to zero for arbitrary $\delta\boldsymbol{q}$ if and only if

$$\frac{\partial \mathcal{L}}{\partial \boldsymbol{q}} = \frac{d}{dt}\frac{\partial \mathcal{L}}{\partial \dot{\boldsymbol{q}}} \,. \tag{2.3}$$

This is the *Euler-Lagrange equation*, and for n degrees of freedom defines n independent second order differential equations describing the motion.

We can reformulate this problem into $2n$ independent first order differential equations for $2n$ variables by use of a Legendre transformation on $\mathcal{L}$ for $(\boldsymbol{q}, \dot{\boldsymbol{q}}, t) \mapsto (\boldsymbol{q}, \boldsymbol{p}, t)$ where $\boldsymbol{p} = \frac{\partial \mathcal{L}}{\partial \dot{\boldsymbol{q}}}$,

$$\begin{aligned} d\mathcal{L} &= \frac{\partial \mathcal{L}}{\partial \boldsymbol{q}} \cdot d\boldsymbol{q} + \frac{\partial \mathcal{L}}{\partial \dot{\boldsymbol{q}}} \cdot d\dot{\boldsymbol{q}} \\ &= \dot{\boldsymbol{p}} \cdot d\boldsymbol{q} + \boldsymbol{p} \cdot d\dot{\boldsymbol{q}} \\ &= \dot{\boldsymbol{p}} \cdot d\boldsymbol{q} + d(\boldsymbol{p} \cdot \dot{\boldsymbol{q}}) - \dot{\boldsymbol{q}} \cdot d\boldsymbol{p} \,. \end{aligned} \tag{2.4}$$

Thus we have

$$d(\boldsymbol{p} \cdot \dot{\boldsymbol{q}} - \mathcal{L}) = -\dot{\boldsymbol{p}} \cdot d\boldsymbol{q} + \dot{\boldsymbol{q}} \cdot d\boldsymbol{p} = dH \,, \tag{2.5}$$

where $H = H(\boldsymbol{q}, \boldsymbol{p}, t)$ is the Hamiltonian. The equations of motion for $\boldsymbol{q}$ and $\boldsymbol{p}$ are then obtained by expanding dH and matching the terms,

$$\dot{\boldsymbol{q}} = \frac{\partial H}{\partial \boldsymbol{p}} \,, \;\; \dot{\boldsymbol{p}} = -\frac{\partial H}{\partial \boldsymbol{q}} \,. \tag{2.6}$$

These are *Hamilton's equations*. The coordinates $\boldsymbol{q}$ and $\boldsymbol{p}$ are referred to as the *canonical* coordinates, where the canonical position q_i and canonical momentum p_i are *canonically conjugate*.

Let us consider how functions of the canonical coordinates evolve in time. We take the total time derivative of some function $f(\boldsymbol{q}, \boldsymbol{p}, t)$,

$$\frac{df}{dt} = \frac{\partial f}{\partial t} + \frac{\partial f}{\partial \boldsymbol{q}} \cdot \dot{\boldsymbol{q}} + \frac{\partial f}{\partial \boldsymbol{p}} \cdot \dot{\boldsymbol{p}} \,. \tag{2.7}$$

Functions, which may be dependent on time, that have a total time derivative equal to zero are called *constants of the motion*. Hamiltonian flows - the evolution of trajectories $(\boldsymbol{q}, \boldsymbol{p})$ - possess a very special property. Consider the probability density function for phase space coordinates $\rho(\boldsymbol{q}, \boldsymbol{p}, t)$ such that $\rho \; d\boldsymbol{q} \cdot d\boldsymbol{p}$ is the probability that the system will be found within the infinitesimal volume $d\boldsymbol{q} \cdot d\boldsymbol{p}$ at time t. The density function must obey the continuity equation

$$\frac{\partial \rho}{\partial t} + \boldsymbol{\nabla} \cdot (\rho \boldsymbol{u}) = 0 \, , \tag{2.8}$$

where in this case $\boldsymbol{u} = (\dot{\boldsymbol{q}}, \dot{\boldsymbol{p}})$. We write this explicitly as

$$\begin{aligned} \frac{\partial \rho}{\partial t} + \boldsymbol{\nabla} \cdot (\rho \boldsymbol{u}) &= \frac{\partial \rho}{\partial t} + \frac{\partial}{\partial \boldsymbol{q}} \cdot (\rho \dot{\boldsymbol{q}}) + \frac{\partial}{\partial \boldsymbol{p}} \cdot (\rho \dot{\boldsymbol{p}}) \\ &= \frac{\partial \rho}{\partial t} + \frac{\partial \rho}{\partial \boldsymbol{q}} \cdot \dot{\boldsymbol{q}} + \frac{\partial \rho}{\partial \boldsymbol{p}} \cdot \dot{\boldsymbol{p}} + \rho \frac{\partial \dot{\boldsymbol{q}}}{\partial \boldsymbol{q}} + \rho \frac{\partial \dot{\boldsymbol{p}}}{\partial \boldsymbol{p}} \\ &= \frac{\partial \rho}{\partial t} + \frac{\partial \rho}{\partial \boldsymbol{q}} \cdot \dot{\boldsymbol{q}} + \frac{\partial \rho}{\partial \boldsymbol{p}} \cdot \dot{\boldsymbol{p}} = 0 \, . \end{aligned} \tag{2.9}$$

By substitution of Eq. (2.6), the continuity equation is equivalent to Eq. (2.7). We therefore see that $d\rho/dt = 0$; the phase space density ρ is a constant of the motion. This is *Liouville's theorem*. If you draw some volume in phase space enclosing a region of coordinates, and evolve those coordinates in time, the volume remains invariant, even if it may stretch or rotate or distort. The motion is *volume preserving*.

Let's revisit Eq. (2.7). Substituting in Eq. (2.6) we obtain

$$\frac{df}{dt} = \frac{\partial f}{\partial t} + \{f, H\} \, , \tag{2.10}$$

where

$$\{f, H\} = \frac{\partial f}{\partial \boldsymbol{q}} \cdot \frac{\partial H}{\partial \boldsymbol{p}} - \frac{\partial f}{\partial \boldsymbol{p}} \cdot \frac{\partial H}{\partial \boldsymbol{q}} \, , \tag{2.11}$$

is the *Poisson bracket* of f and H. It is easy to show that

$$\{q_i, q_j\} = \{p_i, p_j\} = 0 \ , \ \ \{q_i, p_j\} = \delta_{ij} \ . \tag{2.12}$$

The preservation of these *fundamental Poisson brackets* is equivalent to saying that the flow is *symplectic*, or that the flow resides on a symplectic manifold. Note that phase space volume preservation is a necessary but not sufficient condition for symplecticity; the fundamental Poisson brackets must be conserved.

Constants of the motion that do not depend explicitly on time are called *integrals* of the motion, satisfying $\{f, H\} = 0$; f and H are said to be *in involution* in this case. Classical mechanics for (quasi-) periodic systems - such as a pendulum or a particle accelerator or the orbits of planets - really boils down to the search of integrals of the motion. For example, once we have some integral $f_i(\boldsymbol{q}, \boldsymbol{p})$, then we know that the motion lies on the hypersurface

$$f_i(\boldsymbol{q}, \boldsymbol{p}) = \text{constant} \ . \tag{2.13}$$

Obviously, we search for *functionally independent* integrals f_i, such that we cannot write one as a function of the other; functional independence implies that the gradients of each f_i around some point $(\boldsymbol{q}_0, \boldsymbol{p}_0)$ are linearly independent. For an n degree of freedom system, if we can find n functionally independent integrals which are also in involution[1], the system is said to be *Liouville integrable*. In this case, the phase space motion lies specifically on an n-torus. The canonical coordinates for a Liouville integrable system can be transformed via a *canonical transformation* to the *action-angle variables*: $(\boldsymbol{q}, \boldsymbol{p}) \mapsto (\boldsymbol{\phi}, \boldsymbol{J})$. these are canonical coordinates where each momentum J_i is an invariant called the action/amplitude, and each position ϕ_i evolves linearly with time and is called the angle. In this

[1] As we will see later, this basically means that each f_i flow can be treated independently

case, the Hamiltonian is only a function of the actions $H(\boldsymbol{J})$. If the transformation to action-angle variables exists, we can also use the real Floquet variables $(\bar{q}_i, \bar{p}_i) = \left(\sqrt{2J_i}\cos\phi_i, \sqrt{2J_i}\sin\phi_i\right)$. Pictorially, if we look at a Poincaré section, then in Floquet variables the motion forms circles. This is also called the *normal form*.

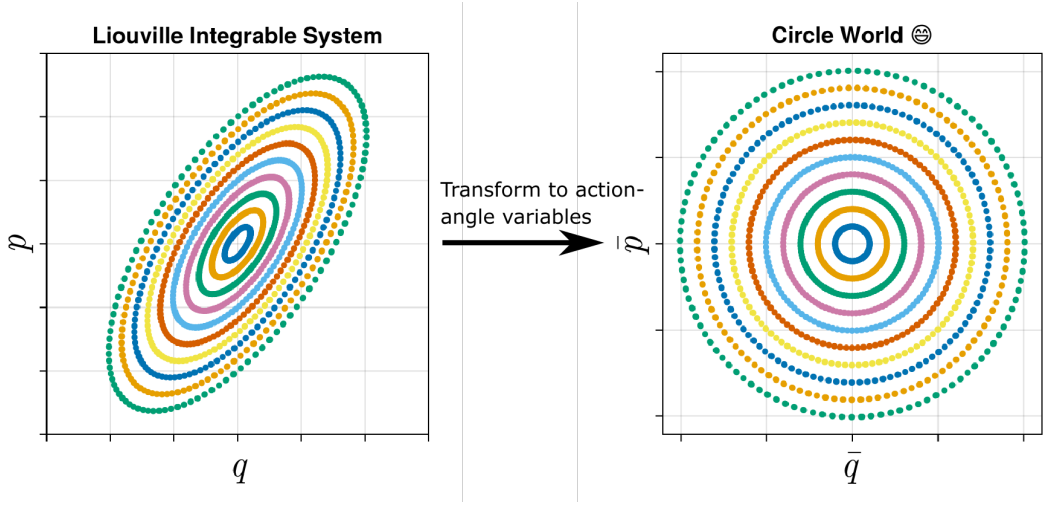

Figure 2.1: Poincaré sections of a 1-D integrable quasiperiodic system, both in its initial canonical coordinates and in real Floquet variables, where $\bar{q} = \sqrt{2J}\cos\phi$ and $\bar{p} = \sqrt{2J}\sin\phi$.

The dynamics in circle world evaluated on a Poincaré section are simply amplitude dependent rotations by an angle $\mu(\boldsymbol{J})$ where $2J_i = \bar{q}_i^2 + \bar{p}_i^2$. Explicitly,

$$\begin{pmatrix} \bar{q}_1 \\ \bar{p}_1 \\ \vdots \\ \bar{q}_n \\ \bar{p}_n \end{pmatrix}_{t_0+T} = \underbrace{\begin{pmatrix} \mathsf{R}_2(\mu_1(\boldsymbol{J})) & & \\ & \ddots & \\ & & \mathsf{R}_2(\mu_n(\boldsymbol{J})) \end{pmatrix} \begin{pmatrix} \bar{q}_1 \\ \bar{p}_1 \\ \vdots \\ \bar{q}_n \\ \bar{p}_n \end{pmatrix}_{t_0}}_{\boldsymbol{r}(\bar{\zeta}_0)}, \quad \mathsf{R}_2(\alpha) = \begin{pmatrix} \cos\alpha & \sin\alpha \\ -\sin\alpha & \cos\alpha \end{pmatrix}. \tag{2.14}$$

Note that the map $\boldsymbol{r}$ is nonlinear due to the μ_i dependence on $\boldsymbol{J}$. In the

normal form, it is clear that each phase space coordinate lies on the torus defined by $\boldsymbol{J}$. As we will see in Sec. 2.2.4, the normal form makes it very easy to analyze the dynamics on each torus. Furthermore, resonances are encapsulated by the $\mu_i(\boldsymbol{J})$. Therefore, our goal is to find some canonical transformation to make the Hamiltonian only a function of the actions $\boldsymbol{J}$. Unfortunately, however, only the very idealized models in the textbooks are fully Liouville integrable. To handle either non-integrable systems or systems that are very hard to solve for the integrals, we need perturbation theory.

2.2 Map-Based Perturbation Theory

2.2.1 Lie Algebraic Methods

We specify a single phase space coordinate as $\boldsymbol{z}(t) = (q_1, p_1, ..., q_n, p_n)^T$ for n-dimensional phase space. The basic approach with perturbation theory is to consider some known, given trajectory $\boldsymbol{z}_0(t)$. We want to understand trajectories *near* this given trajectory. We introduce the new coordinates

$$\boldsymbol{\zeta} = \boldsymbol{z} - \boldsymbol{z}_0 \,, \tag{2.15}$$

which, as a (time-dependent) translation of the original coordinates, are canonical. The new Hamiltonian for these coordinates $H^{\zeta}(\boldsymbol{\zeta}, t)$, given the Hamiltonian in the original coordinates $H^{z}(\boldsymbol{z}, t)$, can be shown [26] to be

$$H^{\zeta}(\boldsymbol{\zeta}, t) = H^{z}(\boldsymbol{z}_0 + \boldsymbol{\zeta}, t) = \sum_{m=2}^{\infty} H_m(\boldsymbol{\zeta}, t) \,, \tag{2.16}$$

where we express it as a Taylor series in $\boldsymbol{\zeta}$ for each homogenous polynomial

of order m specified by H_m. Henceforth, we will work entirely with the canonical coodinates ζ, and therefore write H for H^{ζ}.

The basic idea with perturbation theory is that if this system is Liouville integrable for dynamics to first-order in ζ (corresponding to second-order in the Hamiltonian), then we will solve that part, go into action-angle variables, and then solve sequentially for the higher order parts order-by-order (transforming the dynamics to circle world for each order). At this point, there are two different approaches to perturbation theory that we can take; a time-dependent Hamiltonian approach formulated by Deprit [21], or map-based approach of successive time-independent (autonomous) flows formulated by Dragt and Finn [27][2]. In accelerator physics, our rings are basically sequences of many different kinds of magnets which the beam travels through. This means our accelerator Hamiltonian is almost discontinuous at the magnet edges, which can cause convergence issues for a time-dependent Hamiltonian approach [30, 9, 10]. Furthermore, in accelerator physics, we usually consider the dynamics at specific points in the ring (e.g. a beam position monitor (BPM), or the interaction point). Therefore, a one-turn map-based approach is not only more appropriate from a computational standpoint, but also more natural to the accelerator physicist. We therefore will use the map-based approach of Dragt and Finn.

Let us return to the definition of the Poisson bracket in Eq. (2.11). The Poisson bracket has some interesting properties, that together reveal a rich underlying mathematical structure which we can take advantage of in our quest for circle world. These properties are, for arbitrary functions $f(\zeta, t)$, $g(\zeta, t)$ and $h(\zeta, t)$:

[2]The interested reader is pointed to [40] for a detailed comparison of the two methods.

1. **Anticommutativity:** $\{f, g\} = -\{g, f\}$
2. **Bilinearity:** $\{af + bg, h\} = a\{f, h\} + b\{g, h\}$ and $\{h, af + bg\} = a\{h, f\} + b\{h, g\}$ where $a, b \in \mathbb{R}$
3. **Jacobi condition:** $\{f, \{g, h\}\} + \{g, \{h, f\}\} + \{h, \{f, g\}\} = 0$

There are infinitely many functions of ζ, t which can be formed, all of which satisfy these properties. In math lingo, the set of these functions form a *linear vector space*. With the Poisson bracket as the multiplication operation between such functions, they form a *Lie algebra*. Specifically, for the vector space of functions of the canonical coordinates and time, the *Lie bracket/product* is the Poisson bracket.

Each function in the vector space has an associated *Lie operator*, also called a *vector field*, that can act on another function in the vector space. The Lie operator associated with a function f when acting on a function g, using the notation of Dragt [24], is

$$: f : g = \{f, g\} . \tag{2.17}$$

The Lie operator is a *derivation* of the multiplication rule of the Poisson bracket Lie algebra, in that it acts like the product rule that is taught in introductory calculus (formally Leibniz rule); it can be shown that

$$: f : (gh) = (: f : g)h + g(: f : h) . \tag{2.18}$$

This can be viewed abstractly as a directional derivative of gh along f. This is why $: f :$ is called a vector field; it maps all functions (vectors in this space) to a corresponding "tangent" vector (function). With Eq. (2.17) and (2.11), Eq. (2.6) can be rewritten in terms of the Lie operator $: H :$ of the Hamiltonian $H(\zeta, t)$,

$$\frac{d\zeta}{dt} = - : H : \zeta , \tag{2.19}$$

where the Lie operator acts on each coordinate in ζ. This is quite sensical, if you think about it: the directional derivative of ζ along the Hamiltonian H is the time evolution of ζ. Thus far, we have shown that the space of functions of ζ, t with the Poisson bracket as the multiplication rule forms a Lie algebra. We have also shown that each function in this space has an associated Lie operator, defined by Eq. (2.17). Now we will briefly get a bit abstract. We can form a *second* Lie algebra for the space of *Lie operators*, with the multiplication operation

$$\begin{aligned}
[: f :, : g :] &=: f :: g : - : g :: f : \\
&\qquad \downarrow \text{ Anticommutativity + Jacobi identity} \\
&=: \{f, g\} : \ . \qquad (2.20)
\end{aligned}$$

In the math lingo this means that the two Lie algebras are homomorphic.

Given that Lie operators with the Lie bracket defined in Eq. (2.20) form a Lie algebra, and that this Lie algebra is homomorphic to the Poisson bracket Lie algebra, we can solve Eq. (2.19). If the Hamiltonian H commutes with itself at all times such that

$$\{H(\zeta, t_1), H(\zeta, t_2)\} = 0 \xrightarrow{\text{Eq.(2.20)}} [: H(\zeta, t_1) :, : H(\zeta, t_2) :] = 0 \ , \qquad (2.21)$$

then the solution to Eq. (2.19) is

$$\zeta(t) = \mathcal{M}\, \zeta(t_0) \ , \quad \mathcal{M} = \exp\left(- \int_{t_0}^{t} : H(\zeta(t_0), t') : \ dt' \right) . \qquad (2.22)$$

Per Eq. (2.16), we can write

$$- \int_{t_0}^{t} H(\zeta(t_0), t')\, dt' = \sum_{m=2}^{\infty} h_m(\zeta(t_0), t; t_0) \ , \qquad (2.23)$$

where each h_m is a homogenous polynomial of order m in $\zeta(t_0)$, so that

$$\mathcal{M} = \exp\left(: \sum_{m=2}^{\infty} h_m(\zeta(t_0), t; t_0) : \right) , \qquad (2.24)$$

in the commuting case. This *Lie exponent/Lie transformation* is defined by the exponential series

$$\exp(:f:)g = \sum_{n=0}^{\infty} \frac{:f:^n}{n!} g = g + \{f, g\} + \frac{1}{2!}\{f, \{f, g\}\} + \dots . \tag{2.25}$$

Equation (2.24) shows a significant result: we already know that if the equations of motion are derived from some arbitrary Hamiltonian function, then the motion will be symplectic. Equation (2.24) shows that the exponentiation of the Lie operator for some arbitrary function of phase space *generates a symplectic map*! In the words of Forest [30], we "got ourselves factory for making symplectic... maps". There is another important point to make here; all symplectic maps are canonical transformations. Therefore, with this Lie algebraic framework, we can easily generate canonical transformations. This is fundamental to our quest to find a canonical transformation to the normal form. Using Eqs. (2.18) and (2.25), it can be shown that

$$\exp(:f:)(gh) = [\exp(:f:)g][\exp(:f:)h] . \tag{2.26}$$

The Lie exponent acting on a product of two functions is equal to the Lie exponent acting on each function individually and then taking the product. This result is actually quite interesting: letting $\boldsymbol{\zeta} = (q_1, p_1, ..., q_n, p_n)^T$, suppose we have a function $g_{11}(\boldsymbol{\zeta}) = c_{11} q_1 p_1$ where $c_{11} \in \mathbb{R}$. Then we know that $\exp(:f:)g_{11}(\boldsymbol{\zeta}) = [\exp(:f:)q_1][\exp(:f:)p_1] = g_{11}[\exp(:f:)\boldsymbol{\zeta}]$. More generally, suppose we have a function which is a monomial with arbitrary orders in each component of $\boldsymbol{\zeta}$, with orders specified by the multi-index $\boldsymbol{\alpha} = (\alpha_{q1}, \alpha_{p1}, ..., \alpha_{qn}, \alpha_{pn}), \alpha_i \in \mathbb{N}_0$,

$$g_{\boldsymbol{\alpha}}(\boldsymbol{\zeta}) = c_{\alpha} \boldsymbol{\zeta}^{\boldsymbol{\alpha}} , \; c_{\boldsymbol{\alpha}} \in \mathbb{R} . \tag{2.27}$$

By Eq. (2.26), the action of $\exp(:f:)$ on $g_{\boldsymbol{\alpha}}$ can be shown to be

$$\exp(:f:)g_{\boldsymbol{\alpha}}(\boldsymbol{\zeta}) = g_{\boldsymbol{\alpha}}[\exp(:f:)\boldsymbol{\zeta}] . \tag{2.28}$$

Because we can expand any general function $g(\boldsymbol{\zeta})$ as a Taylor series in $\boldsymbol{\zeta}$, and because $\exp(:f:)$ is a linear operator, we obtain

$$\exp(:f:)g(\boldsymbol{\zeta}) = g[\exp(:f:)\boldsymbol{\zeta}] = g \circ [\exp(:f:)\boldsymbol{\zeta}] \,, \tag{2.29}$$

where $\circ$ denotes composition. This is a remarkable result; the Lie transform of an arbitrary function is equal to the Lie transform of its arguments, plugged into that same function. Because the Lie transform of a function results in another function, then

$$\exp(:f:)\exp(:g:)h(\boldsymbol{\zeta}) = h \circ [\exp(:f:)\exp(:g:)\boldsymbol{\zeta}] \,, \tag{2.30}$$

$$= h \circ [\exp(:g:)\boldsymbol{\zeta}] \circ [\exp(:f:)\boldsymbol{\zeta}] \,. \tag{2.31}$$

Note how the order of the Lie exponents is "reversed" when acting on functions of phase space.

Using these Lie exponent identities, and with Eq. (2.24), we see that we can rewrite the commuting Hamiltonian case in Eq. (2.22) as

$$\boldsymbol{\zeta}(t) = \mathcal{M}\boldsymbol{\zeta}(t_0) = \boldsymbol{m}[\boldsymbol{\zeta}(t_0)] \,, \tag{2.32}$$

where $\boldsymbol{m}$ is a map constructed by $\mathcal{M}\boldsymbol{\zeta}(t_0)$ that maps $\boldsymbol{\zeta}(t_0)$ to $\boldsymbol{\zeta}(t)$. Henceforth we refer to the construct $\boldsymbol{m}$ as a differential-algebraic (DA) map.

If the Hamiltonian does not commute with itself at all times, then using Eq. (2.31) we can write the solution as a product of the Lie exponents for each timeframe where it does commute,

$$\zeta(t_n) = \mathcal{M}\zeta(t_0) \,, \tag{2.33}$$

where

$$\mathcal{M} = \mathcal{M}_1 ... \mathcal{M}_n = \exp\left(:\sum_{m=2}^{\infty} h_m(\boldsymbol{\zeta}(t_0), t_1; t_0):\right) ... \exp\left(:\sum_{m=2}^{\infty} h_m(\boldsymbol{\zeta}(t_{n-1}), t_n; t_{n-1}):\right), \tag{2.34}$$

so that

$$\boldsymbol{\zeta}(t_n) = \boldsymbol{m}_n \circ \boldsymbol{m}_{n-1} ... \circ \boldsymbol{m}_1 \circ \boldsymbol{\zeta}(t_0) \, . \tag{2.35}$$

Note again the "reverse order" of $\mathcal{M}$. In this case, $\mathcal{M}$ is not a single Lie exponent, but a product of many. For this reason, we refer to $\mathcal{M}$ as a *Lie map/compositional map*. One might attempt to combine the Lie exponents into a single Lie exponent using the Baker–Campbell–Hausdorff (BCH) formula, which tells us how to combine Lie exponents of two vectors X and Y in a Lie algebra,

$$\exp(X)\exp(Y) = \exp\left(X + Y + \frac{1}{2}[X,Y] + \frac{1}{12}[X,[X,Y]] + \frac{1}{12}[Y,[Y,X]] + ...\right), \tag{2.36}$$

where we have truncated the higher commutators of X and Y. The resulting series will not converge in general; only in the cases of small X and Y such that $\exp(X)$ and $\exp(Y)$ are "near-identity" transformations. We will see later that in our analyses the BCH formula is never really explicitly used. However we will use that property that if $[X,Y] = 0$, then the resulting Lie exponent is just $X + Y$, and that we can apply $\exp(X)$ and $\exp(Y)$ in any order. For the general non-commuting Hamiltonian case defined in Eq. (2.34), we cannot always combine the Lie exponents into a single Lie exponent per the BCH formula divergence, hence why we do not generally refer to $\mathcal{M}$ as a Lie exponent. Ultimately, we see that for a general Lie map $\mathcal{M}$ which may be a product of infinitely many Lie transformations,

$$\mathcal{M}f = f \circ \boldsymbol{m} \, , \quad \boldsymbol{m} = \mathcal{M}\boldsymbol{\zeta} \, . \tag{2.37}$$

This is why $\mathcal{M}$ is called a compositional map. It also called a composition/Koopman operator. It is important to remember that while the DA map it generates $\boldsymbol{m}$ operates on the phase space coordinates, the compositional map $\mathcal{M}$ operates on *functions* of the phase space coordinates; this has the profound implication of replacing our nonlinear problem of finite dimension, with a linear problem of infinite dimension. To understand this, consider how our space

of the phase space functions is infinite dimensional. Because we are expanding in powers of $\boldsymbol{\zeta}$, let's use the monomial basis as defined in Eq. (2.27) for the basis functions to construct arbitrary functions of phase space. Consider a 1-D system where we write $\boldsymbol{\zeta} = (q, p)$. If we truncate at 2nd order in $\boldsymbol{\zeta}$, then a general function of phase space can be written as

$$f(\boldsymbol{\zeta}) = \begin{pmatrix} c_{00} \\ c_{10} \\ c_{01} \\ c_{20} \\ c_{11} \\ c_{02} \end{pmatrix} \cdot \begin{pmatrix} 1 \\ q \\ p \\ q^2 \\ qp \\ p^2 \end{pmatrix} . \tag{2.38}$$

where "$\cdot$" is the dot product. The map $\boldsymbol{m}$ can be written as

$$\boldsymbol{m}(\boldsymbol{\zeta}) = \begin{pmatrix} 0 & m_{1,10} & m_{1,01} & m_{1,20} & m_{1,11} & m_{1,02} \\ 0 & m_{2,10} & m_{2,01} & m_{2,20} & m_{2,11} & m_{2,02} \end{pmatrix} \begin{pmatrix} 1 \\ q \\ p \\ q^2 \\ qp \\ p^2 \end{pmatrix} . \tag{2.39}$$

where we see that $m_{1,00} = m_{2,00} = 0$ due to the necessary choice of coordinates in Eq. (2.15) which has the mapping $\boldsymbol{m}(\mathbf{0}) = \mathbf{0}$. Note that these vectors and matrices would be infinite dimensional if we did not truncate at order 2. We can then write

$$
\begin{aligned}
& f \circ \boldsymbol{m} \\
&= \begin{pmatrix} c_{00} \\ c_{10} \\ c_{01} \\ c_{20} \\ c_{11} \\ c_{02} \end{pmatrix} \cdot \begin{pmatrix} 1 \\ m_{1,10}q + m_{1,01}p + m_{1,20}q^2 + m_{1,11}qp + m_{1,02}p^2 \\ m_{2,10}q + m_{2,01}p + m_{2,20}q^2 + m_{2,11}qp + m_{2,02}p^2 \\ m_{1,10}^2 q^2 + 2m_{1,10}m_{1,01}pq + m_{1,01}^2 p^2 \\ m_{1,10}m_{2,10}q^2 + (m_{1,10}m_{2,01} + m_{2,10}m_{1,01})qp + m_{1,01}m_{2,01}p^2 \\ m_{2,10}^2 q^2 + 2m_{2,10}m_{2,01}pq + m_{2,01}^2 p^2 \end{pmatrix} \\
&= \underbrace{\begin{bmatrix} \begin{pmatrix} 1 & 0 & 0 & 0 & 0 & 0 \\ 0 & m_{1,10} & m_{2,10} & 0 & 0 & 0 \\ 0 & m_{1,01} & m_{2,01} & 0 & 0 & 0 \\ 0 & m_{1,20} & m_{2,20} & m_{1,10}^2 & m_{1,10}m_{2,10} & m_{2,10}^2 \\ 0 & m_{1,11} & m_{2,11} & 2m_{1,10}m_{1,01} & m_{1,10}m_{2,01} + m_{2,10}m_{1,01} & 2m_{2,10}m_{2,01} \\ 0 & m_{1,02} & m_{2,02} & m_{1,01}^2 & m_{1,01}m_{2,01} & m_{2,01}^2 \end{pmatrix} \end{bmatrix}}_{\mathcal{M}} \underbrace{\begin{bmatrix} \begin{pmatrix} c_{00} \\ c_{10} \\ c_{01} \\ c_{20} \\ c_{11} \\ c_{02} \end{pmatrix} \end{bmatrix}}_{f} \cdot \begin{pmatrix} 1 \\ q \\ p \\ q^2 \\ qp \\ p^2 \end{pmatrix},
\end{aligned}
\tag{2.40}
$$

where the compositional map $\mathcal{M}$ has been written as a matrix. Here it is clear how the compositional map acts on functions of phase space by a linear transformation of each monomial coefficient; it has replaced our nonlinear problem of finite dimension with a linear problem of infinite dimension.

We remark here that if we have found some integral of the motion/invariant $J_i(\zeta)$, then $\mathcal{M}J_i = J_i$. These invariants could be computed in the monomial basis by finding the eigenvectors with unit eigenvalue of the matrix corresponding to $\mathcal{M}$ in Eq. (2.40).

There is one more tool we need before we can go to the normal form. It has

been shown by Dragt and Finn [28] that a symplectic compositional map $\mathcal{M}$ can be written as a product of infinite Lie transformations

$$\mathcal{M} = \underbrace{\mathcal{L}}_{\substack{\text{Linear}\\ \text{part}}} \underbrace{\exp(:f_3:)\exp(:f_4:)\exp(:f_5:)...}_{\text{Nonlinear part}} , \tag{2.41}$$

where each $f_m(\boldsymbol{\zeta}, t)$ is a homogeneous polynomial of order m in $\boldsymbol{\zeta}$. For brevity we will not include the proof here.

We now have all the tools we need, and a goal: given some map $\boldsymbol{m}$, we need to compute some symplectic transformation $\boldsymbol{a}$ to get the $\boldsymbol{r}$ in Eq. (2.14), or the normal form,

$$\boldsymbol{r} = \boldsymbol{a}^{-1} \circ \boldsymbol{m} \circ \boldsymbol{a} = \left(\mathcal{A}\mathcal{M}\mathcal{A}^{-1}\right)\boldsymbol{\zeta} = \mathcal{R}\boldsymbol{\zeta} \ . \tag{2.42}$$

By expanding around the fixed point, we can compute $\boldsymbol{a}$ as a Taylor series in $\boldsymbol{\zeta}$, truncated at some chosen order, and symplectic up to that order.

Before we describe the algorithm to compute $\boldsymbol{a}$, let's consider what the compositional map $\mathcal{R}$ actually looks like. We know that its corresponding DA map, $\boldsymbol{r}$, is that in Eq. (2.14). It can be shown that, for $n \in \mathbb{N}_0$ and $\mu_i \in \mathbb{R}$,

$$(:\mu_i J_i:)^n \bar{q}_i = \frac{\mu_i^n}{2^n}\left(:\bar{q}_i^2 + \bar{p}_i^2:\right)^n \bar{q}_i \qquad = \begin{cases} (-1)^{n/2}\mu_i^n \bar{q}_i & \text{for even } n \\ (-1)^{(n+1)/2}\mu_i^n \bar{p}_i & \text{for odd } n \end{cases} , \tag{2.43}$$

$$(:\mu_i J_i:)^n \bar{p}_i = \frac{\mu_i^n}{2^n}\left(:\bar{q}_i^2 + \bar{p}_i^2:\right)^n \bar{p}_i \qquad = \begin{cases} (-1)^{n/2}\mu_i^n \bar{p}_i & \text{for even } n \\ (-1)^{(n-1)/2}\mu_i^n \bar{q}_i & \text{for odd } n \end{cases} . \tag{2.44}$$

Considering Eqs. (2.43) and (2.44) with Eq. (2.25), and the Taylor expansions for sin and cos, we can write

$$\exp(:\mu_i J_i:)\bar{q}_i = \cos(\mu_i)\bar{q}_i - \sin(\mu_i)\bar{p}_i \ , \tag{2.45}$$

$$\exp(:\mu_i J_i:)\bar{p}_i = \sin(\mu_i)\bar{q}_i + \cos(\mu_i)\bar{p}_i \ . \tag{2.46}$$

Using the fundamental Poisson brackets in Eq. (2.12), we have $\{J_i, J_j\} = \{\bar{q}_i, \bar{q}_j\} = \{\bar{p}_i, \bar{p}_j\} = 0$ and $\{\bar{q}_i, \bar{p}_j\} = \delta_{ij}$. Therefore,

$$\exp\left(-:\boldsymbol{\mu}\cdot\boldsymbol{J}:\right)\bar{\boldsymbol{\zeta}} = \begin{pmatrix} \mathsf{R}_2(\mu_1) & & \\ & \ddots & \\ & & \mathsf{R}_2(\mu_n) \end{pmatrix}\bar{\boldsymbol{\zeta}}\,. \tag{2.47}$$

This almost looks like the $\boldsymbol{r}$ in Eq. (2.14), except for the fact that the rotations are independent of $\boldsymbol{J}$. We want to instead have $\boldsymbol{\mu} = \boldsymbol{\mu}(\boldsymbol{J})$. In perturbation theory, our goal is to write this $\boldsymbol{\mu}(\boldsymbol{J})$ as a truncated power series in the $\boldsymbol{J}$. Let's revisit Eqs. (2.43) and (2.44) in a more general sense, where we instead evaluate it for the monomial $c_{\boldsymbol{\alpha}}\boldsymbol{J}^{\boldsymbol{\alpha}}$, where $\boldsymbol{\alpha}$ is a multi-index specifying the orders of each J_i. Specifically, $\boldsymbol{\alpha} = (\alpha_1, ..., \alpha_n),\ \alpha_i \in \mathbb{N}_0$. To do so, we will need to derive a couple more identities. For notational brevity, we define "unit" vectors of the multi-index, $\hat{\boldsymbol{\alpha}}_i$, such that we can write $\boldsymbol{\alpha} = \alpha_1\hat{\boldsymbol{\alpha}}_{\boldsymbol{1}} + ... + \alpha_n\hat{\boldsymbol{\alpha}}_{\boldsymbol{n}}$. We can then write

$$\begin{aligned}
:c_{\boldsymbol{\alpha}}J^{\boldsymbol{\alpha}}:\bar{q}_i &= c_{\boldsymbol{\alpha}}:J_i^{\alpha_i}\boldsymbol{J}^{\boldsymbol{\alpha}-\alpha_i\hat{\boldsymbol{\alpha}}_i}:\bar{q}_i \\
&\quad\downarrow \text{ Leibniz rule + fundamental Poisson bracket} \\
&= c_{\boldsymbol{\alpha}}\boldsymbol{J}^{\boldsymbol{\alpha}-\alpha_i\hat{\boldsymbol{\alpha}}_i}:J_i^{\boldsymbol{\alpha_i}}:\bar{q}_i \\
&= c_{\boldsymbol{\alpha}}\boldsymbol{J}^{\boldsymbol{\alpha}-\alpha_i\hat{\boldsymbol{\alpha}}_i}:\frac{\left(\bar{q}_i^2+\bar{p}_i^2\right)^{\alpha_i}}{2^{\alpha_i}}:\bar{q}_i \\
&= -c_{\boldsymbol{\alpha}}\boldsymbol{J}^{\boldsymbol{\alpha}-\alpha_i\hat{\boldsymbol{\alpha}}_i}\left(\alpha_i\frac{\left(\bar{q}_i^2+\bar{p}_i^2\right)^{\alpha_i-1}}{2^{\alpha_i}}2\bar{p}_i\right) \\
&= -c_{\boldsymbol{\alpha}}\alpha_i\boldsymbol{J}^{\boldsymbol{\alpha}-\alpha_i\hat{\boldsymbol{\alpha}}_i}J_i^{\alpha_i-1}\bar{p}_i \\
&= -c_{\boldsymbol{\alpha}}\frac{\partial\boldsymbol{J}^{\boldsymbol{\alpha}}}{\partial J_i}\bar{p}_i\,.
\end{aligned} \tag{2.48}$$

Likewise,

$$:c_{\boldsymbol{\alpha}}J^{\boldsymbol{\alpha}}:\bar{p}_i = c_{\boldsymbol{\alpha}}\frac{\partial\boldsymbol{J}^{\boldsymbol{\alpha}}}{\partial J_i}\bar{q}_i\,. \tag{2.49}$$

Let $\boldsymbol{\beta}$ correspond to another multi-index. Using the Leibniz rule, it is easy to

show that $\{\boldsymbol{J}^{\boldsymbol{\alpha}}, \boldsymbol{J}^{\boldsymbol{\beta}}\} = 0$. Then, using the Leibniz rule again,

$$: \boldsymbol{J}^{\boldsymbol{\alpha}} : (\boldsymbol{J}^{\boldsymbol{\beta}} \bar{q}_i) = -\boldsymbol{J}^{\boldsymbol{\beta}} \frac{\partial \boldsymbol{J}^{\boldsymbol{\alpha}}}{\partial J_i} \bar{p}_i \,, \tag{2.50}$$

$$: \boldsymbol{J}^{\boldsymbol{\alpha}} : (\boldsymbol{J}^{\boldsymbol{\beta}} \bar{p}_i) = \boldsymbol{J}^{\boldsymbol{\beta}} \frac{\partial \boldsymbol{J}^{\boldsymbol{\alpha}}}{\partial J_i} \bar{q}_i \,. \tag{2.51}$$

Therefore, Eqs. (2.43) and (2.44) can be written generally for one monomial in $\boldsymbol{J}$ as

$$(: c_{\boldsymbol{\alpha}} \boldsymbol{J}^{\boldsymbol{\alpha}} :)^n \bar{q}_i = \begin{cases} (-1)^{n/2} \left(c_{\boldsymbol{\alpha}} \frac{\partial \boldsymbol{J}^{\boldsymbol{\alpha}}}{\partial J_i} \right)^n \bar{q}_i & \text{for even } n \\ (-1)^{(n+1)/2} \left(c_{\boldsymbol{\alpha}} \frac{\partial \boldsymbol{J}^{\boldsymbol{\alpha}}}{\partial J_i} \right)^n \bar{p}_i & \text{for odd } n \end{cases} , \tag{2.52}$$

$$(: c_{\boldsymbol{\alpha}} \boldsymbol{J}^{\boldsymbol{\alpha}} :)^n \bar{p}_i = \begin{cases} (-1)^{n/2} \left(c_{\boldsymbol{\alpha}} \frac{\partial \boldsymbol{J}^{\boldsymbol{\alpha}}}{\partial J_i} \right)^n \bar{p}_i & \text{for even } n \\ (-1)^{(n-1)/2} \left(c_{\boldsymbol{\alpha}} \frac{\partial \boldsymbol{J}^{\boldsymbol{\alpha}}}{\partial J_i} \right)^n \bar{q}_i & \text{for odd } n \end{cases} . \tag{2.53}$$

Ultimately, we want to build up a Taylor polynomial in $\boldsymbol{J}$, a sum of many monomials. Letting $a_{\boldsymbol{\alpha}} \in \mathbb{R}$ and $b_{\boldsymbol{\beta}} \in \mathbb{R}$, we can write

$$: \left(\sum_{\boldsymbol{\alpha}} a_{\boldsymbol{\alpha}} \boldsymbol{J}^{\boldsymbol{\alpha}} \right) : \left[\left(\sum_{\boldsymbol{\beta}} b_{\boldsymbol{\beta}} \boldsymbol{J}^{\boldsymbol{\beta}} \right) f(\bar{\boldsymbol{\zeta}}) \right] = \left(\sum_{\boldsymbol{\beta}} b_{\boldsymbol{\beta}} \boldsymbol{J}^{\boldsymbol{\beta}} \right) : \left(\sum_{\boldsymbol{\alpha}} a_{\boldsymbol{\alpha}} \boldsymbol{J}^{\boldsymbol{\alpha}} \right) : f(\bar{\boldsymbol{\zeta}}) \,. \tag{2.54}$$

Because the entire sum in $\boldsymbol{J}_{\boldsymbol{\beta}}$ is a function that commutes with the function of the Lie operator, it can be "factored out". This shows that, given the identities we have derived, all we have to do is sum over the multi-index.

Putting this all together,

$$\exp\left(- : \sum_{\boldsymbol{\alpha}} c_{\boldsymbol{\alpha}} \boldsymbol{J}^{\boldsymbol{\alpha}} : \right) \bar{q}_i = \cos\left(\mu_i(\boldsymbol{J})\right) \bar{q}_i + \sin\left(\mu_i(\boldsymbol{J})\right) \bar{p}_i \,, \tag{2.55}$$

$$\exp\left(- : \sum_{\boldsymbol{\alpha}} c_{\boldsymbol{\alpha}} \boldsymbol{J}^{\boldsymbol{\alpha}} : \right) \bar{p}_i = -\sin\left(\mu_i(\boldsymbol{J})\right) \bar{q}_i + \cos\left(\mu_i(\boldsymbol{J})\right) \bar{p}_i \,, \tag{2.56}$$

where

$$\mu_i(\boldsymbol{J}) = \frac{\partial}{\partial J_i} \sum_{\boldsymbol{\alpha}} c_{\boldsymbol{\alpha}} \boldsymbol{J}^{\boldsymbol{\alpha}} \,. \tag{2.57}$$

The sum $\sum_{\boldsymbol{\alpha}} c_{\boldsymbol{\alpha}} \boldsymbol{J}^{\boldsymbol{\alpha}}$ can be expressed in terms of $\boldsymbol{\mu}$ by taking the path integral,

$$\int^{\boldsymbol{J}} \boldsymbol{\mu}(\boldsymbol{J}) \cdot d\boldsymbol{J} = \sum_{\boldsymbol{\alpha}} c_{\boldsymbol{\alpha}} \boldsymbol{J}^{\boldsymbol{\alpha}} \,. \tag{2.58}$$

Finally,

$$\mathcal{R}\bar{\boldsymbol{\zeta}} = \exp\left(-: \int^{\boldsymbol{J}} \boldsymbol{\mu}(\boldsymbol{J}) \cdot d\boldsymbol{J} :\right)\bar{\boldsymbol{\zeta}} = \underbrace{\begin{pmatrix} \mathsf{R}_2(\mu_1(\boldsymbol{J})) & & \\ & \ddots & \\ & & \mathsf{R}_2(\mu_n(\boldsymbol{J})) \end{pmatrix}\begin{pmatrix} \bar{q}_1 \\ \bar{p}_1 \\ \vdots \\ \bar{q}_n \\ \bar{p}_n \end{pmatrix}}_{\boldsymbol{r}(\bar{\zeta})} . \tag{2.59}$$

The compositional map $\mathcal{R}$ is a Lie exponent which is *only* a function of the actions $\boldsymbol{J}$. When we consider the Hamiltonian in action-angle variables which must only be a function of $\boldsymbol{J}$, and Eq. (2.22), this is exactly the result we expect. Thus the normalizing transformation $\mathcal{A}$ should transform $\mathcal{M}$ such that the Lie exponent is only a function of the actions.

2.2.2 Normal Form

To compute $\mathcal{A}$, we will first do the linear part, and then apply an order-by-order algorithm to do the nonlinear part. This algorithm is implemented for the vector field described in Sec. 2.2.3, in the software package `NonlinearNormalForm.jl`.

Linear Part

To normalize the linear part of a map $\boldsymbol{m}$, we consider the linear part of $\mathcal{M}$ in the matrix representation in Eq. (2.40), which we refer to as M^T. Being in the mono-

mial basis, we see that this matrix is the transpose of the matrix representing the linear transport in the basis of phase space coordinates shown in Eq. (2.39), which we refer to as M.

First, let us consider some important properties of M. Because $\boldsymbol{m}$ is a symplectic map, the fundamental Poisson brackets must be preserved after transfer through $\boldsymbol{m}$. For general functions of phase space f and g, we can rewrite the Poisson bracket definition as

$$\{f,g\} = \begin{pmatrix} \frac{\partial f}{\partial \zeta_1} \\ \frac{\partial f}{\partial \zeta_2} \\ \vdots \\ \frac{\partial f}{\partial \zeta_{2n-1}} \\ \frac{\partial f}{\partial \zeta_{2n}} \end{pmatrix}^T \underbrace{\begin{pmatrix} \mathsf{S}_2 & & \\ & \ddots & \\ & & \mathsf{S}_2 \end{pmatrix}}_{\mathsf{S}} \begin{pmatrix} \frac{\partial g}{\partial \zeta_1} \\ \frac{\partial g}{\partial \zeta_2} \\ \vdots \\ \frac{\partial g}{\partial \zeta_{2n-1}} \\ \frac{\partial g}{\partial \zeta_{2n}} \end{pmatrix} = (\boldsymbol{\nabla} f)^T \mathsf{S} (\boldsymbol{\nabla} g), \quad \mathsf{S}_2 = \begin{pmatrix} 0 & 1 \\ -1 & 0 \end{pmatrix}. \tag{2.60}$$

The matrix S captures the fundamental Poisson brackets,

$$\{\zeta_i, \zeta_j\} = \mathsf{S}_{ij} \,. \tag{2.61}$$

For a symplectic map $\boldsymbol{m}(\boldsymbol{\zeta}_0) = \boldsymbol{\zeta}_f$,

$$\{\zeta_{0,i}, \zeta_{0,j}\} = \{m_i(\boldsymbol{\zeta}_0), m_j(\boldsymbol{\zeta}_0)\} = \mathsf{S}_{ij} \,, \tag{2.62}$$

where we are *evaluating both Poisson brackets wrt the initial coordinates* (e.g. $\partial/\partial\zeta_{0,i}$). Using Eq. (2.60),

$$(\boldsymbol{\nabla} m_i)^T \mathsf{S} (\boldsymbol{\nabla} m_j) = \mathsf{S}_{ij} \,. \tag{2.63}$$

Note that $\partial_j m_i = \mathsf{M}_{ij} + N_{ij}(\boldsymbol{\zeta}_0)$. Plugging this into Eq. (2.63),

$$\begin{aligned} \mathsf{S}_{ij} = (\partial_k m_i)\mathsf{S}_{k\ell}(\partial_\ell m_j) &= [\mathsf{M}_{ik} + N_{ik}(\boldsymbol{\zeta}_0)]\mathsf{S}_{k\ell}[\mathsf{M}_{j\ell} + N_{j\ell}(\boldsymbol{\zeta}_0)] \\ &= \mathsf{M}_{ik}\mathsf{S}_{k\ell}\mathsf{M}_{j\ell} + O(\boldsymbol{\zeta}_0) \,. \end{aligned} \tag{2.64}$$

Collecting terms in the above expression, to satisfy the symplectic condition we see that $O(\zeta_0) = 0$ and

$$\mathsf{M}\mathsf{S}\mathsf{M}^T = \mathsf{S} \, . \tag{2.65}$$

Matrices which satisfy Eq. (2.65) are called symplectic matrices. Using Eq. (2.65) and $\det(\mathsf{S}) = 1$, it is easy to see that $\det(\mathsf{M}) = \pm 1$. In fact, it can be shown that symplectic matrices always have $\det(\mathsf{M}) = +1$ specifically. Furthermore, using the fact that $\mathsf{S}^T = \mathsf{S}^{-1}$, it can be shown that

$$\mathsf{M}^T\mathsf{S}\mathsf{M} = \mathsf{S} \, . \tag{2.66}$$

We now consider the eigenvectors of a symplectic matrix. Firstly, for a real M with eigenvector $\boldsymbol{v}_i$ and eigenvalue λ_i, we know that $\boldsymbol{v}_i^*$ is also an eigenvector with eigenvalue λ_i^*. Furthermore, it is easy to show that

$$\mathsf{M}^{-T} = \mathsf{S}\mathsf{M}\mathsf{S}^{-1} \, . \tag{2.67}$$

M^{-T} and M are similar matrices; they must share the same eigenvalues. And if λ_i is an eigenvalue of M, then $1/\lambda_i$ must be an eigenvalue of M^{-1}, which must also be an eigenvalue of M^{-T}. Therefore, for a symplectic matrix M with eigenvalue λ_i, $1/\lambda_i$ and λ_i^* must also be eigenvalues.

If we decompose an arbitrary phase space coordinate ζ as a linear combination of the eigenvectors, we see that for linear stable long-term motion, with repeated application of M, all eigenvalues must lie on the unit circle in the complex plane. Else, the phase space coordinate will "blow-up". In this case, for some eigenvalue $\lambda_i = e^{\mathrm{i}\mu_i}$, we have $1/\lambda_i = \lambda_i^*$ also as an eigenvalue.

Letting V denote a matrix where each pair of columns are a pair of the complex-conjugate eigenvectors, the diagonalization of M looks like

$$\mathsf{VMV}^{-1} = \begin{pmatrix} e^{-\mathrm{i}\mu_1} & & & & \\ & e^{+\mathrm{i}\mu_1} & & & \\ & & \ddots & & \\ & & & e^{-\mathrm{i}\mu_n} & \\ & & & & e^{+\mathrm{i}\mu_n} \end{pmatrix}. \tag{2.68}$$

We see that a similarity transformation of M to the new basis defined with V gives us rotations in the complex plane - this is a complex representation of the linear normal form! This is called the *phasors basis*. From here, we can now easily apply another transformation to get our real $\boldsymbol{r}$ as in Eq. (2.14) in real Floquet variables. Letting

$$\mathsf{C} = \begin{pmatrix} \mathsf{C}_2 & & \\ & \ddots & \\ & & \mathsf{C}_2 \end{pmatrix}, \quad \mathsf{C}_2 = \frac{1}{\sqrt{2}} \begin{pmatrix} 1 & 1 \\ -\mathrm{i} & \mathrm{i} \end{pmatrix}, \tag{2.69}$$

we can write

$$\mathsf{CVMV}^{-1}\mathsf{C}^{-1} = \mathsf{R}(\boldsymbol{\mu}) = \begin{pmatrix} \mathsf{R}_2(\mu_1) & & \\ & \ddots & \\ & & \mathsf{R}_2(\mu_n) \end{pmatrix}, \tag{2.70}$$

where the matrix R_2 is defined in Eq. (2.14). For a symplectic matrix M, we see that CV defines *a* linear transformation where the motion lies on circles.

So, because the compositional map $\mathcal{A}$ is defined in the monomial basis, in order to compute the linear part as a matrix, which we will refer to as A, do we just need to repeat this above process for the matrix M^T? Not quite! One important caveat that we overlooked was that the transformation CV must be

symplectic. Letting V now denote the eigenvectors of M^T, we now require that

$$\begin{aligned} \mathsf{V}^T\mathsf{C}^T\mathsf{S}\mathsf{C}\mathsf{V} &= \mathrm{i}\mathsf{V}^T\mathsf{S}\mathsf{V} = \mathsf{S}\,, \\ \rightarrow \mathsf{V}^T\mathsf{S}\mathsf{V} &= -\mathrm{i}\mathsf{S}\,. \end{aligned} \tag{2.71}$$

The eigenvectors must be normalized such that Eq. (2.71) is satisfied in order to ensure symplecticity. Once this is done, we have for the linear part of $\mathcal{A}$ the matrix $\mathsf{A} = \mathsf{V}^{-1}\mathsf{C}^{-1}$. The compositional map which normalizes the linear part of $\mathcal{M}$ (corresponding to the matrix A) we refer to as $\mathcal{A}_1$.

We remark that A is not unique; we see in Eq. (2.70) that the result is a block diagonal "rotation" matrix with SO(2) matrices along the diagonal. The SO(2) group is abelian, so $\mathsf{R}_2(\alpha_1)\mathsf{R}_2(\alpha_2)\mathsf{R}_2(\alpha_1)^{-1} = \mathsf{R}_2(\alpha_2)$. Therefore we could choose any $\mathsf{A} = \mathsf{C}^{-1}\mathsf{V}^{-1}\mathsf{R}^{-1}(\boldsymbol{\alpha})$ where $\boldsymbol{\alpha}$ is a vector of arbitrary phases, and still get the $\mathsf{R}(\boldsymbol{\mu})$ in Eq. (2.14). In fact, this property extends to nonlinear (amplitude-dependent) rotations too.

Nonlinear Part

Applying $\mathcal{A}_1$ to a map $\mathcal{M}$ truncated at order k, we have

$$\begin{aligned} \mathcal{N}_1 = \mathcal{A}_1\mathcal{M}\mathcal{A}_1^{-1} &= \mathcal{A}_1\mathcal{L}\exp(:f_3:)\ldots\exp(:f_k:)\mathcal{A}_1^{-1} \\ &= \underbrace{\mathcal{A}_1\mathcal{L}\mathcal{A}_1^{-1}}_{\mathcal{R}_1}\mathcal{A}_1\exp(:f_3:)\mathcal{A}_1^{-1}\ldots\mathcal{A}_1\exp(:f_k:)\mathcal{A}_1^{-1} \\ &= \mathcal{R}_1\exp(\mathcal{A}_1 : f_3 : \mathcal{A}_1^{-1})\ldots\exp(\mathcal{A}_1 : f_k : \mathcal{A}_1^{-1})\,, \end{aligned} \tag{2.72}$$

where we have used the general result that $\mathcal{M}\exp(:f:)\mathcal{M}^{-1} = \exp(\mathcal{M} : f : \mathcal{M}^{-1})$, as can be shown using Eq. (2.25). Note that we are specifying the linear normalized map with an underscore "1", while it would be generated from a Lie operator that is a homogeneous polynomial of order 2; we will use the convention

that the subscript of a compositional map will specify the order corresponding to the map, while the subscript of the Lie operator will specify the order of the Lie operator. Using a test function g and letting $\boldsymbol{a}_1$ be the DA map corresponding to $\mathcal{A}_1$ we see that

$$\begin{aligned}\mathcal{A}_1 : f_k : \mathcal{A}_1^{-1} g &= \mathcal{A}_1 : f_k : (g \circ \boldsymbol{a}_1^{-1}) \\ &= \mathcal{A}_1\{f_k, g \circ \boldsymbol{a}_1^{-1}\} \\ &= \{f_k, g \circ \boldsymbol{a}_1^{-1}\} \circ \boldsymbol{a}_1 \\ &= \{f_k \circ \boldsymbol{a}_1, g\}\,, \end{aligned} \tag{2.73}$$

so

$$\mathcal{A}_1 : f_k : \mathcal{A}_1^{-1} =: \mathcal{A}_1 f_k :=: f_k \circ \boldsymbol{a}_1 :\,, \tag{2.74}$$

and therefore

$$\mathcal{N}_1 = \mathcal{A}_1 \mathcal{M} \mathcal{A}_1^{-1} = \mathcal{R}_1 \exp(: \mathcal{A}_1 f_3 :) \ldots \exp(: \mathcal{A}_1 f_k :)\,. \tag{2.75}$$

After the linear normalization, we see that the linear part of the map is an amplitude-**independent** rotation, and that the nonlinear part is unchanged except for being transformed into Floquet variables. In order to get the full form of $\boldsymbol{r}$ in Eq. (2.14), we need to go order-by-order in the compositional map, computing some symplectic map $\exp(: g_{i+1} :)$ at order i such that $\exp(: g_{i+1} :)\mathcal{N}_{i-1} \exp(- : g_{i+1} :)$ leaves an amplitude-dependent rotation up to order i; this means the similarity transformation must remove any terms in the $(i+1)$-th order Lie operator for $\mathcal{N}_{i-1}$ which are not solely functions of the actions (i.e. are angle-dependent).

At a given step, we will have

$$\mathcal{N}_{i-1} = \underbrace{\mathcal{R}_1 \exp(: k_{3\to i}[\boldsymbol{J}(\bar{\boldsymbol{\zeta}})] :)}_{\text{Normalized part}} \underbrace{\exp(: h_{i+1}(\bar{\boldsymbol{\zeta}}) :) \exp(: h_{i+2}(\bar{\boldsymbol{\zeta}}) :) \ldots}_{\text{Unnormalized part}} \tag{2.76}$$

where $k_{3\to i}[\boldsymbol{J}(\bar{\boldsymbol{\zeta}})]$ corresponds to a Taylor polynomial up to order i in the Floquet variables $\bar{\boldsymbol{\zeta}}$ (*not* in $\boldsymbol{J}$, reminder: $2J_i = \bar{q}_i^2 + \bar{p}_i^2$), and h_k are some homogeneous polynomials of order k in $\bar{\boldsymbol{\zeta}}$ which will be different each iteration step. The $k_{3\to i}$, being lower order, will not change each iteration step. Identifying and collecting which monomials in some function of $\bar{\boldsymbol{\zeta}}$ are only $\boldsymbol{J}$-dependent is challenging in the Floquet basis, considering the binomial expansion of $(\bar{q}_i^2 + \bar{p}_i^2)^k$ and other oscillation modes. Instead, it is easiest to work in the phasors basis, via the transformation defined in Eq. (2.69). In this basis, we express the i-th pair of variables as $(\tilde{\zeta}_i, \tilde{\zeta}_i^*) = \left(\sqrt{J_i}e^{+\mathrm{i}\phi_i},\ \sqrt{J_i}e^{-\mathrm{i}\phi_i}\right)$, and the transformed phase space vector as $\tilde{\boldsymbol{\zeta}}$. Using $\boldsymbol{\alpha}$ again as a multi-index, we see that the term $\boldsymbol{J}^{\boldsymbol{\alpha}} = (\tilde{\zeta}_1\tilde{\zeta}_1^*)^{\alpha_1}...(\tilde{\zeta}_n\tilde{\zeta}_n^*)^{\alpha_n}$; it is much easier to identify purely action-dependent terms in the Taylor series in the phasors basis, because each pair of variables will always have the same order in such cases. However, an important caveat: the transformation in Eq. (2.69) is *not* symplectic. In order to ensure that $\mathcal{A}_1$ was symplectic, we normalized the phasors (eigenvectors) to satisfy Eq. (2.71). In order to ensure that the fully nonlinear $\mathcal{A}$ is symplectic, we have to make sure that Eq. (2.71) remains satisfied. In effect, this "redefines" the Poisson bracket Lie operator in the phasors basis. Using the notation of Forest [32], in the phasors basis we have

$$\stackrel{\star}{} f \stackrel{\star}{} g = -\mathrm{i} : f : g \,. \tag{2.77}$$

Letting C specify the compositional map corresponding to the phasors transformation C in Eq. (2.69),

$$\tilde{\mathcal{N}}_{i-1} = C\mathcal{N}_{i-1}C^{-1} = \underbrace{\tilde{\mathcal{R}}_1 \exp\left(\stackrel{\star}{} \tilde{k}_{3\to i}[\boldsymbol{J}(\tilde{\boldsymbol{\zeta}})] \stackrel{\star}{}\right)}_{\text{Normalized part}} \underbrace{\exp\left(\stackrel{\star}{} \tilde{h}_{i+1}(\tilde{\boldsymbol{\zeta}}) \stackrel{\star}{}\right) \exp\left(\stackrel{\star}{} \tilde{h}_{i+2}(\tilde{\boldsymbol{\zeta}}) \stackrel{\star}{}\right)...}_{\text{Unnormalized part}} \,. \tag{2.78}$$

In the phasor's basis, it is clear that $\tilde{k}_{3\to i}$ actually only consists of monomials of *even* orders, because the complex conjugate phasors must come in pairs in order

to be only action-dependent. To get the map at the next iteration, $\tilde{\mathcal{N}}_i$, we need to compute the Lie operator $\tilde{g}_{i+1}$ so that

$$\begin{aligned}
\tilde{\mathcal{N}}_i &= \exp(:\tilde{g}_{i+1}:)\tilde{\mathcal{N}}_{i-1}\exp(-:\tilde{g}_{i+1}:) \\
&= \exp(:\tilde{g}_{i+1}:)\tilde{\mathcal{R}}_1\exp(:\tilde{k}_{3\to i}:)\exp(:\tilde{h}_{i+1}:)\ldots\exp(-:\tilde{g}_{i+1}:) \\
&= \tilde{\mathcal{R}}_1\tilde{\mathcal{R}}_1^{-1}\exp(:\tilde{g}_{i+1}:)\tilde{\mathcal{R}}_1\exp(:\tilde{k}_{3\to i}:)\exp(:\tilde{h}_{i+1}:)\ldots\exp(-:\tilde{g}_{i+1}:) \\
&= \tilde{\mathcal{R}}_1\exp(\tilde{\mathcal{R}}_1^{-1}:\tilde{g}_{i+1}:\tilde{\mathcal{R}}_1)\exp(:\tilde{k}_{3\to i}:)\exp(:\tilde{h}_{i+1}:)\ldots\exp(-:\tilde{g}_{i+1}:)\,, \qquad (2.79)
\end{aligned}$$

is an amplitude dependent rotation up to order i. To simplify this expression further, we will use the BCH theorem in Eq. (2.36). For two functions of phase space f_i and g_j which are homogeneous polynomials of order i and j respectively in the phase space coordinates, the order of $\{f_i, g_j\}$ will be $(i-1)(j-1)$. If both i and j are at least 3, which we have in the Lie exponents of Eq. (2.79), then the Poisson bracket will be $> \max(i, j)$. Therefore, continuing from Eq. (2.79),

$$\begin{aligned}
\tilde{\mathcal{N}}_i &= \tilde{\mathcal{R}}_1\exp(:\tilde{k}_{3\to i}:)\exp(\tilde{\mathcal{R}}_1^{-1}:\tilde{g}_{i+1}:\tilde{\mathcal{R}}_1 + :O(\tilde{\zeta}^{2i}):)\exp(:\tilde{h}_{i+1}:)\ldots\exp(-:\tilde{g}_{i+1}:) \\
&= \tilde{\mathcal{R}}_1\exp(:\tilde{k}_{3\to i}:)\exp(\tilde{\mathcal{R}}_1^{-1}:\tilde{g}_{i+1}:\tilde{\mathcal{R}}_1 - :\tilde{g}_{i+1}: + :\tilde{h}_{i+1}: + :O(\tilde{\zeta}^{i+2}):)\,. \qquad (2.80)
\end{aligned}$$

Ignoring the higher order terms which will be taken care of in the next steps of the order-by-order algorithm, we seek the $\tilde{g}_{i+1}$ such that

$$\tilde{\mathcal{R}}_1^{-1}:\tilde{g}_{i+1}:\tilde{\mathcal{R}}_1 - :\tilde{g}_{i+1}: + :\tilde{h}_{i+1}: = :\tilde{k}_{i+1}[\boldsymbol{J}(\tilde{\zeta})]:\,, \qquad (2.81)$$

i.e., $\tilde{k}_{i+1}$ is solely a function of the actions. Using Eq. (2.74),

$$:\tilde{\mathcal{R}}_1^{-1}\tilde{g}_{i+1}: - :\tilde{g}_{i+1}: + :\tilde{h}_{i+1}: = :\tilde{k}_{i+1}:\,. \qquad (2.82)$$

Because of the linearity of the Poisson bracket operator, we can drop the $:\ldots:$ and

$$\begin{aligned}
\tilde{k}_{i+1} &= \tilde{\mathcal{R}}_1^{-1}\tilde{g}_{i+1} - \tilde{g}_{i+1} + \tilde{h}_{i+1} \\
&= (\tilde{\mathcal{R}}_1^{-1} - \mathcal{I})\tilde{g}_{i+1} + \tilde{h}_{i+1}\,, \qquad (2.83)
\end{aligned}$$

where $\mathcal{I}$ is the identity compositional map. Both the LHS and the RHS will be homogeneous polynomials of order $i+1$ in the phasors basis $\tilde{\boldsymbol{\zeta}}$. Let's consider each monomial now, using a multi-index notation where each variable has its own order. Let the multi-index $\boldsymbol{m} = (\boldsymbol{m}^+, \boldsymbol{m}^-)$ where

$$\tilde{\boldsymbol{\zeta}}^{\boldsymbol{m}} = (\tilde{\zeta}_1)^{m_1^+}(\tilde{\zeta}_1^*)^{m_1^-}\ldots(\tilde{\zeta}_n)^{m_n^+}(\tilde{\zeta}_n^*)^{m_n^-} \,. \tag{2.84}$$

Note that when $\boldsymbol{m}^+ - \boldsymbol{m}^- = 0$, the monomial is fully action-dependent. Because the phasors are the eigenfunctions of $\mathcal{R}_1$, we have $\mathcal{R}_1^{-1}\tilde{\boldsymbol{\zeta}}^{\boldsymbol{m}} = e^{+\mathrm{i}\boldsymbol{\mu}\cdot(\boldsymbol{m}^+-\boldsymbol{m}^-)}\tilde{\boldsymbol{\zeta}}^{\boldsymbol{m}}$. Therefore with Eq. (2.83), dropping the subscript $i+1$ for notational brevity and using a subscript of the multi-index $\boldsymbol{m}$ to specify which monomial, we get a very simple expression

$$\tilde{k}_{\boldsymbol{m}} = [e^{+\mathrm{i}\boldsymbol{\mu}\cdot(\boldsymbol{m}^+-\boldsymbol{m}^-)} - 1]\tilde{g}_{\boldsymbol{m}} + \tilde{h}_{\boldsymbol{m}} \,. \tag{2.85}$$

Now let's try to solve for $\tilde{g}_{\boldsymbol{m}}$ to make $\tilde{k}_{\boldsymbol{m}}$ zero,

$$\tilde{g}_{\boldsymbol{m}} = \frac{\tilde{h}_{\boldsymbol{m}}}{1 - \exp\left[\mathrm{i}\boldsymbol{\mu}\cdot(\boldsymbol{m}^+ - \boldsymbol{m}^-)\right]} \,. \tag{2.86}$$

Equation (2.86) is central to perturbation theory. We see immediately that if $\boldsymbol{m}^+ - \boldsymbol{m}^- = 0$, we would get a denominator of 0 if we tried to remove that term; terms which are only functions of the action cannot be removed. Furthermore, we see more generally that if $\frac{\boldsymbol{\mu}}{2\pi}\cdot(\boldsymbol{m}^+ - \boldsymbol{m}^-) \in \mathbb{Z}$, we similarly will get a denominator of 0. This occurs in the case of a resonance. If the system is too close to a resonance such that the "resonance denominator" blows up, then we cannot remove it, and instead must leave that one resonance in the map. In such a case, we have a *one resonance normal form* from which we can do further analysis to extract more information, e.g. the amplitudes of the fixed points. The interested reader is pointed to [71] for an excellent example of one resonance normal form analysis.

Letting $\boldsymbol{\lambda}^* = \mathrm{diag}\,(\tilde{\mathsf{R}}^{-1})$ where $\tilde{\mathsf{R}}$ is the diagonalized matrix corresponding to

$\tilde{\mathcal{R}}_1$, Eq. (2.86) can be rewritten as

$$\tilde{g}_{\boldsymbol{m}} = \frac{\tilde{h}_{\boldsymbol{m}}}{1 - \prod_{k=1}^{2n} (\lambda_k^*)^{m_k}} \,. \tag{2.87}$$

2.2.3 Including Damping

Everything we have shown thus far, which uses the Poisson bracket Lie operator : ... :, holds for symplectic maps. However there are several problems with this:

1. The order of the polynomial Lie operator is one order higher than the map it generates, which can vastly complicate a computer program that needs to compute and keep track of the higher order derivatives
2. When in the phasors basis, the "special" Poisson bracket $\star$ ... $\star$ defined in Eq. (2.77) has to be used in order to ensure the normalizing transformation in the real variables is symplectic
3. Non-symplectic maps cannot be naturally handled in the same framework

In order to resolve this issue, we should have a similar framework which works for maps that are non-symplectic (e.g. including radiation damping), however retains symplecticity for maps which are symplectic.

A most general, arbitrary first order differential equation, which may or may not be Hamiltonian, is

$$\frac{d}{dt}\boldsymbol{\zeta} = \boldsymbol{F}(\boldsymbol{\zeta}) \,. \tag{2.88}$$

In the symplectic case, we showed in Eq. (2.10) that the Poisson bracket defines how functions of the phase space evolve in time. This then defined the Poisson bracket Lie operator, which we used in the rest of the analysis. Now, we want

to define a Lie operator which similarly describes how functions of the phase space evolve,

$$\begin{aligned}\frac{d}{dt}f(\boldsymbol{\zeta}(t)) &= \frac{d\boldsymbol{\zeta}}{dt}\cdot\boldsymbol{\nabla}f(\boldsymbol{\zeta}(t)) \\ &= \boldsymbol{F}\cdot\boldsymbol{\nabla}f\ .\end{aligned} \tag{2.89}$$

In this more general framework, the operator $\boldsymbol{F}\cdot\boldsymbol{\nabla}$ defines how functions of the phase space evolve in time. Consider the commutator,

$$[\boldsymbol{F}\cdot\boldsymbol{\nabla},\boldsymbol{G}\cdot\boldsymbol{\nabla}] = (\boldsymbol{F}\cdot\boldsymbol{\nabla}\boldsymbol{G}-\boldsymbol{G}\cdot\boldsymbol{\nabla}\boldsymbol{F})\cdot\boldsymbol{\nabla}\ . \tag{2.90}$$

It can be shown that, for the vector space of the operators $\boldsymbol{F}\cdot\boldsymbol{\nabla}$, the commutator is bilinear, anticommutative, and satisfies the Jacobi identity; with the commutator as the multiplication operation, we have a Lie algebra for the vector space of the operators $\boldsymbol{F}\cdot\boldsymbol{\nabla}$. Henceforth, we will refer to the multiplication operation for a Lie algebra as the Lie bracket.

Now that we know we have a Lie algebra, much of the preceding analysis we did using the Poisson bracket Lie algebra is very similar. Now, however, the formalism can work even for systems with large damping (non-Hamiltonian). Furthermore, the force vector $\boldsymbol{F}$ when expanded as a Taylor series in $\boldsymbol{\zeta}$ will be of the same truncation order as the DA map it generates, simplifying and improving the performance of a computer implementation significantly. In the case of a symplectic system, the force $\boldsymbol{F}$ is given by $\boldsymbol{F} = -\mathsf{S}\boldsymbol{\nabla}H$, where S is the matrix defined in Eq. (2.60). In general, for a symplectic system we can correspond the Poisson bracket Lie operators with the more general Lie operators

$$:h: = (-\mathsf{S}\boldsymbol{\nabla}h)\cdot\boldsymbol{\nabla}\ . \tag{2.91}$$

Using Eq. (2.91) and Eq. (2.59), in action-angle variables we can write the normal

form compositional map $\mathcal{R}$ as

$$\mathcal{R} = \exp\left(-: \int^{\boldsymbol{J}} \boldsymbol{\mu}(\boldsymbol{J}) \cdot d\boldsymbol{J} :\right) = \exp\left(\boldsymbol{\mu}(\boldsymbol{J}) \cdot \frac{\partial}{\partial \boldsymbol{\phi}}\right). \tag{2.92}$$

In computing the normalizing map $\mathcal{A}$, the linear part is treated the exact same; in the symplectic case we must normalize the eigenvectors per Eq. (2.71), and in the nonsymplectic case there is no harm in doing so. The nonlinear part is similar, except for the fact the identity in Eq. (2.74) is very different for this Lie operator,

$$\begin{aligned}
\mathcal{A}_1(\boldsymbol{F}\cdot\boldsymbol{\nabla})\mathcal{A}_1^{-1} g &= \mathcal{A}_1 F_i \partial_i (g \circ \boldsymbol{a}_1^{-1}) \\
&= \mathcal{A}_1 F_i \left[(\partial_i g) \circ \boldsymbol{a}_1^{-1}\right] \partial_i \boldsymbol{a}_1^{-1} \\
&= (F_i \circ \boldsymbol{a}_1)\,(\partial_i g)\left(\partial_i \boldsymbol{a}_1^{-1} \circ \boldsymbol{a}_1\right) \\
&= \left[F_i \partial_i \boldsymbol{a}_1^{-1} \circ \boldsymbol{a}_1\right] \partial_i g \\
&= \left[(\boldsymbol{F}\cdot\boldsymbol{\nabla}\boldsymbol{a}_1^{-1}) \circ \boldsymbol{a}_1\right] \cdot \boldsymbol{\nabla} g\,,
\end{aligned} \tag{2.93}$$

where we have used the fact that a compositional map acting on a product of functions, is equal to acting on each function individually and then multiplying the product (see Eq. (2.26), which extends for arbitrary compositional maps). Therefore,

$$\mathcal{A}_1(\boldsymbol{F}\cdot\boldsymbol{\nabla})\mathcal{A}_1^{-1} = \left[(\boldsymbol{F}\cdot\boldsymbol{\nabla}\boldsymbol{a}_1^{-1}) \circ \boldsymbol{a}_1\right] \cdot \boldsymbol{\nabla}\,. \tag{2.94}$$

The procedure up to Eq. (2.81) is the same, so we start with that. Note that now we do not need to do anything "special" to transform in and out of the phasors basis, because the transformation to the phasors basis is now a part of this new Lie group with our new Lie operator. To normalize the i-th order, we have

$$\tilde{\mathcal{R}}_1^{-1}(\tilde{\boldsymbol{G}}_i\cdot\boldsymbol{\nabla})\tilde{\mathcal{R}}_1 - \tilde{\boldsymbol{G}}_i\cdot\boldsymbol{\nabla} + \tilde{\boldsymbol{H}}_i\cdot\boldsymbol{\nabla} = \tilde{\boldsymbol{K}}_i\cdot\boldsymbol{\nabla}\,, \tag{2.95}$$

where we now want to make $\tilde{\boldsymbol{K}}_i$ fully action dependent. Note that, unlike in Eq. (2.81) where the Poisson bracket Lie operators are one order higher than the

map it generates, with this Lie operator the homogenous polynomial is of the same order as the DA map. With Eq. (2.94), letting $\tilde{\boldsymbol{r}}_1$ be the DA map corresponding to the compositional map $\tilde{\mathcal{R}}_1$ we can write

$$\left[(\tilde{\boldsymbol{G}}_i \cdot \boldsymbol{\nabla}\tilde{\boldsymbol{r}}_1) \circ \tilde{\boldsymbol{r}}_1^{-1}\right] \cdot \boldsymbol{\nabla} - \tilde{\boldsymbol{G}}_i \cdot \boldsymbol{\nabla} + \tilde{\boldsymbol{H}}_i \cdot \boldsymbol{\nabla} = \tilde{\boldsymbol{K}}_i \cdot \boldsymbol{\nabla} \, . \tag{2.96}$$

We can now drop the $\cdot\boldsymbol{\nabla}$. Also dropping the subscript i which specifies the order for notational brevity, we have

$$\left[(\tilde{\boldsymbol{G}} \cdot \boldsymbol{\nabla}\tilde{\boldsymbol{r}}_1) \circ \tilde{\boldsymbol{r}}_1^{-1}\right] - \tilde{\boldsymbol{G}} + \tilde{\boldsymbol{H}} = \tilde{\boldsymbol{K}} \, . \tag{2.97}$$

Because we are in the phasor basis, the map $\tilde{\boldsymbol{r}}_1$ is just a diagonal matrix, which we write as $\tilde{\mathsf{R}}$. However, unlike in the symplectic case where each μ_i is fully real (so that each eigenvalue sits on the unit circle), when there is damping each μ_i will have an imaginary part $\mathrm{i}\alpha_i$ such that each eigenvalue now sits inside the unit circle in the complex plane with radius $e^{-\alpha_i}$, $\alpha_i \in \mathbb{R}_{\geq 0}$. Letting $\boldsymbol{\lambda} = \mathrm{diag}\,(\tilde{\mathsf{R}})$,

$$(\tilde{\boldsymbol{G}} \cdot \boldsymbol{\nabla}\tilde{\boldsymbol{r}}_1) \circ \tilde{\boldsymbol{r}}_1^{-1} = \boldsymbol{\lambda}(\tilde{\boldsymbol{G}} \circ \tilde{\boldsymbol{r}}_1^{-1}) = \boldsymbol{\lambda}\tilde{\mathcal{R}}_1^{-1}\tilde{\boldsymbol{G}} \, . \tag{2.98}$$

Note that the multiplication of the vectors $\boldsymbol{\lambda}$ and $\tilde{\mathcal{R}}_1^{-1}\tilde{\boldsymbol{G}}$ is element-wise, and that the length of both vectors is $2n$. We can now simplify Eq. (2.97),

$$\left(\boldsymbol{\lambda}\mathcal{R}_1^{-1} - \mathcal{I}\right)\tilde{\boldsymbol{G}} + \tilde{\boldsymbol{H}} = \tilde{\boldsymbol{K}} \, . \tag{2.99}$$

Following the same procedure in the preceding section, for a given monomial specified by the multi-index $\boldsymbol{m}$, we have for the j-th component of each vector,

$$\tilde{K}_{j,\boldsymbol{m}} = \left(\lambda_j \prod_{k=1}^{2n} (\lambda_k^*)^{m_k} - 1\right)\tilde{G}_{j,\boldsymbol{m}} + \tilde{H}_{j,\boldsymbol{m}} \, . \tag{2.100}$$

The multiplication of λ_j by the product has the effect of "subtracting" an order from the j-th entry of $\boldsymbol{m}$ in the product. Finally, solving for the $\tilde{G}_{j,\boldsymbol{m}}$ to attempt to make $\tilde{K}_{j,\boldsymbol{m}}$ zero,

$$\tilde{G}_{j,\boldsymbol{m}} = \frac{\tilde{H}_{j,\boldsymbol{m}}}{1 - \lambda_j \prod_{k=1}^{2n} (\lambda_k^*)^{m_k}} \, . \tag{2.101}$$

This algorithm was implemented in `NonlinearNormalForm.jl` as a part of this dissertation. See Sec. 9.3 for some examples.

2.2.4 Lattice Functions

Earlier in this dissertation, we said how the normal form makes analysis of the dynamics much simpler. We then described in excruciating detail how to transform some nonlinear map, expressed as a Taylor series in the phase space variables around the fixed point, to the normal form, also expressed as a Taylor series in the phase space variables. Let's now use the normal form to analyze the dynamics in a simple case. For the sake of brevity, we will only consider the **first-order symplectic** analysis here, but it is easy to extend these methods to higher order analyses and include damping (see [30, 32, 71] for more interesting nonlinear applications).

To first order, we have

$$\mathsf{ARA}^{-1} = \mathsf{M}\,, \tag{2.102}$$

where A is the linear matrix corresponding to $\mathcal{A}$, M is the linear matrix corresponding to the DA map $\boldsymbol{m}(\zeta_0)$, and R is a (potentially damped) rotation matrix. To simplify the following discussion, we will assume only a 1-D system, however this formalism can be generalized to n-D including coupling between the modes [32]. Letting I correspond to the identity matrix, Eq. (2.102) implies

that we can write a stable symplectic matrix as

$$\mathsf{M} = \cos(\mu)\mathsf{I} + \sin(\mu)\begin{pmatrix} \underbrace{-\mathsf{A}_{11}\mathsf{A}_{21} - \mathsf{A}_{12}\mathsf{A}_{22}}_{\alpha} & \underbrace{\mathsf{A}_{11}^2 + \mathsf{A}_{12}^2}_{\beta} \\ \underbrace{-\mathsf{A}_{21}^2 - \mathsf{A}_{22}^2}_{-\gamma} & \underbrace{\mathsf{A}_{11}\mathsf{A}_{21} + \mathsf{A}_{12}\mathsf{A}_{22}}_{-\alpha} \end{pmatrix} \tag{2.103}$$

$$= \begin{pmatrix} \cos(\mu) + \alpha\sin(\mu) & \beta\sin(\mu) \\ -\gamma\sin(\mu) & \cos(\mu) - \alpha\sin(\mu) \end{pmatrix}, \tag{2.104}$$

where we use the fact that $\det(\mathsf{A}) = 1$. In the context of accelerator physics, we refer to the α, β, and γ as *lattice functions* or the *Twiss parameters*. The requirement $1 + \alpha^2 = \beta\gamma$ follows from $\det(\mathsf{M}) = 1$.

The Twiss parameters are intimately connected with the second moments. Let $\langle \ldots \rangle$ correspond to an average over many applications of the map. In Floquet variables we have $\bar{q} = \sqrt{2J}\cos\phi$ and $\bar{p} = \sqrt{2J}\sin\phi$ where each application sends $\phi \to \phi + \mu$. Therefore we have $\langle \bar{q}^2 \rangle = J$, $\langle \bar{p}^2 \rangle = J$, and $\langle \bar{q}\bar{p} \rangle = 0$. Consider the moment $\langle q^2 \rangle$,

$$\begin{aligned} \langle q^2 \rangle &= \langle (\mathsf{A}_{11}\bar{q} + \mathsf{A}_{12}\bar{p})^2 \rangle \\ &= \mathsf{A}_{11}^2\langle \bar{q}^2 \rangle + \mathsf{A}_{12}^2\langle \bar{p}^2 \rangle + 2\mathsf{A}_{11}\mathsf{A}_{12}\langle \bar{q}\bar{p} \rangle \\ &= (\mathsf{A}_{11}^2 + \mathsf{A}_{12}^2)J \\ &= \beta J \, . \end{aligned} \tag{2.105}$$

The Twiss parameter β, unsurprisingly referred to as the *beta function*, directly correlates the positional spread with the action J. We can similarly compute the

other second moments,

$$\begin{aligned}\langle p^2\rangle &= \langle(\mathsf{A}_{21}\bar{q} + \mathsf{A}_{22}\bar{p})^2\rangle \\ &= (\mathsf{A}_{21}^2 + \mathsf{A}_{22}^2)J \\ &= \gamma J\,, \end{aligned} \tag{2.106}$$

$$\begin{aligned}\langle qp\rangle &= \langle(\mathsf{A}_{11}\bar{q} + \mathsf{A}_{12}\bar{p})(\mathsf{A}_{21}\bar{q} + \mathsf{A}_{22}\bar{p})\rangle \\ &= \mathsf{A}_{11}\mathsf{A}_{21}\langle\bar{q}^2\rangle + \mathsf{A}_{21}\mathsf{A}_{22}\langle\bar{p}^2\rangle + (\mathsf{A}_{11}\mathsf{A}_{22} + \mathsf{A}_{12}\mathsf{A}_{21})\langle\bar{q}\bar{p}\rangle \\ &= (\mathsf{A}_{11}\mathsf{A}_{21} + \mathsf{A}_{21}\mathsf{A}_{22})J \\ &= -\alpha J\,. \end{aligned} \tag{2.107}$$

As a reminder, earlier it was shown how $\boldsymbol{a}$ is only defined up to an arbitrary (amplitude-dependent) rotation. It can be shown that these lattice functions are unchanged with an arbitrary rotation matrix applied to A_1.

We can also write the invariant in terms of the regular phase space coordinates,

$$J = \frac{1}{2}(\bar{q}^2 + \bar{p}^2) = \frac{1}{2}\left[(q \circ \boldsymbol{a}^{-1})^2 + (p \circ \boldsymbol{a}^{-1})^2\right] \tag{2.108}$$

$$\begin{aligned}&\approx \frac{1}{2}\left[(\mathsf{A}_{22}q - \mathsf{A}_{12}p)^2 + (-\mathsf{A}_{21}q + \mathsf{A}_{11}p)^2\right] \\ &= \frac{1}{2}\left[(\mathsf{A}_{21}^2 + \mathsf{A}_{22}^2)q^2 + 2(-\mathsf{A}_{11}\mathsf{A}_{21} - \mathsf{A}_{12}\mathsf{A}_{22})qp + (\mathsf{A}_{11}^2 + \mathsf{A}_{12}^2)p^2\right] \\ &= \frac{1}{2}\left(\gamma q^2 + 2\alpha qp + \beta p^2\right)\,. \end{aligned} \tag{2.109}$$

It is important to remember that Eq. (2.109), which is also called the *Courant-Snyder invariant*, is only true to first-order, while Eq. (2.108) is true for all orders.

In this map-based perturbation theory, the dynamics are only considered at one Poincaré section. Often we will want to understand the dynamics at many Poincaré sections; in an accelerator ring for example, we want to know what the beam looks like at the various azimuthal positions around the ring. Taking

care to note the difference in notation with Sec. 2.2.2, let $\boldsymbol{a}_1$ correspond to the normalizing map at some position "1" in the ring, $\boldsymbol{a}_2$ the normalizing map at some position "2" in the ring, and $\boldsymbol{m}_{12}$ the map from position 1 to 2. We can then compute the map from position 1 to 2 in "circle world" $\boldsymbol{r}_{12}$ as

$$\boldsymbol{r}_{12} = \boldsymbol{a}_2^{-1} \circ \boldsymbol{m}_{12} \circ \boldsymbol{a}_1 \ . \tag{2.110}$$

Equation (2.110) is expressed pictorially in Fig. 2.2 [32]. The quantity μ_{12} is the

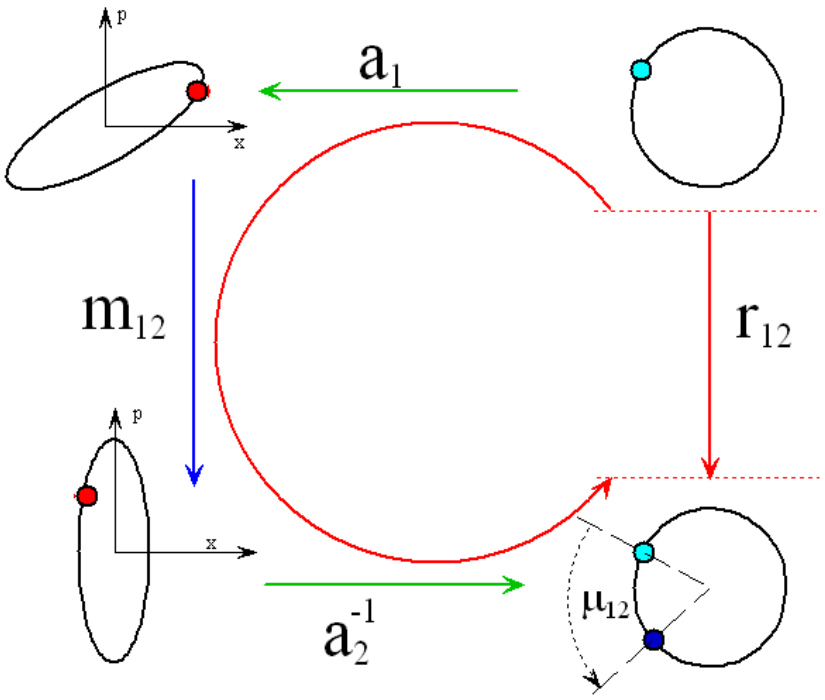

Figure 2.2: Pictorial view of the phase advance taken directly from [32].

phase advance between positions 1 and 2 of the particle in circle world. Note that, because $\boldsymbol{a}_1$ and $\boldsymbol{a}_2$ are only defined up to an (amplitude-dependent) rotation, the quantity μ_{12} *does* depend on this "phase" of $\boldsymbol{a}_1$ and $\boldsymbol{a}_2$. For example, it is possible to apply a rotation to $\boldsymbol{a}_1$ and/or $\boldsymbol{a}_2$ (which does not affect the lattice functions) so that $\mu_{12} = 0$.

In order to have a consistent definition of μ_{12}, we must choose a specific,

unique form for the normalizing maps $\boldsymbol{a}_1$ and $\boldsymbol{a}_2$. Forest refers to this process as the "canonization" of the normalizing map [32]. There a specific choice which turns out to be a most useful, physically measurable one. Consider, in the linear regime, the phase space coordinates of a particle at some position 1 after n applications of the full map, and then observing the coordinates at position 2 [32],

$$\begin{aligned}\boldsymbol{\zeta}_2 &= \mathsf{M}_{12}\mathsf{M}_1^n\boldsymbol{\zeta}_1 \\ &= (\mathsf{A}_2\mathsf{R}_{12}\mathsf{A}_1^{-1})(\mathsf{A}_1\mathsf{R}_1^n\mathsf{A}_1^{-1})\boldsymbol{\zeta}_1 \\ &= \mathsf{A}_2\mathsf{R}_{12}\mathsf{R}_1^n\mathsf{A}_1^{-1}\boldsymbol{\zeta}_1 \\ &= \mathsf{A}_2\mathsf{A}_1^{-1}\ \underbrace{(\mathsf{A}_1\mathsf{R}_{12}\mathsf{R}_1^n\mathsf{A}_1^{-1})}_{\text{De Moirve Expressible}}\ \boldsymbol{\zeta}_1 \end{aligned} \tag{2.111}$$

Using Eq. (2.104) we can write this as

$$\boldsymbol{\zeta}_2 = \mathsf{A}_2\mathsf{A}_1^{-1}\begin{pmatrix}\cos(\Phi)+\alpha_1\sin(\Phi) & \beta_1\sin(\Phi) \\ -\gamma_1\sin(\Phi) & \cos(\Phi)-\alpha_1\sin(\Phi)\end{pmatrix}\boldsymbol{\zeta}_1\ , \tag{2.112}$$

where $\Phi = n\mu + \mu_{12}$. If the phases of each normalizing map A are chosen so that the 12 term is equal to zero,

$$\mathsf{A} = \begin{pmatrix}\sqrt{\beta} & 0 \\ -\frac{\alpha}{\sqrt{\beta}} & \frac{1}{\sqrt{\beta}}\end{pmatrix}, \tag{2.113}$$

then Eq. (2.112) becomes

$$\boldsymbol{\zeta}_2 = \begin{pmatrix}\sqrt{\frac{\beta_2}{\beta_1}} & 0 \\ \frac{\alpha_1-\alpha_2}{\sqrt{\beta_2\beta_1}} & \sqrt{\frac{\beta_1}{\beta_2}}\end{pmatrix}\begin{pmatrix}\cos(\Phi)+\alpha_1\sin(\Phi) & \beta_1\sin(\Phi) \\ -\gamma_1\sin(\Phi) & \cos(\Phi)-\alpha_1\sin(\Phi)\end{pmatrix}\boldsymbol{\zeta}_1\ . \tag{2.114}$$

With this specific choice, the positional phase space coordinate at position 2 is

$$q_2 = \sqrt{\frac{\beta_2}{\beta_1}}\left[\cos(n\mu+\mu_{12})+\alpha_1\sin(n\mu+\mu_{12})\right]\ , \tag{2.115}$$

while at position 1 it is

$$q_1 = \cos(n\mu) + \alpha_1 \sin(n\mu) \,. \tag{2.116}$$

The only differences between Eq. (2.115) and Eq. (2.116) are the scaling factor $\sqrt{\frac{\beta_2}{\beta_1}}$ and the phase μ_{12}. Therefore if we perform a Fourier analysis of the positions we can directly measure μ_{12}. This is one of the main benefits of the unique choice of A in Eq. (2.113), also called the *Courant-Snyder transformation*.

2.3 Single Particle Dynamics in Accelerators

All of the tools we have developed thus far are not specific to accelerator physics. Let us now consider what the theory looks like in the context of particle accelerators.

2.3.1 Magnet Types: Multipole Expansion

Particle accelerators are often just a sequence of electromagnetic "elements" that make the particle beam do what we want it to do. The Lorentz force is

$$\frac{d}{dt}\boldsymbol{P}_k = q(\boldsymbol{E} + \boldsymbol{v} \times \boldsymbol{B}) \,, \tag{2.117}$$

where $\boldsymbol{P}_k$ is the kinetic momentum, $\boldsymbol{E}$ is the electric field, $\boldsymbol{B}$ is the magnetic field, q is the particle charge, and $\boldsymbol{v}$ is the particle velocity. Note that the force from the magnetic field is proportional to the velocity of a particle, unlike for the electric field. For relativistic particles where $v \approx c$, this means that the force from a magnet with strength 1 T would require an electric field of $\approx 3 \times 10^8$ V/m to achieve the same force. A 1 T magnetostatic field is physically feasible,

however a $\approx 3 \times 10^8$ V/m electrostatic field is beyond technical limits. Magnets therefore are typically used to steer medium-to-high energy beams.

Static magnetic fields satisfy the Maxwell equations $\boldsymbol{\nabla} \cdot \boldsymbol{B} = \boldsymbol{\nabla} \times \boldsymbol{B} = 0$. This implies that we can write a static magnetic field as the gradient of a potential $\boldsymbol{B} = -\boldsymbol{\nabla}\psi(\boldsymbol{r})$, where $\boldsymbol{r} = x\hat{\boldsymbol{x}} + y\hat{\boldsymbol{y}} + z\hat{\boldsymbol{z}}$ and $\boldsymbol{\nabla}^2\psi(\boldsymbol{r}) = 0$. We then consider fields which have some axial symmetry about $\hat{\boldsymbol{z}}$, and expand around $x = 0$ and $y = 0$. The idea here is that the "ideal beam" should travel along $\hat{\boldsymbol{z}}$ (the center of the magnet). Because of the axial symmetry, it is easiest to use a complex representation with the variables $(w, \bar{w}$ where $w = x + \mathrm{i}y$. The derivxgative operators are easily obtained,

$$\frac{\partial}{\partial w} = \frac{\partial x}{\partial w}\frac{\partial}{\partial x} + \frac{\partial y}{\partial w}\frac{\partial}{\partial y} = \frac{1}{2}\left(\frac{\partial}{\partial x} - \mathrm{i}\frac{\partial}{\partial y}\right), \tag{2.118a}$$

$$\frac{\partial}{\partial \bar{w}} = \frac{\partial x}{\partial \bar{w}}\frac{\partial}{\partial x} + \frac{\partial y}{\partial \bar{w}}\frac{\partial}{\partial y} = \frac{1}{2}\left(\frac{\partial}{\partial x} + \mathrm{i}\frac{\partial}{\partial y}\right). \tag{2.118b}$$

These are called the Wirtinger derivatives. The Laplacian operator is then written as

$$\boldsymbol{\nabla}^2 = \partial_x^2 + \partial_y^2 + \partial_z^2 = (\partial_w + \partial_{\bar{w}})^2 + (\mathrm{i}\partial_w - \mathrm{i}\partial_{\bar{w}})^2 + \partial_z^2 = 4\partial_w\partial_{\bar{w}} + \partial_z^2 \,. \tag{2.119}$$

A potential must satisfy $\boldsymbol{\nabla}^2\psi = 0$ in order to be Maxwellian. This can be derived [38] to be

$$\psi(x, y, z) = \mathrm{Im}\left[\sum_{\nu,\lambda=0}^{\infty} \frac{(-1)^\lambda \nu!}{(\lambda+\nu)!\lambda!}\left(\frac{w\bar{w}}{4}\right)^\lambda \bar{w}^\nu \Psi_\nu^{[2\lambda]}(z)\right], \tag{2.120}$$

where the index ν describes C_ν symmetry around the $\hat{\boldsymbol{z}}$ axis, and the $[2\lambda]$ denotes a derivative wrt z taken 2λ times. Often, a given magnet in an accelerator is chosen to generate a field described by a single ν. We will briefly show the forms of $\nu = 0, 1, 2$ in a *straight* coordinate system[3].

[3]Curved coordinate systems, such as in a bending magnet, require an entirely different formulation. See [53] for more details.

$\nu = 0$**: Solenoid**

A solenoid has C_0 symmetry. Using Eq. (2.120) for only $\nu = 0$, we have

$$\psi(x, y, z) = \mathrm{Im}\,(\Psi_0) - \frac{1}{4}(x^2 + y^2)\,\mathrm{Im}\,(\Psi_0') + \ \ldots\,, \tag{2.121}$$

where $'$ denotes differentiation wrt z, and we have truncated the result to second order in x and y. This gives a magnetic field

$$B_x = \frac{1}{2}x\,\mathrm{Im}\,(\Psi_0'') + \ \ldots\,, \tag{2.122a}$$

$$B_y = \frac{1}{2}y\,\mathrm{Im}\,(\Psi_0'') + \ \ldots\,, \tag{2.122b}$$

$$B_z = -\,\mathrm{Im}\,(\Psi_0') + \ \ldots\,, \tag{2.122c}$$

where we have truncated the result to first order in x and y. In this first order approximation, a solenoid is primarily a constant field pointing along $\hat{z}$, with a radial field at the fringes.

$\nu = 1$**: Dipole**

A dipole has C_1 symmetry. Using Eq. (2.120) for only $\nu = 1$, we have

$$\psi(x, y, z) = x\,\mathrm{Im}\,(\Psi_1) - y\,\mathrm{Re}\,(\Psi_1) + \ \ldots\,, \tag{2.123}$$

where we have truncated the result to second order in x and y (no second order terms in x and y here). This gives a magnetic field

$$B_x = -\,\mathrm{Im}\,(\Psi_1) + \ \ldots\,, \tag{2.124a}$$

$$B_y = \mathrm{Re}\,(\Psi_1) + \ \ldots\,, \tag{2.124b}$$

$$B_z = -x\,\mathrm{Im}\,(\Psi_1') + y\,\mathrm{Re}\,(\Psi_1') + \ \ldots\,, \tag{2.124c}$$

where we have truncated the result to first order in x and y. In this first order approximation, the dipole consists primarily of a constant field pointing along the vertical, horizontal, or a combination of both, specified respectively by the real and imaginary parts of Ψ_1. These are also referred to as the normal and skew components respectively, where a skew magnet is equal to a normal magnet rotated by an angle $-\pi/(2\nu)$ about $\hat{z}$. Two poles are needed to create this magnet, hence the term "dipole".

$\nu = 2$: Quadrupole

A quadrupole has C_2 symmetry. Using Eq. (2.120) for only $\nu = 2$, we have

$$\psi(x, y, z) = \frac{1}{2} \operatorname{Im}\left[(x - \mathrm{i}y)^2 \Psi_2\right] + \ \ldots , \tag{2.125}$$

where we have truncated the result to second order in x and y. This gives a magnetic field

$$B_x = -x \operatorname{Im}(\Psi_1) + y \operatorname{Re}(\Psi_1) + \ \ldots , \tag{2.126a}$$

$$B_y = x \operatorname{Re}(\Psi_1) + y \operatorname{Im}(\Psi_1) + \ \ldots , \tag{2.126b}$$

$$B_z = \ \ldots , \tag{2.126c}$$

where we have truncated the result to first order in x and y. In this first order approximation, the quadrupole consists primarily of a field with linear dependence in x and y. The normal and skew quadrupole strengths are specified by the real and imaginary parts of Ψ_1 respectively. Quadrupoles are constructed with four equiangular, alternating poles around $\hat{z}$.

2.3.2 Coordinate System and Canonical Coordinates

In Sec. 2.2.2, we performed our perturbation theory using a coordinate system expanded around the fixed point. However, before the fixed point is actually computed, we need to have some coordinate system that we can use to integrate the motion and subsequently find the fixed point. Accelerator physicists usually use coordinate system that moves through the magnets in a way that some "ideal beam" is desired to move, e.g. through center of all magnets at the velocity of the "ideal" beam. As such, the terms "reference orbit/trajectory" and "reference particle" have frequently been used to specify the origin of this coordinate system. This is rather unfortunate, because **this coordinate system in general does not obey the equations of motion, and thus is not a physical trajectory!** The terms "reference orbit" and "reference particle" can cause great confusion for this very reason, and care must be taken to keep in mind that this is simply a coordinate system choice. Fortunately, there is some ongoing effort to change the terminology associated with this coordinate system [29].

With this in mind, Fig. 2.3 shows the curvilinear coordinate system (with curvature $\boldsymbol{g}$) used to specify a particle's coordinates throughout integration. In this dissertation, we may interchange $\hat{\boldsymbol{z}}$ with $\hat{\boldsymbol{s}}$. In accelerators we commonly integrate using the position s in the accelerator as the independent variable. The canonical coordinates we use are $\boldsymbol{z} = (x, p_x, y, p_y, z, p_z)$ where x, y, and z are just the positions at some given s wrt the "reference particle" as shown in Fig. 2.3 and the momenta aren ormalized by the "reference momentum" P_0,

$$p_x = \frac{P_x}{P_0} \ , \ p_y = \frac{P_y}{P_0} \ , \ p_z = \frac{P - P_0}{P_0} \ . \tag{2.127}$$

The reference momentum P_0 is basically the momentum that a particle would have if it were travelling at the same velocity as the "reference particle".

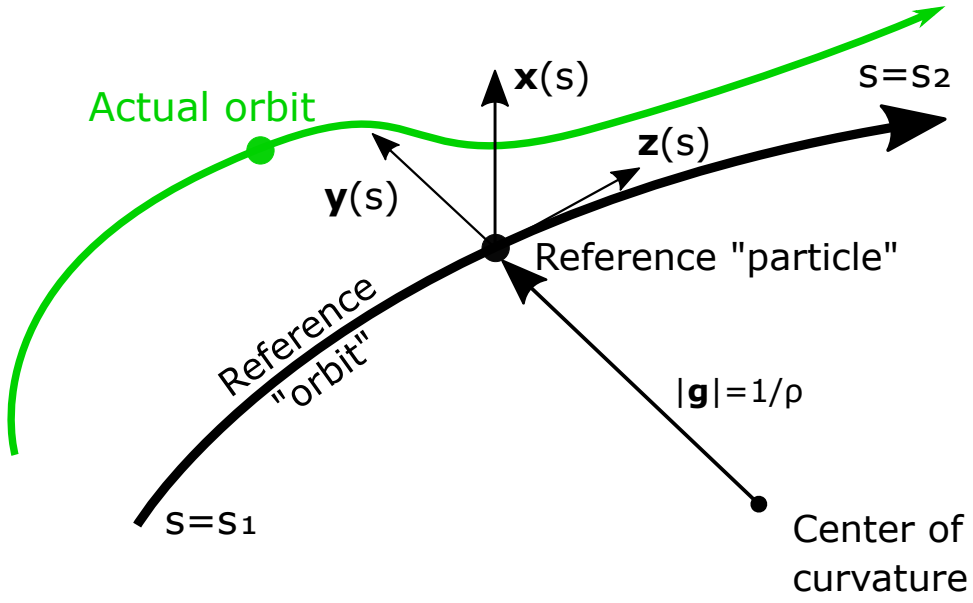

Figure 2.3: Curvilinear coordinate system definition commonly used in accelerator physics, where the basis functions are functions of the arc position s around the accelerator. The terms reference "orbit" and reference "particle" are put in quotes to emphasize that they are not in general real physical trajectories that obey the equations of motion.

CHAPTER 3

SPIN DYNAMICS

In accelerator physics, the spin is often treated as a "spectator" - the orbit affects a particle's spin, but not vice-versa. This means we are neglecting Stern-Gerlach effects, which has historically proven to be a reasonable approximation.

In Sec. 2.2.3, we modified our Lie operator so that systems which may include large damping can be handled equally alongside symplectic systems. Similarly, we can include spin in this entire framework we've already developed with a further modification to our Lie operator.

3.1 Quaternions

First, let us discuss how exactly we will track spin. One way is, for each particle, to simply integrate the 3-vector $\boldsymbol{S}$ of the spin components in each direction. While this sounds the simplest, one major problem is that if we want to reconstruct the rotation matrix representing the spin transport of a single particle, then we need to track three separate particles where the spins are orthogonal but the phase space coordinates are the same. A better alternative would be to instead track an SO(3) rotation matrix per particle, so that only 1 particle's phase space coordinates are being integrated as opposed to three. However, this still involves tracking 9 numbers to capture the spin, and so is suboptimal.

A best method would be to track a *quaternion* with each particle capturing the spin transport. As is clear by now, complex numbers with unit norm represent rotations in 2D. The quaternions extend complex numbers to represent rotations

in 3D. Specifically, for three angles we need three "imaginary numbers",

$$\mathbf{i}_1^2 = \mathbf{i}_2^2 = \mathbf{i}_3^2 = \mathbf{i}_1\mathbf{i}_2\mathbf{i}_3 = -1 \ . \tag{3.1}$$

Letting $\hat{\boldsymbol{i}} = (\mathbf{i}_1, \mathbf{i}_2, \mathbf{i}_3)$, we can express a rotation θ around an axis $\hat{\boldsymbol{u}}$ in a de Moivre representation as

$$\mathbf{q} = \cos\left(\frac{\theta}{2}\right) + \hat{\boldsymbol{u}} \cdot \hat{\boldsymbol{i}} \sin\left(\frac{\theta}{2}\right) = e^{\frac{\theta}{2}\hat{\boldsymbol{u}}\cdot\hat{\boldsymbol{i}}} \ . \tag{3.2}$$

Note that $\theta/2$ is used instead of just θ. The reason for this is because of how quaternions representing a spin vector are transformed. Let $\mathbf{s} = S_x\mathbf{i}_1 + S_y\mathbf{i}_2 + S_z\mathbf{i}_2$ be a quaternion representing the 3-vector $\boldsymbol{S}$. To apply a rotation θ around an axis $\hat{\boldsymbol{u}}$,

$$\mathbf{s}' = e^{\frac{\theta}{2}\hat{\boldsymbol{u}}\cdot\hat{\boldsymbol{i}}}\mathbf{s}e^{-\frac{\theta}{2}\hat{\boldsymbol{u}}\cdot\hat{\boldsymbol{i}}} \ . \tag{3.3}$$

The SO(3) rotation matrix in terms of a quaternion is

$$\mathsf{R}_{ij} = (\mathbf{q}\cdot\overline{\mathbf{q}})\,\delta_{ij} + 2q_iq_j - 2q_0\epsilon_{ijk}q_k \ . \tag{3.4}$$

where δ_{ij} is the Kronecker delta, ϵ_{ijk} is the Levi-Civita tensor, and $\overline{\mathbf{q}}$ is the quaternion conjugate of $\mathbf{q}$ defined as $\overline{\mathbf{q}} = q_0 - q_1\mathbf{i}_1 - q_2\mathbf{i}_2 - q_3\mathbf{i}_3$.

Quaternions offer significant computational advantages over an SO(3) representation of rotations; only four numbers need to be stored, and the concatenation of two successive rotations $\mathbf{q}_1$ and $\mathbf{q}_2$, which is expressed by the multiplication $\mathbf{q}_2\mathbf{q}_1$, has 28 floating point operations compared to the 48 to multiply two SO(3) matrices. Furthermore, quaternions can be used to extend our Lie operator defined in Sec. 2.2.3, and achieve a unified theory for both orbital and spin normal form[1].

[1]This is described in a private extension of [32]. Contact the author of this dissertation at mgs255@cornell.edu for a copy.

3.2 Invariant Spin Field (ISF)

In Ch. 2, we described in detail how the dynamics of (quasi-)periodic systems can be generally analyzed by computing invariants of the motion and a nonlinear transformation to Floquet variables where the motion is amplitude-dependent rotations. Likewise, to analyze spin, the calculation of a spin invariant is required. Then we will compute a transformation to coordinates where the spin precession is an amplitude-dependent rotation *around a single axis*; in our normal form methods developed here, we choose the vertical axis. The calculation of this transformation is shown in Sec. 3.4.

Transforming this vertical axis in circle world back to regular coordinates gives the so-called *invariant spin field (ISF)* $\hat{\boldsymbol{n}}$. This special 1-turn periodic spin field solves the spin equation of motion along orbital trajectories. Explicitly,

$$\hat{\boldsymbol{n}}(\boldsymbol{m}(\boldsymbol{\zeta}_i)) = \mathsf{R}(\boldsymbol{\zeta}_i)\hat{\boldsymbol{n}}(\boldsymbol{\zeta}_i) \,, \tag{3.5}$$

where $\boldsymbol{\zeta}_i = (x, p_x, y, p_y, z, \delta)_i^T$ are the initial canonical phase space coordinates in a coordinate system with its origin on the closed orbit (i.e. $\boldsymbol{\zeta}_{\text{c.o.}} = \boldsymbol{0}$), δ is the relative momentum deviation from the closed orbit momentum p_0, $\boldsymbol{m}$ is the 1-turn map, and R is the spin transport rotation matrix for a particle through one turn. Note we have omitted the azimuthal position around the ring for brevity. The ISF, when it exists, is unique up to a flip in sign ($\hat{\boldsymbol{n}}$ and $-\hat{\boldsymbol{n}}$ both satisfy Eq. (3.5)), and the ISF evaluated on the closed orbit $\hat{\boldsymbol{n}}(\boldsymbol{\zeta}_{\text{c.o.}})$ is referred to as $\hat{\boldsymbol{n}}_0$. Unlike for general orbits, $\hat{\boldsymbol{n}}_0$ can be obtained from the eigenvector with unit eigenvalue of the 1-turn spin rotation matrix on the closed orbit. The projection of any particle's spin along the ISF is called the spin action, $J_s = \boldsymbol{S} \cdot \hat{\boldsymbol{n}}$. The spin action is an adiabatic invariant, in that if some dynamical parameter is varied slowly with respect to the orbital angle evolution, J_s remains constant [39].

3.3 Extending the Lie Algebra to Include Spin

We first extend our DA map to include a quaternion. For two orbital-quaternion maps $T_2 = (\boldsymbol{m}_2, \mathbf{q}_2)$ and $T_1 = (\boldsymbol{m}_1, \mathbf{q}_1)$, the composition rule is

$$T_2 \circ T_1 = \left[\boldsymbol{m}_2 \circ \boldsymbol{m}_1, (\mathbf{q}_2 \circ \boldsymbol{m}_1)\mathbf{q}_1\right] . \tag{3.6}$$

To compose the quaternions, the second quaternion $\mathbf{q}_2$ must be expressed in terms of the variables exiting $\boldsymbol{m}_1$, prior to quaternion concatenation with $\mathbf{q}_1$.

As stated before, the orbital Lie operators act on functions of phase space. When acting a Lie exponent $\mathcal{M} = \exp(\boldsymbol{F} \cdot \boldsymbol{\nabla})$ on the identity DA map $\boldsymbol{\zeta}$, we obtain an ordinary DA map,

$$\boldsymbol{m} = \mathcal{M}\boldsymbol{\zeta} = \exp(\boldsymbol{F} \cdot \boldsymbol{\nabla})\boldsymbol{\zeta} \quad \Rightarrow \quad \mathcal{M}f = f \circ \boldsymbol{m} . \tag{3.7}$$

And when acting a Lie map $\mathcal{M}_1$ on another DA map $\boldsymbol{m}_2$,

$$\mathcal{M}_1\boldsymbol{m}_2 = \exp(\boldsymbol{F}_1 \cdot \boldsymbol{\nabla})\boldsymbol{m}_2 = \boldsymbol{m}_2 \circ \boldsymbol{m}_1, \qquad \boldsymbol{m}_1 = \mathcal{M}_1\boldsymbol{\zeta} . \tag{3.8}$$

Now we want redefine our Lie operator to include a quaternion operator $\breve{\mathbf{f}}$,

$$\mathcal{M} = \exp(\boldsymbol{F} \cdot \boldsymbol{\nabla} + \breve{\mathbf{f}}) , \tag{3.9}$$

where the quaternion operator $\breve{\mathbf{f}}$ *only acts on quaternions because spin is a spectator*. In fact, the Lie operator has to act on a quaternion $\mathbf{q}$ in a special way,

$$(\boldsymbol{F} \cdot \boldsymbol{\nabla} + \breve{\mathbf{f}})\mathbf{q} = \boldsymbol{F} \cdot \boldsymbol{\nabla}\mathbf{q} + \mathbf{q}\mathbf{f} , \tag{3.10}$$

where $\mathbf{f}$ is the quaternion associated with the quaternion operator $\breve{\mathbf{f}}$, and the gradient acts on each component of the quaternion. Note that the quaternion part of the entire Lie operator acts in the *reverse*, putting the quaternion $\mathbf{q}$ in front. This behavior is necessary so that Eq. (3.8) is still satisfied for orbital-quaternion

maps. Letting $(\boldsymbol{m}_1, \mathbf{q}_1) = \mathcal{M}_1(\boldsymbol{\zeta}, \mathbf{1})$ where $\mathbf{1}$ corresponds to the identity quaternion, with this definition of the action of the quaternion operator we indeed have

$$\mathcal{M}_1(\boldsymbol{m}_2, \mathbf{q}_2) = \exp\left(\boldsymbol{F}_1 \cdot \boldsymbol{\nabla} + \breve{\mathbf{f}}_1\right)(\boldsymbol{m}_2, \mathbf{q}_2) = (\boldsymbol{m}_2, \mathbf{q}_2) \circ (\boldsymbol{m}_1, \mathbf{q}_1) \,. \tag{3.11}$$

We now need to define a multiplication operation for the vector space of our new Lie operators. This is just the commutator,

$$[\boldsymbol{F} \cdot \boldsymbol{\nabla} + \breve{\mathbf{f}}, \boldsymbol{G} \cdot \boldsymbol{\nabla} + \breve{\mathbf{g}}] = \boldsymbol{H} \cdot \boldsymbol{\nabla} + \breve{\mathbf{h}} \tag{3.12}$$

where

$$\boldsymbol{H} = \boldsymbol{F} \cdot \boldsymbol{\nabla}\boldsymbol{G} - \boldsymbol{G} \cdot \boldsymbol{\nabla}\boldsymbol{F} \,, \tag{3.13a}$$

$$\breve{\mathbf{h}} = [\mathbf{g}, \mathbf{f}] + \underbrace{\boldsymbol{F} \cdot \boldsymbol{\nabla}\mathbf{g} - \boldsymbol{G} \cdot \boldsymbol{\nabla}\mathbf{f}}_{\text{“Derivation by extension”}} \,, \tag{3.13b}$$

and $\mathbf{f}$ and $\mathbf{g}$ are the quaternions associated with the quaternion operators $\breve{\mathbf{f}}$ and $\breve{\mathbf{g}}$ respectively. Just as we did in Eq. (2.74) and Eq. (2.94), let's see how our new Lie operator transforms. For $\mathcal{A}(\boldsymbol{\zeta}, \mathbf{1}) = (\boldsymbol{a}, \mathbf{q}_a)$ and $\mathcal{A}^{-1}(\boldsymbol{\zeta}, \mathbf{1}) = (\boldsymbol{a}^{-1}, \mathbf{q}_a^{-1} \circ \boldsymbol{a}^{-1})$ let's calculate how our Lie operator transforms,

$$\mathcal{A}(\boldsymbol{F} \cdot \boldsymbol{\nabla} + \breve{\mathbf{f}})\mathcal{A}^{-1} = \boldsymbol{F}_{new} \cdot \boldsymbol{\nabla} + \breve{\mathbf{f}}_{new} \,. \tag{3.14}$$

where it can be shown that

$$\boldsymbol{F}_{new} = (\boldsymbol{F} \cdot \boldsymbol{\nabla}\boldsymbol{a}^{-1}) \circ \boldsymbol{a} \,, \tag{3.15a}$$

$$\mathbf{f}_{new} = (\boldsymbol{F} \cdot \boldsymbol{\nabla}\mathbf{q}_a^{-1})\mathbf{q}_q + \mathbf{q}_a^{-1}(\mathbf{f} \circ \boldsymbol{a})\mathbf{q}_a \,, \tag{3.15b}$$

where $\mathbf{f}_{new}$ is the quaternion associated with quaternion operator $\breve{\mathbf{f}}_{new}$. Because spin is a spectator, we see that the orbital part in Eq. (3.15a) is equivalent to Eq. (2.94).

3.4 Spin Normal Form

As discussed at the beginning of Sec. 3.2, in the spin normal form all particles' spins exhibit amplitude-dependent precessions around the vertical axis. We want to extend our normalizing compositional map $\mathcal{A}$ to include a quaternion part to perform the transformation to this circle world.

First, let $\mathcal{A}_\zeta$ correspond to the map which normalizes the orbital part of $\mathcal{M}$ per Sec. 2.2.2. Because this does not also normalize the quaternion part, after orbital normalization we are left with a compositional map which can be written as

$$\begin{aligned}\mathcal{A}_\zeta \mathcal{M} \mathcal{A}_\zeta^{-1} &= \exp\left[\mu(\boldsymbol{J}) \cdot \frac{\partial}{\partial \phi} - \frac{1}{2}\Omega(\boldsymbol{J}, \phi) \cdot \check{\hat{\boldsymbol{i}}}\right] \\ &= \exp\left[\mu(\boldsymbol{J}) \cdot \frac{\partial}{\partial \phi} - \frac{1}{2}[\mu_{s,0}\hat{\boldsymbol{n}}_0 + \boldsymbol{\omega}(\boldsymbol{J}, \phi)] \cdot \check{\hat{\boldsymbol{i}}}\right] \\ &= \exp\left[\mu(\boldsymbol{J}) \cdot \frac{\partial}{\partial \phi} - \frac{1}{2}\mu_{s,0}\hat{\boldsymbol{n}}_0 \cdot \check{\hat{\boldsymbol{i}}}\right] \exp\left[\boldsymbol{f}(\boldsymbol{J}, \phi) \cdot \check{\hat{\boldsymbol{i}}}\right], \end{aligned} \tag{3.16}$$

where $\mu_{s,0} = 2\pi\nu_0$ and ν_0 is the closed orbit spin tune. The first step is to apply a quaternion map so that the zeroth order part is a rotation around the vertical. This is very easily computed; the axis of rotation is taken to be the cross product of $\hat{\boldsymbol{n}}_0$ and $\hat{\boldsymbol{y}}$, and the rotation angle is that between $\hat{\boldsymbol{n}}_0$ and $\hat{\boldsymbol{y}}$, which is $\alpha = \arccos(\hat{\boldsymbol{n}}_0 \cdot \hat{\boldsymbol{y}})$. This zeroth order quaternion normalizing map, specified as $\mathcal{A}_{s0}$, is

$$\mathcal{A}_{s0} = \exp\left[-\frac{1}{2}\alpha\left(\frac{\hat{\boldsymbol{n}}_0 \times \hat{\boldsymbol{y}}}{|\hat{\boldsymbol{n}}_0 \times \hat{\boldsymbol{y}}|}\right) \cdot \check{\hat{\boldsymbol{i}}}\right] = \exp\left[-\frac{1}{2}\alpha\left(\frac{-\hat{n}_{0s}\check{\hat{\mathbf{i}}}_1 + \hat{n}_{0x}\check{\hat{\mathbf{i}}}_3}{\sqrt{\hat{n}_{0x}^2 + \hat{n}_{0s}^2}}\right)\right]. \tag{3.17}$$

Applying this to our orbital-normalized map,

$$\mathcal{A}_{s0}\mathcal{A}_\zeta \mathcal{M} \mathcal{A}_\zeta^{-1}\mathcal{A}_{s0}^{-1} = \exp\left[\mu(\boldsymbol{J}) \cdot \frac{\partial}{\partial \phi} - \frac{1}{2}\mu_{s,0}\check{\hat{\mathbf{i}}}_2\right] \exp\left[\boldsymbol{a}(\boldsymbol{J}, \phi) \cdot \check{\hat{\boldsymbol{i}}}\right]. \tag{3.18}$$

Now, all we have to do is go order-by-order normalizing the quaternion, similar to how we did the orbital. Following the same procedure as in Sec. 2.2.2, at a

given step we have the quaternion normalized up to order $i-1$,

$$\begin{aligned}
\tilde{\mathcal{N}}_{i-1} &= \exp\left[\tilde{\boldsymbol{\mu}}[\boldsymbol{J}(\tilde{\boldsymbol{\zeta}})]\cdot\boldsymbol{\nabla} - \frac{1}{2}\tilde{\mu}_{s,0\to i-1}[\boldsymbol{J}(\tilde{\boldsymbol{\zeta}})]\breve{\mathbf{i}}_2\right]\exp\left[\tilde{\breve{\mathbf{h}}}_i(\tilde{\boldsymbol{\zeta}})\right]\ldots\,, \\
&= \underbrace{\exp\left[\tilde{\boldsymbol{\mu}}_0\cdot\boldsymbol{\nabla} - \frac{1}{2}\mu_{s,0}\breve{\mathbf{i}}_2\right]}_{=\tilde{\mathcal{R}}_1}\underbrace{\exp\left[\tilde{\boldsymbol{\mu}}_{2\to\infty}[\boldsymbol{J}(\tilde{\boldsymbol{\zeta}})]\cdot\boldsymbol{\nabla} - \frac{1}{2}\tilde{\mu}_{s,2\to i-1}[\boldsymbol{J}(\tilde{\boldsymbol{\zeta}})]\breve{\mathbf{i}}_2\right]}_{=\tilde{\mathcal{R}}_{i-1}}\exp\left[\tilde{\breve{\mathbf{h}}}_i(\tilde{\boldsymbol{\zeta}})\right]\ldots\,, \\
&= \tilde{\mathcal{R}}_1\tilde{\mathcal{R}}_{i-1}\exp\left[\tilde{\breve{\mathbf{h}}}_i(\tilde{\boldsymbol{\zeta}})\right]\ldots\,, \qquad (3.19)
\end{aligned}$$

where we have explicitly separated the first-order rotation $\tilde{\mathcal{R}}_1$ from the nonlinear rotation up to order $i-1$, $\tilde{\mathcal{R}}_{i-1}$, for reasons that will be apparent shortly. The subscript to both $\tilde{\mu}$ and $\tilde{\mu}_s$ specify the orders of the polymonial included, starting at 2 because that is the minimum needed to have a $\boldsymbol{J}$ (reminder: $J_1 = \tilde{\zeta}_1\tilde{\zeta}_1^*$). To normalize the next i-th order, we apply some quaternion operator $\breve{\mathbf{g}}_i$ so that

$$\begin{aligned}
\tilde{\mathcal{N}}_i &= \exp(\tilde{\breve{\mathbf{g}}}_i)\tilde{\mathcal{N}}_{i-1}\exp(-\tilde{\breve{\mathbf{g}}}_i) \\
&= \exp(\tilde{\breve{\mathbf{g}}}_i)\tilde{\mathcal{R}}_1\tilde{\mathcal{R}}_{i-1}\exp[\tilde{\breve{\mathbf{h}}}_i(\tilde{\boldsymbol{\zeta}})]\ldots\exp(-\tilde{\breve{\mathbf{g}}}_i) \\
&= \tilde{\mathcal{R}}_1\tilde{\mathcal{R}}_1^{-1}\exp(\tilde{\breve{\mathbf{g}}}_i)\tilde{\mathcal{R}}_1\tilde{\mathcal{R}}_{i-1}\exp[\tilde{\breve{\mathbf{h}}}_i(\tilde{\boldsymbol{\zeta}})]\ldots\exp(-\tilde{\breve{\mathbf{g}}}_i) \\
&= \tilde{\mathcal{R}}_1\exp(\tilde{\mathcal{R}}_1^{-1}\tilde{\breve{\mathbf{g}}}_i\tilde{\mathcal{R}}_1)\tilde{\mathcal{R}}_{i-1}\exp[\tilde{\breve{\mathbf{h}}}_i(\tilde{\boldsymbol{\zeta}})]\ldots\exp(-\tilde{\breve{\mathbf{g}}}_i) \\
&= \tilde{\mathcal{R}}_1\tilde{\mathcal{R}}_{i-1}\exp[\tilde{\mathcal{R}}_1^{-1}\tilde{\breve{\mathbf{g}}}_i\tilde{\mathcal{R}}_1 + \breve{\mathbf{O}}(\zeta^{i+1})]\exp[\tilde{\breve{\mathbf{h}}}_i(\tilde{\boldsymbol{\zeta}})]\ldots\exp(-\tilde{\breve{\mathbf{g}}}_i) \\
&= \tilde{\mathcal{R}}_1\tilde{\mathcal{R}}_{i-1}\exp[\tilde{\mathcal{R}}_1^{-1}\tilde{\breve{\mathbf{g}}}_i\tilde{\mathcal{R}}_1 + \breve{\mathbf{O}}(\zeta^{i+1})]\exp[\tilde{\breve{\mathbf{h}}}_i(\tilde{\boldsymbol{\zeta}})]\ldots\exp(-\tilde{\breve{\mathbf{g}}}_i) \\
&= \tilde{\mathcal{R}}_1\tilde{\mathcal{R}}_{i-1}\exp[\tilde{\mathcal{R}}_1^{-1}\tilde{\breve{\mathbf{g}}}_i\tilde{\mathcal{R}}_1 + \tilde{\breve{\mathbf{h}}}_i(\tilde{\boldsymbol{\zeta}}) - \tilde{\breve{\mathbf{g}}}_i]\exp[\tilde{\breve{\mathbf{h}}}_{i+1}(\tilde{\boldsymbol{\zeta}}) + \breve{\mathbf{O}}(\zeta^{i+1})]\ldots\,. \qquad (3.20)
\end{aligned}$$

Now, just as we did with the orbital, we try to set the i-th order Lie exponent equal to zero,

$$\tilde{\mathcal{R}}_1^{-1}\tilde{\breve{\mathbf{g}}}_i\tilde{\mathcal{R}}_1 + \tilde{\breve{\mathbf{h}}}_i - \tilde{\breve{\mathbf{g}}}_i = 0\,. \qquad (3.21)$$

Dropping the underscore i specifying the homogenous polynomial order, using Eq. (3.15) we have

$$\exp\left(\frac{1}{2}\mu_{s,0}\mathbf{i}_2\right)(\mathcal{R}_1^{-1}\tilde{\mathbf{g}})\exp\left(-\frac{1}{2}\mu_{s,0}\mathbf{i}_2\right) - \tilde{\mathbf{g}} + \tilde{\mathbf{h}} = 0\,, \qquad (3.22)$$

where we now have removed the " ˘ " operator symbol and are just working with the quaternions associated with the operator. To simplify this equation so that we can easily solve for the $\tilde{\mathbf{g}}_i$, we use the following identity,

$$\exp\left(\frac{1}{2}\theta\mathbf{i}_2\right)\mathbf{i}_\pm \exp\left(-\frac{1}{2}\theta\mathbf{i}_2\right) = e^{\pm \mathrm{i}\theta}\mathbf{i}_\pm\ ,\quad \mathbf{i}_\pm = \frac{1}{2}(\mathbf{i}_1 \pm \mathrm{i}\ \mathbf{i}_3)\ , \tag{3.23}$$

where i is the usual imaginary number. If we instead express each of the $\tilde{\mathbf{g}}_i$, $\tilde{\mathbf{h}}_i$ in Eq. (3.22) in this basis of "eigenquaternions", we can get a very simple form,

$$e^{\pm \mathrm{i}\mu_{s,0}}\mathcal{R}_1^{-1}\tilde{\mathbf{g}}_\pm - \tilde{\mathbf{g}}_\pm + \tilde{\mathbf{h}}_\pm = 0 \ \rightarrow\ (e^{\pm \mathrm{i}\mu_{s,0}}\mathcal{R}_1^{-1} - \mathcal{I})\tilde{\mathbf{g}}_\pm + \tilde{\mathbf{h}}_\pm = 0\ , \tag{3.24}$$

and

$$(\mathcal{R}_1^{-1} - \mathcal{I})\tilde{\mathbf{g}}_2 + \tilde{\mathbf{h}}_2 = 0\ . \tag{3.25}$$

Finally, just as we did in Sec. 2.2.2 and Sec. 2.2.3, we consider a given monomial specified by the multi-index $\boldsymbol{m}$. We obtain the equations for $\tilde{\mathbf{g}}$,

$$\tilde{\mathbf{g}}_{\pm,\boldsymbol{m}} = \frac{\tilde{\mathbf{h}}_{\pm,\boldsymbol{m}}}{1 - e^{\pm \mathrm{i}\mu_{s,0}}\prod_{k=1}^{2n}(\lambda_k^*)^{m_k}}\ , \tag{3.26a}$$

$$\tilde{\mathbf{g}}_{2,\boldsymbol{m}} = \frac{\tilde{\mathbf{h}}_{2,\boldsymbol{m}}}{1 - \prod_{k=1}^{2n}(\lambda_k^*)^{m_k}}\ . \tag{3.26b}$$

Note that spin resonances are clearly defined by the small denominator in Eq. (3.26a). After the fully nonlinear spin normalization, letting $\mathcal{A} = \mathcal{A}_s\mathcal{A}_\zeta$, we have

$$\mathcal{A}\mathcal{M}\mathcal{A}^{-1} = \exp\left(\mu(\boldsymbol{J})\cdot\frac{\partial}{\partial\boldsymbol{\phi}} - \frac{1}{2}\mu_s(\boldsymbol{J})\breve{\mathbf{i}}_2\right). \tag{3.27}$$

where $\nu(\boldsymbol{J}) = \frac{1}{2\pi}\mu_s(\boldsymbol{J})$ corresponds to the *amplitude-dependent spin tune*. With this $\mathcal{A}$ now including spin normalization, the invariant spin field can be easily computed,

$$\mathbf{n} = \mathcal{A}^{-1}\mathbf{i}_2\mathcal{A}\ . \tag{3.28}$$

This spin normalization algorithm has been implemented in the SciBmad package `NonlinearNormalForm.jl` as a part of this dissertation.

3.5 Alternative Methods to Compute the ISF

3.5.1 Stroboscopic Averaging

One way to compute the ISF for a given torus $\boldsymbol{J}$ is to use the fact that the spin action J_s must remain invariant. Therefore, one could imagine that if a particle returns to exactly the same phase space coordinate many times, then the *average* of its spin at the coordinate would point either directly along the ISF or be equal to zero if the spin is directly perpendicular to the ISF. However, technically, if it returns exactly to the same position then this would be sitting on some (potentially high order) orbital resonance. In order to actually achieve this result in a general case, we can start a particle on some torus $\boldsymbol{J}$ at some initial position given by the angle ϕ, track forward and store each $\mathsf{R}_j(\phi_0)$ spin rotation matrix from the initial coordinates through the j-th turn. Then by tracking some test spin $\boldsymbol{S}_0$ *backwards* using $\mathsf{R}_j^{-1}(\phi_0)$ the average over each result will point along the ISF or be equal to zero. This method, which relies on the fact that the ISF of the inverse motion is equal to the ISF of the forward motion, is referred to in the literature as "stroboscopic averaging" [37]. However, it has been suggested that just "averaging" may be a more appropriate name due to its one-turn nature [32].

For some particle on a torus $\boldsymbol{J}$ with initial angle ϕ_0, this is expressed rigrously as

$$\lim_{N\to\infty} \frac{1}{N+1} \sum_{j=0}^{N} \mathsf{R}_j^{-1}(\phi_0)\boldsymbol{S}_0 = \left[\langle \hat{\boldsymbol{n}}(\phi)\rangle_\phi \cdot \boldsymbol{S}_0\right] \hat{\boldsymbol{n}}(\phi_0)\,, \tag{3.29}$$

where $\langle ...\rangle_\phi$ denotes an average over all angle coordinates of the particle [37, 23].

Let

$$\bar{\mathsf{R}}(\phi_0) = \lim_{N\to\infty} \frac{1}{N+1} \sum_{j=0}^{N} \mathsf{R}_j(\phi_0) \,. \tag{3.30}$$

Then using the fact that

$$\lim_{N\to\infty} \frac{1}{N+1} \sum_{j=0}^{N} \mathsf{R}_j^{-1}(\phi_0) = \lim_{N\to\infty} \frac{1}{N+1} \sum_{j=0}^{N} \mathsf{R}_j^{T}(\phi_0) = \left[\lim_{N\to\infty} \frac{1}{N+1} \sum_{j=0}^{N} \mathsf{R}_j(\phi_0) \right]^T = \bar{\mathsf{R}}^T(\phi_0) \,, \tag{3.31}$$

we can rewrite Eq. (3.29) as

$$\bar{\mathsf{R}}^T(\phi_0)\boldsymbol{S}_0 = \left[\langle \hat{\boldsymbol{n}}(\phi)\rangle_\phi \cdot \boldsymbol{S}_0\right] \hat{\boldsymbol{n}}(\phi_0) \,, \tag{3.32}$$

which shows that for *any* $\boldsymbol{S}_0$, multiplication by $\bar{\mathsf{R}}^T$ gives a vector pointing along $\hat{\boldsymbol{n}}(\phi_0)$. This is an important result; it means that the matrix $\bar{\mathsf{R}}^T$ has rank 1, and that $\bar{\mathsf{R}}^T(\phi_0) = \hat{\boldsymbol{n}}(\phi_0)\boldsymbol{v}^T$ where $\boldsymbol{v}$ is some vector. Plugging this into Eq. (3.32) we immediately see that $\boldsymbol{v}^T = \langle \hat{\boldsymbol{n}}(\phi)\rangle_\phi^T$. Therefore we have

$$\bar{\mathsf{R}}^T(\phi_0) = \hat{\boldsymbol{n}}(\phi_0)\langle \hat{\boldsymbol{n}}(\phi)\rangle_\phi^T \,. \tag{3.33}$$

This rank 1 matrix will have one eigenvector with nonzero eigenvalue, that is $\hat{\boldsymbol{n}}(\phi_0)$ with eigenvalue $\langle \hat{\boldsymbol{n}}(\phi)\rangle_\phi \cdot \hat{\boldsymbol{n}}(\phi_0)$. Thus there is no need for even using any test spin $\boldsymbol{S}_0$, simply compute the eigenvectors of $\bar{\mathsf{R}}^T$ and choose that with nonzero eigenvalue (or for finite N, the largest eigenvalue).

The non-transposed, forward-tracked rotation matrix $\bar{\mathsf{R}}$ could alternatively be used in a very similar analysis,

$$\bar{\mathsf{R}}(\phi_0) = \langle \hat{\boldsymbol{n}}(\phi)\rangle_\phi \hat{\boldsymbol{n}}(\phi_0)^T \,. \tag{3.34}$$

Of course, $\bar{\mathsf{R}}$ will have the same eigenvalues as $\bar{\mathsf{R}}^T$. And it can be shown that the nonzero eigenvector for this matrix will thus be $\langle \hat{\boldsymbol{n}}(\phi)\rangle_\phi$.

3.5.2 SODOM-2

SODOM-2 is an algorithm formulated by K. Yokoya [77] to calculate the ISF in an accelerator by decomposing the spin and orbit motion into their Fourier components. The derivation shown here is taken nearly exactly from [37]. We can rewrite the ISF in Eq.(3.5) in terms of the azimuth θ,

$$\hat{\boldsymbol{n}}(z,\theta) = \mathsf{R}(z_0,\theta_0;\theta)\boldsymbol{n}(z_0,\theta_0), \qquad \boldsymbol{n}(z,\theta_0+2\pi) = \boldsymbol{n}(z,\theta_0) \tag{3.35}$$

A particle lies on the invariant torus defined by $\boldsymbol{J}$, where each J_i is the action in the i-th oscillation mode. In the following expressions the actions $\boldsymbol{J}$ are omitted because they are constants. The ISF can be expressed in SU(2) as a spinor $\Psi(\phi,\theta)$ where $\boldsymbol{n}(\phi,\boldsymbol{\theta}) = \Psi^\dagger\boldsymbol{\sigma}\Psi$ and $\boldsymbol{\sigma}$ are the Pauli matrices. Omitting the azimuth position θ, starting at ϕ after one turn the invariant spin direction at the angle coordinates ϕ agrees with the invariant spin direction at $\phi + 2\pi\boldsymbol{Q}$, where $\boldsymbol{Q}$ are the orbital tunes in each mode, up to some arbitrary phase factor $\tilde{\nu}_{\boldsymbol{J}}(\phi)$,

$$\underline{\mathsf{R}}(\phi)\Psi(\phi) = e^{-\mathrm{i}\pi\tilde{\nu}_{\boldsymbol{J}}(\phi)}\Psi(\phi+2\pi\boldsymbol{Q})\,, \tag{3.36}$$

where $\underline{\mathsf{R}}(\phi)$ is the 1-turn spin transport quaternion at initial angle ϕ. A phase function $\varphi_{\boldsymbol{J}}(\phi)$ is used such that the new spinor $\Psi_n(\phi) = e^{\mathrm{i}\frac{1}{2}\varphi_{\boldsymbol{J}}(\phi)}\Psi(\phi)$ has the periodicity condition

$$\underline{\mathsf{R}}(\phi)\Psi_n(\phi) = e^{-\mathrm{i}\pi\nu(\boldsymbol{J})}\Psi_n(\phi)\,, \tag{3.37}$$

where the phase factor $\nu(\boldsymbol{J}) = 2\pi\tilde{\nu}_{\boldsymbol{J}}(\phi) - \varphi_{\boldsymbol{J}}(\phi) + \varphi_{\boldsymbol{J}}(\phi+2\pi\boldsymbol{Q})$ is independent of the angle coordinates ϕ. This is the amplitude-dependent spin tune $\nu(\boldsymbol{J})$. The 1-turn quaternion $\underline{\mathsf{R}}(\phi)$ and the ISF $\Psi_n(\phi)$ are 2π-periodic functions of ϕ and can therefore be expressed as a Fourier series,

$$\underline{\mathsf{R}}(\phi) = \sum_{\boldsymbol{j}} \underline{\mathsf{R}}_{\boldsymbol{j}} e^{\mathrm{i}\boldsymbol{j}\cdot\phi}\,, \quad \Psi_n(\phi) = \sum_{\boldsymbol{j}} \Psi_{n,\boldsymbol{j}} e^{\mathrm{i}\boldsymbol{j}\cdot\phi} \tag{3.38}$$

Equation (3.37) can then be expressed as

$$e^{-\mathrm{i}2\pi \boldsymbol{j}\cdot\boldsymbol{Q}} \sum_{\boldsymbol{k}} \underline{\mathsf{R}}_{\boldsymbol{j}-\boldsymbol{k}} \Psi_{n,\boldsymbol{k}} = e^{-\mathrm{i}\pi\nu} \Psi_{n,\boldsymbol{j}} \quad . \tag{3.39}$$

This is simply an eigenproblem for the matrix $e^{-\mathrm{i}2\pi \boldsymbol{j}\cdot\boldsymbol{Q}} \underline{\mathsf{R}}_{\boldsymbol{j}-\boldsymbol{k}}$. The eigenvalues give the amplitude-dependent spin tune, and an eigenvector gives the Fourier coefficients $\Psi_{n,\boldsymbol{j}}$ which can then be used to construct the ISF as a function of the angle coordinates ϕ per Eq. (3.38). It can be checked that the eigenvector with components $\Psi'_{n,\boldsymbol{j}} = \Psi_{n,\boldsymbol{j}-\boldsymbol{l}}$ for some vector of integers $\boldsymbol{l}$ is also an eigenvector with eigenvalue $e^{-\mathrm{i}\pi(\nu-2\boldsymbol{l}\cdot\boldsymbol{Q})}$, and so the spin tune obtained from the eigenvalue may be any 2×integer multiple of the orbital tunes. The best choice of eigenvector/eigenvalue pair is chosen to be the one with a maximum $|\Psi_{n,(0,0,0)}|$.

The SODOM-2 algorithm was implemented in the Bmad ecosystem in Fortran90 as a part of this dissertation [62].

3.6 Electron Bunch Polarization Time Evolution

The ultimate goal in designing spin polarized rings is to minimize the mechanisms and rates at which spin actions in a beam may be reduced. For electrons in storage rings, bunch polarization evolution is largely dominated by the stochastic emission of synchrotron radiation, which causes three effects: (1) the *Sokolov-Ternov (ST) effect* which is an asymmetry in the spin flip rate during photon emission leading to a buildup of polarization antiparallel to the bending field for electrons at a rate τ_{st}^{-1}, (2) *radiative depolarization* where the instantaneous jump in phase space coordinates after photon emission changes a particle's spin action and rapidly reduces the polarization of a bunch at a rate τ_{dep}^{-1}, and (3) *kinetic polarization* where the asymmetry of the photon emission causes particles' spins

to occasionally be more aligned with the ISF on average after photon emission [68, 2, 3, 22]. The effect of kinetic polarization is only significant when $\hat{\boldsymbol{n}}_0$ is not vertical in significant portions of the ring. All three of these effects balance each other out over time leading to an asymptotic polarization for ultra-relativistic electrons given by the Derbenev-Kondratenko (DK) formula [22],

$$P_{dk} = \frac{8}{5\sqrt{3}} \frac{\oint ds \left\langle |\dot{\hat{\boldsymbol{v}}}|^3 \, \hat{\boldsymbol{b}} \cdot (\hat{\boldsymbol{n}} - \boldsymbol{d}) \right\rangle}{\oint ds \left\langle |\dot{\hat{\boldsymbol{v}}}|^3 \left(1 - \frac{2}{9}(\hat{\boldsymbol{n}} \cdot \hat{\boldsymbol{v}})^2 + \frac{11}{18} |\boldsymbol{d}|^2\right)\right\rangle} \,, \tag{3.40}$$

where $\hat{\boldsymbol{v}}$ is a unit vector in the direction of the particle's velocity, $\dot{\hat{\boldsymbol{v}}}$ is the curvature of the particle trajectory, $\hat{\boldsymbol{b}} = \hat{\boldsymbol{v}} \times \dot{\hat{\boldsymbol{v}}}/|\dot{\hat{\boldsymbol{v}}}|$, $\langle ... \rangle$ denotes an average over the particle ensemble, s is the arc position along the closed orbit, and $\boldsymbol{d} = \gamma_0 \frac{\partial \hat{\boldsymbol{n}}}{\partial \gamma}$ is the so-called *spin-orbit coupling function*. The spin-orbit coupling function captures the dependence of the ISF with energy, and thus defines the degree of radiative depolarization present in a ring. In Eq. (3.40), the $\hat{\boldsymbol{b}} \cdot \boldsymbol{d}$ term corresponds to the kinetic polarizing mechanism, $\frac{11}{18}|\boldsymbol{d}|^2$ term to the radiative depolarization, and the remaining terms to the Sokolov-Ternov effect. The time evolution of a bunch's polarization is

$$P(t) = P_{dk}(1 - e^{-t/\tau_{dk}}) + P_0 e^{-t/\tau_{dk}} \,, \tag{3.41}$$

where $\tau_{dk}^{-1} = \tau_{st}^{-1} + \tau_{dep}^{-1}$, and P_0 is the initial bunch polarization. The Sokolov-Ternov rate and radiative depolarization rate are respectively

$$\tau_{st}^{-1} = \frac{5\sqrt{3}}{8} \frac{r_e \gamma_0^5 \hbar}{m_e} \frac{1}{C} \oint ds \left\langle |\dot{\hat{\boldsymbol{v}}}|^3 \left(1 - \frac{2}{9}(\hat{\boldsymbol{n}} \cdot \hat{\boldsymbol{v}})^2\right)\right\rangle \,, \tag{3.42}$$

$$\tau_{dep}^{-1} = \frac{5\sqrt{3}}{8} \frac{r_e \gamma_0^5 \hbar}{m_e} \frac{1}{C} \oint ds \left\langle |\dot{\hat{\boldsymbol{v}}}|^3 \frac{11}{18} |\boldsymbol{d}|^2 \right\rangle \,, \tag{3.43}$$

where r_e is the classical electron radius, m_e is the electron mass, and C is the circumference of the ring.

For electron rings, the primary task is to reduce $\boldsymbol{d}$ around the ring as much as possible, thus minimizing the radiative depolarization rate and maximizing the asymptotic polarization. In a perfectly midplane symmetric ring without spin rotators, $\boldsymbol{d}$ is already zero everywhere; in such a case the vertical beam size is approximately zero due to radiation damping, and the beam (which lies entirely in the midplane) only sees vertical magnetic fields. The ISF is therefore fully vertical in all occupied areas of phase space. However, once $\hat{\boldsymbol{n}}_0$ is rotated out of the vertical (e.g. by spin rotators or random errors), $\boldsymbol{d}$ will be excited and cause rapid radiative depolarization if left uncorrected.

3.7 First-Order Spin-Orbit Motion

It can be insightful to consider the theory in a simplified model. In this section, we invoke the paraxial approximation and consider the dynamics to first-order in deviations from the closed orbit. Still using a coordinate system that has its origin on the closed orbit ($\boldsymbol{\zeta}_{\text{c.o.}} = \mathbf{0}$), we linearize in $\boldsymbol{\zeta}$ for small deviations around the closed orbit. We also linearize in deviations of the trace space coordinates x', y', where $'$ denotes differentiation with respect to the arc position along the closed orbit s. We define the right-handed orthonormal coordinate system $(\hat{\boldsymbol{x}}(s), \hat{\boldsymbol{y}}(s), \hat{\boldsymbol{s}}(s))$ along the closed orbit (note that $\hat{\boldsymbol{y}}$ may not always point vertically with respect to the geometric layout of the accelerator, for example). The local horizontal and vertical curvatures of the coordinate system are specified by $\boldsymbol{g} = g_x\hat{\boldsymbol{x}} + g_y\hat{\boldsymbol{y}}$. In the absence of electric fields, by definition $g_x = \frac{q}{p_0}B_y|_0$

and $g_y = -\frac{q}{p_0} B_x|_0$ where $\boldsymbol{B}$ is the magnetic field in the closed orbit basis. For example, $\boldsymbol{g}$ will be nonzero when the closed orbit through a quadrupole magnet is offset from the magnet centerline. Note that with this definition, $\boldsymbol{g}$ points in the opposite direction of $\hat{\boldsymbol{v}}$. The Thomas-BMT equation in this coordinate system is

$$\frac{d\boldsymbol{S}}{dt} = \boldsymbol{\Omega}_t \times \boldsymbol{S} \,,$$

$$\boldsymbol{\Omega}_t = -\frac{q}{p} v \left[(1 + G\gamma)\boldsymbol{B} - G(\gamma - 1)(\hat{\boldsymbol{\beta}} \cdot \boldsymbol{B})\hat{\boldsymbol{\beta}} + \left(G\gamma\beta + \frac{\gamma\beta}{1+\gamma} \right) \frac{\boldsymbol{E} \times \hat{\boldsymbol{\beta}}}{c} \right] - \frac{ds}{dt} \boldsymbol{g} \times \hat{\boldsymbol{s}} \,, \quad (3.44)$$

where $\boldsymbol{S}$ is a 3-vector of the spin expectation values in the closed orbit basis in the rest frame of the particle, G is the anomalous magnetic moment of the particle, and $\boldsymbol{B}$ and $\boldsymbol{E}$ are the laboratory frame magnetic and electric fields in the closed orbit basis [69, 7, 70, 37]. The $\boldsymbol{g} \times \hat{\boldsymbol{s}}$ term accounts for the rotation of the coordinate system. Expanding around the closed orbit (letting $\boldsymbol{r}_t = x\hat{\boldsymbol{x}} + y\hat{\boldsymbol{y}}$),

$$v \approx \frac{ds}{dt} (1 + \boldsymbol{g} \cdot \boldsymbol{r}_t) \,, \quad (3.45)$$

$$\frac{q}{p} \approx \frac{q}{p_0} (1 - \delta) \,, \quad (3.46)$$

$$\gamma \approx \gamma_0 (1 + \beta_0^2 \delta) \,, \quad (3.47)$$

$$\beta \approx \beta_0 \left(1 + \delta/\gamma_0^2 \right) \,, \quad (3.48)$$

$$\hat{\boldsymbol{\beta}} \approx (x'\hat{\boldsymbol{x}} + y'\hat{\boldsymbol{y}} + \hat{\boldsymbol{s}}) \,, \quad (3.49)$$

$$\boldsymbol{p} \approx p_0 \left[x'\hat{x} + y'\hat{y} + (1 + \delta)\hat{s} \right] \,. \quad (3.50)$$

Note that $\frac{ds}{dt}$ implicitly contains a δ dependence. Multiplying both sides of Eq. (3.44) by $\frac{dt}{ds}$ and substituting Eqs. (3.45) through (3.49), the Thomas-BMT equation can be rewritten as

$$\boldsymbol{S}' = \boldsymbol{\Omega} \times \boldsymbol{S} \quad (3.51)$$

where $\boldsymbol{\Omega} = \boldsymbol{\Omega}_B + \boldsymbol{\Omega}_E - \boldsymbol{g} \times \hat{\boldsymbol{s}}$ and

$$\Omega_{B,x} \approx -\frac{q}{p_0}\left\{\left[(1+G\gamma_0)(1+\boldsymbol{g}\cdot\boldsymbol{r}_t)-\left(1+\frac{G}{\gamma_0}\right)\delta\right]B_x+(G-G\gamma_0)x'B_s\right\}\,, \tag{3.52a}$$

$$\Omega_{B,y} \approx -\frac{q}{p_0}\left\{\left[(1+G\gamma_0)(1+\boldsymbol{g}\cdot\boldsymbol{r}_t)-\left(1+\frac{G}{\gamma_0}\right)\delta\right]B_y+(G-G\gamma_0)y'B_s\right\}\,, \tag{3.52b}$$

$$\Omega_{B,s} \approx -\frac{q}{p_0}\left\{(1+G)(1+\boldsymbol{g}\cdot\boldsymbol{r}_t-\delta)B_s+(G-G\gamma_0)(x'B_x+y'B_y)\right\}, \tag{3.52c}$$

$$\Omega_{E,x} \approx -\frac{q}{p_0}\left\{\left[G\beta_0\gamma_0+\frac{\beta_0\gamma_0}{1+\gamma_0}\right]\left[(1+\boldsymbol{g}\cdot\boldsymbol{r}_t)\frac{E_y}{c}-y'\frac{E_s}{c}\right]+\frac{\beta_0\gamma_0}{1+\gamma_0}\left[\frac{1}{\gamma_0}-1\right]\delta\frac{E_y}{c}\right\}\,, \tag{3.53a}$$

$$\Omega_{E,y} \approx -\frac{q}{p_0}\left\{\left[G\beta_0\gamma_0+\frac{\beta_0\gamma_0}{1+\gamma_0}\right]\left[x'\frac{E_s}{c}-(1+\boldsymbol{g}\cdot\boldsymbol{r}_t)\frac{E_x}{c}\right]+\frac{\beta_0\gamma_0}{1+\gamma_0}\left[1-\frac{1}{\gamma_0}\right]\delta\frac{E_x}{c}\right\}\,, \tag{3.53b}$$

$$\Omega_{E,s} \approx -\frac{q}{p_0}\left\{\left[G\beta_0\gamma_0+\frac{\beta_0\gamma_0}{1+\gamma_0}\right]\left[y'\frac{E_x}{c}-x'\frac{E_y}{c}\right]\right\}\,. \tag{3.53c}$$

We now consider only magnetostatic fields, expanded around the closed orbit to first-order. For convenience we define the quantities

$$K_s = \frac{q}{p_0}\,B_s|_{\mathbf{0}}\,, \tag{3.54}$$

$$K_1 = \frac{q}{p_0}\,\partial_y B_x\big|_{\mathbf{0}}\,, \tag{3.55}$$

$$\tilde{K}_1 = \frac{q}{2p_0}\left(\partial_x B_x|_{\mathbf{0}}-\partial_y B_y\big|_{\mathbf{0}}\right)\,. \tag{3.56}$$

In the special case where the closed orbit is aligned with the magnet centerlines, these quantities are equivalent to the normalized solenoid, quadrupole, and skew quadrupole strengths respectively. The general magnetic field satisfying the Maxwell equations $\boldsymbol{\nabla}\times\boldsymbol{B}=\boldsymbol{\nabla}\cdot\boldsymbol{B}=0$ to first-order is

$$B_x \approx -\frac{p_0}{q}\left(\frac{1}{2}K_s'x+g_y-K_1y+\tilde{K}_1x\right), \tag{3.57a}$$

$$B_y \approx -\frac{p_0}{q}\left(\frac{1}{2}K_s'y-g_x-K_1x-\tilde{K}_1y\right), \tag{3.57b}$$

$$B_s \approx -\frac{p_0}{q}\left(-K_s-g_x'y+g_y'x\right)\,. \tag{3.57c}$$

Substituting Eq. (3.57) into Eq. (3.52), we split $\boldsymbol{\Omega}$ into a zeroth order part $\boldsymbol{\Omega}_0$ on the closed orbit and a perturbative part $\boldsymbol{\omega}(\boldsymbol{\zeta})$ first-order in the phase space variables,

$$\Omega_{0,x} \approx G\gamma_0 g_y \,, \tag{3.58a}$$

$$\Omega_{0,y} \approx -G\gamma_0 g_x \,, \tag{3.58b}$$

$$\Omega_{0,s} \approx -(1+G)K_s \,, \tag{3.58c}$$

$$\omega_x \approx (1+G\gamma_0)\left(\frac{1}{2}K_s' x + g_y \boldsymbol{g}\cdot\boldsymbol{r}_t - K_1 y + \tilde{K}_1 x\right) + (G\gamma_0 - G)\,K_s x' - \left(1+\frac{G}{\gamma_0}\right) g_y \delta \,, \tag{3.59a}$$

$$\omega_y \approx (1+G\gamma_0)\left(\frac{1}{2}K_s' y - g_x \boldsymbol{g}\cdot\boldsymbol{r}_t - K_1 x - \tilde{K}_1 y\right) + (G\gamma_0 - G)\,K_s y' + \left(1+\frac{G}{\gamma_0}\right) g_x \delta \,, \tag{3.59b}$$

$$\omega_s \approx (1+G)\left(-K_s \boldsymbol{g}\cdot\boldsymbol{r_t} + K_s\delta - g_x' y + g_y' x\right) + (G\gamma_0 - G)\left(g_x y' - g_y x'\right) \,. \tag{3.59c}$$

Equivalent, alternative expressions for ω_x and ω_y can be obtained by substituting in the orbital equations of motion. Substituting Eqs. (3.45), (3.49), (3.50) and (3.57) into $\frac{d\boldsymbol{p}}{dt} = qv\hat{\boldsymbol{\beta}}\times\boldsymbol{B}$, we obtain

$$x'' - K_s y' - g_x\delta \approx \frac{1}{2}K_s' y - g_x \boldsymbol{g}\cdot\boldsymbol{r}_t - K_1 x - \tilde{K}_1 y \,, \tag{3.60}$$

$$-y'' - K_s x' + g_y\delta \approx \frac{1}{2}K_s' x + g_y \boldsymbol{g}\cdot\boldsymbol{r}_t - K_1 y + \tilde{K}_1 x \,. \tag{3.61}$$

Substituting Eq. (3.60) into Eq. (3.59b) and Eq. (3.61) into Eq. (3.59a) gives

$$\omega_x \approx -(1+G\gamma_0)\,y'' - (1+G)\,K_s x' + \left(G\gamma_0 - \frac{G}{\gamma_0}\right) g_y\delta \,, \tag{3.62a}$$

$$\omega_y \approx (1+G\gamma_0)\,x'' - (1+G)\,K_s y' - \left(G\gamma_0 - \frac{G}{\gamma_0}\right) g_x\delta \,. \tag{3.62b}$$

3.8 Traditional Methods to Minimize Radiative Depolarization

3.8.1 Strong Synchrobeta Spin Matching

To minimize the effects of radiative depolarization, a *strong synchrobeta spin match* should first be applied [6, 15]: the magnet strengths and spin rotator configuration are chosen so that the 1-turn spin dependence on the orbit motion is removed at as many azimuths as possible. By minimizing the 1-turn spin-orbit coupling where photons are emitted, $\boldsymbol{d}$ is also minimized. This is usually done to first-order in the phase space coordinates' deviation from the closed orbit. To do so, we first construct a right-handed orthonormal coordinate system $(\hat{\boldsymbol{n}}_0, \hat{\boldsymbol{m}}_0, \hat{\boldsymbol{l}}_0)$ where $\hat{\boldsymbol{l}}_0$ and $\hat{\boldsymbol{m}}_0$ solve the Thomas-BMT equation along the closed orbit. Note that this coordinate system is not 1-turn periodic, with $\hat{\boldsymbol{m}}_0$ and $\hat{\boldsymbol{l}}_0$ having precessed by the closed orbit spin tune ν_0 around $\hat{\boldsymbol{n}}_0$ after one turn. We can approximate any particle's spin for small deviations from $\hat{\boldsymbol{n}}_0$ as

$$\boldsymbol{S} \approx \hat{\boldsymbol{n}}_0 + \kappa_1 \hat{\boldsymbol{m}}_0 + \kappa_2 \hat{\boldsymbol{l}}_0 \,, \tag{3.63}$$

to first-order in κ_1 and κ_2. Substituting Eq. (3.63) into Eq. (3.51), we obtain

$$\frac{d\kappa_1}{ds} \approx \boldsymbol{\omega}(\zeta) \cdot \hat{\boldsymbol{l}}_0 \,, \; \frac{d\kappa_2}{ds} \approx -\boldsymbol{\omega}(\zeta) \cdot \hat{\boldsymbol{m}}_0 \,. \tag{3.64}$$

Defining $\boldsymbol{k}_0 = \hat{\boldsymbol{l}}_0 - \mathrm{i}\hat{\boldsymbol{m}}_0$, the first-order 1-turn spin-orbit coupling at some position s_0 is removed when

$$\int_{s_0}^{s_0+C} \boldsymbol{\omega}(\zeta) \cdot \boldsymbol{k}_0 \, ds = 0 \,, \tag{3.65}$$

where C is the total length of the closed orbit. Which ζ should we evaluate Eq. (3.65) for? We can express any ζ as a linear combination of the linear compositional map eigenvectors $\boldsymbol{v}_i$ in each plane $i = \pm I, \pm II, \pm III$, defined in Sec. 2.2.2. In a weakly-coupled ring, satisfying Eq. (3.65) with $\zeta = \boldsymbol{v}_{\pm I}$ would be referred to as a "horizontal strong synchrobeta spin match".

3.8.2 Harmonic Closed Orbit Spin Matching

In real rings, random closed orbit distortions will, generally, reduce the polarization further. In HERA, *harmonic closed orbit spin matching* (HCOSM) was employed to correct this additional depolarization [5, 4]. HCOSM focuses on correcting the tilt of $\hat{\boldsymbol{n}}_0$ from its design direction caused by the random errors, by using vertical orbit bumps that optimally cancel the integer Fourier harmonics of the tilt precession nearest to ν_0. To quantify the tilt, a 1-turn periodic orthonormal coordinate system $(\hat{\boldsymbol{n}}_0, \hat{\boldsymbol{m}}, \hat{\boldsymbol{l}})$ is constructed in the *ideal* ring where

$$\hat{\boldsymbol{m}}(s) + \mathrm{i}\hat{\boldsymbol{l}}(s) = e^{-\mathrm{i}\psi(s)} \left(\hat{\boldsymbol{l}}_0(s) + \mathrm{i}\hat{\boldsymbol{m}}_0(s) \right) , \tag{3.66}$$

and $\psi(s)$ is the so-called spin phasing function which must be chosen so that $\psi(s_0 + C) - \psi(s_0) = 2\pi\nu_0$ for 1-turn periodicity. For HERA, the spin phasing function was chosen to linearly evolve with s so that

$$\psi(s) = \psi(s_0) + 2\pi\nu_0 \frac{s - s_0}{C} . \tag{3.67}$$

Assuming small closed orbit perturbations, various vertical orbit bumps in the ring are turned on and the original unperturbed $\hat{\boldsymbol{l}}$ and $\hat{\boldsymbol{m}}$ are attached to the

new perturbed closed orbits. A Fourier transform of the projections of the new $\hat{\boldsymbol{n}}_0$ on $\hat{\boldsymbol{l}}$ and $\hat{\boldsymbol{m}}$ for each bump can then be taken, and each bump's impact on the integer harmonics nearest to ν_0 can be calculated. Finally, groups of the bumps are formed *ab initio* to construct special bumps that ideally only impact a single integer harmonic of the $\hat{\boldsymbol{n}}_0$ tilt along $\hat{\boldsymbol{l}}$ or $\hat{\boldsymbol{m}}$. These bumps are then varied to correct the depolarization caused by random closed orbit distortions.

While HCOSM did prove effective for HERA, it suffers from various disadvantages. Firstly, HCOSM of course is only intended to be applied for correcting the depolarization in a ring with random closed orbit distortions, not for increasing polarization in the ideal ring. Secondly, HCOSM indirectly attacks the real problem, which is $\boldsymbol{d}$: it assumes that tilts to $\hat{\boldsymbol{n}}_0$ are always bad, and that bumps that maximally impact the integer spin harmonics nearest to ν_0 will optimally correct the tilt and optimally impact $\boldsymbol{d}$. Thirdly, HCOSM as applied in HERA provided no systematic way of dealing with the spurious vertical dispersion created by the bumps, and coupling if there are sextupoles between the corrector coils in a bump. Fourthly, HCOSM does not ensure minimal orbit excursions for a maximum impact on the Fourier harmonics. A new more powerful method called Best Adjustment Groups for ELectron Spin, introduced in Ch. 7, does not have any of these setbacks, and is preferred for correcting polarization in operation.

3.9 Computational Methods

Computation of Eqs. (3.40), (3.42), and (3.43) directly can be costly, and some useful approximations may be made to speed up the calculation and obtain a

reasonable estimate. Firstly, instead of averaging over the ensemble, we can approximate by evaluating the integral only on the closed orbit, i.e. $\hat{\boldsymbol{n}} \approx \hat{\boldsymbol{n}}_0$, $\boldsymbol{d} \approx \boldsymbol{d}(\mathbf{0})$, $\hat{\boldsymbol{\beta}} \approx \hat{\boldsymbol{\beta}}(\mathbf{0})$, $\hat{\boldsymbol{v}} \approx \hat{\boldsymbol{v}}(\mathbf{0})$, and $\dot{\hat{\boldsymbol{v}}} \approx \dot{\hat{\boldsymbol{v}}}(\mathbf{0})$. Secondly, using Eqs. (3.47) and (3.48) it is easy to show that in the ultra relativistic case $\boldsymbol{d}(\mathbf{0}) = \gamma_0 \frac{\partial \hat{\boldsymbol{n}}}{\partial \gamma}\Big|_{\mathbf{0}} = \frac{\partial \hat{\boldsymbol{n}}}{\partial \delta}\Big|_{\mathbf{0}}$. This term can be easily extracted as a coefficient in the first-order truncated power series expansion of $\hat{\boldsymbol{n}}$ around the closed orbit.

These approximations give a generally excellent estimate for the Sokolov-Ternov terms (those NOT $\propto \boldsymbol{d}$). However, $\boldsymbol{d}$ can vary significantly even with small variations from the closed orbit. Nonlinearities in the orbital motion that excite a larger beam size may exacerbate the problem. Therefore, to accurately estimate the effects of radiative depolarization, nonlinear Monte Carlo spin tracking including radiation damping and radiation fluctuations is necessary. In such tracking spin-flip effects should be excluded and the initial beam distribution should be in radiative equilibrium. Then, τ_{dep} can be obtained directly from the slope of P vs. t, and P_{dk} can be approximated as

$$P_{dk} \approx P_{st} \frac{\tau_{st}^{-1}}{\tau_{st}^{-1} + \tau_{dep}^{-1}} , \tag{3.68}$$

where P_{st} is just P_{dk} with $\boldsymbol{d} = \mathbf{0}$.

In this dissertation, we will refer to the approximation $\boldsymbol{d} \approx \boldsymbol{d}(\boldsymbol{z}_{\text{c.o.}})$ as the *analytical* calculation because with this approximation the DK integral can be calculated quickly without tracking.

CHAPTER 4

ELECTRON-ION COLLIDER: ELECTRON STORAGE RING (ESR)

4.1 Overview

The ESR will provide longitudinally-polarized electron bunches at each of roughly 5, 10, and 18 GeV in both a 1- and 2-colliding interaction point (IP) configuration using the spin rotator shown in Fig. 4.1. The spin rotator of the ESR, consists of a symmetric arrangement of four solenoid modules and four bend modules around the IP [43]. Each "solenoid module" consists of two half solenoids, separated by either 5 (short) or 7 (long) quadrupoles with strengths chosen for decoupling and spin matching, as shown in Fig. 4.2. See Sec. 4.3 for a description of the minimal number of quadrupoles in each module needed to achieve both decoupling and spin matching. For each energy (which defines the bend spin precession ψ_j), the solenoid strengths ϕ_i are set for longitudinal spin at the IP. The spin rotator configuration was chosen so that at roughly 5 GeV, only the short solenoid modules are turned on, and at roughly 18 GeV, only the long solenoid modules are turned on (Table 1). In these two cases, the "on" solenoid module rotates $\hat{\boldsymbol{n}}_0$ from the vertical to the horizontal, and the bend module(s) (where spin precession is proportional to γ_0) rotates $\hat{\boldsymbol{n}}_0$ from the horizontal to the longitudinal. For the 10 GeV case, all solenoid modules must be used.

To avoid depolarizing integer spin resonances, the exact operating energies are those closest to 5, 10, and 18 GeV that give a half-integer fractional closed-orbit spin tune ν_0. At 5 and 18 GeV, because of the special rotator configuration chosen, the "net" spin precession of $\hat{\boldsymbol{l}}_0$ and $\hat{\boldsymbol{m}}_0$ across the rotator is exactly equal to 180°; in these special cases, the contribution to ν_0 of the rotator is equivalent

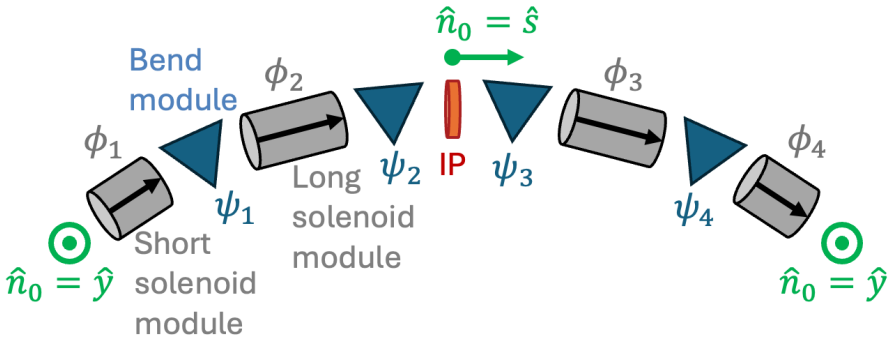

Figure 4.1: Top-down view of the spin rotator of the ESR, with the spin precession angles in each module labelled.

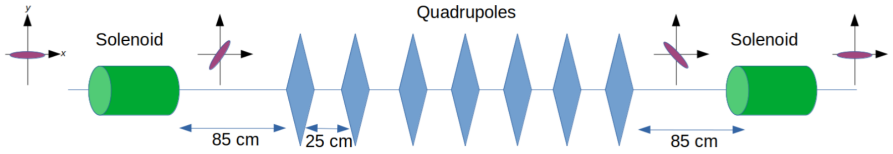

Figure 4.2: "Solenoid modules" consist of two half-solenoids separated by either 5 or 7 quadrupoles for decoupling and spin matching [44].

to that with the rotator been turned off. Therefore, for 5 and 18 GeV, $\nu_0 = a\gamma_0$, and there is no difference in the energies of the 1-IP and 2-IP lattices. The 10 GeV lattice does not have this special configuration, and so there is a small difference in the energy (and solenoid settings) between the 1-IP and 2-IP lattices to maintain a half-integer ν_0; numerical solution was required to calculate the exact γ_0's closest to 10 GeV.

4.2 Polarization Figures-Of-Merit

Helicity is the projection of a particle's spin onto the direction of its momentum, with a positive helicity corresponding to the spin pointing along the momentum and a negative helicity corresponding to the spin pointing opposite the

Table 4.1: Solenoid ($\hat{s}$) and bend ($\hat{y}$) module spin precession angles at different energies using the right-handed basis ($\hat{x}, \hat{y}, \hat{s}$) with $\hat{s}$ pointing along the longitudinal in Fig. 4.1

	Solenoids		**Bends**	
	$\phi_{1,4}$	$\phi_{2,3}$	$\psi_{1,4}$	$\psi_{2,3}$
17.846 GeV 1-IP/2-IP	0°	−90°	N/A	−90°
9.781 GeV 1-IP	−52.2°	−126.0°	−124.4°	−49.3°
9.650 GeV 2-IP	−51.7°	−124.4°	−122.7°	−48.7°
5.068 GeV 1-IP/2-IP	−90°	0°	−64.4°	−25.6°

momentum. In HERA, all bunches had the same helicities at the IP. Unpolarized bunches were injected and self-polarized using the Sokolov-Ternov effect, up to the asymptotic polarization P_{dk}. Therefore, after self-polarization, P_{dk} quantified the time-averaged polarization at the IP, and was a good polarization figure-of-merit for HERA.

In the EIC-ESR, bunches with both positive and negative helicities at the IP(s) will be stored simultaneously, in order to minimize systematic errors in the collisions [1]. This can be achieved by having two types of bunches circulating at the same time in the ring: bunches with polarizations pointing antiparallel to the arc fields (outside the rotator), and bunches with polarizations pointing parallel to the arc fields. Per Fig. 4.1, we see that, for electrons, the antiparallel-polarized bunches (with polarizations pointing in the $+\hat{y}$ direction outside the rotator) have positive helicity at the IP, and the parallel-polarized bunches (with polarizations pointing in the $-\hat{y}$ direction outside the rotator) have negative helicity at the IP. For this case, we cannot simply inject unpolarized bunches and

use the Sokolov-Ternov effect to build up polarization, because all bunches will have polarizations building up along the same direction. Instead, we must inject *polarized* bunches with the correct directions for positive/negative helicities, and swap-out each bunch once sufficiently depolarized with a fresh, polarized bunch. However, the Sokolov-Ternov effect will work *against* the parallel-polarized bunches, and *for* the antiparallel-polarized bunches. Therefore, in order to maintain a sufficient time averaged polarization for each bunch type at the IP(s), the parallel-polarized bunch replacement time T_- must be less than the antiparallel-polarized bunch replacement time T_+.

For the EIC-ESR, we require that a time-averaged polarization of $|\langle P\rangle_t| \geq 70\%$ is maintained. The time-averaged polarizations for antiparallel-polarized bunches and parallel-polarized bunches are respectively

$$\langle P_+\rangle_t = \frac{1}{T_+}\int_0^{T_+} P(P_0^+;t)\,dt\,, \quad \langle P_-\rangle_t = \frac{1}{T_-}\int_0^{T_-} P(P_0^-;t)\,dt\,, \tag{4.1}$$

where P_0^+ is the initial antiparallel-polarized bunch polarization at injection, and likewise P_0^- for the parallel-polarized bunch. The polarization time evolution is defined in Eq. (3.41). In all studies presented in this dissertation, we assume that $P_0^+ = -P_0^- = P_0 = 85\%$, where we choose the convention that antiparallel polarization is positive [74]. Furthermore, we also require that $\langle P_+\rangle_t = -\langle P_-\rangle_t = \langle P\rangle_t \geq 70\%$. Performing the integrations in Eq. (4.1) we have

$$\langle P_\pm\rangle_t = \pm\langle P\rangle_t = P_{dk} - \frac{\tau_{dk}}{T_\pm}\left(P_{dk} \mp P_0\right)\left(1 - e^{-T_\pm/\tau_{dk}}\right)\,. \tag{4.2}$$

We can solve for $T_\pm$, obtaining

$$T_\pm = \tau_{eq}\left[\tilde{P}_\pm + W_k(-\tilde{P}_\pm e^{-\tilde{P}_\pm})\right]\,,\ \tilde{P}_\pm = \frac{P_{dk} \mp P_0}{P_{dk} \mp \langle P\rangle_t} \tag{4.3}$$

where W_k is the k-th branch of the Lambert W function. Because $T_\pm$ must be real, we have the $k = 0$ branch which covers the domain $[-1/e, \infty)$ and the $k = -1$

branch which covers the domain $[-1/e, 0)$. To determine which branch, consider the identities

$$W_0(-xe^{-x}) = -x \quad \text{for } x \leq 1 \,, \tag{4.4}$$

$$W_{-1}(-xe^{-x}) = -x \quad \text{for } x \geq 1 \,. \tag{4.5}$$

Considering Eq. (4.3), we see that if W_0 is used when $\tilde{P}_\pm \leq 1$, or if W_{-1} is used when $\tilde{P}_\pm \geq 1$, then we have a trivial solution $T_\pm = 0$, which we do not want. Let's consider the form of $\tilde{P}_\pm$ in Eq. (4.3), where we defined P_0, P_{dk}, and $\langle P \rangle_t$ as solely positive quantities. Note that if $\langle P \rangle_t \geq P_{dk}$, then we must have $P_0 \geq \langle P \rangle_t$ else the requirement that $\langle P_+ \rangle_t = \langle P \rangle_t$ is unachievable, because the positive polarization will decay to P_{dk}. Alternatively, if we have $\langle P \rangle_t \leq P_{dk}$, then there is *no possible* P_0 such that $P_0^+ = -P_0^- = P_0$ to achieve $\langle P_- \rangle_t = -\langle P \rangle_t$, as the negative polarization will only decrease from P_0. Therefore, in order to maintain symmetry for ech type of bunch in the ESR, we can only have $\langle P \rangle_t \geq P_{dk}$ and therefore $P_0 \geq \langle P \rangle_t$. With such conditions, per Eq. (4.3) we see that $\tilde{P}_\pm \geq 1$. Therefore, we must use the $k = 0$ branch of the Lambert W function. This leaves us with

$$T_\pm = \tau_{dk} \left[\tilde{P}_\pm + W_0(-\tilde{P}_\pm e^{-\tilde{P}_\pm}) \right] \,. \tag{4.6}$$

At the time of this dissertation-writing, the Rapid Cycling Synchrotron (RCS), shown in Fig. 1.1, is planned to replace bunches in the ESR with a maximal rate of $f_{RCS,max} = 1$ bunch/second. Using this rate, there are two good figures-of-merit we will use to quantity the polarization performance in the ESR.

The first figure-of-merit corresponds to the bunch replacement times necessary to maintain a time-averaged polarization of exactly $\langle P \rangle_t = 70\%$. Specifically, we solve for $T_\pm$ in Eq. (4.6) where $\langle P \rangle_t = 70\%$. With these T_- and T_+ consider that at any given time the EIC-ESR must have N bunches circulating in the ring, N_+ of which have antiparallel polarization and N_- having parallel polarization. We

require that $N_+ = N_- = N/2$. At 5 and 10 GeV, $N = 1160$, and at 18 GeV, $N = 290$. In order to maintain sufficient polarization, each of the N_+ bunches must be replaced every T_+ minutes, therefore requiring an average bunch replacement rate of N_+/T_+ for the (+) bunches. Likewise, each of the N_- bunches must be replaced every T_- minutes, therefore requiring an average bunch replacement rate of N_-/T_- for the (−) bunches. Using the fact that $N_+ = N_- = N/2$, for some long time t the total number of bunches replaced N_{tot} to maintain sufficient polarization is

$$N_{tot}(t) = \frac{N}{2}\left(\frac{1}{T_+} + \frac{1}{T_-}\right)t \,. \tag{4.7}$$

This must be ≤ the number of bunches the RCS can possibly replace in that same time,

$$\frac{N}{2}\left(\frac{1}{T_+} + \frac{1}{T_-}\right) \leq f_{RCS,max} \,. \tag{4.8}$$

Both sides of Eq. (4.8) correspond to rates in bunches/time. With some minor massaging of this inequality, we can obtain the requirement in units of time to replace N bunches specifically,

$$T \geq \frac{N}{f_{RCS,max}} \,, \quad T = \frac{2T_-T_+}{T_- + T_+} \,. \tag{4.9}$$

The T in Eq. (4.9) is the first figure-of-merit we use to quantify polarization in the ESR. Note that the N bunches replaced in these times do NOT necessarily correspond to $N/2$ antiparallel-polarized bunches and $N/2$ parallel-polarized bunches, rather just N bunches. E.g., because $T_- < T_+$, then N consists of more (−) than (+) bunches. The reason why T is used instead of T/N throughout this dissertation is simply a matter of convenience: this figure-of-merit is independent of the number of bunches stored in the ring, which instead defines the minimum allowed amount. This figure-of-merit T we refer to as the *N bunch replacement time*.

The second figure-of-merit is computed differently; now, we consider what possible time-averaged polarization is achieved assuming that the RCS replaces the bunches with its maximum possible rate of $f_{RCS,max}$. Setting $\langle P_+ \rangle_t = -\langle P_- \rangle_t$, we have two unknowns T_- and T_+. Letting the T in Eq. (4.9) equal $N/f_{RCS,max}$, we can connect T_- to T_+ and get an equation with only one unknown. This can be solved for numerically, and we can then obtain the $\langle P \rangle_t$ achievable. Of course, once $\langle P \rangle_t = P_{dk}$, then the (+) bunches are never replaced, i.e. $T_+ \to \infty$, and all of the bunches replaced by the RCS are (−) bunches. Therefore, if we maintain the symmetry requirement that $\langle P_+ \rangle_t = -\langle P_- \rangle_t$, then no further improvements to polarization can be made beyond this point. Per Eq. (4.9), when $T_+ \to \infty$, $T_- \to T/2$.

In this work, we use both of these figures-of-merit. It is insightful to consider how T, T_-, T_+, and $\langle P \rangle_t$ are related to P_{dk}. To do so, we use the following approximations: (i) those described at the beginning of Sec. 3.9, (ii) Eq. (3.68) which neglects kinetic effects, and (iii) neglect changes to τ_{st} and P_{st} with changes to τ_{dep} – this is reasonable by observation of Eq. (3.42) and Eq. (3.40), where we see that if the closed orbit and $\hat{n}_0$ are approximately unchanged, then these quantities (in their current approximations) will not change. With these approximations, we can numerically compute relations of T and $\langle P \rangle_t$ with P_{dk}. Figures 4.3 and 4.4 show the relation of T and $\langle P \rangle_t$ vs. P_{dk} for the 18 GeV 1-IP ESR respectively. For this lattice, $P_{st} = 86.7\%$, $\tau_{st} = 36.3$ min, and $N = 290$. Given the RCS's maximum replacement rate of 60 bunches/second we require $T \geq 4.8$ min per Eq. (4.9). For $\langle P \rangle_t$, we simply require $\langle P \rangle_t \geq 70\%$. Both of these figures may be useful in interpreting the plots presented throughout this dissertation.

4.3 Strong Synchrobeta Spin Match

The ESR satisfies a horizontal strong synchrobeta spin match everywhere outside of the spin rotator for each energy case. A vertical strong synchrobeta spin match is not feasible due to its complexity. At 5 and 10 GeV the effects of synchrotron radiation make a longitudinal strong synchrobeta spin match not necessary, but at 18 GeV the effect is significant. Early versions of the 18 GeV EIC-ESR had a longitudinal strong synchrobeta spin match, however this later had

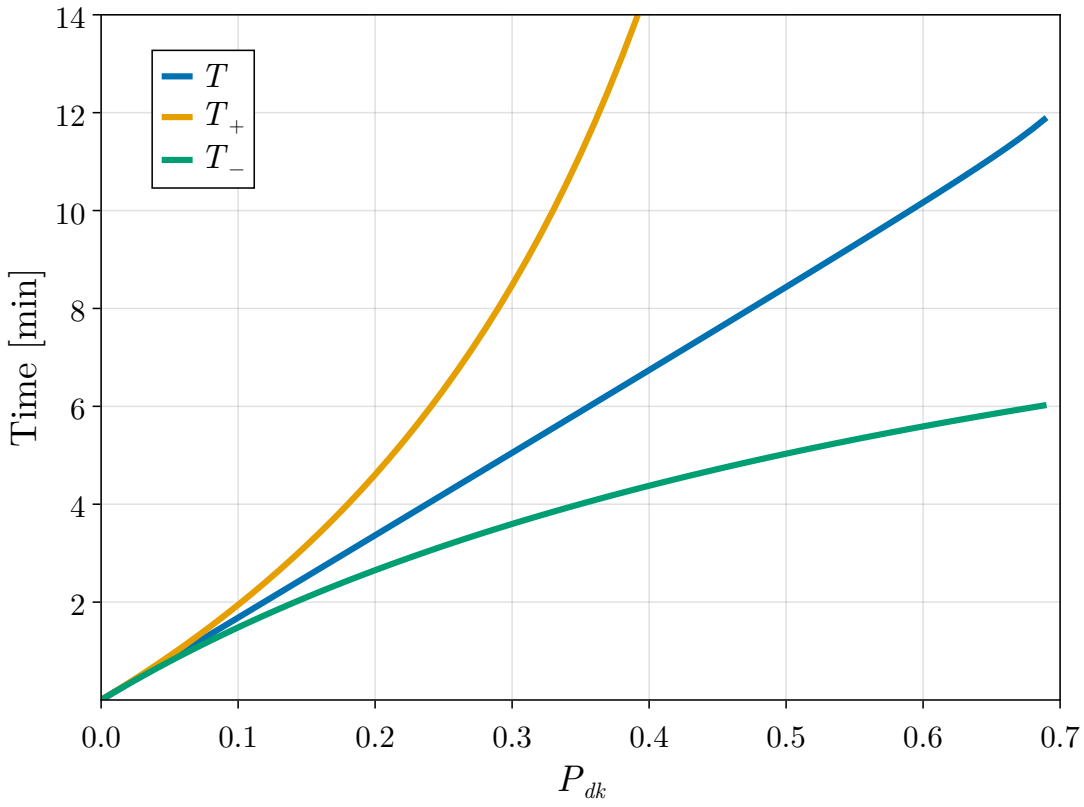

Figure 4.3: N bunch replacement time T, (defined in Eq. (4.9)), T_+, and T_- vs. P_{dk} for the 1-IP 18 GeV EIC-ESR in order to maintain a time averaged polarization of 70%. This lattice has P_{st} = 86.7%, and τ_{st} = 36.3 min. T must be $\geq$ 4.8 min, which is the minimal N bunch replacement time achievable by the RCS.

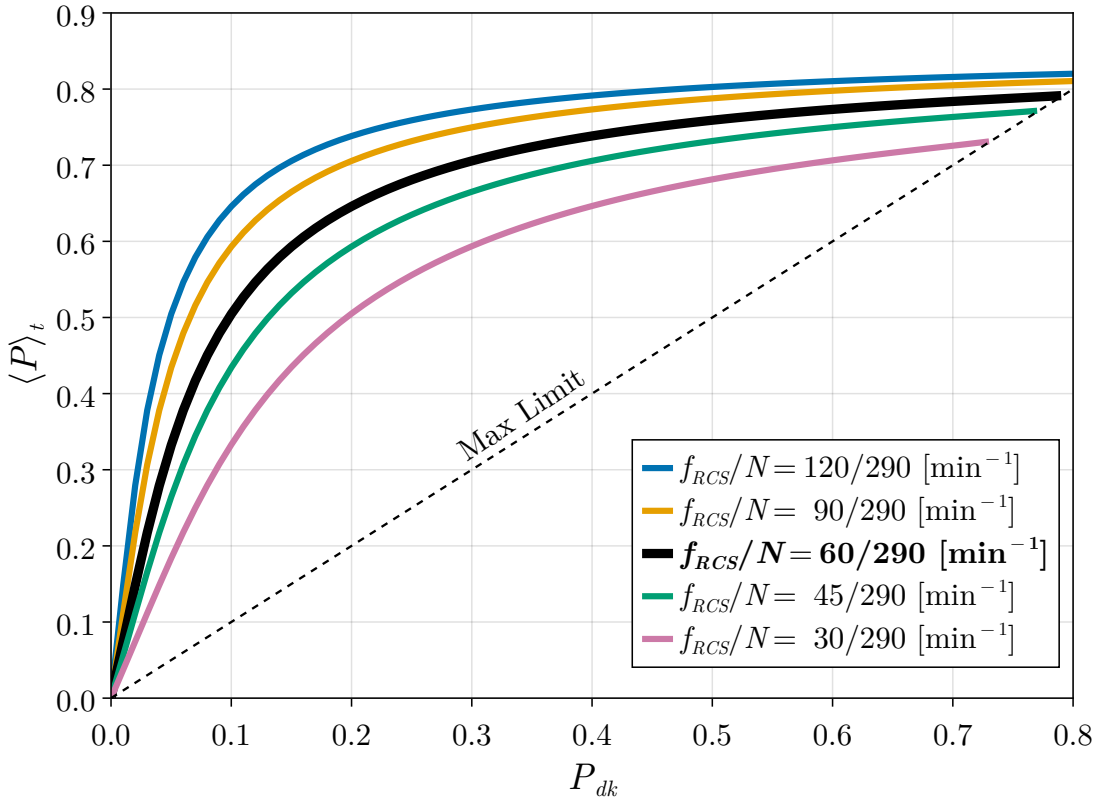

Figure 4.4: Time-averaged polarization achieved for both parallel- and antiparallel-polarized bunches $\langle P \rangle_t$ vs P_{dk} in the 18 GeV 1-IP EIC-ESR, assuming N bunches in the ring and a bunch replacement rate of f_{RCS}. The bold entry corresponds to the planned value for the EIC-ESR.

to be dropped because it required either 11 Tesla solenoids or geometry changes to the current RHIC tunnel, both of which are infeasible. The lack of a longitudinal spin match has severe consequences on the polarization at 18 GeV; Figure 4.5 shows the difference in the N bunch replacement time between an early 1-IP ESR version that had a longitudinal spin match (LSM) vs. a later one where the LSM was dropped. Chapter 6 shows an attempt to resolve this problem via a "partial" longitudinal spin match, and Ch. 7 shows a novel approach that not only solves this problem, but also provides a solution for general simultaneous

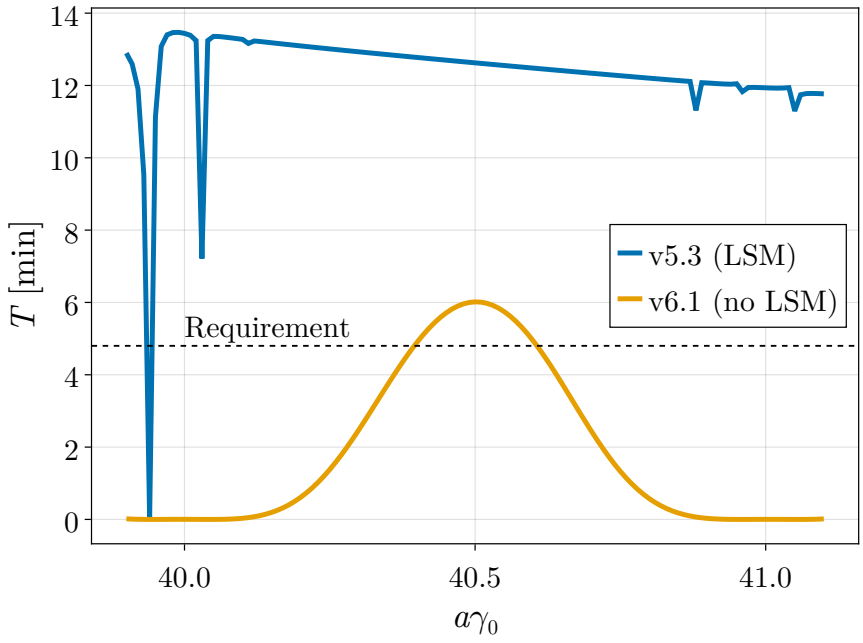

Figure 4.5: Energy scan of the N bunch replacement time for two versions of the 1-IP 18 GeV EIC-ESR, one which has a longitudinal spin match (LSM) and one without an LSM.

control of the orbit, optics, and polarization in electron rings. The spin matching conditions for the EIC-ESR, derived by V. Ptitsyn [48], are now re-derived in detail to a simple general form [64]. Evaluating the integrand in Eq. (3.65) using Eqs. (3.62a), (3.62b), and (3.59c) for the EIC-ESR spin rotator gives

$$\begin{aligned}
\boldsymbol{\omega}\cdot\boldsymbol{k}_0 &= K_s\left[-(1+a)(x'k_{0,x}+y'k_{0,y}-\delta k_{0,s})\right]+g_x\left[(a\gamma_0-a)y'k_{0,s}-\left(a\gamma_0-\frac{a}{\gamma_0}\right)\delta k_{0,y}\right]\\
&\quad -g_x'(1+a)yk_{0,s}+(1+a\gamma_0)(x''k_{0,y}-y''k_{0,x})\\
&= K_s\left[-(1+a)(x'k_{0,x}+y'k_{0,y}-\delta k_{0,s})\right]+g_x\left[(a\gamma_0-a)y'k_{0,s}-\left(a\gamma_0-\frac{a}{\gamma_0}\right)\delta k_{0,y}\right]\\
&\quad -g_x'(1+a)yk_{0,s}+(1+a\gamma_0)\left[(x'k_{0,y})'-x'k_{0,y}'-(y'k_{0,x})'+y'k_{0,x}'\right],
\end{aligned} \tag{4.10}$$

where the convention for electrons $G \to a$ is used. Substitution of $\boldsymbol{k}_0$ into $\boldsymbol{S}' = \boldsymbol{\Omega}_0 \times \boldsymbol{S}$ using Eq. (3.58) gives

$$k'_{0,x} = (1+a)K_s k_{0,y} - a\gamma_0 g_x k_{0,s} \,, \tag{4.11a}$$

$$k'_{0,y} = -(1+a)K_s k_{0,x} \,, \tag{4.11b}$$

$$k'_{0,s} = a\gamma_0 g_x k_{0,x} \,. \tag{4.11c}$$

With these equations, the integrand is

$$\begin{aligned}\boldsymbol{\omega}\cdot\boldsymbol{k}_0 = K_s(1+a)\left[a\gamma_0\left(x'k_{0,x}+y'k_{0,y}\right)+\delta k_{0,s}\right] - g_x\left[(a+a^2\gamma_0^2)y'k_{0,s}+\left(a\gamma_0-\frac{a}{\gamma_0}\right)\delta k_{0,y}\right] \\ - g'_x(1+a)yk_{0,s} + (1+a\gamma_0)\left[(x'k_{0,y})' - (y'k_{0,x})'\right] \,.\end{aligned} \tag{4.12}$$

Horizontal Spin Match

We now substitute $\boldsymbol{\zeta} = \boldsymbol{v}_I$, the horizontal-like eigenvector, into Eq. (4.12). With this substitution, the integrals over the $(y'k_{0,x})'$ and $(x'k_{0,y})'$ terms are automatically zero: at the start and exit of the spin rotator we demand no transverse coupling, so $v_{I,p_y}(s_{in}) = v_{I,p_y}(s_{out}) = 0$, and $\hat{\boldsymbol{n}}_0$ is vertical, so $k_{0,y}(s_{in}) = k_{0,y}(s_{out}) = 0$. Furthermore, because there is no transverse coupling in the bends, $v_{I,y} = v_{I,p_y} = 0$ in the bends. Finally, $v_{I,\delta} = 0$. This leaves integrals only over the eight solenoids (two per solenoid module). Using the fact that $x' = p_x + \frac{1}{2}K_s y$ and $y' = p_y - \frac{1}{2}K_s x$, this is expressed in terms of the canonical components of $\boldsymbol{v}_I$ as

$$\int_{s_{in}}^{s_{out}} \boldsymbol{\omega}\cdot\boldsymbol{k}_0 \, ds = \int_{8\text{ sols}} K_s(1+a)a\gamma_0\left[\left(v_{I,p_x}+\frac{1}{2}K_s v_{I,y}\right)k_{0,x}+\left(v_{I,p_y}-\frac{1}{2}K_s v_{I,x}\right)k_{0,y}\right] ds \,. \tag{4.13}$$

Solving the equations of motion in Eq. (3.60) and Eq. (3.61) for a solenoid shows that x' and y' rotate together at a rate of K_s radians per unit length. Likewise, solving the equations of motion in Eq. (4.11a) and Eq. (4.11b) for a solenoid

shows that the transverse spin components $k_{0,x}$ and $k_{0,y}$ rotate and at a rate of $(1 + a)K_s$ radians per unit length. For electrons, $a \approx 0.00116$. In the ESR spin matching conditions derivation, it is assumed that a is sufficiently small so that $(1+a) \approx 1$. With this assumption, the spin and velocity precess at approximately the same rate, and so $\left(x'k_{0,x} + y'k_{0,y}\right)$ is constant within each solenoid. Letting L be the length of an individual solenoid, this leaves a sum over each of the eight solenoids in the rotator,

$$a\gamma_0 \sum_{j=1}^{8\,\text{sols}} (K_s L)_j \left[\left(v_{I,p_x} + \frac{1}{2}K_s v_{I,y}\right)k_{0,x} + \left(v_{I,p_y} - \frac{1}{2}K_s v_{I,x}\right)k_{0,y}\right]_j = 0\,. \tag{4.14}$$

Because the summand is constant within a single solenoid, it can be evaluated at the start, end, or anywhere in between inside that single solenoid. Once again, there are four solenoid modules each consisting of two equal strength solenoids with equal length L. It is convenient to express the spin matching conditions in terms of each solenoid module (each consecutive pair of single solenoids), because we can evaluate the summand right at the start of the first solenoid entering the module, and at the end of the second solenoid exiting the module. With the spin precession through the entire i-th solenoid module as $\phi_i = -2(K_s L)_i(1 + a) \approx -2(K_s L)_i$, we express the horizontal spin matching conditions as

$$a\gamma_0 \sum_{i=1}^{4} H_i = 0\,, \tag{4.15}$$

$$\begin{aligned} H_i = -\frac{\phi_i}{2}\Bigg\{&\left[\left(v_{I,p_x} + \frac{1}{2}K_s v_{I,y}\right)k_{0,x} + \left(v_{I,p_y} - \frac{1}{2}K_s v_{I,x}\right)k_{0,y}\right]_{enter} \\ &+ \left[\left(v_{I,p_x} + \frac{1}{2}K_s v_{I,y}\right)k_{0,x} + \left(v_{I,p_y} - \frac{1}{2}K_s v_{I,x}\right)k_{0,y}\right]_{exit}\Bigg\}_i\,. \end{aligned} \tag{4.16}$$

$(\boldsymbol{v}_I)_{exit}$ can be expressed in terms of $(\boldsymbol{v}_I)_{enter}$ multiplied by the orbital transfer matrix over the i-th solenoid module, and $(\boldsymbol{k}_0)_{exit}$ can be expressed in terms of $(\boldsymbol{k}_0)_{enter}$ multiplied by the spin rotation matrix over the solenoid module. Fur-

thermore, there is no coupling entering and exiting each solenoid module, and so $\left(v_{I,y}\right)_{enter} = \left(v_{I,p_y}\right)_{enter} = \left(v_{I,y}\right)_{exit} = \left(v_{I,p_y}\right)_{exit} = 0$. Explicitly,

$$(v_{I,x})_{exit} = (v_{I,x})_{enter} m_{11} + (v_{I,p_x})_{enter} m_{12} \,, \tag{4.17}$$

$$(v_{I,p_x})_{exit} = (v_{I,x})_{enter} m_{21} + (v_{I,p_x})_{enter} m_{22} \,, \tag{4.18}$$

$$(k_{0,x})_{exit} = (k_{0,x})_{enter} \cos\phi_i - (k_{0,y})_{enter} \sin\phi_i \,, \tag{4.19}$$

$$(k_{0,y})_{exit} = (k_{0,x})_{enter} \sin\phi_i + (k_{0,y})_{enter} \cos\phi_i \,. \tag{4.20}$$

Thus,

$$H_i = \frac{\phi_i}{2} \left\{ v_{I,p_x} \left[k_{0,x} \left(1 + m_{22} \cos\phi_i + m_{12} \frac{1}{2} K_s \sin\phi_i \right) + k_{0,y} \left(m_{22} \sin\phi_i - m_{12} \frac{1}{2} K_s \cos\phi_i \right) \right] \right.$$
$$\left. v_{I,x} \left[k_{0,x} \left(m_{21} \cos\phi_i + m_{11} \frac{1}{2} K_s \sin\phi_i \right) + k_{0,y} \left(-\frac{1}{2} K_s + m_{21} \sin\phi_i - m_{11} \frac{1}{2} K_s \cos\phi_i \right) \right] \right\}_{enter} . \tag{4.21}$$

The horizontal spin matching conditions can be satisfied by setting H_i for each solenoid module such that the sum in Eq. (4.15) is equal to zero. One way of doing this is setting each $H_i = 0$. We also seek a solution which does not depend on the incoming eigenvector. The goal therefore is to choose the transfer matrix components over the solenoid module so that the terms proportional to $v_{I,x}$ and proportional to v_{I,p_x} are each zero. First, we consider the solution which is independent of the incoming $\boldsymbol{k}_0$, such that each term proportional to the components of $\boldsymbol{k}_0$ is zero. Solving the system for m_{22} and m_{12} (proportional to v_{I,p_x} and for m_{21} and m_{11} (proportional to $v_{I,x}$), and taking care to never divide by $\cos\phi_i$ which will equal zero when $\phi_i = 90°$, gives the transfer matrix elements for an arbitrary incoming $\boldsymbol{k}_0$, the so-called *universal solution*,

$$\mathsf{M}_{i,x} = \begin{pmatrix} -\cos\phi_i & -\frac{2}{K_s} \sin\phi_i \\ \frac{K_s}{2} \sin\phi_i & -\cos\phi_i \end{pmatrix} . \tag{4.22}$$

It seems, by coincidence, that the universal solution satisfies the symplectic condition $\det(\mathsf{M}) = 1$. Now, we consider possible other solutions dependent on the

incoming $\boldsymbol{k}_0$. From this point forward, we will omit the subscript *enter* and assume it is implied. We rewrite Eq. (4.21) as

$$H_i = \frac{\phi_i}{2}\left\{ v_{I,p_x}\left[m_{22}\left(k_{0,x}\cos\phi_i + k_{0,y}\sin\phi_i\right) + m_{12}\left(k_{0,x}\frac{1}{2}K_s\sin\phi_i - k_{0,y}\frac{1}{2}K_s\cos\phi_i\right) + k_{0,x}\right]\right.$$
$$\left. v_{I,x}\left[m_{21}\left(k_{0,x}\cos\phi_i + k_{0,y}\sin\phi_i\right) + m_{11}\left(k_{0,x}\frac{1}{2}K_s\sin\phi_i - k_{0,y}\frac{1}{2}K_s\cos\phi_i\right) - \frac{1}{2}K_s k_{0,y}\right]\right\} . \tag{4.23}$$

Let

$$A = k_{0,x}\cos\phi_i + k_{0,y}\sin\phi_i \, , \tag{4.24}$$
$$B = k_{0,x}\frac{1}{2}K_s\sin\phi_i - k_{0,y}\frac{1}{2}K_s\cos\phi_i \quad . \tag{4.25}$$

The spin matching conditions for any incoming $\boldsymbol{k}_0$ can be written as

$$Am_{22} + Bm_{12} = -k_{0,x} \, , \tag{4.26}$$
$$Am_{21} + Bm_{11} = \frac{1}{2}K_s k_{0,y} \, . \tag{4.27}$$

Including the symplectic condition, we calculate $m_{11}\times$(Eq. (4.26)) $-$ $m_{12}\times$(Eq. (4.27)) to be

$$A\left(m_{11}m_{22} - m_{12}m_{21}\right) + B\left(m_{12}m_{11} - m_{12}m_{11}\right) = -k_{0,x}m_{11} - \frac{1}{2}K_s k_{0,y}m_{12} \, ,$$
$$\rightarrow A = -k_{0,x}m_{11} - \frac{1}{2}K_s k_{0,y}m_{12} \, . \tag{4.28}$$

Writing out the full form of A, and expressing this in terms of the real and imaginary parts of $\boldsymbol{k}_0$ (defined previously as $\boldsymbol{k}_0 = \hat{\boldsymbol{l}}_0 + \mathrm{i}\hat{\boldsymbol{m}}_0$), this is

$$-\begin{pmatrix} l_{0,x}\cos\phi_i + l_{0,y}\sin\phi_i \\ m_{0,x}\cos\phi_i + m_{0,y}\sin\phi_i \end{pmatrix} = \begin{pmatrix} l_{0,x} & \frac{1}{2}K_s l_{0,y} \\ m_{0,x} & \frac{1}{2}K_s m_{0,y} \end{pmatrix}\begin{pmatrix} m_{11} \\ m_{12} \end{pmatrix} . \tag{4.29}$$

Similarly, with $m_{22}\times$(Eq. (4.27)) $-$ $m_{21}\times$(Eq. (4.26)),

$$\frac{1}{2}K_s\begin{pmatrix} l_{0,x}\sin\phi_i - l_{0,y}\cos\phi_i \\ m_{0,x}\sin\phi_i - m_{0,y}\cos\phi_i \end{pmatrix} = \begin{pmatrix} l_{0,x} & \frac{1}{2}K_s l_{0,y} \\ m_{0,x} & \frac{1}{2}K_s m_{0,y} \end{pmatrix}\begin{pmatrix} m_{21} \\ m_{22} \end{pmatrix} . \tag{4.30}$$

Solving Eqs. (4.29) and (4.30) gives the symplectic transfer matrix components that satisfy the horizontal spin matching conditions, granted that the matrix is also decoupled. Notably, infinitely many solutions will exist when the projections of $\hat{\boldsymbol{l}}_0$ and $\hat{\boldsymbol{m}}_0$ on the xy-plane lie along the same line (so the rows of the matrix are not linearly independent). This is *always* the case for the first and last solenoid modules, where the entering $\hat{\boldsymbol{n}}_0$ lies entirely in the xy-plane. In every other case, the universal solution is the only solution.

Only three quadrupoles are necessary for decoupling the solenoid module [42], and because the symplectic condition connects Eqs. (4.29) and (4.30), only three more quadrupoles are necessary for spin matching. However, when the entering/exiting $\hat{n}_0$ lies in the XY-plane (e.g. is vertical), the matrix in Eqs. (4.29) and (4.30) is degenerate. This leaves one variable free, and therefore only 5 quadrupoles are necessary for the outer-most (short) solenoid modules.

Longitudinal Spin Match

In the case of a coasting beam, to achieve a longitudinal spin match we would substitute a particle on the dispersive orbit $\boldsymbol{\zeta} = (\eta_x, \eta_{p_x}, \eta_y, \eta_{p_y}, 0, 1)^T$ into Eq. (4.12). With RF, we would substitute the longitudinal eigenvector $\boldsymbol{v}_{III}$. The dispersion is easiest to substitute, and in the limit of $Q_s << Q_{x,y}$ it is a fine approximation. As with the horizontal spin matching conditions, integrals over the terms $(y'k_{0,x})'$ and $(x'k_{0,y})'$ are again zero; at the start and exit of the rotator there is no vertical dispersion and $\hat{\boldsymbol{n}}_0$ is vertical. Furthermore, terms proportional to y, y' in the bends will be zero because there is no vertical dispersion.

This leaves

$$\int_{s_{in}}^{s_{out}} \boldsymbol{\omega} \cdot \boldsymbol{k}\, ds = \int_{8\text{ sols}} K_s(1+a)\left\{a\gamma_0\left[\left(\eta_{p_x} + \frac{1}{2}K_s\eta_y\right)k_{0,x} + \left(\eta_{p_y} - \frac{1}{2}K_s\eta_x\right)k_{0,y}\right] + k_{0,s}\right\} ds - \int_{4\text{ bends}} g_x\left(a\gamma_0 - \frac{a}{\gamma_0}\right)k_{0,y}\, ds\,. \tag{4.31}$$

Assuming $(1+a) \approx 1$ so that $(x'k_{0,x} + y'k_{0,y})$ is constant within a solenoid, the terms proportional to $a\gamma_0$ in the integral over the solenoids gives the exact same conditions as the horizontal spin matching conditions. This is because there is zero vertical dispersion and zero coupling entering and exiting the solenoid module, and the horizontal dispersion will propagate over the solenoid module according to the same 2×2 horizontal transfer matrix. Defining $\phi_i = 2(K_sL)_i(1+a) \approx 2(K_sL)_i$ as the spin precession in the i-th solenoid module, $\psi_j = a\gamma_0(g_xL)_j$ the spin precession in the j-th bend module, and finally assuming $a/\gamma_0 \approx 0$, the longitudinal spin matching conditions are

$$a\gamma_0\sum_{i=1}^{4} H_i + \sum_{i=1}^{4} k_{0s,i}\phi_i - \sum_{j=1}^{4} k_{0y,j}\psi_j = 0\,. \tag{4.32}$$

Therefore, a longitudinal spin match can be achieved by choosing the geometry (spin rotation angles in the bends) and solenoids strengths (spin rotation angles in the solenoids), and having a horizontal spin-match.

4.4 Spin Rotator Configurations

At the time of this dissertation writing, the spin rotator configuration (solenoid strengths and bend angles) is "finalized", for those values shown in Table 4.1. A longitudinal strong synchrobeta spin match is *not* satisfied at 18 GeV, however the polarization has been rescued by a novel method developed in this dissertation called *Best Adjustment Groups for ELectron Spin (BAGELS)*. BAGELS also

enables simultaneous polarization, orbit, and optics control in electron storage rings, providing an effective method to correct polarization in operation, preserve high polarization while correcting the optics, and preserve high polarization while generating vertical emittance (necessary for beam-size matching with the hadron beam at the IP). BAGELS, which has become an essential and necessary part of the EIC-ESR design, is discussed and presented in detail in Ch.7. Nonetheless, much work was done leading to the development of BAGELS. To set the stage for the next several chapters, in this section we describe various choices for the solenoid strengths and bend angles, and their implications on the design. The SymPy symbolic computer algebra system was used extensively for the derivations in this section [46].

Following Fig. 4.1, for a vertical incoming $\hat{\boldsymbol{n}}_0$ we require some $\psi_{1,2,3,4}$ and $\phi_{1,2,3,4}$ to rotate $\hat{\boldsymbol{n}}_0$ to the longitudinal at the IP, then rotate back to vertical. A configuration symmetric about the IP, such that $\psi_1 = \psi_4$, $\psi_2 = \psi_3$, $\phi_1 = \phi_4$, and $\phi_2 = \phi_3$, is also sought; it can be shown that if $\hat{\boldsymbol{n}}_0$ is rotated from vertical to $\pm\hat{z}$, then a symmetric arrangement will rotate it back to vertical. Now, we consider the solenoid spin precession angles ϕ_1 and ϕ_2 that we would need to rotate $\hat{\boldsymbol{n}}_0$ from vertical in the arc to longitudinal at the IP, given the bend precession angles ψ_1 and ψ_2. Letting $\mathsf{R}_x(\alpha)$, $\mathsf{R}_y(\alpha)$, and $\mathsf{R}_z(\alpha)$ correspond to the SO(3) rotation matrices around the x, y, and z axes respectively by an angle α, from arc-to-IP we have

$$\begin{pmatrix} 0 \\ 0 \\ \sigma \end{pmatrix} = \mathsf{R}_y(\psi_2)\mathsf{R}_z(\phi_2)\mathsf{R}_y(\psi_1)\mathsf{R}_z(\phi_1)\begin{pmatrix} 0 \\ 1 \\ 0 \end{pmatrix}, \tag{4.33}$$

where $\sigma = \pm 1$. After multiplying the rotations, this gives three equations constraining the angles. The first two equations, however, can be expressed as a

linear homogeneous system in $\cos\phi_1$ and $\sin\phi_2$. Therefore, because we cannot simultaneously have $\cos\phi_1 = \sin\phi_2 = 0$the determinant of this system must be zero. This determinant equation, along with the third equation in the overall system, gives the general conditions

$$\sin(\psi_1)\sin(\psi_2)\cos(\phi_2) - \cos(\psi_1)\cos(\psi_2) = 0\,, \tag{4.34a}$$

$$\left[\sin(\psi_1)\cos(\psi_2) + \sin(\psi_2)\cos(\psi_1)\cos(\phi_2)\right]\sin(\phi_1) + \sin(\psi_2)\sin(\phi_2)\cos(\phi_1) = \sigma\,. \tag{4.34b}$$

The solutions to these conditions have several cases which we must consider carefully. For $n, m, k \in \mathbb{Z}$,

1. If $\psi_1 = n\pi$ then we must have $\psi_2 = m\pi - \frac{\pi}{2}$ to satisfy Eq. (4.34a). Substituting this into Eq. (4.34b) gives

   $$\sin(\phi_2)\cos(\phi_1) + (-1)^n\cos(\phi_2)\sin(\phi_1) = (-1)^{m+1}\sigma\,, \tag{4.35}$$

   which simplifies to

   $$\sin(\phi_2 + (-1)^n\phi_1) = (-1)^{m+1}\sigma\,. \tag{4.36}$$

   Therefore,

   $$\phi_2 + (-1)^n\phi_1 = \frac{\pi}{2}(-1)^{m+1}\sigma + 2k\pi\,. \tag{4.37}$$

2. If $\psi_2 = n\pi$ then we must have $\psi_1 = m\pi - \frac{\pi}{2}$ to satisfy Eq. (4.34a). Substituting this in Eq. (4.34b) gives

   $$\sin(\phi_1) = (-1)^{n+m+1}\sigma\,. \tag{4.38}$$

   Therefore,

   $$\phi_1 = \frac{\pi}{2}(-1)^{n+m+1}\sigma + 2k\pi\,,\ \phi_2 \text{ free}\,. \tag{4.39}$$

   In this case ϕ_2 is free, because $\hat{\boldsymbol{n}}_0$ will be pointing along the $\pm\hat{\boldsymbol{z}}$ direction when it reaches that solenoid module after being rotated by ϕ_1.

3. If $\psi_1 \neq n\pi$ and $\psi_2 \neq m\pi$, then we can solve Eq. (4.34a) directly. With some algebra, we obtain the solution

$$\phi_1 = \text{atan2}\left[\sigma\frac{\cos(\psi_2)}{\sin(\psi_1)},\ s\sigma\sin(\psi_2)\sqrt{1-\cot^2(\psi_1)\cot^2(\psi_2)}\right], \tag{4.40a}$$

$$\phi_2 = \text{atan2}\left[s\sqrt{1-\cot^2(\psi_1)\cot^2(\psi_2)},\ \cot(\psi_1)\cot(\psi_2)\right], \tag{4.40b}$$

where $s = \pm 1$. In order to have a solution, $-1 < \cot(\psi_1)\cot(\psi_2) < 1$.

We now consider which angles would provide a longitudinal strong synchro-beta spin match. Per Eq. (4.32), if a horizontal spin match is satisfied then for a longitudinal spin match we have

$$\sum_{i=1}^{4} k_{0s,i}\phi_i - \sum_{j=1}^{4} k_{0y,j}\psi_j = 0\ . \tag{4.41}$$

This sum can be evaluated for arbitrary choice of angles, and those angles which make the real and imaginary parts equal to zero yield a longitudinal spin match. We now consider this sum for the three cases of solutions (let $n, m, k \in \mathbb{Z}$):

1. For $\psi_1 = n\pi$, $\psi_2 = m\pi - \frac{\pi}{2}$, and $\phi_2 + (-1)^n\phi_1 = \frac{\pi}{2}(-1)^{m+1}\sigma + 2k\pi$, the real part of the sum simplifies to $0 = 0$ and the imaginary part simplifies to the requirement

$$\sin(\phi_1) = \sigma\frac{(-1)^{m+n}(2m-1)}{2n}\ ,\ n \neq 0\ . \tag{4.42}$$

Therefore solutions only exist when

$$|2m-1| \leq |2n|\ . \tag{4.43}$$

2. For $\psi_2 = n\pi$, $\psi_1 = m\pi - \frac{\pi}{2}$, and $\phi_1 = \frac{\pi}{2}(-1)^{n+m+1}\sigma + 2k\pi$, ϕ_2 free, the real and imaginary parts both simplify to the same condition,

$$(-1)^{n+1}\cos(\phi_2) + \frac{1}{2m-1}\sin(\phi_2) = (-1)^n\frac{2n}{2m-1}\ . \tag{4.44}$$

Using the harmonic addition theorem, we can rewrite the LHS of this equation as a single sinusoid. After some simplification,

$$\cos\left[\phi_2 + (-1)^n \operatorname{atan2}\left(1,\ 2m-1\right)\right] = -\frac{2n}{\sqrt{1+(2m-1)^2}}\ . \tag{4.45}$$

Therefore solutions only exist when

$$|2n| \leq \sqrt{1+(2m-1)^2}\ . \tag{4.46}$$

3. For $\psi_1 \neq n\pi$, $\psi_2 \neq m\pi$, and ϕ_1, ϕ_2 satisfy Eqs. (4.40), a simple algebraic expression giving the longitudinal spin matching conditions is not obtainable – numerical solution is required.

Finally, it is insightful to consider the spin phase advance of $\boldsymbol{k}_0$ over the rotator, which we will refer to as α_s, given some choice of spin rotation angles. This is most easily obtained from the spin transport quaternion over the entire rotator, which will be some rotation around the vertical axis; this angle is α_s. In general, this gives

$$\sin\left(2\pi\alpha_s/2\right) = \sin\left(\psi_1\right)\cos\left(\psi_2\right)\cos\left(\phi_2\right) + \cos\left(\psi_1\right)\sin\left(\psi_2\right)\ . \tag{4.47}$$

Therefore, for each class of solution,

1. For $\psi_1 = n\pi$, $\psi_2 = m\pi - \frac{\pi}{2}$, and $\phi_2 + (-1)^n\phi_1 = \frac{\pi}{2}(-1)^{m+1}\sigma + 2k\pi$, we obtain $\alpha_s = \frac{1}{2}(-1)^{m+n+1}$.
2. For $\psi_2 = n\pi$, $\psi_1 = m\pi - \frac{\pi}{2}$, and $\phi_1 = \frac{\pi}{2}(-1)^{n+m+1}\sigma + 2k\pi$, ϕ_2 free, we obtain $\alpha_s = \frac{(-1)^{n+m+1}}{\pi}\arcsin\left[\cos\left(\phi_2\right)\right]$.
3. For $\psi_1 \neq n\pi$, $\psi_2 \neq m\pi$, and ϕ_1, ϕ_2 satisfy Eqs. (4.40), we obtain the simple form $\alpha_s = \frac{1}{\pi}\arcsin\left[\cos\left(\psi_1\right)/\sin\left(\psi_2\right)\right]$.

We remark that case 1 is "special", because it is impossible to distinguish a rotation of $+\pi$ from a rotation of $-\pi$, and therefore the values of m and n really do not matter. Furthermore, in this case if the solenoids were turned off, α_s would be $\frac{2(n\pi+m\pi-\pi/2)}{2\pi} = n + m - \frac{1}{2}$. Because only the fractional part of the spin tune has any meaning and n, m are integers, α_s over the rotator is still just π. Therefore, for case 1 the closed orbit spin tune is unchanged if the solenoids are turned on vs. off.

Each solution case, its requirement for a longitudinal spin match, and α_s is summarized in Table 4.2.

Table 4.2: With Fig. 4.1, the various solutions for ϕ_1 and ϕ_2 to rotate $\hat{\boldsymbol{n}}_0$ to $\sigma\hat{\boldsymbol{z}}$, $\sigma = \pm 1$, from $\hat{\boldsymbol{y}}$ given some ψ_1, ψ_2 and assuming a symmetric layout such that $\phi_1 = \phi_4$, $\phi_2 = \phi_3$, $\psi_1 = \psi_4$, and $\psi_2 = \psi_3$. Here $n, m, k \in \mathbb{Z}$, LSM stands for longitudinal spin match, and α_s corresponds to the spin phase advance of $\boldsymbol{k}_0$ across the rotator.

	Case 1	**Case 2**	**Case 3**
Bends	$\psi_{1,4} = n\pi \rightarrow \psi_{2,3} = m\pi - \dfrac{\pi}{2}$	$\psi_{2,3} = n\pi \rightarrow \psi_{1,4} = m\pi - \dfrac{\pi}{2}$	$\psi_2 \neq n\pi, \psi_2 \neq m\pi$
Solenoids	$\phi_2 + (-1)^n \phi_1 = \dfrac{\pi}{2}(-1)^{m+1}\sigma + 2k\pi$	$\phi_1 = \dfrac{\pi}{2}(-1)^{n+m+1}\sigma + 2k\pi\ ,\ \phi_2$ free	$c_2 = \cot(\psi_1)\cot(\psi_2)$ $\phi_1 = \operatorname{atan2}\left[\sigma\dfrac{\cos(\psi_2)}{\sin(\psi_1)},\ s\sigma\sin(\psi_2)\sqrt{1-c_2^2}\right],$ $\phi_2 = \operatorname{atan2}\left[s\sqrt{1-c_2^2},\ c_2\right],$
LSM Condition	$\phi_1 = \sigma(-1)^{m+n}\arcsin\left[\dfrac{2m-1}{2n}\right]$	$\phi_2 = \arccos\left[-\dfrac{2n}{\sqrt{1+(2m-1)^2}}\right]$ $+ (-1)^{n+1}\operatorname{atan2}(1,\ 2m-1)$	Numerical solution required
α_s **[2π]**	$\dfrac{(-1)^{m+n+1}}{2}$	$\dfrac{(-1)^{n+m+1}}{\pi}\arcsin\left[\cos(\phi_2)\right]$	$\dfrac{1}{\pi}\arcsin\left[\dfrac{\cos(\psi_1)}{\sin(\psi_2)}\right]$

4.5 Lattice Versions

Per Eq. (3.58), we have $\psi_1 = -\theta_1 a\gamma_0$ where θ_1 is the *orbit* precession in the first bend module; the spin precession in bend modules is directly connected to the geometry of the ring. Therefore, since we don't want to change the geometry of the ESR for the various energy cases, it is insightful to consider the solutions presented in Table 4.2 given some choice of ψ_1 and ψ_2. Figure 4.6 shows, for a given ψ_1 and ψ_2 the regions where ϕ_1 and ϕ_2 can (green) and cannot (red) be set to achieve longitudinal spin at the IP, as well as a black line corresponding to when a longitudinal spin match (LSM) is possible. The corners of each tile correspond to either case 1 or 2, and the bodies of each tile correspond to case 3. In this plot, a given geometry will correspond to a straight line that goes through the origin with slope $\psi_2/\psi_1 = \theta_2/\theta_1$. Then, once the energy is defined at one point along this line, the energies at all different points are defined; as γ_0 is changed, the position along the line changes linearly.

Early versions of the 18 GeV EIC-ESR, specifically those $\leq$ v5.6, had the first class of solutions with $\psi_1 = -\pi$ and $\psi_2 = -\pi/2$. This corresponds to the right-most "x" of the yellow line in Fig. 4.6. In this case, the closed orbit spin tune is unchanged if the rotator is on vs. off, and so we can select the exact energy for a half-integer spin tune using the formula for a perfectly flat, aligned ring with only dipoles and regular quadrupoles, $\nu_0 = a\gamma_0$. The 18 GeV case was therefore selected to have $a\gamma_0 = 40.5$, which corresponds to the exact energy $E = 17.846$ GeV.

The 18 GeV v5.3 specifically had a longitudinal spin match, and therefore per Eqs. (4.37) and (4.42) required the specific solenoid module spin rotation

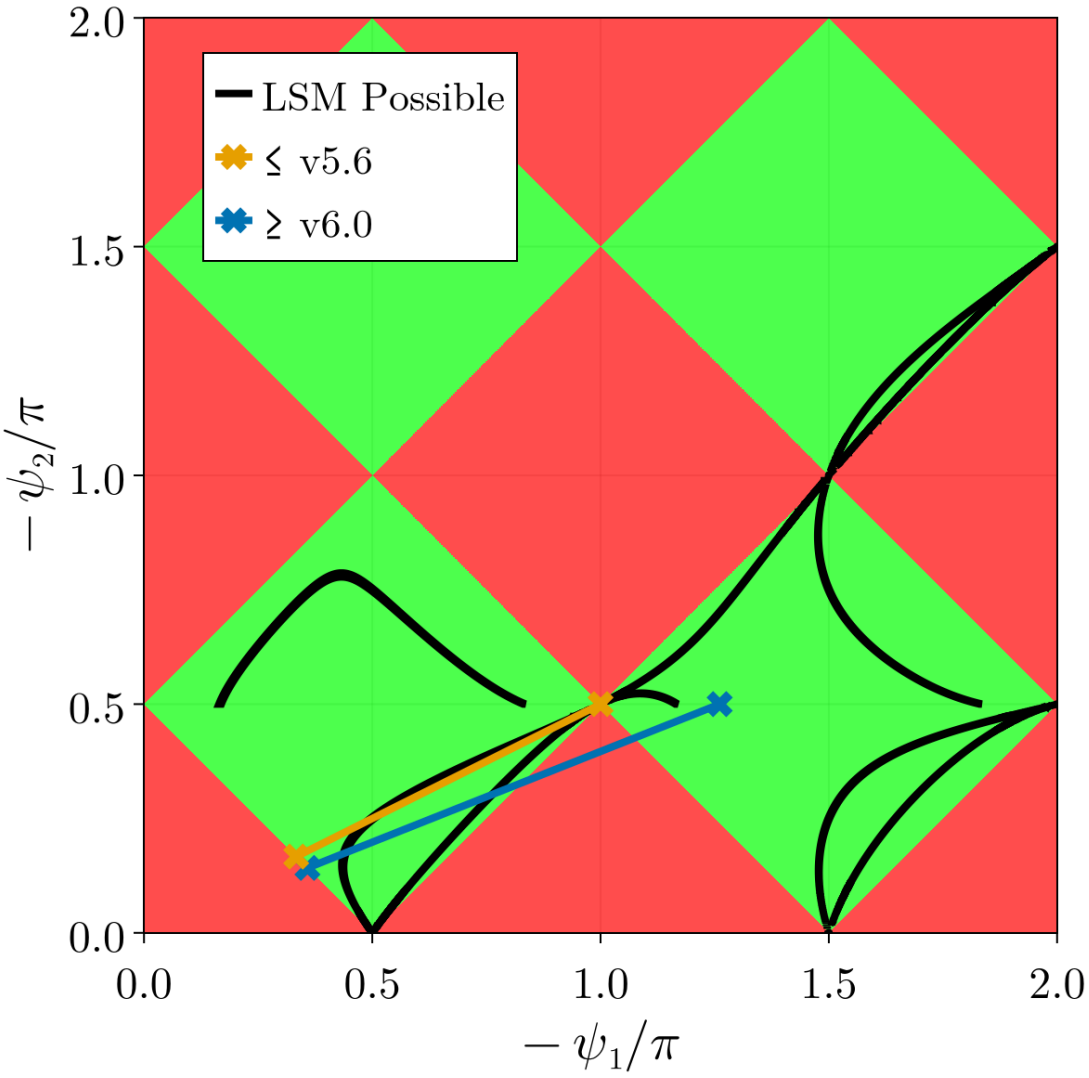

Figure 4.6: Regions where longitudinal spin at the IP is achievable (green) and not achievable (red) for the spin rotator in Fig. 4.1, given some bend module spin precession angles ψ_1 and ψ_2. The black lines specify where a longitudinal spin match (LSM) is possible, and straight lines going through the origin correspond to constant bend geometries.

angles $\phi_1 = (-30^\circ)\sigma$ and $\phi_2 = (-120^\circ)\sigma$. Using Eq. (3.58), for the long solenoid module this corresponds to the integrated field

$$|B_s L| = \frac{p_0}{q}\frac{120\frac{\pi}{180}}{1+a} = 124.53 \text{ T m} . \tag{4.48}$$

This is massive. In the v5.3, each of the two solenoids in the long solenoid module was 9 m long, corresponding to 6.9 T field strengths. In the v5.6, the solenoids in the long module were only 5.5 m long, which would correspond to 11.3 T field strengths to achieve a longitudinal spin match. This is impractical, and ultimately led to the dropping of the LSM. Instead for v5.6, per case 1 in Table 4.2, the solution $\phi_1 = 0$, $\phi_2 = -\frac{\pi}{2}$ was selected so that only the long solenoid module is "on" at 18 GeV. This corresponds to a slightly more reasonable 8.5 T for the long solenoids in v5.6, at the cost of a LSM. However, now that we have chosen an energy for a point on the plot of Fig. 4.6, the energies at all other points are also defined. In this case, the lowest energy case we can achieve in the v5.6 (the left-most "x" of the yellow line in Fig. 4.6) is 5.95 GeV; this is a quite a lot higher than the 5 GeV requested by the high energy physics experimentalists.

If we would like to support a low-energy closer to 5 GeV, then we can do two things. Firstly, we could keep the ratio θ_2/θ_1 constant, but add some angle to both θ_1 and θ_2 so that the lowest possible energy case is closer to 5 GeV – this would make the 18 GeV case "move up" along the yellow line. The problem with this, however, is that for $\psi_2 > \pi/2$, the long solenoid precession angle solution ϕ_2 essentially "continues" from the 120° at the corner of the tile, not 90°; the new solution is not near $\phi_2 = -\pi/2$ but near $\phi_2 = -120°$. The integrated field strength would then still be too large.

Alternatively, we could keep θ_2 constant so that the more manageable $\phi_2 = -\pi/2$ remains the solution for 18 GeV, and increase θ_1 until the lower bound of the new line with slope θ_2/θ_1 allows for 5 GeV. This was ultimately the solution decided for the v6.0 lattice, and remains the current bend configuration at the time of this dissertation writing. One thing to note per Fig.4.6 is that the lower

bound is defined by the curve $\psi_2 = \frac{\pi}{2} - \psi_1$, and so therefore at the lower bound $\cos(\psi_1) = \sin(\psi_2)$. From Table 4.2, this corresponds to a $\alpha_s = \frac{1}{2}$; the closed orbit spin tune is unchanged if the rotator is on vs. off for the low energy bound. Therefore, the amount of θ_1 added corresponded to making $a\gamma_0 = 11.5$ ($E = 5.07$ GeV) at the right at the lower bound. Furthermore, by keeping the 18 GeV case at $\psi_2 = -\pi/2$ and having $\phi_1 = 0$, it can be shown that α_s is also unchanged whether or not the rotator is on. Therefore the 18 GeV case is kepy at $a\gamma_0 = 40.5$. The "finalized" geometry for v6.0+ is defined by the blue line in Fig. 4.6, with the left-most "x" corresponding to $E = 5.07$ GeV and the right-most "x" corresponding to $E = 17.846$ GeV.

The solenoid and bend module spin precession angles for the various 18 GeV ESR versions are summarized in Table 4.3.

Table 4.3: Solenoid ($\hat{\boldsymbol{s}}$) and bend ($\hat{\boldsymbol{y}}$) module spin precession angles for various 18 GeV ESR lattices, using the right-handed basis ($\hat{\boldsymbol{x}}, \hat{\boldsymbol{y}}, \hat{\boldsymbol{s}}$) with $\hat{\boldsymbol{s}}$ pointing along the longitudinal in Fig. 4.1

	Solenoids		**Bends**	
	$\phi_{1,4}$	$\phi_{2,3}$	$\psi_{1,4}$	$\psi_{2,3}$
ESR v5.3 (LSM)	$-30°$	$-120°$	$-180°$	$-90°$
ESR v5.6 (No LSM)	$0°$	$-90°$	N/A	$-90°$
ESR v6.0 (No LSM)	$0°$	$-90°$	N/A	$-90°$

CHAPTER 5

ESR WORKING POINT OPTIMIZATION

5.1 Background

Early versions of the EIC-ESR (v5.3) had a longitudinal spin match. However, those same lattices showed significant problems in nonlinear Monte Carlo tracking studies. In particular, the vertical emittances blew up beyond first-order analytical predictions, and the polarization likewise deteriorated much faster than the prediction in Eq. (3.43) using the approximations in Sec. 3.9 [65]. Difficulties with the dynamic aperture were also found [45]. These effects were apparently resolved in a newer version (v5.6), which has dropped the longitudinal spin match and turned off the short solenoid module entirely. Nonetheless, understanding the cause of the negative effects was necessary to ensure the new solution is sufficient and robust. In this chapter, we use various Monte Carlo tracking methods to identify the cause as a 2^{nd} order synchro-beta resonance excited by vertical dispersion in quadrupoles. By moving off of this resonance in the v5.3, the emittance agrees well with the analytical approximation, as does the polarization. The reason why this effect only presented itself in the 18 GeV v5.3, and not the v5.6, is because in the v5.3 the short solenoid modules were turned on to achieve a longitudinal spin match and had nonzero dispersion entering/exiting which got locally coupled into the vertical in the solenoid module quadrupoles. In the 18 GeV v5.6, the short solenoid modules were turned off entirely, and the long solenoid modules have zero dispersion entering/exiting. Nonetheless, because this resonance can be readily exciting by misalignments, the tunes had to be changed to avoid this dangerous resonance.

5.2 Methods

In this chapter, long term tracking is done using the *long_term_tracking* program, which is part of the Bmad ecosystem of programs. Bmad [53] is a toolkit (software library) for charged particle and X-ray simulations in accelerators and storage rings. Lattice manipulation used the *Tao* [55] program which is also part of the Bmad ecosystem.

All Monte Carlo tracking results include radiation damping and fluctuations. The `taper` command in the *Tao* program was used to fix the closed orbit sawtooth effect due to radiation. *Map Tracking* uses truncated Taylor series maps which include spin transport. The truncation order is user-specified. With map tracking, radiation effects are applied at the bend centers and maps are used to transport the beam from bend center to bend center. *Bmad Tracking* uses fully nonlinear, element-by-element tracking unless otherwise specified. *PTC Tracking* is element-by-element symplectic integration using the PTC [33]. Both Bmad tracking and PTC tracking apply radiation effects step-by-step. The emittances obtained from tracking are the bunch eigen-emittances calculated from the 6D beam distribution. The three normal modes labeled "a", "b", and "c" correspond to the horizontal-like, vertical-like, and longitudinal-like modes [75]. In an abuse of notation, we refer to the tunes in each plane as Q_x, Q_y, and Q_z respectively. All tracking reported in this chapter uses 5,000 to 10,000 particles, with an initial 6D distribution equal to the analytical equilibrium beam distribution.

Table 5.1: RMS emittances for the 18 GeV v5.3 ESR lattice with fractional tunes $(Q_x, Q_y, Q_s) = (0.12, 0.10, 0.05)$.

	$\epsilon_{a,\mathrm{RMS}}$ [nm]	$\epsilon_{b,\mathrm{RMS}}$ [nm]
Analytical	27.7	~ 0
1^{st} Order Map Tracking	27.7	~ 0
2^{nd} Order Map Tracking	31.4	2.4
3^{rd} Order Map Tracking	28.9	10.6
Bmad Tracking	28.7	12.3
PTC Tracking	28.8	12.3

5.3 Core Emittance

Table 5.1 shows the RMS equilibrium emittances obtained from various tracking methods versus the analytical calculation. While $\epsilon_{a,\mathrm{RMS}}$ shows good agreement in the fully nonlinear case, $\epsilon_{b,\mathrm{RMS}}$ significantly exceeds the linear prediction.

Because the ESR is a nonlinear ring with high strength solenoids and sextupoles, one suspicion was that the nonlinearities were driving the tails of the distribution in the vertical to large amplitudes. In such a case, the RMS emittance is not the best measure of the beam distribution. Rather, the *core emittance* should be used. There are various definitions of a core emittance in the literature [36]. In this paper, the core emittance for a given mode and a given core size (expressed as some percentage of the total number of particles) is calculated using the following algorithm: the particles with the largest amplitudes for the given mode are removed until the percentage of particles left matches the given core size. The eigenmodes are then recalculated, and, starting with the entire beam,

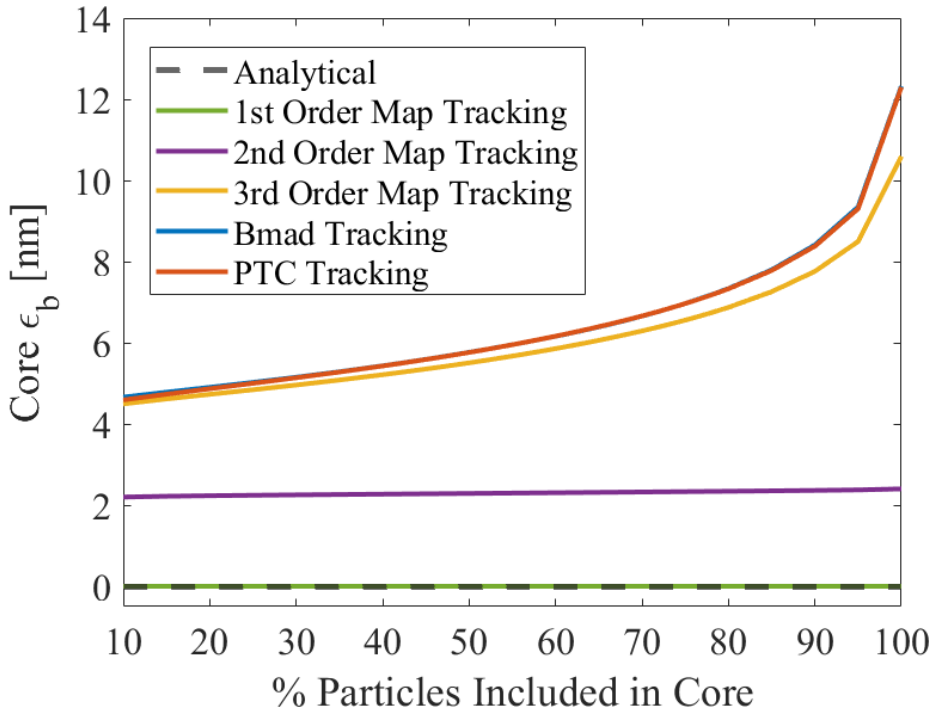

Figure 5.1: Vertical (b-mode) core emittances for varying percents of particles included in the core for the 18 GeV v5.3 ESR lattice with fractional tunes $(Q_x, Q_y, Q_s) = (0.12, 0.10, 0.05)$. The Bmad Tracking line is almost identical with the PTC Tracking line and so is indistinguishable.

the removal process is repeated. A Gaussian is then fit to this final core distribution, giving the core emittance. This algorithm is called the "non-combined core emittance" calculation and is detailed in the *long_term_tracking* program manual [54]. With this definition, a perfectly Gaussian distribution would yield the same core emittance regardless of the cutoff amplitude. Near 0% only particles near the center of the beam are included and at 100% the full beam is included.

Figure 5.1 shows the vertical core emittances as a function of the number of particles included in the core. For the tracking that includes the most nonlinear effects (Bmad, PTC and 3rd order map tracking) ϵ_b is about 5 nm even in the

core, which is significantly larger than the analytical (first-order) calculation. It should be noted that for 2nd order tracking the distribution remains Gaussian (the core emittance is constant regardless of cutoff percent). However, $\epsilon_b \approx 2$ nm in this case. This strongly suggests that there is some nonlinear effect present that blows up the beam vertically even in the core.

5.4 Source of Effects

In the ESR v5.3, which has a longitudinal spin match, vertical enlargement could only be generated by nonlinear coupling effects. There are several possible causes including nonlinear effects in the solenoids and/or quadrupoles in the solenoid modules where there is localized coupling, as well as closed orbit deviations through the sextupoles due to radiation. To narrow down the exact element(s) and order at which the effect becomes most prominent, nonlinear Bmad tracking was performed except at select elements, where tracking was done with 1st, 2nd, or 3rd order Taylor maps. Figures 5.2 and 5.3 shows the core ϵ_a and core ϵ_b respectively where only the quadrupoles in between the solenoids ("rotator quads") are tracked with varying order maps, and the rest of the ring is fully nonlinear including the solenoids. As is apparent, the full effect, in particular the "blow-up" in vertical emittance, presents once 2nd order orbit motion in the quadrupoles between the solenoids is included in the tracking. Notably, the effect was not observed if the dispersion entering the solenoid module was made to be zero.

While we will focus primarily on the vertical-like core emittance in the rest of this chapter, the "spike" in the horizontal-like emittance around 70% of particles

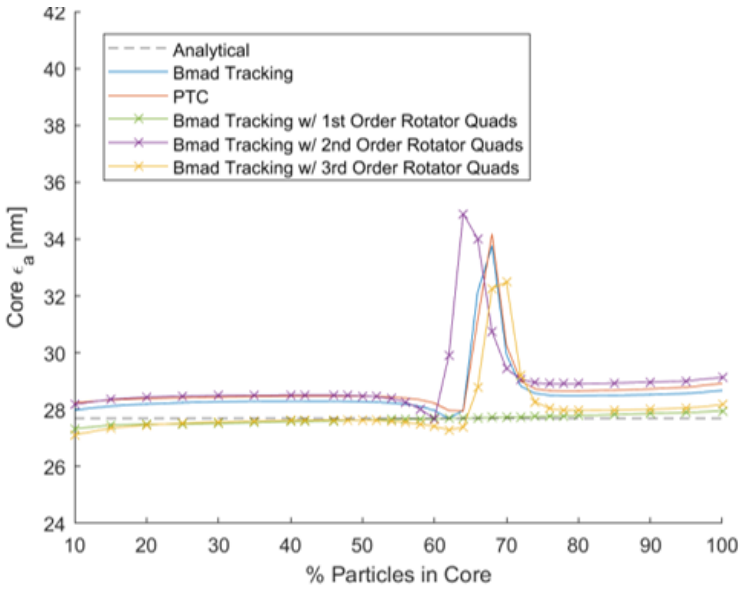

Figure 5.2: Horizontal (a-mode) core emittances for the 18 GeV ESR v5.3 with varying order map tracking through the rotator quadrupoles but fully nonlinear in the rest of the ring.

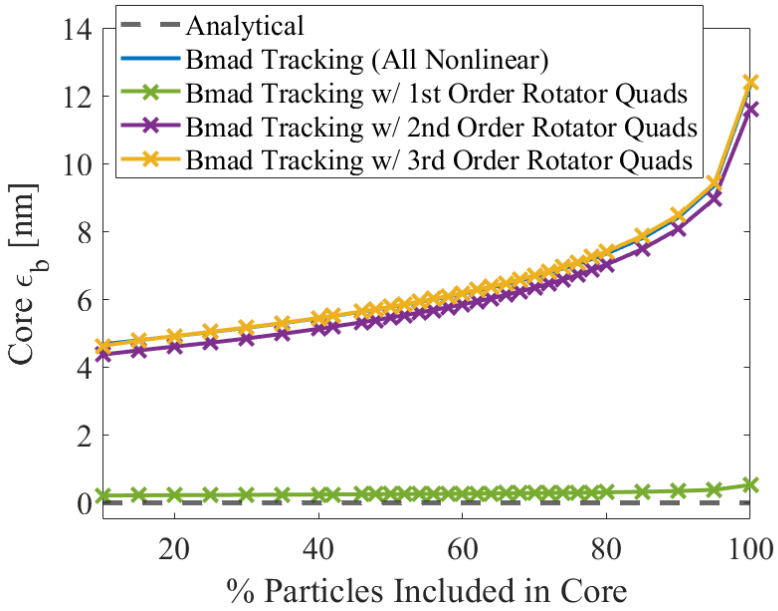

Figure 5.3: Vertical (b-mode) core emittances for the 18 GeV ESR v5.3 with varying order map tracking through the rotator quadrupoles but fully nonlinear in the rest of the ring.

included in the core was an interesting finding. The nature of this artifact hasn't been fully resolved at the time of this dissertation writing. However we did find that, when those particular percentages of particles were included in the core emittance calculation, the directions of the eigenvectors computed from the beam sigma matrix were different than in the other percentages.

5.5 Identification of Resonance

A sweep of the synchrotron tune Q_s reveals a 2nd order resonance as shown in Figure 5.4. This figure shows the 80% core ϵ_b obtained from 3rd order map tracking as a function of Q_s. As a control, each of the core ϵ_b obtained with 1st order map tracking was verified with the linear calculation. As shown, there is a spike in ϵ_b at the current working point (WP) of Q_s = 0.05. This peak is at the $Q_y - 2Q_s$ 2nd order synchro-beta resonance. The polarization shows similar results; Figure 5.5 shows the average bunch replacement time to maintain a time-averaged polarization of no less than 70% for each bunch vs. Q_s.

These rotator quadrupoles are the only places in the ring where there is vertical dispersion in quadrupoles; The horizontal dispersion is locally coupled into the vertical within a solenoid module. Therefore, thus exciting the resonance in the decoupling quadrupoles.

While the undesirable effects can be removed by zeroing dispersion entering each solenoid, with misalignments this is not fully achievable. And, because dispersion cannot be suppressed in the short solenoid module, the short solenoids must be turned off and the longitudinal spin match dropped. As shown in Fig. 5.5, when sufficiently off resonance, excellent polarization is

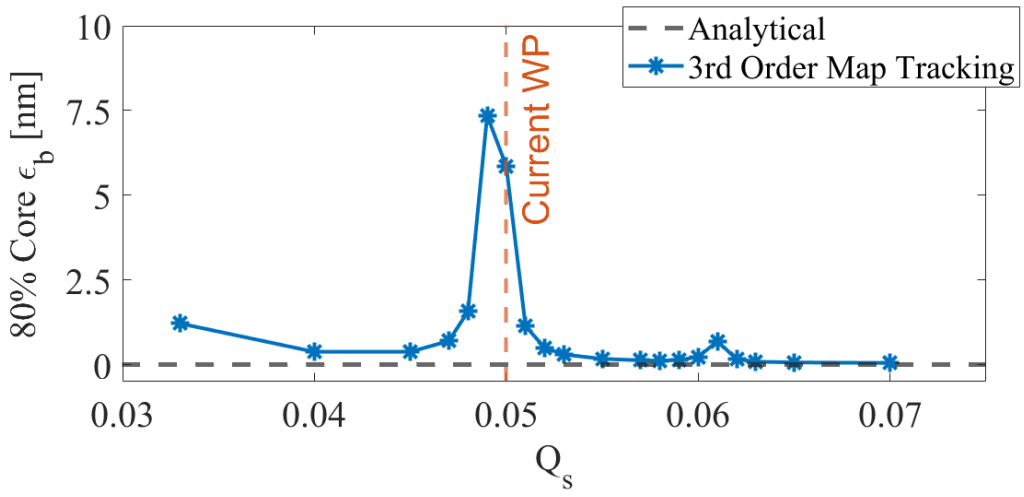

Figure 5.4: 80% core ϵ_b obtained from 3rd order map tracking of the ESR v5.3 for varying Q_s with constant $(Q_x, Q_y) = (0.12, 0.10)$.

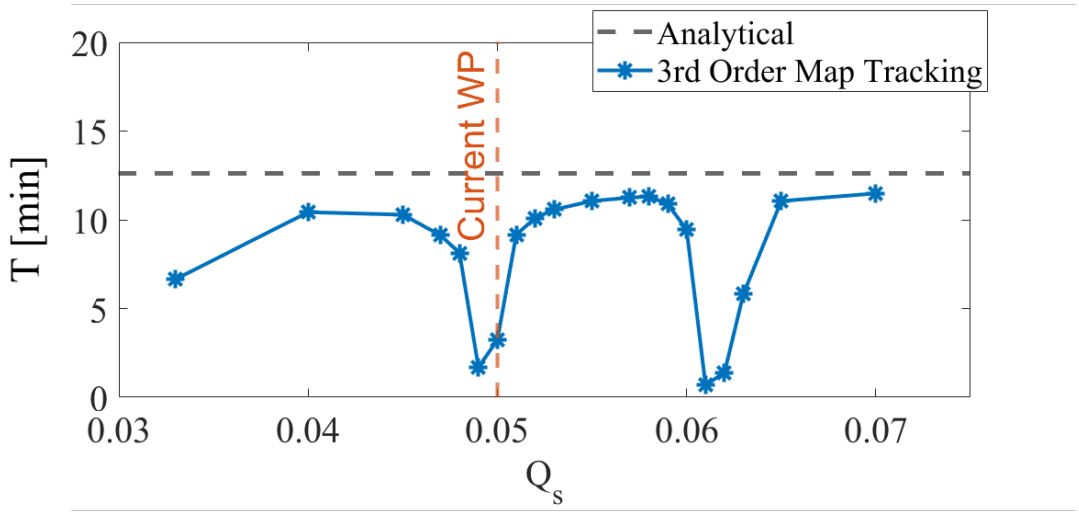

Figure 5.5: N bunch replacement time vs. Q_s with constant $(Q_x, Q_y) = (0.12, 0.10)$ for the ESR v5.3.

achievable. Finally, both the 5 and 10 GeV ESR lattices have small but nonzero dispersion in the solenoids. Thus, a new working point must be determined.

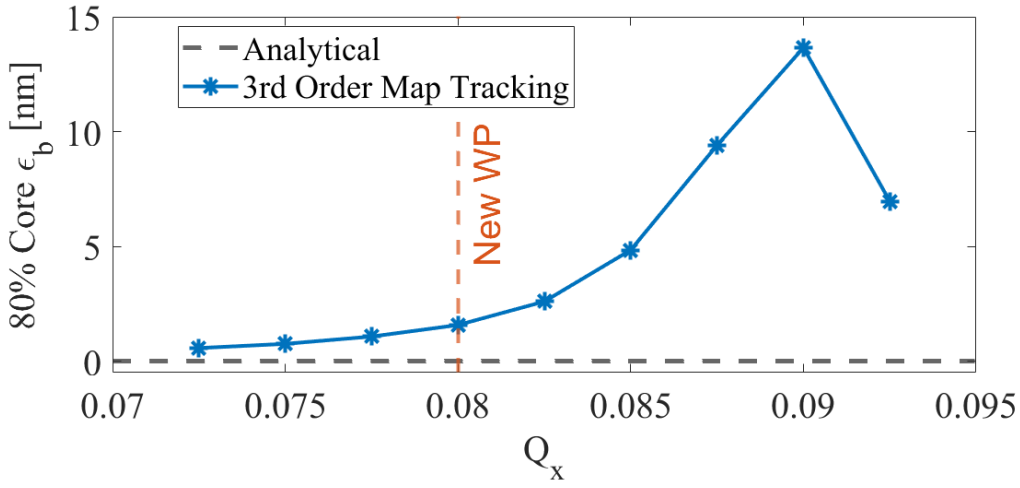

Figure 5.6: 80% core ϵ_b obtained from 3rd order map tracking of the ESR v5.3 for varying Q_x with $Q_s = 0.05$ and $Q_y = 0.14$.

5.6 New Tunes

Changing Q_s to avoid the resonance is not possible due to strict requirements on the RF bucket size. Beam-beam simulations suggested a new fractional tunes of $(Q_x, Q_y) = (0.08, 0.14)$. These tunes were implemented in the ESR lattice presented in this work by varying the arc quadrupoles. Figure 5.6 shows the 80% core ϵ_b for constant $Q_s = 0.05$ and $Q_y = 0.14$, but now varying Q_x. Again, as a control, the core emittances calculated from tracking using a 1st order map corresponded well with the linear calculation.

For these new tunes, the $Q_y - Q_s - Q_x$ resonance is particularly apparent. While not shown here, the 80% core ϵ_a vs. Q_x plot shows the same trend but decreasing near $Q_x = 0.09$ instead of increasing. This lattice, however, has the same sextupole settings optimized for the original $(0.12, 0.10)$ fractional tunes; with new settings, this effect will likely be suppressed. This shows the importance

of iteratively selecting a new WP while considering all of beam-beam effects, dynamic aperture, and polarization.

5.7 Conclusions

The cause of various undesirable effects observed in the 18 GeV ESR lattice - including low asymptotic polarization, ϵ_b exceeding radiation-integral predictions, and dynamic aperture difficulties - was determined to be the $Q_y - 2Q_s$ 2nd order synchro-beta resonance, excited by vertical dispersion in decoupling quadrupoles. Because misalignments will inevitably create some vertical dispersion, and the 5 and 10 GeV ESR lattices have nonzero dispersion entering the solenoid modules where it is coupled into the vertical, this resonance must be avoided. Dispersion therefore is allowable in the solenoid modules. The short solenoid module no longer needs to be turned off, and a longitudinal spin match may be possible. When sufficiently away from this resonance, excellent polarization is observed in the 18 GeV ESR lattice with longitudinal spin matching. Finally, Monte Carlo tracking results of a new working point with fractional tunes $(Q_x, Q_y) = (0.08, 0.14)$ were shown for the same ESR lattice, where significant effects of another synchro-beta resonance $Q_y - Q_s - Q_x$ were apparent. However, with optimized sextupole settings for the new tunes, these effects are expected to be significantly suppressed.

CHAPTER 6

ESR PARTIAL LONGITUDINAL SPIN MATCH

6.1 Background

As shown in Fig. 4.5, the lack of a longitudinal spin match has severe consequences on the polarization for the 18 GeV case of the EIC-ESR. Furthermore, the eventual insertion of a vertical emittance creator in the ESR – necessary to match the electron and ion beam sizes – will have detrimental effects on polarization unless carefully implemented. Misalignments will also degrade the polarization further. Without some kind of further polarization correction, achieving the minimum polarization requirement poses a significant, if not fatal, problem.

The longitudinal spin match was originally dropped going from v5.3 to v5.6 primarily due to various undesirable nonlinear effects, including low polarization [65], that resolved when turning off the short solenoid module (thus losing the LSM) and setting the dispersion to zero in the long solenoid module. As shown in Ch. 5, hese effects were later determined to be caused by a 2^{nd} order synchrobeta resonance excited by vertical dispersion in quadrupoles - as is the case when entering a solenoid module with nonzero horizontal dispersion. By changing the tunes, the effects may be resolved; the nonlinear polarization can have excellent agreement with the analytical calculation [67]. While this finding led to a change in the working point, it also re-opened the question of whether or not a LSM should be achieved in the ESR. Unfortunately, as described in Sec. 4.5, the integrated field strengths in the solenoids required for a longitudinal spin match are simply too large to feasibly engineer. Therefore, another

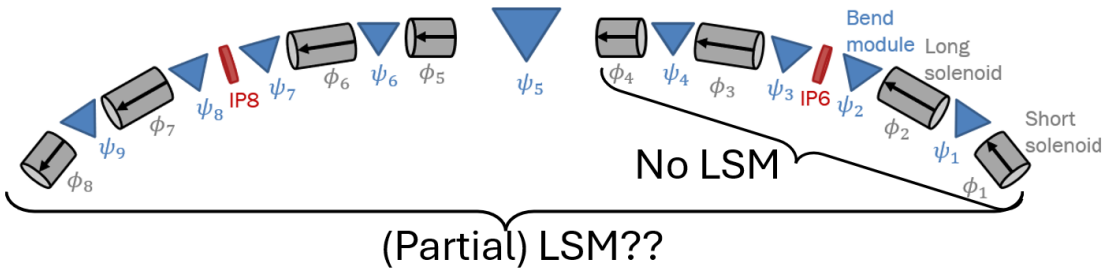

Figure 6.1: Schematic displaying the idea of a partial longitudinal spin match (LSM) using the second spin rotator.

solution must be found.

One idea to remedy this problem is to use turn on the solenoids in the second interaction region in some way such that a partial LSM is achieved, as shown in Fig. 6.1. In this chapter, an in-depth study is performed analyzing the feasibility and efficacy of such an approach.

6.2 Methods

Various Monte Carlo tracking results and polarization analyses of previous and current ESR lattices are shown. We also present the results of a vertical chicane as a vertical emittance creator, and the effects on polarization. All Monte Carlo tracking studies presented here include radiation damping and fluctuations, with radiation kicks at each bend center. *Map Tracking* uses damped maps of a user-specified order between bend centers, generated by PTC. *Bmad Tracking* uses fully nonlinear, element-by-element damped maps, and has been extensively benchmarked against PTC symplectic integration tracking.

6.3 Partial LSM and Results

While a full LSM over a single IR is not feasible, it may be possible to achieve a partial LSM around the ring; for the 1-IP case, using the solenoids in the 2nd IR we can attempt to spin match from the start of the 6 o'clock IR to the end of the last active solenoid in the 8 o'clock IR. The spin matching condition for this case looks the same as that in Eq. (4.32), but the solenoid sums are now over 8 solenoid modules and the bend sum is over 9 bend modules (including the bend between IR-6 and IR-8, ψ_5). Thus, with horizontal spin matching $H_i = 0$ for each i, and assuming a constant geometry (constant ψ_i's), the goal is to minimize g in Eq. (6.1) where ϕ_5, ϕ_8 are the IR-8 short solenoid module precession angles and ϕ_6, ϕ_7 the long solenoid module precession angles.

$$g(\phi_5, \phi_6, \phi_7, \phi_8) = \sum_{i=1}^{8\text{ sol}} \phi_i k_{0s,i} - \sum_{j=1}^{9\text{ bend}} \psi_j k_{0y,j} \ . \tag{6.1}$$

Each ϕ_i must be chosen so that $\hat{n}_0$ returns to vertical. For the v6.0, due to the bend module precession angles, in the symmetric case this leaves only $\phi_{5,8} = 0$ and $\phi_6 = \phi_7$. For the v5.6, there are three simple symmetric cases: 1) $\phi_5 = \phi_8$ and $\phi_6 = \phi_7$; 2) $\phi_5 = \phi_6$ and $\phi_7 = \phi_8$; 3) $\phi_5 = -\phi_7$ and $\phi_6 = -\phi_8$. We start with the v5.6. For each of the three cases, surfaces of $|g|$ like Fig. 6.2 may be generated. With the IR-8 solenoids all off, $|g| = \pi$. Because the choice of angles for minimum $|g|$ is not unique, the angles which minimize the length of the section we attempt to partially LSM are selected as optimal.

The same minimum value $|g_{\min}| = 2.2561$ was obtained for each case, and is dependent on the spin precession angle in the bend between IR-6 and IR-8 (ψ_5). In fact, if $\psi_5 = n\pi$, $n \in \mathbb{Z}$, then $g_{\min} = 0$ and thus a full LSM using the 2nd IR

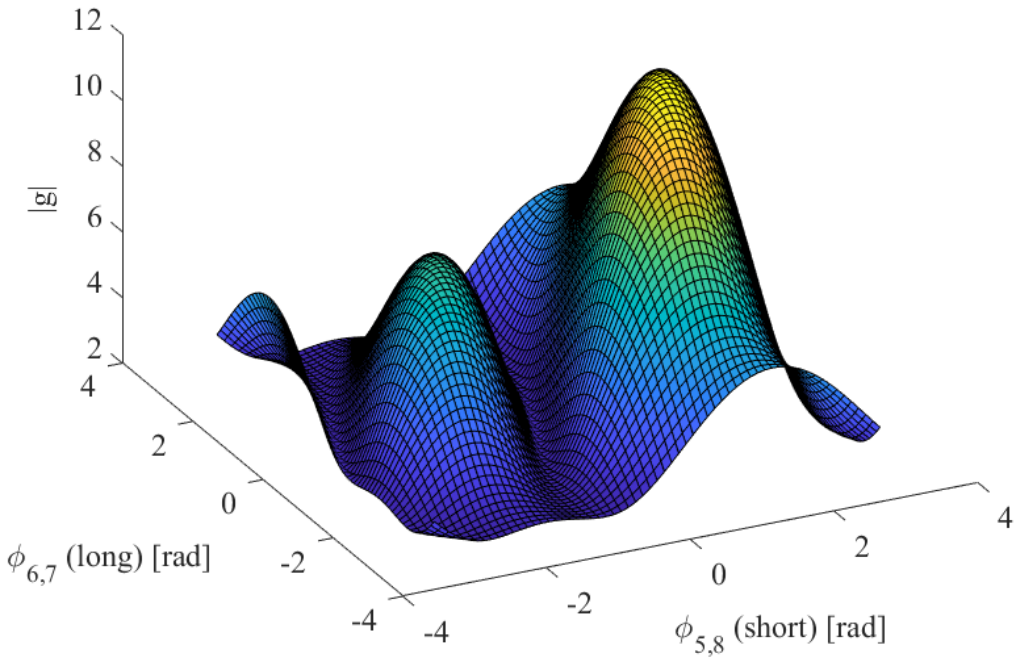

Figure 6.2: $|g(\phi_5, \phi_6)|$ with $\phi_5 = \phi_8$ and $\phi_6 = \phi_7$ (case 1) for the ESR v5.6.

is achievable. Unfortunately, this is not the case, and such geometry changes to make $\psi_5 = n\pi$ are not feasible. We determined the best scheme to be one of case 2 with $\phi_{7,8} = 0$, so that only the first set of solenoids before IP-8 are on; this achieves a partial LSM at the earliest point in the lattice. The scheme was implemented into a Bmad lattice and both optics matched and horizontally spin matched using Tao. The resulting increase in T was 0.4 min, as shown in Table 6.1. For the v6.0, which has only one valid solenoid setting ($\phi_{5,8} = 0$ and $\phi_6 = \phi_7$), $|g_{\min}| = 2.2564$. Thus, we expect the result to be similar to that for the v5.6.

For the 2-IP v5.6, where both IR-6 and IR-8 have the same solenoid settings, $|g| = 5.7858$. By flipping the polarity of the IR-8 solenoids (and thus the sign of the polarization at IP-8), $|g| = 2.45$. This simple change significantly improves T,

as shown in Table 6.1. A similar result is seen in the v6.0.

Table 6.1: Replacement Times for 18 GeV ESR Lattices

18 GeV ESR Lattices	T_+ **[min]**	T_- **[min]**	T **[min]**
v5.3 1-IP, LSM	77.8	6.9	12.6
v5.3 2-IP, LSM	29.2	6.4	10.6
v5.6 1-IP, no LSM	11.0	4.1	6.0
v5.6 1-IP, partial LSM	11.5	4.4	6.4
v5.6 2-IP, no LSM	4.0	2.5	3.1
v5.6 2-IP, flip IR-8 polarity	7.8	3.9	5.2
v6.0 1-IP, no LSM	9.8	3.8	5.5
v6.0 2-IP, no LSM	4.7	2.8	3.5
v6.0 2-IP, flip IR-8 polarity	7.5	4.0	5.2

6.4 Vertical Chicane for Vertical Emittance Creation

It is necessary to match the electron and ion beam sizes at the IP due to beam-beam effects. A scheme must be implemented in the ESR that gives $\epsilon_y \sim 0.1\epsilon_x$ while also maintaining sufficient polarization and satisfying the optics requirements. Vertical emittance can be created by photon radiation in the vertical direction, radiation in the horizontal direction in regions with vertical dispersion, and coupling the horizontal emittance into the vertical. There are many different ways to do each, or a mix, of these. One method is to insert a vertical chicane as a closed vertical dispersion bump. This was done in the v5.6 in the longest, dispersion-free drift. Four dipoles - up, down, down, up - with the same chord

length as the arc dipoles were used, and the bend angle varied so that $\epsilon_y = 0.1\epsilon_x$. The field strength necessary to achieve this ratio was $B = 0.657$ T, which is impractical. Furthermore, T dropped to 2.8 min, which is below the minimum 4.8 min. Finally, with this scheme, the emittance ratio will not be maintained at 5 GeV due to the use of superbends at that energy. Another solution must be found to safely generate vertical emittance while preserving high polarization.

6.5 Conclusions

The significance of achieving a longitudinal spin match in the ESR at 18 GeV was presented, with analytical calculations suggesting a 6.6 min difference in the average bunch replacement time. However, both the infeasibility of a LSM due to the required solenoid field strengths, as well as a 6 GeV low energy case instead of the desired 5 GeV, supports the adopting of a new ESR lattice with no possibility for a LSM. A study to achieve a partial LSM using the 2$^{\text{nd}}$ IR was also performed, but only a marginal gain in the average replacement time was observed. For the 2-IP lattice, flipping the polarity of the 2$^{\text{nd}}$ IR solenoids proved highly beneficial to polarization, and will be adopted. Finally, the use of a vertical chicane as a vertical emittance creator in the ESR was ruled out due to the necessity for spin matching, excessively high field strengths, and inability to maintain $\epsilon_y \sim 0.1\epsilon_x$ for the 5 GeV case which uses superbends.

CHAPTER 7

BEST ADJUSTMENT GROUPS FOR ELECTRON SPIN (BAGELS)

7.1 Theory

7.1.1 Initial Approach

As evident by the spin-orbit integral in Eq. (3.65), to achieve a spin match one must set $\boldsymbol{\omega}$ and/or $\boldsymbol{k}_0$ so the spin-orbit coupling cancels. Per Eq. (3.62), $\boldsymbol{k}_0$ corresponds to $\hat{\boldsymbol{n}}_0$ and the spin tune evolution around the ring (zeroth order spin precession on the closed orbit), while $\boldsymbol{\omega}$ corresponds to the first-order magnetic fields around the closed orbit (the optics) given the $\boldsymbol{k}_0$. Changes to $\boldsymbol{k}_0$ are usually viewed as challenging, as they are connected with the geometry of the ring (spin precession in the bends) and solenoid strengths. In the ESR, analytical conditions were derived using Eq. (3.65) to achieve both a horizontal and longitudinal spin match outside the spin rotator [48, 64]. The horizontal spin match is achieved by choosing the optics in each solenoid module (setting $\boldsymbol{\omega}$), while the longitudinal spin match is achieved by both having a horizontal spin match and choosing special solenoid strengths (setting $\boldsymbol{k}_0$). However, the solenoid strength necessary for such is 11 Tesla, which is obviously infeasible. The lack of a longitudinal spin match excites a significant $\boldsymbol{d}$ around the ring.

Without any other systematic method to change $\boldsymbol{k}_0$, the only way to achieve some longitudinal spin match is to "steal" from part of the horizontal spin match by changing $\boldsymbol{\omega}$. Thus, we seek a method that minimizes the leftover $\boldsymbol{d}$ by intentionally tilting $\hat{\boldsymbol{n}}_0$ near and through the rotator using vertical orbit bumps.

The corresponding changes to $\boldsymbol{k}_0$ should accumulate spin-orbit coupling which perfectly cancels that leftover by the rotator. The orbit bumps therefore should be placed in the periodic FODO arcs directly around the spin rotator, and basically have a net effect of "walking down" the spin orbit coupling function to zero on either side of the rotator. Furthermore, the bumps must have essentially no impact on the optics around the ring.

An arbitrary choice of vertical orbit bump in the periodic arc section will create both delocalized vertical dispersion and delocalized transverse coupling (caused by the skew quadrupole feed-down term from a nonzero vertical closed orbit through the sextupoles). Both of these effects must, at least to first-order in the phase space coordinates, cancel by design of the bump. First, let us consider the coupling caused by the nonzero vertical orbits through the sextupoles. Because the chromatic beta-beat oscillates with $2\times$ the betatron oscillation frequency, chromatic sextupoles that are separated by 90° in betatron phase will work against each other. Therefore, to coherently cancel the chromatic beta-beat, the sextupoles in a periodic arc are usually split into either two (for a 90° betatron phase advance per cell) or three (for a 60° betatron phase advance per cell) families per transverse plane, with each sextupole in a family separated by 180° in betatron phase. We can take advantage of the chromatic sextupoles' regular placement to construct a bump that automatically cancels its own generated coupling. Consider the case of a 90° phase advance per cell, as in the arcs of the 18 GeV EIC-ESR. If we turn on a π bump, the orbit will go through all four different strength sextupoles (two families per plane) once with a positive vertical offset. Therefore, in order to cancel this generated coupling, we need to use another π bump of opposite strength such that the orbit goes through the four sextupoles again with the same magnitude but opposite sign. There-

fore, we can place the second opposite π bump anywhere $\pi n,\ n \in \mathbb{Z}$, in betatron phase away from the first bump in order to cancel the coupling. However, if we would also like to cancel the vertical dispersion wave generated by the first, then the first corrector coil of the second π bump must be $(2n+1)\pi$ away from the last corrector coil of the first π bump. This type of vertical orbit bump, which we henceforth refer to as an "opposite π pair" shown in Fig. 7.1, has minimal impacts on the optics, creating no delocalized transverse coupling nor delocalized vertical dispersion. With bending magnets between the corrector coils, a delocalized tilt to $\hat{\boldsymbol{n}}_0$ is produced. This makes the opposite π pair ideal for spin matching by intentionally changing $\boldsymbol{k}_0$.

If the orbit excursions in the sextupoles are kept small, we can overlap all different opposite π pairs in an arc and still have the orbit close and generate no delocalized vertical dispersion nor delocalized coupling. As such, we can construct special vertical orbit bumps, each composed of a linear combination of many opposite π pairs, to minimize $\boldsymbol{d}$ in the bends where its contribution to radiative depolarization is most significant. Henceforth, we will refer to any choice of vertical orbit bump type that makes up a composite vertical orbit bump as a *basis bump*. In this case, for spin matching, the basis bump choice is the opposite π pair.

If all bends in the ring have nearly the same length and strength, then considering only $\boldsymbol{d}$ at all bends is sufficient to capture the effects of radiative depolarization. More generally, per Eq. (3.43), $\boldsymbol{d}\sqrt{L|\boldsymbol{g}|^3}$ at the ends of all bends could be considered, where $\boldsymbol{g}$ and L are respectively the bend curvature and length. For the following formulation, we will assume all the bends have the same strengths and lengths for notational simplicity. Parametrizing the strength of each se-

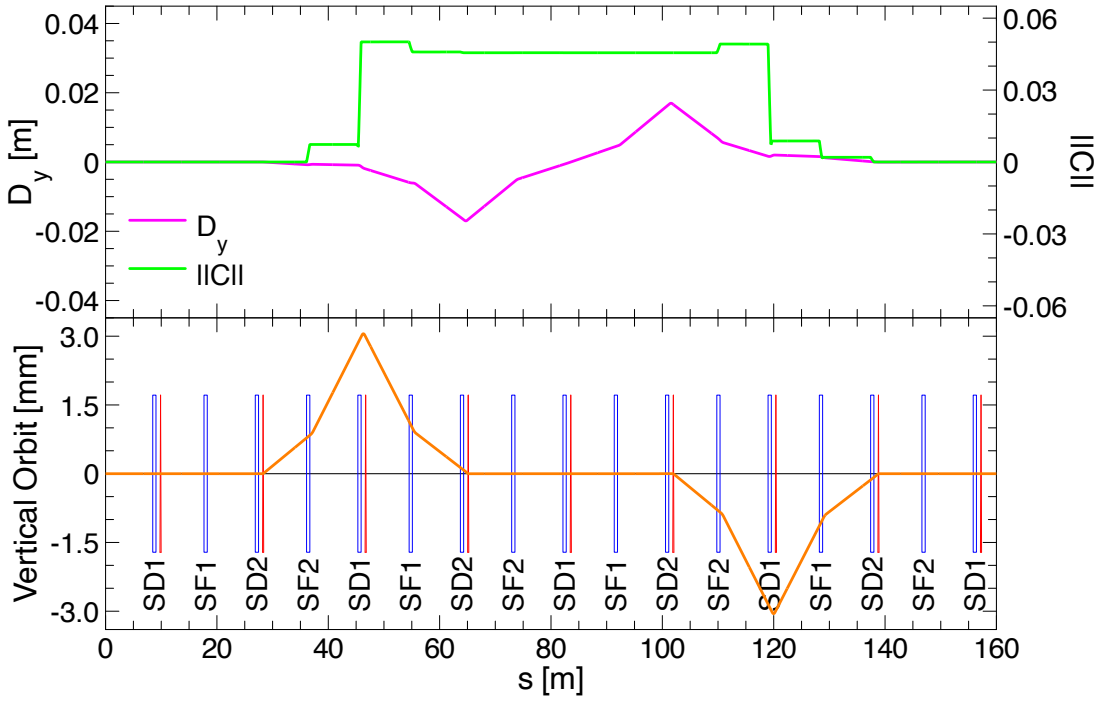

Figure 7.1: Opposite π pair placed in a periodic FODO beamline with 90° phase advance per cell and two sextupole families per plane (SF for the horizontal, SD for the vertical). Sextupoles are specified as blue rectangles, vertical corrector coils as red triangles, and the quadrupoles and bends are not shown. The bump's corresponding vertical dispersion D_y and normalized coupling matrix norm $\|\bar{C}\|$ are plotted above [56]. The opposite π pair creates only localized coupling and localized vertical dispersion, but a delocalized tilt to $\hat{\boldsymbol{n}}_0$ due to the bending magnets between the corrector coils, making it ideal for spin matching.

lected basis bump as θ_i, the values of $\boldsymbol{d}$ at r selected bends can be written as a function of c selected basis bumps, to first-order in the strengths $\boldsymbol{\theta} = (\theta_1, ..., \theta_c)^T$, as

$$\boldsymbol{f_d} \approx (\boldsymbol{f_d})_0 + \mathsf{R}_d \boldsymbol{\theta} \,, \tag{7.1}$$

$$\boldsymbol{f_d} = \begin{pmatrix} \boldsymbol{d}_1 \\ \vdots \\ \boldsymbol{d}_r \end{pmatrix}, \; \mathsf{R}_{\boldsymbol{d}} = \begin{pmatrix} \frac{\partial \boldsymbol{d}_1}{\partial \theta_1} & \cdots & \frac{\partial \boldsymbol{d}_1}{\partial \theta_c} \\ \vdots & \ddots & \vdots \\ \frac{\partial \boldsymbol{d}_r}{\partial \theta_1} & \cdots & \frac{\partial \boldsymbol{d}_r}{\partial \theta_c} \end{pmatrix}_{\mathbf{0}} , \tag{7.2}$$

where $\mathsf{R}_{\boldsymbol{d}}$ is the response matrix of $\boldsymbol{d}$ for each basis bump. Any arbitrary $\boldsymbol{\theta}$ defines a composite vertical closed orbit bump - a linear combination of the basis bumps - that can be scaled up and down using a knob in the control room of the real accelerator. We seek a $\boldsymbol{\theta}$ that sets the LHS of Eq. (7.1) closest to zero. Almost always, $3r > c$, and for this overdetermined system we can use any modern linear algebra software package to calculate a least-squares solution that minimizes $||\mathsf{R}_{\boldsymbol{d}}\boldsymbol{\theta} + (\boldsymbol{f_d})_0||^2$. However, the problem with this approach is that the least-squares solution will have too large strengths for the basis bumps that have little impacts on $\boldsymbol{d}$ in the bends, exceeding the linear response regime and creating large orbit excursions. Naively, one could just iteratively exclude basis bumps that have the smallest columns in $\mathsf{R}_{\boldsymbol{d}}$. However, this approach is not general, as it is entirely possible, and in fact likely, that basis bumps that have large impacts alone may have little impact when paired together in a linear combination, and vice-versa. We thus require a systematic way to reduce our space to a minimal number k of special $\boldsymbol{\theta}$'s that maximally scale when multiplied by $\mathsf{R}_{\boldsymbol{d}}$. Specifically, we seek

$$\underset{\boldsymbol{\theta}_1,...,\boldsymbol{\theta}_k}{\operatorname{argmax}} \frac{||\mathsf{R}_{\boldsymbol{d}}\boldsymbol{\theta}||^2}{||\boldsymbol{\theta}||^2} = \underset{\boldsymbol{\theta}_1,...,\boldsymbol{\theta}_k}{\operatorname{argmax}} \frac{\boldsymbol{\theta}^T \mathsf{A} \boldsymbol{\theta}}{\boldsymbol{\theta}^T \boldsymbol{\theta}} , \tag{7.3}$$

where $\mathsf{A} = \mathsf{R}_{\boldsymbol{d}}^T \mathsf{R}_{\boldsymbol{d}}$ and $\boldsymbol{\theta}_1, ..., \boldsymbol{\theta}_k$ are all orthogonal to each other. These correspond to composite vertical orbit bumps which we can use to maximally, and orthogonally, impact the spin-orbit coupling function in the bends. Readers may recognize this well-known dimensionality reduction technique as princi-

pal component analysis (PCA). The quotient in Eq. (7.3) is called the *Rayleigh quotient* of A and $\boldsymbol{\theta}$, and we seek its maximizers. We follow the approach in [35]. It is obvious that we can express this problem equivalently as maximizing $\boldsymbol{\theta}^T \mathsf{A} \boldsymbol{\theta}$ subject to the constraint $\boldsymbol{\theta}^T \boldsymbol{\theta} = 1$. Using the method of Lagrangian multipliers, the Lagrangian is

$$\mathcal{L} = \boldsymbol{\theta}^T \mathsf{A} \boldsymbol{\theta} + \lambda \left(\boldsymbol{\theta}^T \boldsymbol{\theta} - 1 \right) . \tag{7.4}$$

The stationary points of the Lagrangian are calculated as the solutions to

$$\frac{\partial \mathcal{L}}{\partial \boldsymbol{\theta}} = 2\mathsf{A}\boldsymbol{\theta} - 2\lambda\boldsymbol{\theta} = 0 \;\rightarrow\; \mathsf{A}\boldsymbol{\theta} = \lambda\boldsymbol{\theta} , \tag{7.5}$$

where we use the fact that, because the covariance matrix A is symmetric, $\partial_{\boldsymbol{\theta}}(\boldsymbol{\theta}^T \mathsf{A} \boldsymbol{\theta}) = 2\mathsf{A}\boldsymbol{\theta}$. Also, because $\boldsymbol{\theta}^T \mathsf{A} \boldsymbol{\theta} = \|\mathsf{R}_{\boldsymbol{d}} \boldsymbol{\theta}\|^2 \geq 0$ for all $\boldsymbol{\theta}$ (A is *positive semidefinite* by construction), all eigenvalues of A will be non-negative. Thus, the maximizers will be those eigenvectors $\boldsymbol{v}_i$ of A with the largest eigenvalues. These are the special linear combinations, or groups, of basis bumps that we can use to minimize the radiative depolarization in the real accelerator. In our reduced space of only k knobs, we rewrite the least-squares problem as

$$\begin{aligned} -(\boldsymbol{f_d})_0 &= \mathsf{R}_{\boldsymbol{d}}(w_1 \boldsymbol{v}_1 + ... + w_k \boldsymbol{v}_k) \\ \rightarrow\; -(\boldsymbol{f_d})_0 &= \tilde{\mathsf{R}}_{\boldsymbol{d}} \boldsymbol{w} , \end{aligned} \tag{7.6}$$

where $\tilde{\mathsf{R}}_{\boldsymbol{d}} = \mathsf{R}_{\boldsymbol{d}} \begin{pmatrix} \boldsymbol{v}_1 & \dots & \boldsymbol{v}_k \end{pmatrix}$ and $\boldsymbol{w} = (w_1, ..., w_k)^T$. In the ideal lattice, all we need to do now is calculate the least-squares solution to Eq. (7.6) to obtain the strengths for each of the composite bumps that minimize $\boldsymbol{d}$ in the bends. In the

real ring where random closed orbit distortions will degrade the spin match, we could just vary the strengths of these k bumps until the polarization is re-maximized.

7.1.2 Improving and Generalizing the Method

By doing a principal component analysis over the space of selected opposite π pairs in the ring, we thus far have a method to construct a minimal number of groups of basis bumps that have a *maximal* impact on the spin-orbit coupling. However, at the same time we would also like the groups to have a *minimal* impact on the orbit excursions, which the initial approach does not account for directly. Letting R_A specify the responses of the quantities we wish to maximally affect, and R_B specify the responses of those quantities we wish to minimally affect, we seek

$$\underset{\boldsymbol{\theta}_1,\ldots,\boldsymbol{\theta}_k}{\operatorname{argmax}} \frac{\|\mathsf{R}_A\boldsymbol{\theta}\|^2}{\|\mathsf{R}_B\boldsymbol{\theta}\|^2} = \underset{\boldsymbol{\theta}_1,\ldots,\boldsymbol{\theta}_k}{\operatorname{argmax}} \frac{\boldsymbol{\theta}^T\mathsf{A}\boldsymbol{\theta}}{\boldsymbol{\theta}^T\mathsf{B}\boldsymbol{\theta}} , \tag{7.7}$$

where $\mathsf{A} = \mathsf{R}_A^T\mathsf{R}_A$ and $\mathsf{B} = \mathsf{R}_B^T\mathsf{R}_B$. In this case, we would let $\mathsf{R}_A = \mathsf{R}_d$ to maximally affect the spin-orbit coupling function at the bends, and $\mathsf{R}_B = \mathsf{R}_y$, where R_y is the response matrix of the vertical closed orbit at many positions around the ring, to minimally affect the closed orbit.

The quotient in Eq. (7.7) is called the *generalized Rayleigh quotient* of A, B, and $\boldsymbol{\theta}$, and we seek its maximizers. We once again follow the approach in [35]. Assuming that B is symmetric and *positive definite* such that $\boldsymbol{\theta}^T\mathsf{B}\boldsymbol{\theta} = \|\mathsf{R}_B\boldsymbol{\theta}\|^2 > 0$ for all $\boldsymbol{\theta}$, we can perform a Cholesky decomposition so that $\mathsf{B} = \mathsf{L}\mathsf{L}^T$. We then

can rewrite the generalized Rayleigh quotient in Eq. (7.7) as

$$\frac{\boldsymbol{\theta}^T \mathsf{A} \boldsymbol{\theta}}{(\boldsymbol{\theta}^T \mathsf{L})(\mathsf{L}^T \boldsymbol{\theta})} = \frac{\tilde{\boldsymbol{\theta}}^T \mathsf{L}^{-1} \mathsf{A} \mathsf{L}^{-T} \tilde{\boldsymbol{\theta}}}{\tilde{\boldsymbol{\theta}}^T \tilde{\boldsymbol{\theta}}} \ , \ \ \tilde{\boldsymbol{\theta}} = \mathsf{L}^T \boldsymbol{\theta} \ . \tag{7.8}$$

To calculate those $\tilde{\boldsymbol{\theta}}$ that maximize Eq. (7.8), the same Lagrangian as in Eq. (7.4) is obtained except with $\boldsymbol{\theta} \to \tilde{\boldsymbol{\theta}}$. Expressing this in terms of $\boldsymbol{\theta}$, we have

$$\mathcal{L} = \boldsymbol{\theta}^T \mathsf{A} \boldsymbol{\theta} + \lambda \left(\boldsymbol{\theta}^T \mathsf{B} \boldsymbol{\theta} - 1 \right) \ . \tag{7.9}$$

Therefore, the problem of Eq. (7.7) is equivalently expressed as finding the maximizers of $\boldsymbol{\theta}^T \mathsf{A} \boldsymbol{\theta}$ subject to the constraint $\boldsymbol{\theta}^T \mathsf{B} \boldsymbol{\theta} = 1$. The stationary points of the Lagrangian are calculated as the solutions to

$$\frac{\partial \mathcal{L}}{\partial \boldsymbol{\theta}} = 2\mathsf{A}\boldsymbol{\theta} - 2\lambda \mathsf{B}\boldsymbol{\theta} = 0 \ \to \ \mathsf{A}\boldsymbol{\theta} = \lambda \mathsf{B}\boldsymbol{\theta} \ . \tag{7.10}$$

In this case, the generalized eigenvectors of A and B with largest eigenvalues define groups of basis bumps that have a *maximal* impact on the spin-orbit coupling, a *minimal* impact on the orbit, and, by choice of the basis bumps, have no delocalized transverse coupling nor delocalized vertical dispersion. For spin matching purposes, these groups are truly the "Best Adjustment Groups for ELectron Spin" (BAGELS). We can use these BAGELS bumps to both optimally spin match the ideal ring via Eq. (7.6), and to optimally fix the spin match degradation caused by random closed orbit distortions in the real accelerator, by turning knobs that control these bumps in the control room. Being a more direct approach that also ensures minimal orbit excursions and no delocalized transverse coupling nor delocalized vertical dispersion, BAGELS effectively makes

harmonic closed orbit spin matching obsolete for correcting polarization in operation.

When calculating the generalized eigenvectors on a computer, floating point roundoff errors caused by the potentially vastly different scales of R_A and R_B (e.g. the closed orbit responses being orders of magnitude smaller than the spin-orbit coupling responses) may affect the numerical solution. Therefore, in practice, the two matrices should be normalized to minimize this error. We use the matrix 2-norm so that $\bar{\mathsf{R}}_A = \mathsf{R}_A/||\mathsf{R}_A||$ and likewise for R_B. We then let $\mathsf{A} = \bar{\mathsf{R}}_A^T\bar{\mathsf{R}}_A$ and likewise for B.

In this generalized approach, the positive definiteness of B is required in order to obtain a solution. This is apparent by the fact that if B is only positive semidefinite and not positive definite, then an attempt at inversion/Cholesky decomposition of B to solve for the generalized eigenvectors in Eq. (7.10) will fail. In order to ensure $\boldsymbol{\theta}^T\mathsf{B}\boldsymbol{\theta} = ||\bar{\mathsf{R}}_B\boldsymbol{\theta}||^2 > 0$ for all $\boldsymbol{\theta}$, all selected basis bumps must be orthogonal to each other - that is, no single selected basis bump should expressable as a linear combination of the other selected basis bumps. To construct an orthogonal basis for the opposite π pair basis bump, we sequentially choose as our basis bumps all opposite π pairs with a separation of only π in betatron phase advance between each of the bumps in a pair. With this choice, those opposite π pairs with separation $(2n+1)\pi,\ n \neq 1$ can be constructed as a linear combination of our orthogonal basis bumps.

While we have thus far shown how BAGELS is used to calculate the best vertical orbit bumps for spin matching purposes, the method is not limited to spin matching. BAGELS can also be applied in applications where a *minimal* impact on polarization is desired, amongst other things; suppose we in-

stead would like to calculate bumps that maximally change some other quantity x around the ring, but minimally impact both the spin-orbit coupling and the closed orbit excursions. To calculate such bumps, we can combine the responses of the spin-orbit coupling function and the orbit excursions into the response matrix $\bar{\mathsf{R}}_B$ (properly normalized), let $\bar{\mathsf{R}}_A = \mathsf{R}_x/\|\mathsf{R}_x\|$, and then choose those eigenvectors with the largest eigenvalues. This approach is used to calculate "polarization-safe" bumps to optimally correct global coupling in Sec. 7.3.2, and "polarization-safe" vertical emittance creation bumps for beam size matching in Sec. 7.3.3. Finally, while it is not explored in this paper, the basis vectors of the "groups" do not need to be vertical orbit bumps, but could instead be single corrector coil strengths, or some other magnet strengths, for example. The only requirement is that a sufficiently linear relationship exists between the input and output, and that the input forms an orthogonal basis. With such generality, BAGELS allows for computation of the "Best Adjustment Groups for ELectron Spin" in any application.

In summary, to apply BAGELS:

1. **Choose the basis bumps/vectors:** The choice of basis vectors should be guided by the goal. For spin matching, every orthogonal opposite π pair, which creates neither delocalized vertical dispersion nor delocalized coupling, is ideal. In Sec. 7.3.2 and Sec. 7.3.3 we define two different types of useful basis vectors for different applications.
2. **Construct the response matrices:** All quantities in consideration must have a sufficiently linear relationship with the basis vectors. When combining the response matrices of multiple quantities into either R_A or R_B, each submatrix may also be normalized to weigh the treatment of the dif-

ferent responses.

3. **Calculate the generalized eigenvectors of the covariance matrices to obtain the Best Adjustment Groups for ELectron Spin:** The best groups will be those eigenvectors with the largest eigenvalues for maximal/minimal impact on polarization.

7.2 Methods

When performing BAGELS, the analytical approximation for $\boldsymbol{d}$ described in Sec. 3.9 is used. Then for verification, nonlinear Monte Carlo tracking is performed. Here we track through 3$^{\text{rd}}$ order damped maps expanded around the closed orbit generated by the Polymorphic Tracking Code (PTC) [33], between the centers of every bend in the lattice. At the bend centers, stochastic kicks simulating the effects of photon emission are applied to each particle. While the damped maps are not symplectic due to the map truncation, we expect the symplectic error to be minimal because there are separate maps used between every bend center in the ring. All tracking points include a bunch of at least 1000 particles, initialized to have the linear equilibrium emittances in each plane. After tracking for approximately four damping times at least, so the beam is in nonlinear radiative equilibrium (2000 turns for the 18 GeV EIC-ESR), the nonlinear τ_{dep} is calculated from the following approximately 10 damping times (the next 5000 turns).

The Bmad accelerator software toolkit is used both for the analytical polarization calculations and the nonlinear tracking (as an interface to PTC) in this paper [52]. Routines to perform BAGELS were implemented in an open source

Julia interface to Bmad's general purpose Tao program [60].

7.3 Results: EIC-ESR

7.3.1 Spin Match the Ideal Ring

1-IP 18 GeV EIC-ESR

To apply BAGELS in the ideal 1-IP 18 GeV EIC-ESR, we use an orthogonal basis consisting of opposite π pairs in the four arcs surrounding the spin rotator, two on either side. With radiation damping turned off, we calculate for each basis bump the responses of $\boldsymbol{d}\sqrt{L|\boldsymbol{g}|^3}$ at the ends of each bend (which we aim to maximize), as well as the vertical orbit y at many positions around the ring (which we aim to minimize). Specifically, we sampled the ends of every lattice element (all drifts, quadrupoles, sextupoles, bends, solenoids) for y. Henceforth for notational brevity, $\mathsf{R}_{\boldsymbol{d}}$ denotes the response matrix of $\boldsymbol{d}\sqrt{L|\boldsymbol{g}|^3}$ at all bends. We compute the top four maximizers of Eq. (7.7), and use them as our knobs to achieve a spin match. Finally, in this reduced space of only four knobs, we solve Eq. (7.6) for the least-squares solution to obtain the strengths of the four knobs in the ideal lattice. The before-and-after result is shown in Fig. 7.2, with the interaction point at $s = 0$ m.

The radiation damping will cause a "sawtooth" closed orbit, which must be corrected. Because we use the 1-IP ESR lattice for the random error studies in Sec. 7.3.2, we use the proposed orbit correction scheme for the ring at the time of paper writing to correct the sawtooth closed orbit. This consists of dual plane

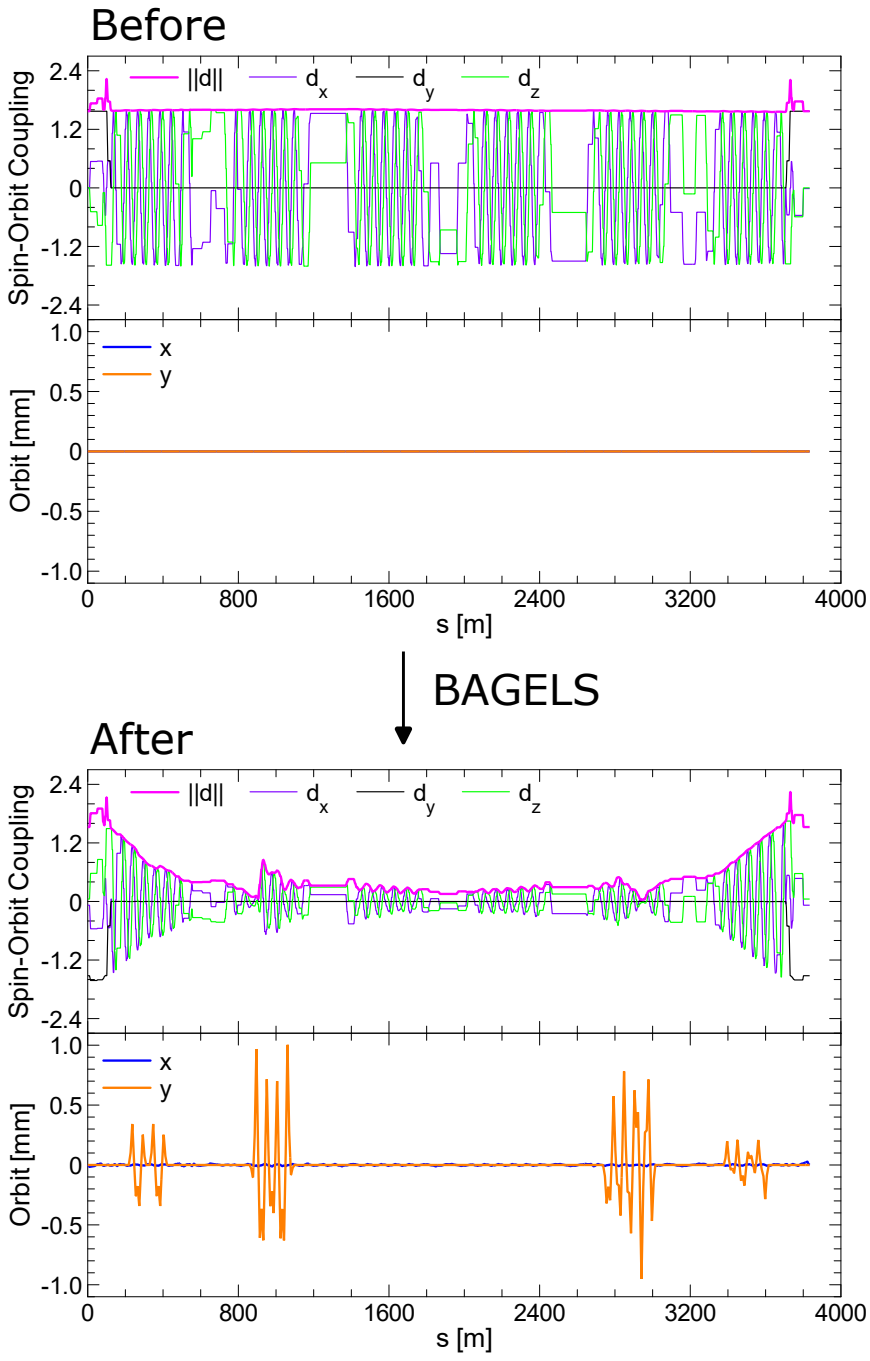

Figure 7.2: The spin-orbit coupling function $\boldsymbol{d}$ and closed orbit in the ideal 1-IP 18 GeV EIC-ESR before (top) and after (bottom) applying BAGELS, using only four BAGELS vertical orbit bumps. The interaction point at the center of the spin rotator shown in Fig. 4.1 is located at $s = 0$ m.

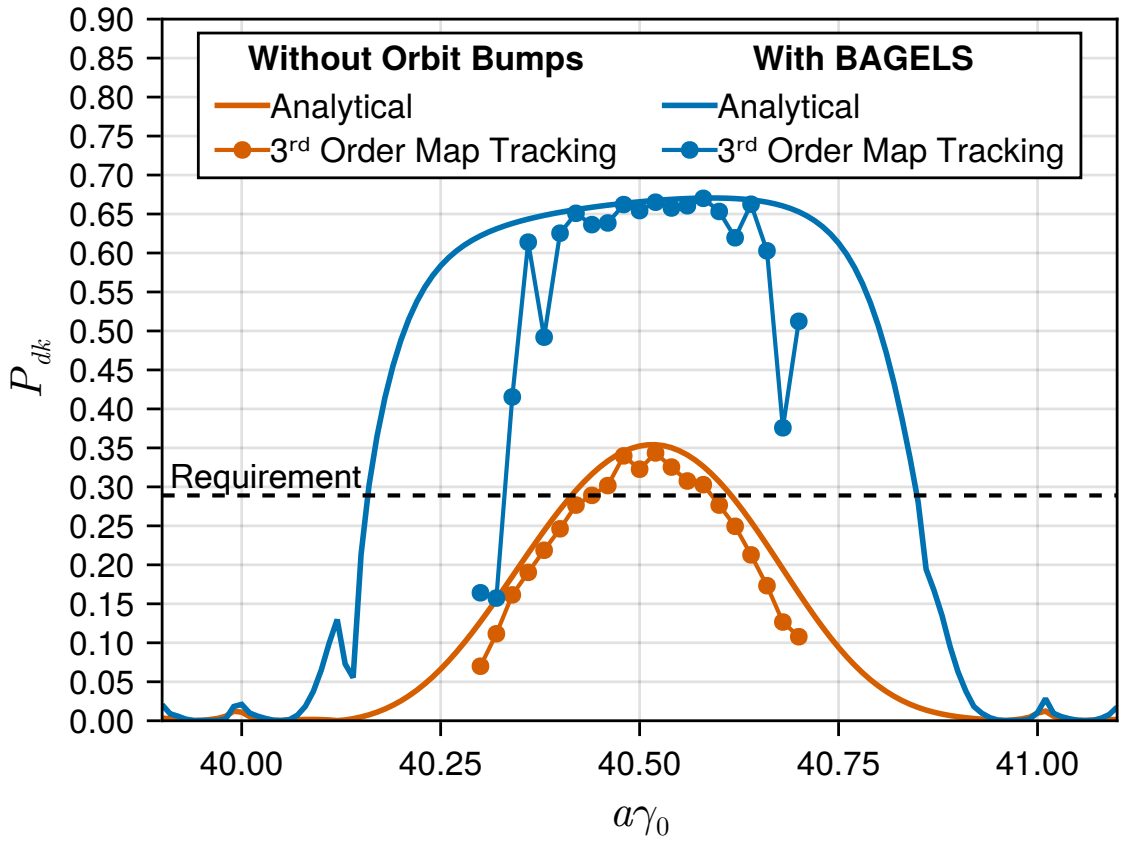

Figure 7.3: An energy scan of the asymptotic polarization in the ideal 1-IP 18 GeV EIC-ESR, both before and after applying BAGELS. Using only four BAGELS vertical orbit bumps, the asymptotic polarization is nearly doubled in nonlinear tracking.

BPMs and vertical corrector coils at each vertically-focusing quadrupole outside of the interaction region, and horizontal corrector coils at each horizontally-focusing quadrupole outside of the interaction region. In the interaction region, dual plane BPMs and dual plane correctors are used at each quadrupole. The RMS closed orbit was then minimized using the *Tao* program in the *Bmad* ecosystem.

Figure 7.3 shows an energy scan of P_{dk} of the 1-IP ESR before and after applying BAGELS. Note that polarized bunches will be injected into the ESR, and

then replaced once sufficiently depolarized. The "Requirement" line shows the minimum allowable P_{dk} in order to ensure a time-averaged polarization of 70% is maintained. Using only four BAGELS bumps, which create a maximum orbit excursion of ≈ 1 mm, we nearly double the asymptotic polarization.

We could have alternatively used only two of the arcs surrounding the IP instead of four, and similarly achieved a good solution. However, the orbit excursions must grow larger in order to solve Eq. (7.6) for the least-squares solution, whereas with four arcs the orbit excursions are minimal.

We remark that because this is the ideal ring (no random closed orbit distortions causing any tilts to $\hat{\boldsymbol{n}}_0$), the "Without Orbit Bumps" case in Fig. 7.3 has a *full harmonic closed orbit spin match already*. HCOSM therefore cannot improve this case, even though it is clearly suboptimal. This result shows that, for the general case where the spin rotator may not have a full strong synchrobeta spin match, as in the EIC-ESR, tilts to $\hat{\boldsymbol{n}}_0$ can actually be hugely beneficial, and that BAGELS can be used to directly find the optimal solution, while HCOSM would lead away from the optimal solution.

2-IP 18 GeV EIC-ESR

In the 2-IP ESR, both interaction points including spin rotators are separated by one periodic arc section. To spin match this lattice, we use an orthogonal basis consisting of opposite π pairs in the four arcs surrounding both spin rotators, i.e. two arcs upstream of the first spin rotator and two arcs downstream the second spin rotator. Once again applying BAGELS, with radiation damping turned off we calculate the responses of $\boldsymbol{d}\sqrt{L|\boldsymbol{g}|^3}$ at the ends of each bend and

of the vertical orbit y at the ends of each element. We compute the top four maximizers of Eq. (7.7), and use them to solve for a least-squares solution to Eq. (7.6). Figure 7.4 shows the spin-orbit coupling function and closed orbit after applying BAGELS to the ideal 2-IP 18 GeV ESR.

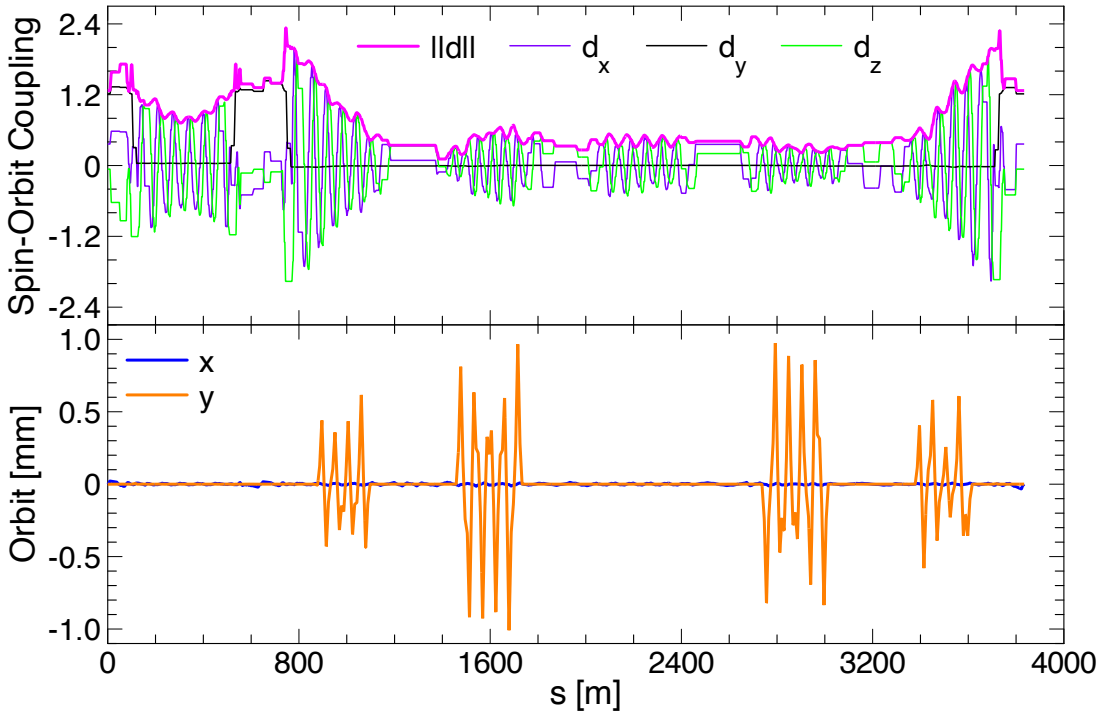

Figure 7.4: The spin-orbit coupling function $\boldsymbol{d}$ and closed orbit in the ideal 2-IP 18 GeV EIC-ESR before after applying BAGELS, using only four BAGELS vertical orbit bumps. The IPs at the center of the spin rotators (each shown in Fig. 4.1) are located at $s = 0$ m and $s = 640.758$ m.

Unlike the 1-IP lattice in this manuscript, to correct the sawtooth closed orbit caused by radiation damping in the 2-IP lattice we use the `taper` command in the *Tao* program; this command provides a quick-and-dirty solution by varying all magnet strengths in the ring proportionally to the local closed orbit momentum deviation. In reality, however, the ESR will not use tapering to correct the sawtooth. To ensure accuracy, we compared using `taper` vs. a proper orbit

correction in the 1-IP lattice, and did not observe a significant difference in the tracking results.

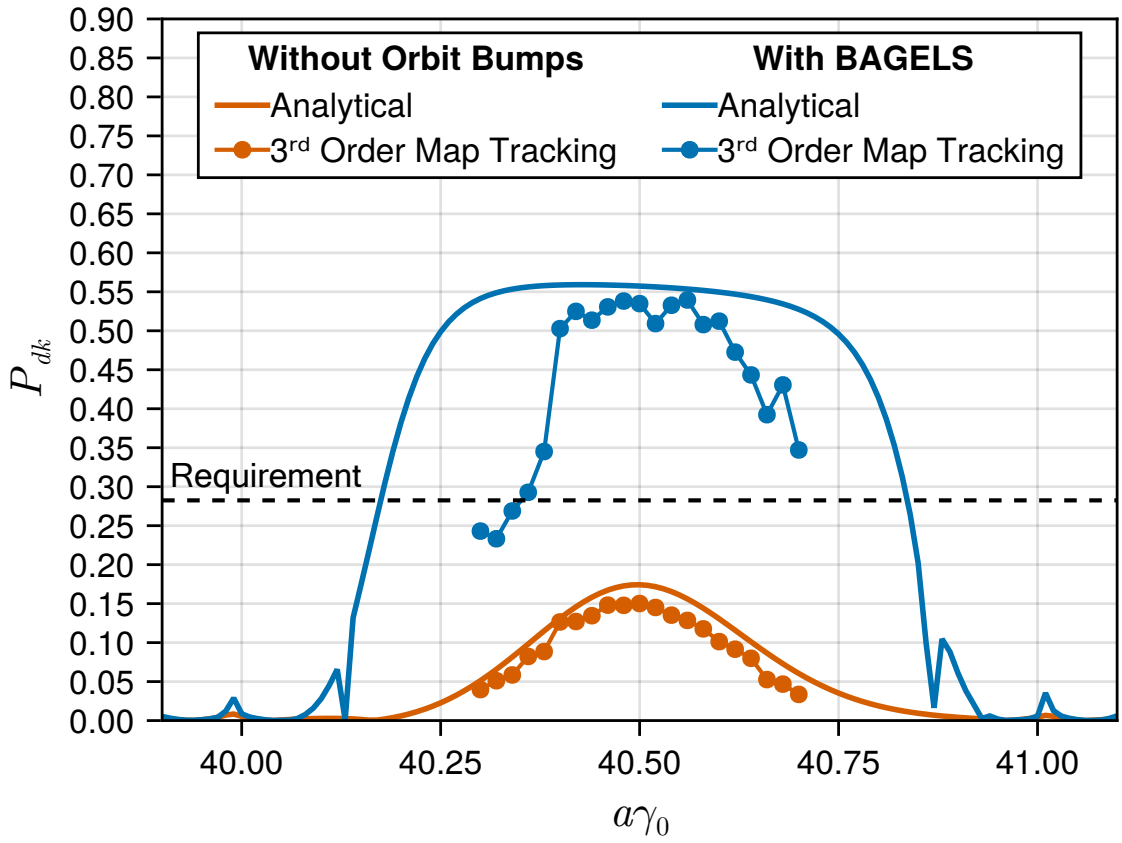

Figure 7.5: An energy scan of the asymptotic polarization in the ideal 2-IP 18 GeV EIC-ESR, both before and after applying BAGELS. Using only four BAGELS vertical orbit bumps, the asymptotic polarization is more than tripled in nonlinear tracking.

Figure 7.5 shows an energy scan of P_{dk} of the 2-IP ESR before and after applying BAGELS. Using only four BAGELS bumps, which create a maximum orbit excursion of $\approx$ 1 mm, we more than triple the asymptotic polarization. Before BAGELS, the 2-IP 18 GeV ESR does not provide the sufficient time-averaged polarization at the interaction points [63]. After application of BAGELS, the polarization requirements are exceeded.

7.3.2 Random Errors and Global Coupling Correction

In the real ring, the BAGELS spin matching knobs can be used to optimally restore the spin match degradation caused by random closed orbit distortions. However before this is done, the global, delocalized transverse coupling caused by the random errors must be corrected. One way to do so is by using vertical orbit bumps through the sextupoles to create coupling that cancels out the coupling caused by the random errors. By applying BAGELS, we can compute a minimal number of such bumps which maximally, and orthogonally, impact the coupling, while minimally impacting the spin-orbit coupling function and creating minimal orbit excursions.

We use the coupling formalism defined in [56]. The 1-turn transverse transport matrix is decomposed as

$$\mathsf{M}_{4\times4} = \mathsf{G}^{-1}\bar{\mathsf{V}}\bar{\mathsf{U}}\bar{\mathsf{V}}^{-1}\mathsf{G}\,, \tag{7.11}$$

$$\mathsf{G} = \begin{pmatrix} \mathsf{G}_a & 0 \\ 0 & \mathsf{G}_b \end{pmatrix},\ \bar{\mathsf{V}} = \begin{pmatrix} \chi 1 & \bar{\mathsf{C}} \\ -\bar{\mathsf{C}}^{+} & \chi 1 \end{pmatrix},\ \bar{\mathsf{U}} = \begin{pmatrix} \bar{\mathsf{U}}_a & 0 \\ 0 & \bar{\mathsf{U}}_b \end{pmatrix},$$

where G is a linear normalizing transformation (i.e. G_a and G_b are Courant-Snyder transformations up to a rotation of the "a" and "b" modes), $\bar{\mathsf{V}}$ is a symplectic matrix that defines the amount of coupling between the transverse planes (where the + denotes the symplectic conjugate), and $\bar{\mathsf{U}}$ is an uncoupled rotation. In order to ensure the symplecticity of $\bar{\mathsf{V}}$, we demand $\chi^2 + \det(\bar{\mathsf{C}}) = 1$. If there is no transverse coupling, then $\chi = 1$, $\bar{\mathsf{C}} = 0$, and the "a" mode corresponds to the horizontal and the "b" mode the vertical. The matrix $\bar{\mathsf{C}}$ is referred to as

the *normalized coupling matrix*, and provides a good measure of the coupling at a point in the ring.

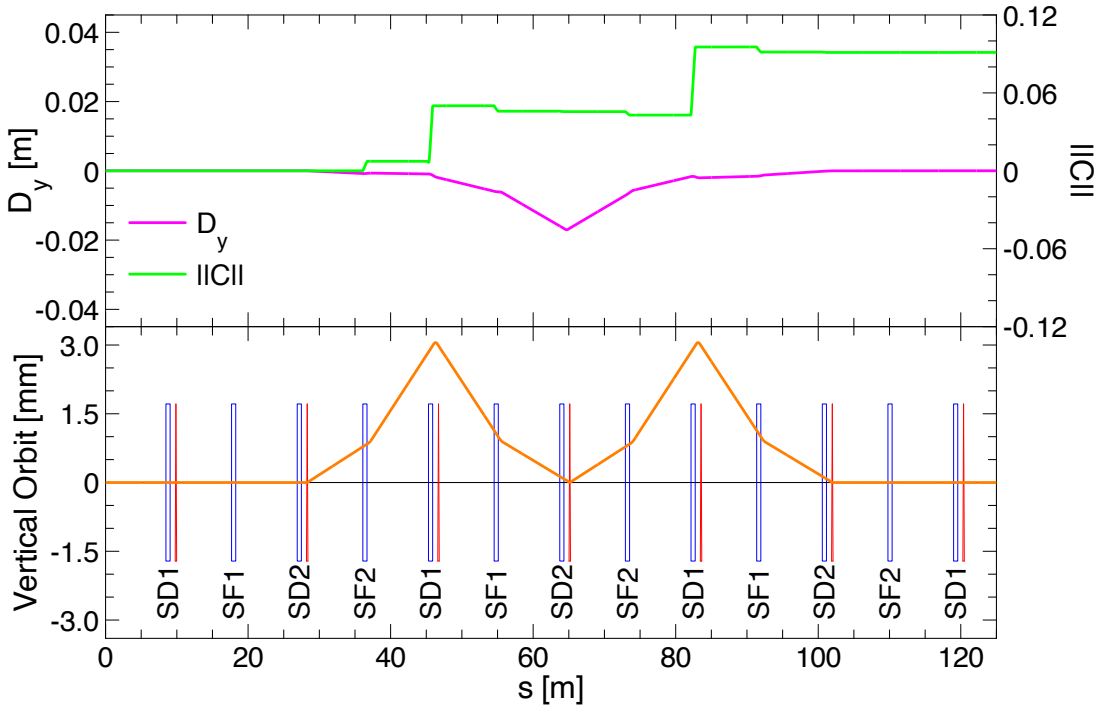

Figure 7.6: Equal π pair placed in a periodic FODO beamline with 90° phase advance per cell and two sextupole families per plane (SF for the horizontal, SD for the vertical). Sextupoles are specified as blue rectangles, vertical corrector coils as red triangles, and the quadrupoles and bends are not shown. The bump's corresponding vertical dispersion D_y and normalized coupling matrix norm $||\bar{C}||$ are plotted above [56]. The equal π pair creates delocalized transverse coupling but localized vertical dispersion.

We apply BAGELS seeking groups that maximally impact the normalized coupling matrix components $\bar{C} = (\bar{C}_{11}, \bar{C}_{12}, \bar{C}_{21}, \bar{C}_{22})^T$ at each element in the ring, while minimally impacting both the spin-orbit coupling function at the bends and the orbit excursions at all elements. Following the recipe at the end of

Sec. 7.1.2, we first must choose a basis bump. Ideally, we choose a bump that generates delocalized transverse coupling, but no delocalized vertical dispersion. Taking advantage of the periodic layout of the sextupole families in the arcs, two equivalent π bumps directly next to each other, as shown in Fig. 7.6, is exactly such a basis bump. By sequentially choosing each equal π pair in each arc, we obtain an orthogonal basis about which to construct our BAGELS global coupling correction knobs.

Next, we must construct the response matrices. Following the notation in Eq. (7.7), we use

$$\mathsf{R}_A = \mathsf{R}_{\bar{C}},\ \mathsf{R}_B = \begin{pmatrix} \mathsf{R}_d/||\mathsf{R}_d|| \\ \mathsf{R}_y/||\mathsf{R}_y|| \end{pmatrix} \tag{7.12}$$

to calculate bumps that maximally impact the coupling matrix components but minimally impact both the orbit and the spin-orbit coupling function. Here, the submatrix normalizations serve an important purpose. The different responses may be multiplied by any arbitrary scalars to give a greater/lesser weight to those responses in the eigenvector calculation. To ensure equal treatment of all responses, we choose to normalize each submatrix by its 2-norm. This is now in addition to minimizing the floating point roundoff errors caused by the potentially vastly different scales.

Finally, we compute the generalized eigenvectors and obtain the BAGELS bumps for global coupling correction via vertical orbits through the sextupoles. We chose only the top four BAGELS bumps for optimal, polarization-safe coupling correction. Knobs that control these bumps could be varied freely to correct the coupling, with minimal impacts on both the polarization and the closed

orbit. BAGELS allows for the decoupling (no pun intended) of global coupling compensation and the polarization.

To test the efficacy of both the four BAGELS global coupling correction knobs and the four BAGELS spin matching knobs including random closed orbit distortions, we generated 10 1-IP ESR lattices with different error seeds using the RMS errors shown in Table 7.1.

Table 7.1: RMS Errors used in the Random Errors Study

RMS Error	x [mm]	y [mm]	Roll [mrad]	$\Delta B/B$ [%]
Dipoles	0.2	0.2	0.5	0.1
Quadrupoles	0.2	0.2	0.5	0.1
Sextupoles	0.2	0.2	0.5	0.2
High-β Dipoles	0.2	0.2	0.5	0.05
Final Focus Quads	0.1	0.1	0.5	0.05

After first minimizing the RMS orbit for each seed using the orbit correction scheme outlined in Sec. 7.3.1, we varied the four BAGELS global coupling correction knobs until the RMS normalized coupling matrix components at each BPM were minimized. Then after resetting the tunes of the ring to their design values using the arc quadrupoles, the four BAGELS spin matching knobs were varied until the polarization was maximized. Figure 7.7 shows the upper and lower bounds of the vertical orbits for the 10 seeds after the full correction.

One good measure of the transverse coupling around the ring is the "vertical-like" equilibrium eigenemittance ϵ_b, as calculated in [75]; if the transverse coupling has been sufficiently corrected, then ϵ_b should be restored to a value much smaller than the horizontal-like emittance. Therefore, to measure

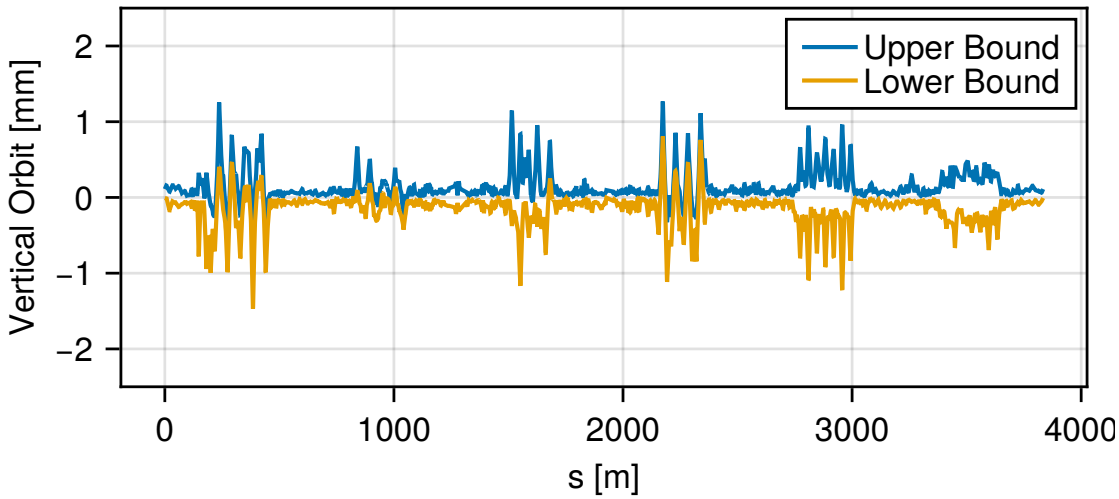

Figure 7.7: Upper and lower bounds of the vertical closed orbit across 10 error seeds of the 1-IP 18 GeV EIC-ESR after orbit correction, coupling correction using four BAGELS global coupling correction bumps, and spin match restoration using four BAGELS spin matching bumps. The IP is located at s = 1277.948 m.

the efficacy of the BAGELS transverse coupling correction knobs, we use the vertical-like eigenemittance ϵ_b as our figure-of-merit. In all cases, the analytical (first-order) ϵ_b was reduced to < 0.61 nm. The analytical (first-order) P_{dk} for all errors seeds was $\geq 55\%$, with the average analytical P_{dk} amongst all 10 seeds equal to 62.7%.

We now describe the results of nonlinear tracking for each seed. Figure 7.8 shows an energy scan of the resulting asymptotic polarizations and mean $\epsilon_{b,RMS}$ obtained from 3$^{\text{rd}}$ order map tracking for each seed. For all 10 error seeds, the polarization requirements for the 1-IP ESR are well exceeded. For two of the error seeds, linear coupling correction does not result in a sufficient reduction of the nonlinear vertical emittance. While nonlinear emittance control is not the topic of this paper, it is remarkable that even in these cases BAGELS leads to sufficient P_{dk} to achieve the polarization goals of the ESR. For 7 of the 10 seeds,

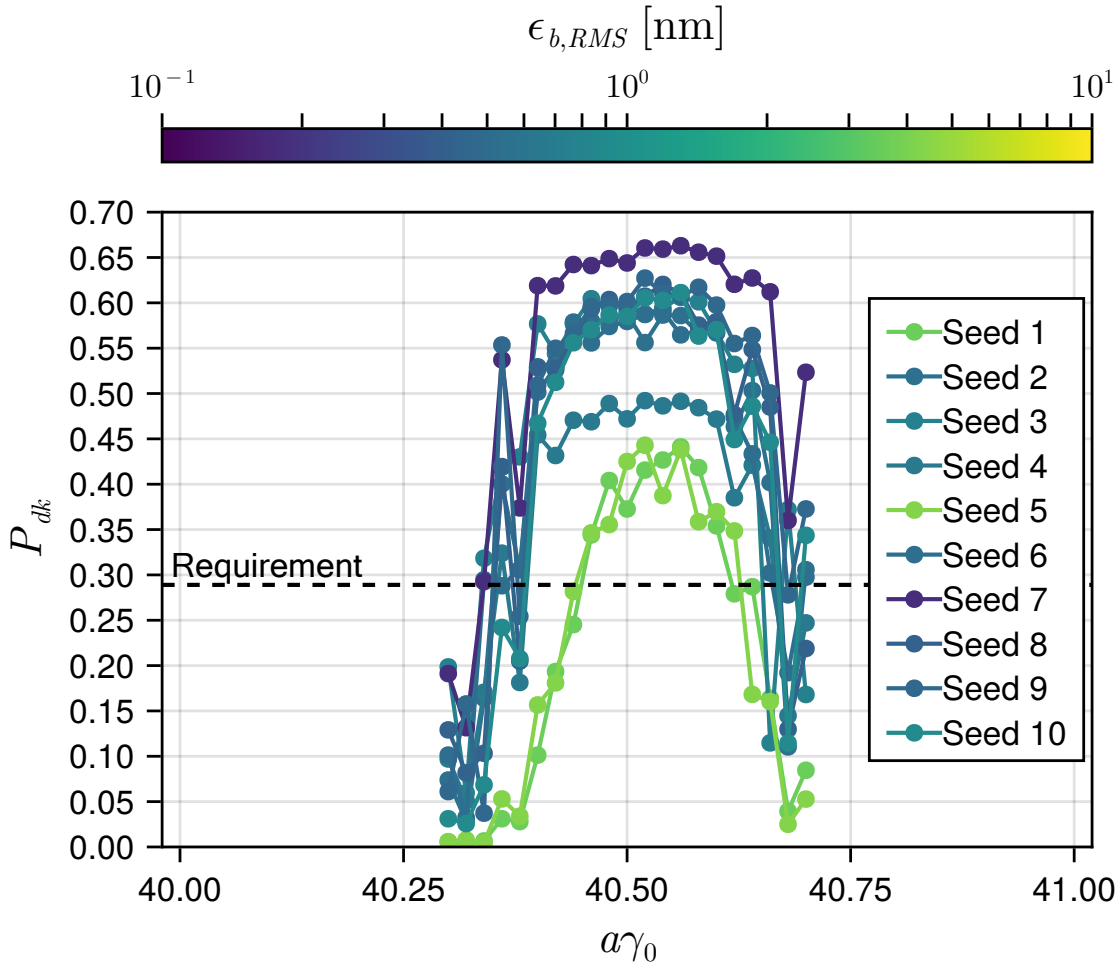

Figure 7.8: A 3^{rd} order map tracking energy scan of the asymptotic polarizations in 10 different 1-IP 18 GeV EIC-ESR lattices including the RMS errors listed in Table 7.1. Four BAGELS global coupling correction knobs were used to correct the coupling, followed by four BAGELS spin matching knobs to restore the spin match. The line colors correspond to the vertical-like mean equilibrium eigenemittance obtained in tracking for each seed.

asymptotic polarizations of $\approx$ 60% or more are achieved while having vertical equilibrium emittances in nonlinear tracking that agree very well with their linear calculations, suggesting excellent coupling control. For the two seeds with lower asymptotic polarization and a nonlinear $\epsilon_{b,RMS}$ increase, it is likely that a further optimization of the chromatic solution and/or harmonic sextupoles may

gain control of the nonlinear $\epsilon_{b,RMS}$ and obtain a corresponding increase in P_{dk}. In this case, because the BAGELS transverse coupling correction knobs rely on the sextupole strengths, some iteration will be required for an optimal solution. Overall, these results suggest that the four BAGELS spin matching bumps are highly efficacious and robust against random closed orbit distortions, and that the four BAGELS global coupling correction bumps can be used for excellent polarization-safe coupling control.

7.3.3 Vertical Emittance Creation

In order to achieve maximum luminosity in the EIC, the beam sizes of the electron and hadron beams must be matched. Because of radiation damping, the electron beam vertical emittance will be approximately zero, and if the vertical dispersion at the IP is to be kept to zero, then the vertical emittance must be intentionally increased in order to achieve a beam size match, specifically $\epsilon_y \approx 2$ nm. However, a nonzero vertical emittance is notoriously bad for electron polarization, and without a careful approach is all but guaranteed to significantly reduce the asymptotic polarization.

There are many different ways to generate vertical emittance. One way is to use a large vertical chicane as a local vertical dispersion bump, so that a vertical amplitude is excited when photons are emitted in the chicane. This was attempted in the ESR, however to achieve the necessary emittance the chicane requires too strong magnetic fields, geometrically is extremely challenging to fit in the ring, and degrades the spin match significantly [66]. Alternatively, a localized region with a large amount of coupling where photons are emitted may

be used to effectively "couple" part of the horizontal emittance into the vertical. However this has not been investigated in-depth, and will also certainly degrade the spin match significantly without a careful approach.

Instead of a localized approach, vertical emittance could be created by using vertical orbit bumps that either (1) generate delocalized transverse coupling via the skew quadrupole feed-down term in the sextupoles, or (2) generate delocalized vertical dispersion, caused by the corrector coils themselves, so that photon emission causes a vertical amplitude excitation. We investigate both such approaches using BAGELS. We also investigate a third approach where, using BAGELS, delocalized vertical dispersion is generated while simultaneously matching the dispersion to zero at the IP.

Delocalized Transverse Coupling

The BAGELS global coupling correction bumps we calculated in Sec. 7.3.2 have a maximum impact on the normalized coupling matrix components around the ring, a minimal impact on both the spin-orbit coupling function and the orbit, and by design create no delocalized vertical dispersion. This makes the BAGELS coupling correction bump with the largest eigenvalue perfect for creating vertical emittance via a delocalized transverse coupling wave. In the ideal 1-IP ESR, we simply turned this knob until the linear $\epsilon_b \approx 2$ nm.

The working point of this ESR lattice is $(Q_x, Q_y, Q_s) = (0.08, 0.14, 0.05)$. Interestingly, we found in nonlinear tracking that delocalized coupling readily excited the $Q_y - Q_x - Q_s$ resonance, causing an uncontrolled vertical emittance increase. Because the correction of this effect is not the topic of this paper,

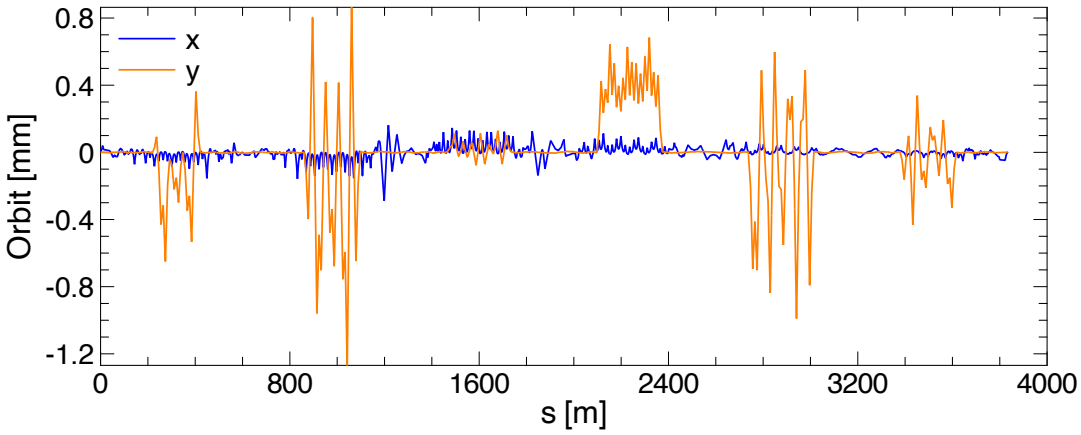

Figure 7.9: Closed orbit in a 1-IP 18 GeV EIC-ESR after using a single BAGELS coupling-creation bump to generate sufficient vertical emittance for beam size matching. The small horizontal orbit is due to radiation damping. The IP is located at $s = 0$ m.

we adjusted the working point slightly to $(0.08, 0.15, 0.045)$ by varying the arc quadrupoles and RF cavity voltages, to move away from this resonance.

We observed essentially zero impact on the analytical polarization after adjusting the BAGELS coupling-creating knob for linear $\epsilon_b \approx 2$ nm; only miniscule adjustments to the four BAGELS spin matching bumps were needed to re-maximize the analytical polarization. The closed orbit after using the BAGELS bumps is shown in Fig. 7.9.

As shown in the energy scan in Fig. 7.10, using one BAGELS coupling-creation bump and four BAGELS spin matching bumps, polarization requirements are well exceeded while simultaneously achieving sufficient vertical emittance in nonlinear tracking, even with a small nonlinear increase in ϵ_b. The disagreement of the analytical polarization calculation with nonlinear tracking is not surprising; the spin-orbit coupling function can vary significantly with

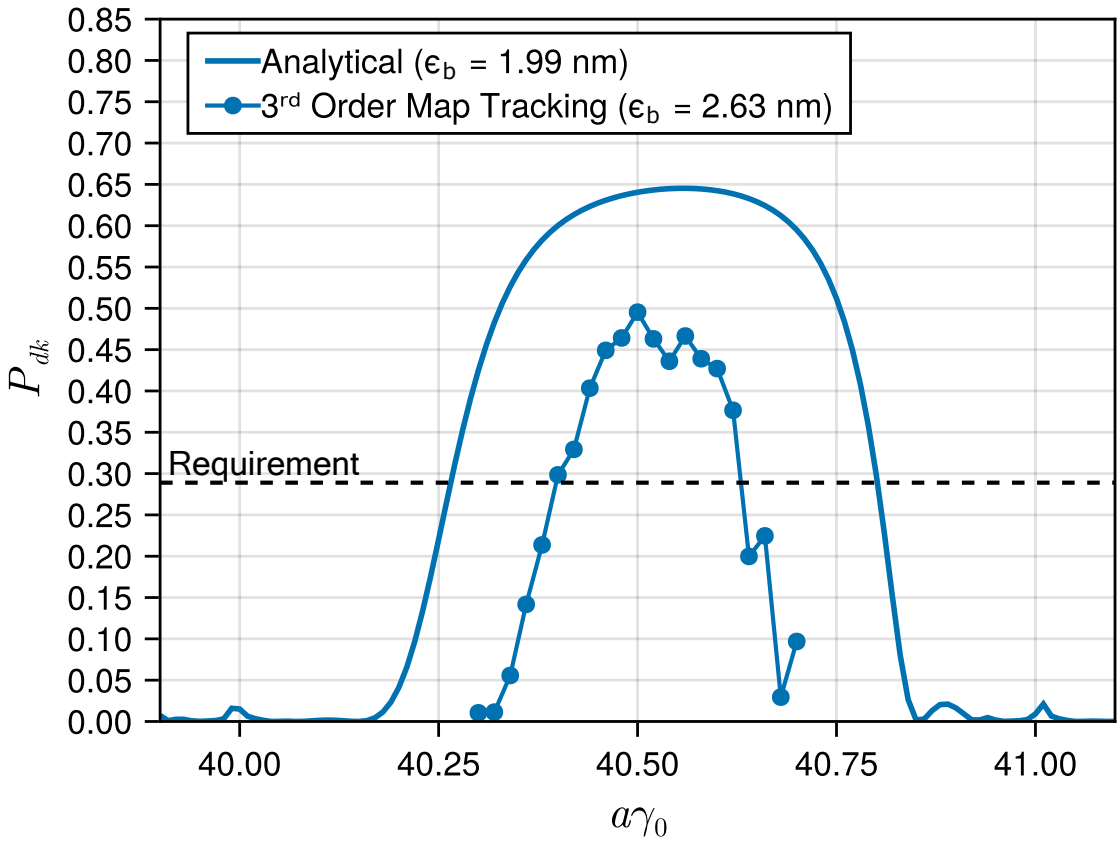

Figure 7.10: An energy scan of the asymptotic polarization in the ideal 1-IP 18 GeV EIC-ESR after using a single BAGELS coupling-creation bump to set the analytical vertical emittance to 1.99 nm. The disagreement of the analytical calculation with non-linear tracking is expected because the phase space dependence of the spin-orbit coupling function, which can vary significantly in the vertical, is neglected in the analytical calculation.

the vertical orbital amplitude, and the analytical calculation only evaluates the spin-orbit coupling function on the closed orbit.

Delocalized Vertical Dispersion

Using the coupling formalism as in Sec. 7.3.2, we can define a- and b-mode periodic dispersions as

$$\begin{pmatrix} \eta_a \\ \eta'_a \\ \eta_b \\ \eta'_b \end{pmatrix} = \mathsf{G}^{-1}\bar{\mathsf{V}}^{-1}\mathsf{G} \begin{pmatrix} \eta_x \\ \eta'_x \\ \eta_y \\ \eta'_y \end{pmatrix} . \tag{7.13}$$

The excitation of a "b"-mode (vertical-like) amplitude caused by photon emission is directly characterized by

$$\mathcal{H}_b = \bar{\eta}_{b1}^2 + \bar{\eta}_{b2}^2 , \quad \bar{\eta}_{b1} = \frac{\eta_b}{\sqrt{\beta_b}} , \; \bar{\eta}_{b2} = \frac{\alpha_b \eta_b + \beta_b \eta'_b}{\sqrt{\beta_b}} , \tag{7.14}$$

in places where photons are emitted [57, 52]. The Twiss parameters are defined by the Courant-Snyder form of G_b. Thus, to generate vertical emittance by radiation in areas where a vertical amplitude is excited, we seek a single BAGELS bump that maximally impacts $\mathcal{H}_b$ in the bends, but minimally impacts the spin-orbit coupling function in the bends and the orbit in all elements. The bump should also by construction generate no delocalized transverse coupling.

Once again, we follow the recipe at the end of Sec. 7.1.2. First, we need to choose a basis bump. To cancel the coupling created by a single π bump in a periodic FODO section, we need to place an opposite π bump positioned πn away in betatron phase. For the "opposite π pair" we used for spin matching, we positioned the second bump exactly π away from the first, to cancel both the

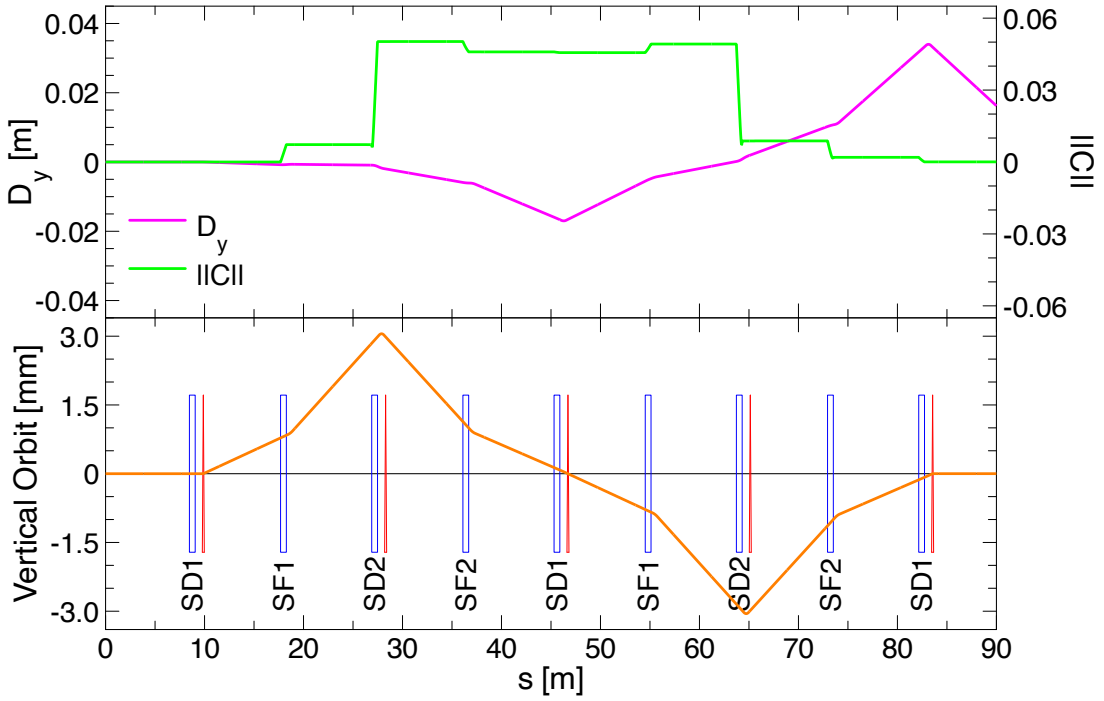

Figure 7.11: 2π bump placed in a periodic FODO beamline with 90° phase advance per cell and two sextupole families per plane (SF for the horizontal, SD for the vertical). Sextupoles are specified as blue rectangles, vertical corrector coils as red triangles, and the quadrupoles and bends are not shown. The bump's corresponding vertical dispersion D_y and normalized coupling matrix norm $\|\bar{C}\|$ are plotted above [56]. The 2π bump creates delocalized vertical dispersion but localized coupling.

coupling and vertical dispersion. In this case, we want to coherently build vertical dispersion while cancelling the coupling, so instead we can place the second π bump $2\pi n$ away from the first in betatron phase. To construct an orthogonal basis fully spanning the space, we position the second directly following the first so that $n = 0$, and sequentially select all such combinations in each arc. We refer to this basis bump, shown in Fig. 7.11, as a "2π bump" for the obvious reason. The 2π bump, which generates delocalized vertical dispersion but no

delocalized coupling, is the perfect basis bump to use for generating vertical emittance via delocalized vertical dispersion.

Now that we have chosen a basis bump, we must construct the response matrices. One of the requirements for BAGELS to work is a sufficiently linear dependence of the quantities with the basis vectors. In this case, $\mathcal{H}_b$ does not vary linearly with the 2π bump strength, however $\bar{\eta}_{b1}$ and $\bar{\eta}_{b2}$ do. Following the notation in Eq. (7.7), for a maximal impact on $\bar{\eta}_{b1}$ and $\bar{\eta}_{b2}$ with a minimal impact on the spin-orbit coupling function $\boldsymbol{d}$ and the orbit y we use

$$\mathsf{R}_A = \mathsf{R}_{(\bar{\eta}_{b1},\bar{\eta}_{b2})}\ ,\ \mathsf{R}_B = \begin{pmatrix} \mathsf{R}_{\boldsymbol{d}}/\|\mathsf{R}_{\boldsymbol{d}}\| \\ \mathsf{R}_y/\|\mathsf{R}_y\| \end{pmatrix}, \tag{7.15}$$

to calculate bumps that maximally impact $\mathcal{H}_b$ and minimally impact the spin-orbit coupling and orbit. Finally, we use the one group with largest eigen-

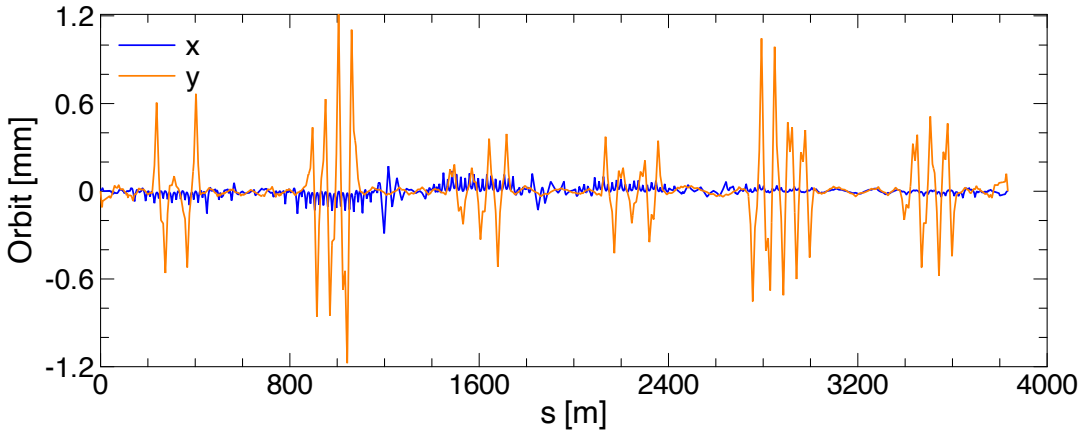

Figure 7.12: Closed orbit in a 1-IP 18 GeV EIC-ESR after using a single BAGELS vertical dispersion-creation bump to generate sufficient vertical emittance for beam size matching. The small horizontal orbit is due to radiation damping. The IP is located at $s = 0$ m.

value as our polarization-safe vertical dispersion creation bump, and vary that until $\epsilon_b \approx 2$ nm in the analytical calculation. Varying the BAGELS vertical dispersion creation bump caused essentially no changes to the polarization; only miniscule changes to the BAGELS spin matching knobs were made to re-maximize the analytical polarization. The closed orbit after using the BAGELS bumps is shown in Fig. 7.12.

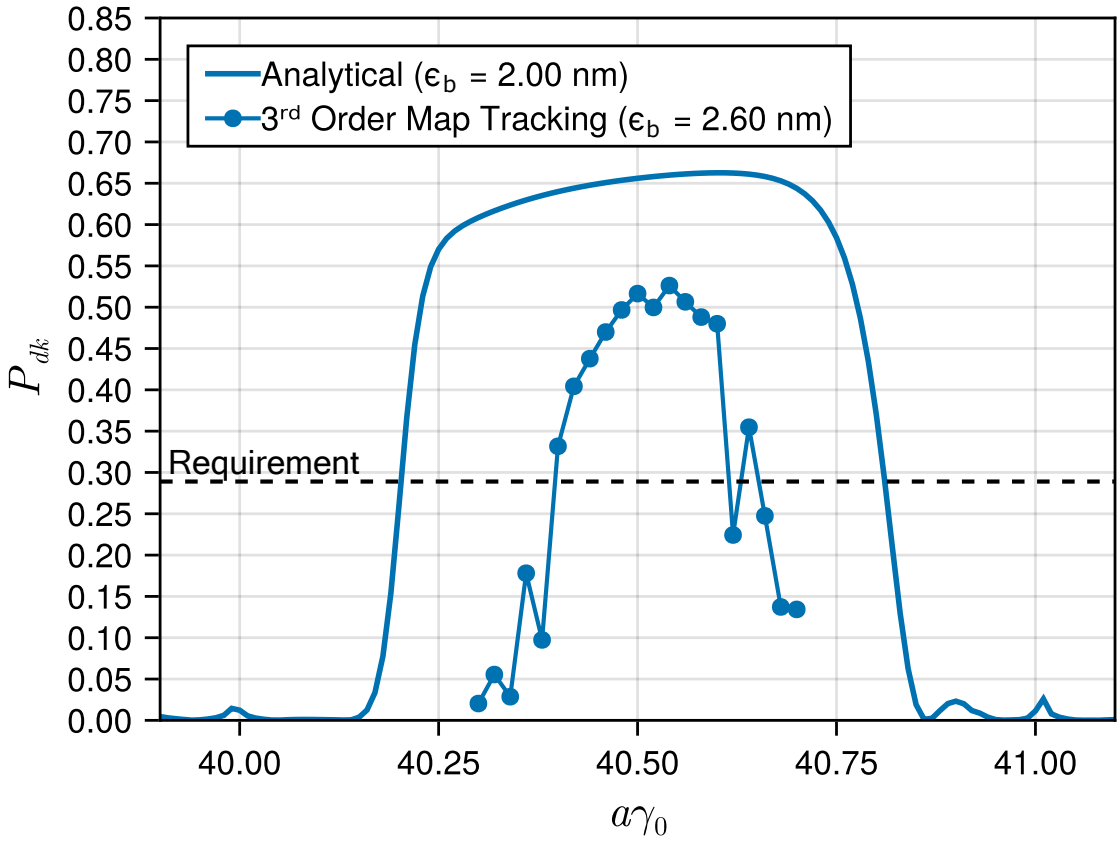

Figure 7.13: An energy scan of the asymptotic polarization in the ideal 1-IP 18 GeV EIC-ESR after using a single BAGELS vertical dispersion-creation bump to set the analytical vertical emittance to 2.00 nm. The disagreement of the analytical calculation with nonlinear tracking is expected because the phase space dependence of the spin-orbit coupling function, which can vary significantly in the vertical, is neglected in the analytical calculation.

Figure 7.13 shows an energy scan of the asymptotic polarization using the one BAGELS vertical dispersion creation bump for beam size matching. Excellent polarization, well exceeding the requirement, is achieved while simultaneously creating sufficient vertical emittance in nonlinear tracking. Just as with the delocalized coupling creation method in Sec. 7.3.3, only a small nonlinear increase in ϵ_b was observed, and with BAGELS the polarization requirements are still well-exceeded. Because the BAGELS vertical dispersion-creating bump does not require any change to the working point of the lattice to avoid nonlinear resonances, this method is recommended for polarization-safe beam size matching in the EIC-ESR.

Delocalized Vertical Dispersion with IP Match

The BAGELS bump in Sec. 7.3.3 simultaneously (1) achieves sufficient vertical emittance via a delocalized vertical dispersion wave, (2) has minimal impacts to the polarization and orbit, and (3) generates no delocalized transverse coupling by use of 2π bumps as the basis bumps. However, it does not ensure the vertical dispersion and vertical dispersion slope is set to zero at the IP. To include this requirement in the BAGELS solution, we simply include η_b and η'_b at the IP in the response matrix of quantities to minimally affect. Once again using the 2π bump as the basis bump, and following the notation in Eq. (7.7), we perform BAGELS using

$$\mathsf{R}_A = \mathsf{R}_{(\bar{\eta}_{b1},\bar{\eta}_{b2})}\ ,\ \mathsf{R}_B = \begin{pmatrix} \mathsf{R}_d/||\mathsf{R}_d|| \\ \mathsf{R}_y/||\mathsf{R}_y|| \\ \mathsf{R}_{\eta_b,IP}/||\mathsf{R}_{\eta_b,IP}|| \\ \mathsf{R}_{\eta'_b,IP}/||\mathsf{R}_{\eta'_b,IP}|| \end{pmatrix}, \tag{7.16}$$

where $\mathsf{R}_{\eta_b,IP}$ and $\mathsf{R}_{\eta'_b,IP}$ specify the responses of η_b and η'_b at the IP for each 2π bump respectively. The resulting group with the largest eigenvalue defines

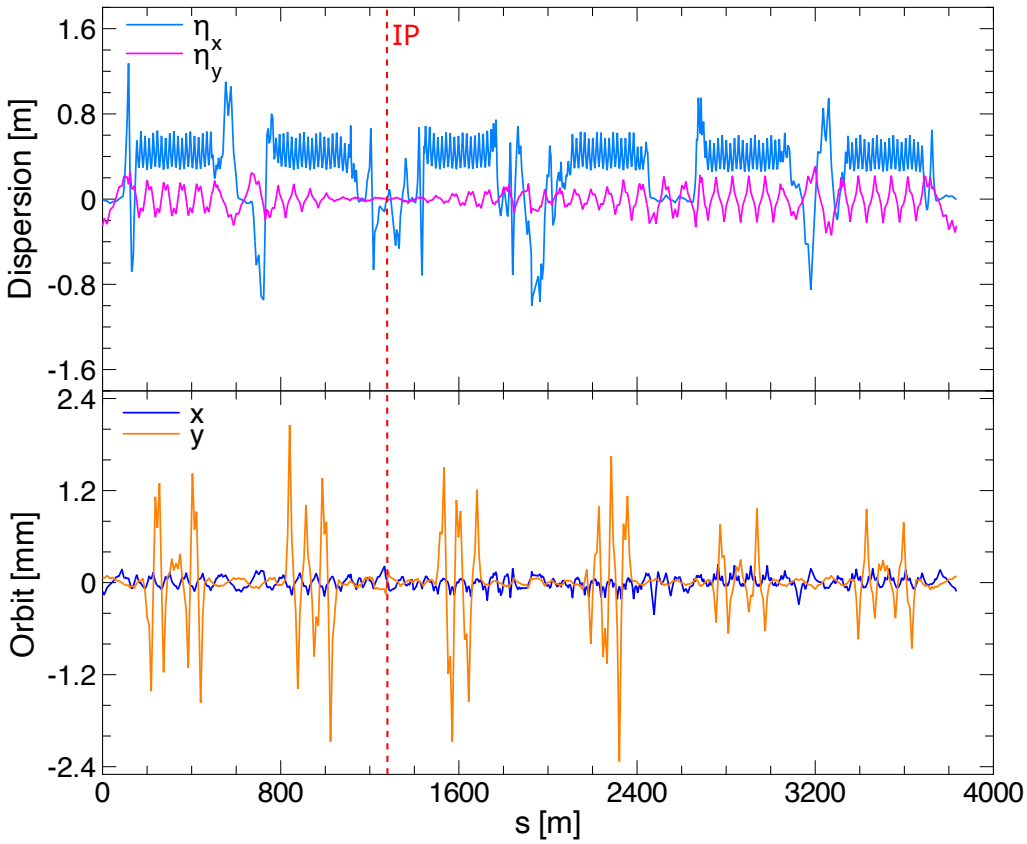

Figure 7.14: Dispersion and closed orbit in a 1-IP 18 GeV EIC-ESR after using a single BAGELS simultaneous vertical dispersion-creation and IP dispersion matching bump to generate sufficient vertical emittance for beam size matching. The small horizontal orbit is due to radiation damping. The IP is located at s = 1277.948 m and is denoted by the red dashed line.

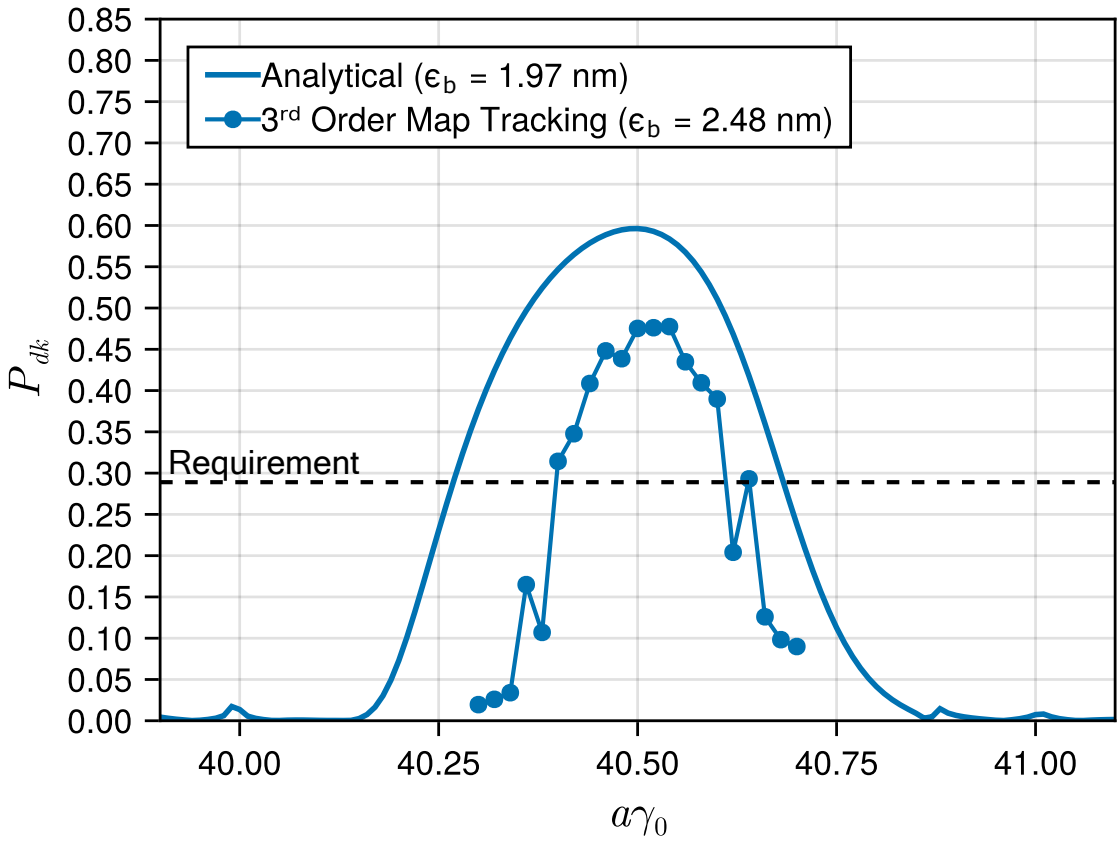

Figure 7.15: An energy scan of the asymptotic polarization in the ideal 1-IP 18 GeV EIC-ESR after using a single BAGELS simultaneous vertical dispersion-creation and IP dispersion matching bump to set the analytical vertical emittance to 1.97 nm. The disagreement of the analytical calculation with nonlinear tracking is expected because the phase space dependence of the spin-orbit coupling function, which can vary significantly in the vertical, is neglected in the analytical calculation.

a BAGELS bump that achieves all the effects of the bump in Sec. 7.3.3, *while also ensuring minimal impacts to the dispersion at the IP*; the bump can be varied to create a polarization-safe delocalized vertical dispersion wave that automatically cancels itself at the IP.

The BAGELS bump was varied so that the analytical $\epsilon_b \approx 2$ nm, and the four BAGELS spin matching bumps were varied to re-maximize the analytical

polarization. The periodic dispersion and closed orbit after using the BAGELS bumps are shown in Fig. 7.14. As shown, the BAGELS bump maintains the dispersion match at the IP.

Figure 7.15 shows an energy scan of the asymptotic polarization using the one BAGELS simultaneous vertical dispersion-creation and IP dispersion matching bump. Remarkably, while the analytical polarization is slightly deteriorated when compared with the unmatched-IP BAGELS bump in Sec. 7.3.3, the polarization obtained in nonlinear tracking shows very similar performance; the polarization requirements are well exceeded, and only a small nonlinear increase in ϵ_b was observed.

7.4 Conclusions

Best Adjustment Groups for ELectron Spin (BAGELS) provides a rigorous framework to construct a minimal number of control parameter groups, or knobs, that have optimal impacts on the radiative depolarization, orbit, and optics. For spin matching purposes, we used BAGELS to compute special vertical orbit bumps, each a linear combination of basis bumps, that maximally affect the radiative depolarization around the ring while creating minimal orbit excursions and no delocalized vertical dispersion nor delocalized coupling. The BAGELS spin matching bumps work by intentionally tilting $\hat{\boldsymbol{n}}_0$ to create spin-orbit coupling which can be used to cancel the spin-orbit coupling in the ring, e.g. caused by spin rotators or random errors. For the design of the EIC-ESR, we used only four BAGELS spin matching knobs to significantly increase the asymptotic polarizations in nonlinear trackings of the 1- and 2-IP 18 GeV

lattices, almost doubling P_{dk} in the former and more than tripling P_{dk} in the latter. For the EIC-ESR we also applied BAGELS in various applications where a minimal impact on polarization was desired: first, we calculated four BAGELS vertical orbit bumps that can be used to maximally correct the global transverse coupling caused by random errors, while minimally impacting the orbit and radiative depolarization. We then tested both these four BAGELS transverse coupling correction knobs and the four BAGELS spin matching knobs for 10 different error seeds in the 1-IP 18 GeV EIC-ESR, and showed excellent simultaneous polarization and transverse coupling control. Secondly, we calculated three different types of vertical emittance creation knobs that can each be varied with truly minimal impacts to the radiative depolarization and orbit: one that creates delocalized coupling, one that creates delocalized vertical dispersion, and one that creates delocalized vertical dispersion while maintaining a dispersion match at the IP. All knobs showed excellent simultaneous polarization and vertical emittance control in nonlinear tracking. BAGELS has solved the challenges of simultaneously maximizing polarization, correcting coupling, and creating the necessary vertical emittance ratio in the design of the EIC-ESR. These BAGELS knobs will be provided to the control room for operational optimizations. BAGELS will find similar utility in any present or future polarized lepton ring.

CHAPTER 8

ESR BEAM-BEAM EFFECT ON POLARIZATION

8.1 Background

The beam-beam effect is the effect of the colliding beam at the interaction point(s) on each of the beams. This can be modelled as either a "strong-strong" interaction, in which both beams have an effect on each other, or a "weak-strong" interaction, in which one beam is assumed to be unaffected by the other. The difference can be understood by considering a gravitational slingshot, where the sun is slingshotting a planet. In the strong-strong model, this is a two-body problem where the planet affects the sun and the sun affects the planet. In the weak-strong model, the sun is assumed to have "infinite mass" so it is unaffected by the planet, effectively turning it into a single-body problem. The weak-strong interaction is therefore much easier to model, at the cost of some physical accuracy.

Bassetti and Erskine derived the transverse kick a particle would experience from a 2D Gaussian beam distribution, essentially an infinite wire [8]. In one oscillation mode, this kick has the transverse dependence shown in Fig. 8.1. For the weak-strong model, to handle the real longitudinal variation of the strong beam, 2D slices are made at various longitudinal points, where at each slice a Bassetti-Erskine kick is applied.

As is apparent by Fig. 8.1, for very small transverse positions the kick is approximately linear, but at larger amplitudes the kick is very nonlinear, asymptotically approaching zero. Essentially, for very small amplitudes this effect is a

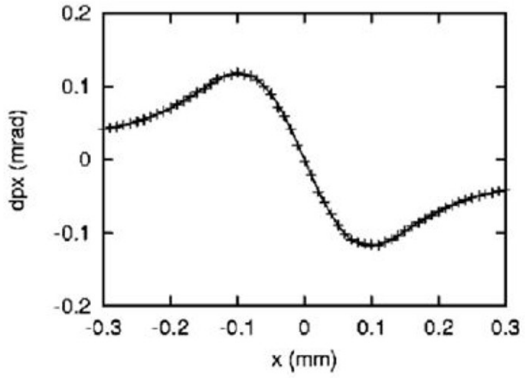

Figure 8.1: Transverse kick as a function of transverse position due to a weak-strong model of the beam-beam interaction.

linear restoring force in both planes, but at large amplitudes no kick is given. In a ring, this would create a potentially large spread in the tunes of each particle in a bunch; particles with large amplitudes would have tunes equal to the "bare lattice tunes" (no beam-beam), and particles in the "core" would have a tune equal to that if the lattice had a linear focusing element in both planes at the IP. And in an electron ring with the stochastic emission of synchrotron radiation, all particles will explore all parts of this tune space.

In HERA, the beam-beam interaction, using a weak-strong model, was predicted to have drastic effects on the polarization in simulations [14, 11]. However, in real life, it ended up not actually having much of an effect. To make matters even more puzzling, HERA's spin match *was* dependent on the periodic lattice functions, and so one would fully expect a degradation in the spin match by just naively putting a beam-beam element into the lattice and having the resulting beta-beating around the ring; even in the linear calculation, the beam-beam effect causes significant degradation in polarization models for HERA.

While we hope for similar findings in real life for the ESR (good in real life), it is important for us to understand how our beam-beam model affects polarization, and have a procedure in place to fix it in case we aren't as lucky.

8.2 Methods

Like the previous chapters, here the Monte Carlo tracking results use damped maps of specified orders between each bend center generated by PTC, and a stochastic radiation kick is applied at the bend centers. Bmad is used as an interface to PTC. Each tracking result includes 500-5000 particles, for 5000-7000 turns. The depolarization time is obtained by the slope of P vs. t in the tracking, and the eigen-emittances computed from the bunch distribution matrix.

The beam-beam effect is treated separately from the maps around the ring, following the algorithm described in the Bmad manual [53], also described in Appendix C of [76], which also includes an energy kick. 100 longitudinal slices are used for the beam-beam effect. In this chapter, the "nonlinear" beam-beam effect corresponds to the full Bassetti-Erskine kick, while the "linear" beam-beam effect corresponds to assuming that all particles see the same linear kick, and is an approximation to see what's happening in the core. With the linear beam-beam effect, the tune shift is the same for all particles. The ESR version used for all studies presented in this chapter is the v6.1 18 GeV 1-IP lattice.

8.3 Results

8.3.1 Linear and Nonlinear Beam-Beam

In the ESR, unlike HERA, by integrating over the whole rotator and carefully setting the sum in Eq. (4.21) equal to zero for any orbital eigenvector, the spin match is only dependent on the transfer matrix over each solenoid module, independent of the optics and independent of anything outside the solenoid module. Therefore, we would expect the beam-beam effect to, within the linear approximation, have no impact on the polarization.

Figure 8.2 shows an energy scan of τ_{dep} in a baseline ESR lattice with varying order maps in the rest of the ring and a linear beam-beam interaction, and Fig. 8.3 shows the same but with a nonlinear beam-beam interaction.

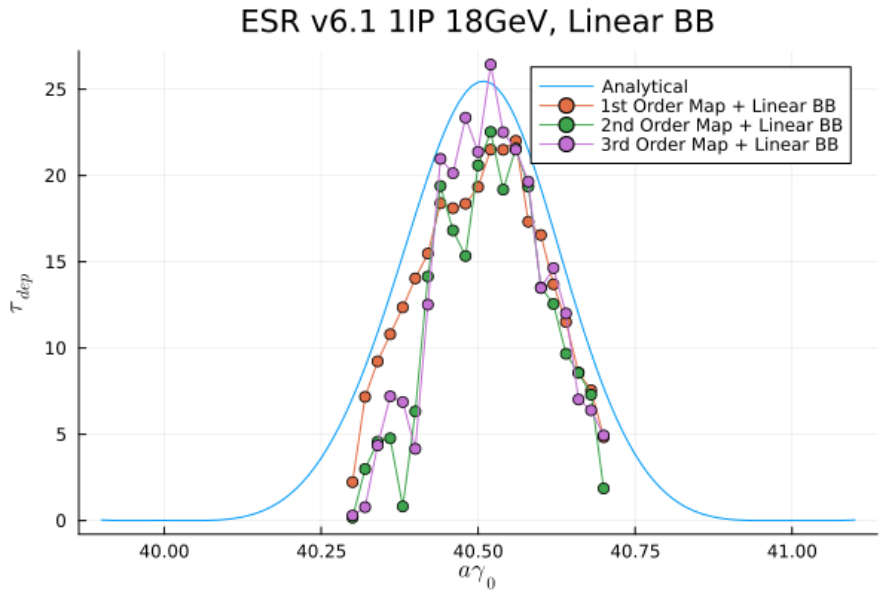

Figure 8.2: Energy scan of the radiative depolarization time τ_{dep} in the v6.1 18 GeV 1-IP ESR with a linear weak-strong beam-beam kick.

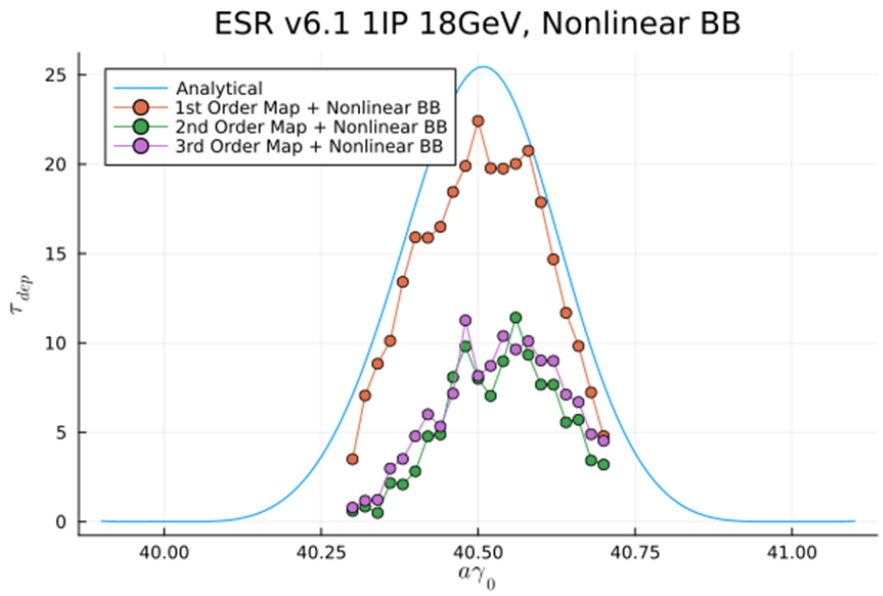

Figure 8.3: Energy scan of the radiative depolarization time τ_{dep} in the v6.1 18 GeV 1-IP ESR with the fully nonlinear weak-strong beam-beam kick.

As shown in Fig. 8.2, with a linear beam-beam kick the radiative depolarization is indeed unaffected, as predicted. However, Fig. 8.3 shows a massive degradation in the radiative depolarization time when including a fully nonlinear beam-beam effect, paired specifically with 2nd order maps in the rest of the ring. This effect must be better understood, determined if it is real problem, and how we could potentially solve it.

To check if the coupling in the solenoid modules are the source of the problem, similar to the study in Ch. 5 we tried 1st, 2nd, and 3rd order maps for solenoid modules and found no correlation. Some 2nd order effect in the magnetic elements in the ring, paired with the nonlinear beam-beam effect, is causing some major depolarization.

The nonlinear beam-beam effect causes a large tune spread of the bunch, from the bare lattice tunes to the core tunes, which all electrons in the bunch

will eventually explore. Therefore, one hypothesis we have is that a strong depolarizing resonance in located somewhere in this "tune footprint" which the electrons all cross through. To better understand this, we perform tune scans of Q_x and Q_y for three different cases: 1) no beam-beam, 2) linear beam-beam, and 3) nonlinear beam-beam. For each case, we evaluate the equilibrium eigenemittances and radiative depolarization times obtained in nonlinear tracking. Each tracking point for each tune scan corresponds to 1000 particles for 7000 turns. The arc quadrupoles were adjusted to change the tunes.

8.3.2 Tune Scan, No Beam-Beam

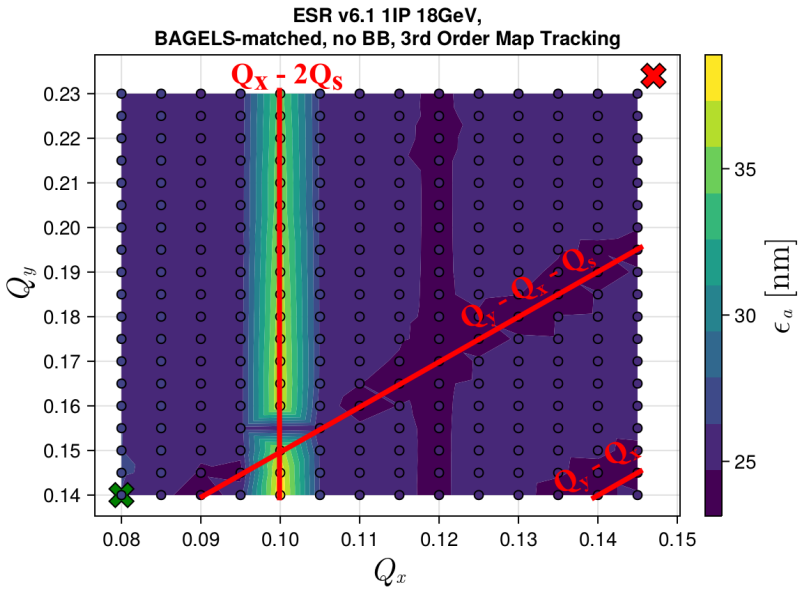

Figure 8.4: Tune scan of the horizontal eigenemittance with no beam-beam. The green cross corresponds to the bare lattice WP and the red cross the core WP with beam-beam.

Figures 8.4 and 8.5 show the horizontal and vertical eigenemittances for a lattice without any beam-beam interaction, attemping to scan the entire tune

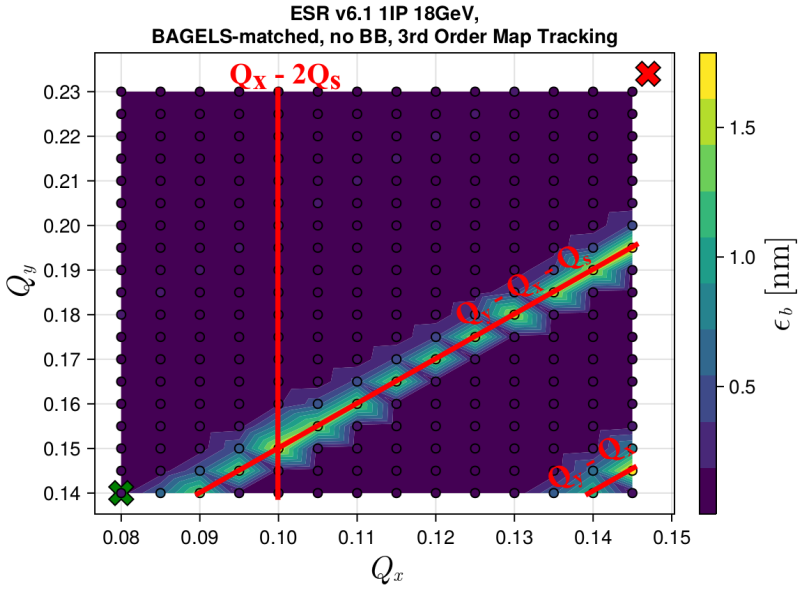

Figure 8.5: Tune scan of the vertical eigenemittance with no beam-beam. The green cross corresponds to the bare lattice WP and the red cross the core WP with beam-beam.

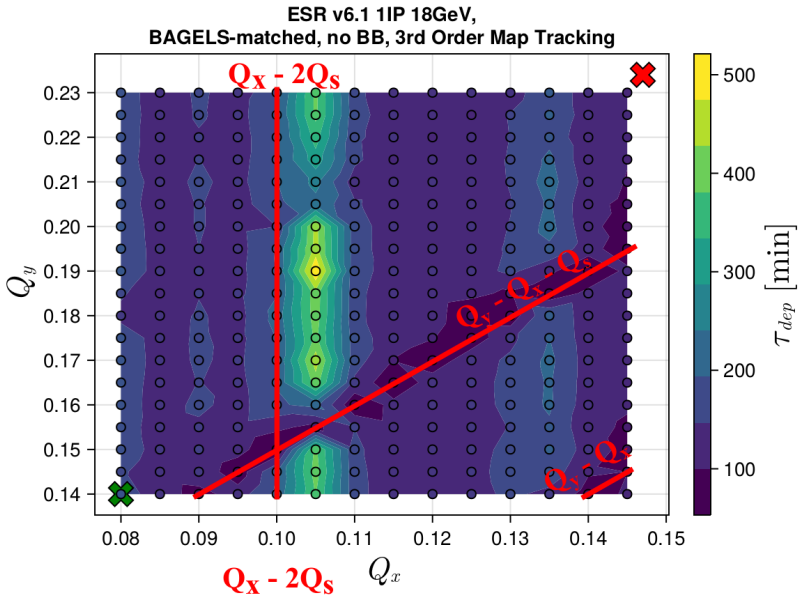

Figure 8.6: Tune scan of the radiative depolarization time with no beam-beam. The green cross corresponds to the bare lattice WP and the red cross the core WP with beam-beam.

footprint between the bare lattice tunes and the core tunes with beam-beam. As shown, there is a vertical emittance increase along $Q_y - Q_x$ and its synchrotron sidebands. Figure 8.6 shows the radiative depolarization time, which is also smallest along $Q_y - Q_x - Q_s$ likely explainable by the uncontrolled vertical emittance, which is notoriously bad for polarization. However, there aren't any "clear" spin resonance lines shown in this plot. Interestingly, there is a large increase in the radiative depolarization time near $Q_x - 2Q_s$; this may be explainable by the difference resonance causing a smaller longitudinal action, thereby reducing the longitudinal spin-orbit coupling.

8.3.3 Tune Scan, Linear Beam-Beam

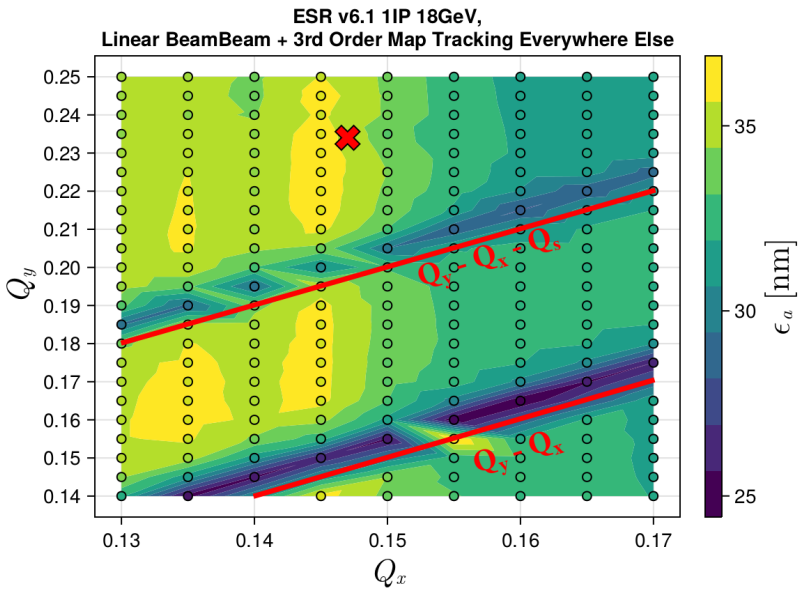

Figure 8.7: Tune scan of the horizontal eigenemittance with linear beam-beam. The red cross corresponds to the core WP with beam-beam.

In order to help narrow down the cause, for this tune scan and all subse-

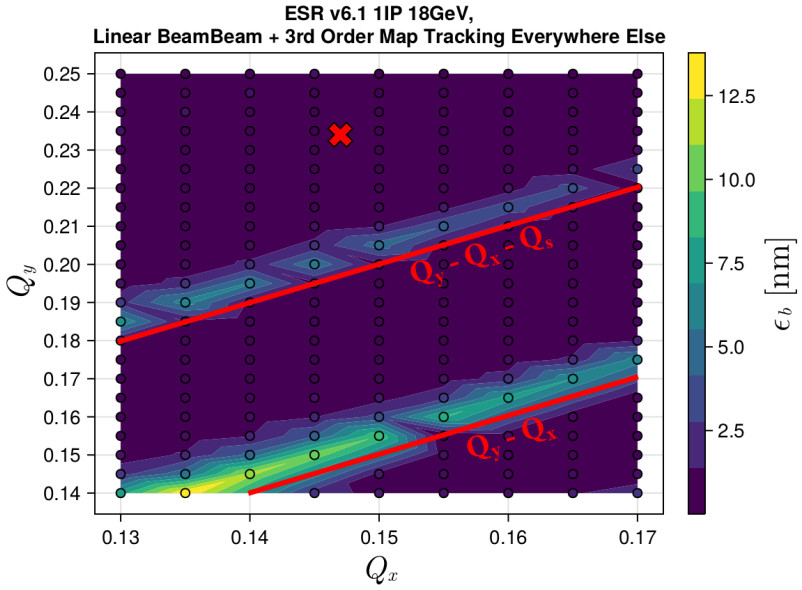

Figure 8.8: Tune scan of the vertical eigenemittance with linear beam-beam. The red cross corresponds to the core WP with beam-beam.

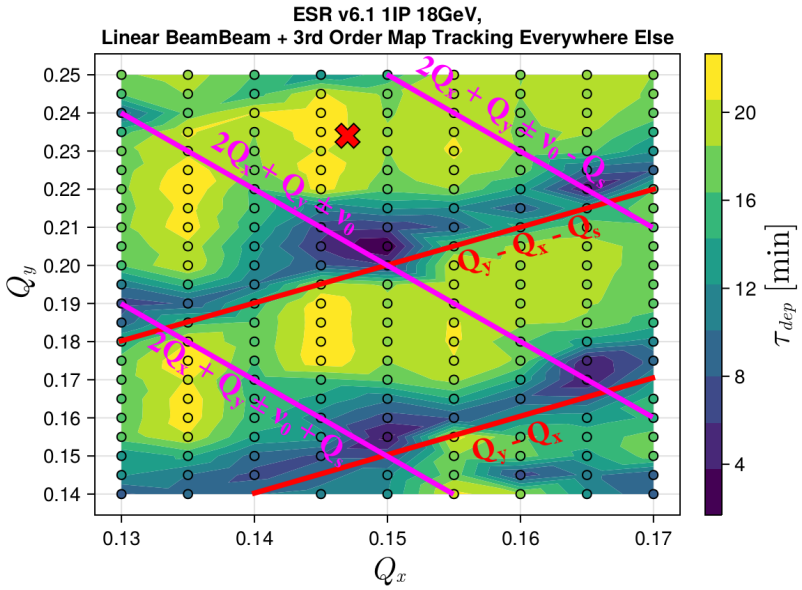

Figure 8.9: Tune scan of the radiative depolarization time with linear beam-beam. The red cross corresponds to the core WP with beam-beam.

quent ones the baseline ESR lattice (not BAGELS-matched) is used. Figures 8.7 and 8.8 show the horizontal and vertical eigenemittances respectively for the ESR with the linear beam-beam interaction. These figures don't show anyhting very interesting – just the expected vertical emittance increase along the $Q_y - Q_x$ resonance and its synchrotron sideband.

Arguably the most important result of this entire chapter is presented in Fig. 8.9, which shows the radiative depolarization times for each point in the scan, shows an important result. Every time the spin resonance $2Q_x + Q_y \pm \nu_0$ crosses over $Q_y - Q_x$ or its synchrotron sidebands, the radiative depolarization time decreases substantially. The tune footprint with nonlinear beam-beam extends from the red cross (the core WP) downwards to the lower left of the plot – and so with the nonlinear beam-beam the particles would transiently be crossing these resonances.

8.3.4 Tune Scan, Nonlinear Beam-Beam

Finally, we consider a tune scan with the nonlinear beam-beam effect included; here, the tunes refer to the core tunes, as the particle tunes will vary between the core tunes and the bare lattice tunes. Because of this washing out of the tunes, we don't expect to see much resonance structure. Nonetheless, it would still be insightful to see if there is any region where an improvement could be achieved.

Figures 8.10 and 8.11 show the horizontal and vertical eigenemittances respectively for the ESR with the fully nonlinear beam-beam interaction. While there isn't really anything remarkable shown in these plots, we do note that the horizontal eigenemittance creeps up to around 38 nm.

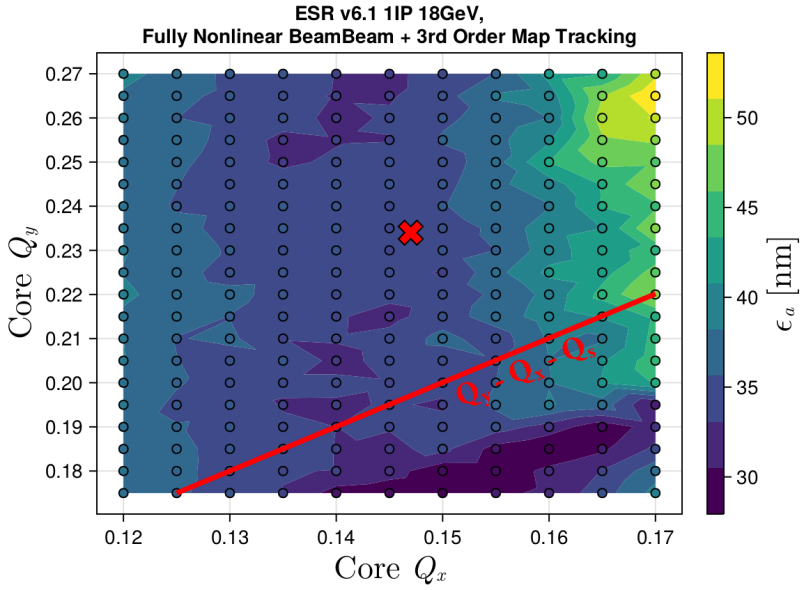

Figure 8.10: Tune scan of the horizontal eigenemittance with nonlinear beam-beam. The red cross corresponds to the core WP with beam-beam.

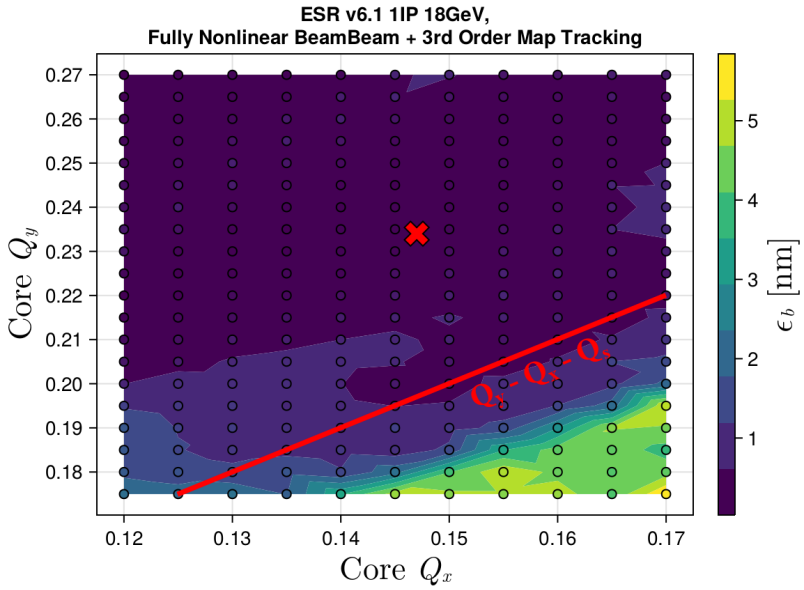

Figure 8.11: Tune scan of the vertical eigenemittance with nonlinear beam-beam. The red cross corresponds to the core WP with beam-beam.

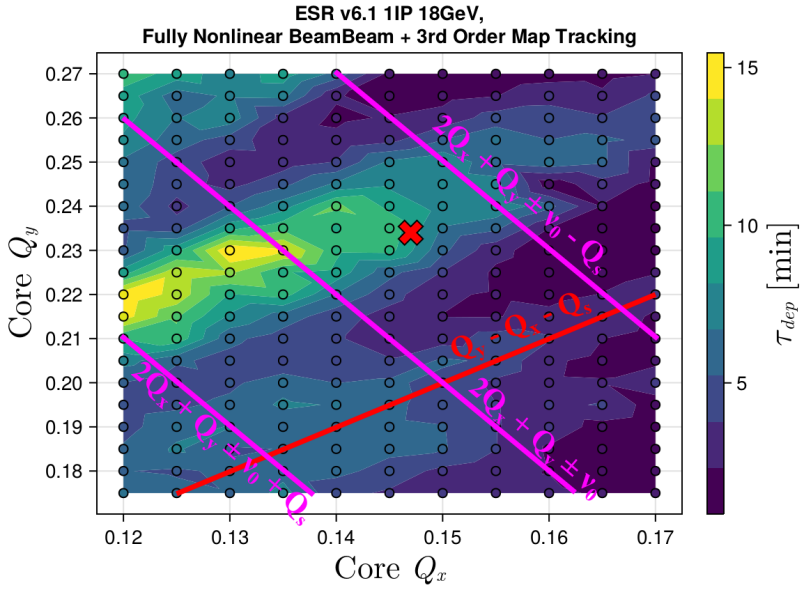

Figure 8.12: Tune scan of the radiative depolarization time with nonlinear beam-beam. The red cross corresponds to the core WP with beam-beam.

Figure 8.12 shows the radiative depolarization time in the ESR when including the fully nonlinear beam-beam effect. Nominally, this lattice has a radiative depolarization time of around 25 min (before application of BAGELS). As shown in the plot, the radiative depolarization time including the nonlinear beam-beam effect degrades to 9 min at the working point. It can be increased to roughly 15 min by reducing Q_x, but this is still far below its original 25 min. One possible explanation for this increase is that is moves the tune footprint further away from the intersection of $2Q_x + Q_y \pm \nu_0$ with $Q_y - Q_x - Q_s$, which shows strong depolarization in Fig. 8.9.

8.3.5 Different Sextupole Settings

Because the effect presents with 2nd order maps in the rest of the ring, as shown in Fig. 8.3, it is insightful to consider how dependent the radiative depolarization time is on the sextupole settings in the ring. Before the "finalized" chromatic solution for this lattice was prepared, we prepared our own rudimentary chromatic solution so that our Monte Carlo studies could proceed without losing particles. These sextupole settings are referred to as "Matt's sextupole settings". The Montague W-functions [47] for Matt's sextupole settings and for the chromatic solution are shown in Figs. 8.13 and 8.14 respectively. Figure 8.15

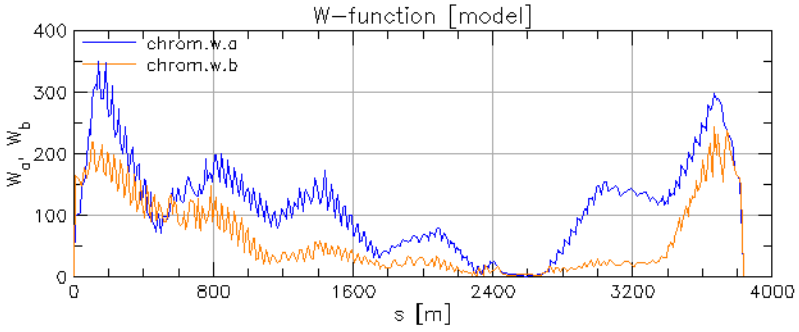

Figure 8.13: Montague functions for "Matt's sextupole settings" of the 1-IP 18 GeV v6.1 ESR.

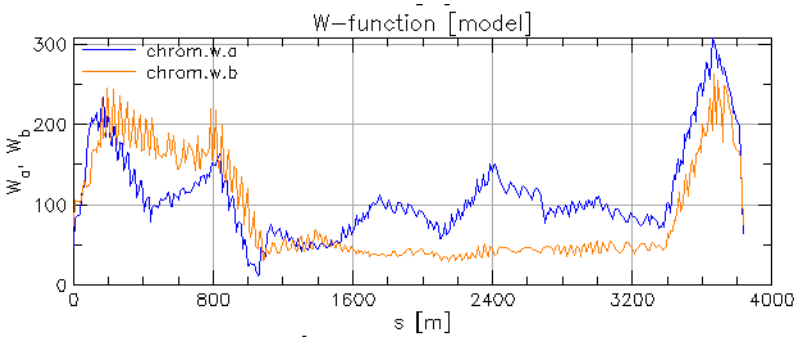

Figure 8.14: Montague functions for the chromatic solution of the 1-IP 18 GeV v6.1 ESR.

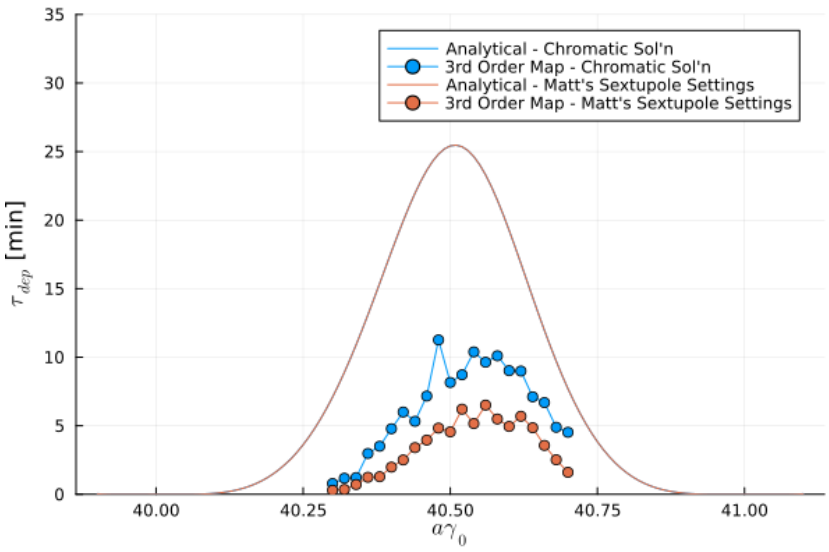

Figure 8.15: Energy scan of the radiative depolarization time τ_{dep} in the v6.1 18 GeV 1-IP ESR with the fully nonlinear weak-strong beam-beam kick for different sextupole settings.

shows the difference in the radiative depolarization times for both sextupole settings, including the analytical and nonlinear tracking results; the effect shows a clear dependence on the sextupole settings.

8.4 Conclusions

Weak-strong models of the beam-beam interaction in the 18 GeV ESR show significant polarization loss in simulations, even though the linear theory shows no reduction in polarization. Monte Carlo studies show the effect appears in simulations with a nonlinear beam-beam effect paired with 2nd order maps in the rest of the ring. Tune scans around the core tunes and the bare lattice tunes show that a possible explanation is the overlap of the $Q_y - Q_x - Q_s$ resonance with the spin resonance $2Q_x + Q_y \pm \nu_0$ in the tune footprint of the bunch, as well

as a clear dependence of the effect on the sextupoles. Future work will aim to resolve this effect by minimizing the resonance driving terms associated with the $Q_y - Q_x - Q_s$ resonance, as well as the $2Q_x + Q_y \pm \nu_0$ spin resonance strength.

CHAPTER 9

SCIBMAD

9.1 Overview

If one were to imagine a wishlist of features available in a modern accelerator physics simulation code, some points that might be conjured up are:

- Fully usable in high-level programming languages (Python and Julia)
- Modular and easy to integrate with other programs/machine learning tools/optimizers
- Fully nonlinear, non-paraxial, symplectic integration including spin
- Super fast by SIMD/SIMT-parallelization on both the CPU and GPU
- Nonlinear parametric normal form analysis including spin and radiation
- Arbitrary interdependent and time-dependent lattice parameters
- Advanced lattice definition and design tools
- Forwards-, backwards-, and Taylor-differentiable

As a part of this dissertation, the new SciBmad code has been developed, which achieves all points on this list. SciBmad is a new open source, high-performance, CPU/GPU compatible, polymorphic, and forwards-/backwards-/Taylor-differentiable accelerator physics simulation ecosystem, usable within either Python and Julia, and at the time of dissertation writing consists of a set of modular packages:

- **BeamTracking.jl**: Universally polymorphic, differentiable, portable, and parallelized integrators for simulating charged particle beams on the CPU and various GPUs including NVIDIA CUDA, Apple Metal, Intel oneAPI, and AMD ROCm
- **GTPSA.jl**: Fast high-order (Taylor mode) automatic differentiation using the Generalised Truncated Power Series Algebra (GTPSA) library
- **Beamlines.jl**: Defines accelerator lattices in a fast, flexible, fully-polymorphic, and differentiable way, providing both eagerly- and lazily-evaluated deferred expressions for interdependent parameters
- **NonlinearNormalForm.jl**: Map-based perturbation theory of differential-algebraic maps, which may include spin and large damping, using Lie algebraic methods
- **AtomicAndPhysicalConstants.jl**: Library providing physical constants and properties for any atomic or subatomic particle for use in simulations

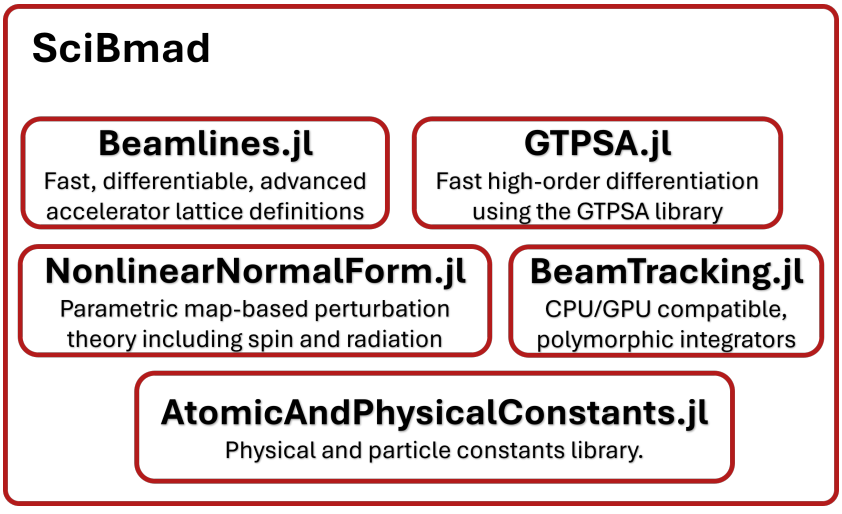

Figure 9.1: Schematic of each package in the modular SciBmad ecosystem.

Figure 9.1 shows a schematic layout of all packages in the SciBmad family. Each subpackage has a very extensive test suite. Full code coverage is a requirement for pull requests to be merged into the main branch.

Because development of SciBmad has been rapidly progressing in the midst of this dissertation writing, this chapter will only provide very high level details of the packages, except for `GTPSA.jl` which has a stable release and completed conference proceeding.

9.2 `GTPSA.jl`

9.2.1 Background

To understand and analyze the beam dynamics in a particle accelerator, we express the motion through the accelerator as a Taylor series expanded around the "reference trajectory" - the closed orbit in a periodic ring, or the "ideal" particle in an open beamline - and optionally the parameters of the accelerator (quadrupole strengths, lengths, etc). This Taylor map is referred to as a (parametric) differential-algebraic (DA) map. Once a DA map is computed, canonical perturbation theory can then be applied to extract *all* information on the dynamics, up to the truncation order of the series; this includes the Twiss parameters, amplitude-dependent tunes, chromatic beta beat, so-called second order dispersion, resonance driving terms (RDTs), etc., and how all of these quantities depend on the parameters.

A code that can compute high order Taylor maps is a necessary tool in the

design of particle accelerators. However, accurately computing all the higher order cross-derivatives is very nontrivial; finite differencing methods for example can be highly sensitive to the chosen step size for each individual variable, can suffer round-off errors that grow with the order of the partial derivative, and can include higher-order errors in the low-order derivatives, proportional to the step size. Furthermore, as the number of variables and truncation order increases, the number of partial derivatives to compute and store grows exponentially.

Automatic differentiation (AD) is a method which computes derivatives without any approximation - being exact to numerical precision - by relying on the fact that the chain rule can be repeatedly applied to a sequence of elementary arithmetic operations and math functions [72]. A "differentiable" code is one whose derivatives can be computed using AD. Truncated Power Series Algebra (TPSA) is a method of AD that is highly-optimized for computing high order derivatives, including potentially many variables and parameters; this makes TPSA ideal for accelerator physics.

Therefore, as has been recognized since the early 1990s [30, 12, 31], accelerator physics simulation codes must be differentiable via a TPSA package to properly compute and analyze DA maps. The Generalised Truncated Power Series Algebra (GTPSA) library, written in C, has been shown to outperform many well-known TPSA libraries [20]. GTPSA also uniquely allows the user to specify custom truncation orders for individual variables and parameters, enabling better flexibility without a performance cost. To harness the power of GTPSA for use both in the new SciBmad accelerator physics code and in the broader optimization and AD community, we have implemented a full fea-

tured interface package in the Julia programming language. GTPSA bindings have also been implemented in two open-source, widely-used Julia packages: `DifferentiationInterface.jl` [17, 58] which enables GTPSA to be used generically alongside any other Julia AD package, and `DiffEqBase.jl` which enables integration of GTPSA maps using any of the differentiable integrators already available in `DifferentialEquations.jl` [49]. And, with the Python package `juliacall` [50], `GTPSA.jl` can be easily called from Python. In this paper, we present all such features implemented in `GTPSA.jl`.

9.2.2 Truncated Power Series Algebra

The most natural AD implementation utilizes *forward-accumulation*, which works by defining a new number type called a *dual*. The dual number stores two numbers: one which acts like a regular number, and one which is the exact partial derivative of any previously evaluated function. All elementary arithmetic operators and functions are properly overloaded for the dual to apply the chain rule and compute this derivative exactly. In this case, the chain rule is traversed from the input to the output, hence the name "forward".

In a fully polymorphic code, higher order derivatives can be computed by nesting dual numbers. However, this can be slow and memory-intensive due to the cost of repeated evaluation of the partial derivatives for higher orders, recursive data structures storing the partials, and the redundant storage of the cross derivatives. TPSA addresses these issues by using the Taylor series directly for higher order partial derivatives, storing the partials in a flattened array in dynamically-allocated memory, and storing no redundant cross terms. The

GTPSA library specifically includes many optimizations beyond this, discussed in detail in [20, 18].

Using Einstein notation for the variable indices, and letting n specify the order up to a maximum truncation order MO, we can express a function f expanded around $\boldsymbol{a}$ as a truncated power series (TPS),

$$f(\boldsymbol{x}) \approx f(\boldsymbol{a}) + \sum_{n=1}^{\mathrm{MO}} \frac{1}{n!} \left.\frac{\partial^n f}{\partial x_{i_1} \ldots \partial x_{i_n}}\right|_{\boldsymbol{a}} \Delta x_{i_1} \ldots \Delta x_{i_n} \,. \tag{9.1}$$

A `TPS` number type stores and propagates all of the monomial coefficients up to the truncation order.

9.2.3 Basic Usage

The Julia programming language is a just-in-time (JIT) compiled, high-level, high performance computing language that, by leveraging multiple dispatch and a powerful type system, enables universally polymorphic code without any performance losses. This makes Julia ideal for writing a simulation code that by default works with both regular numbers and dual numbers/truncated power series.

First the number of variables, parameters, and truncation order(s) must be defined in a `Descriptor`. A vector of the variables Δx_i's as `TPS`s can then be obtained using `vars`. Taylor maps can be computed simply by using these in place of regular numbers. E.g., to compute the multivariate Taylor expansion of the $\mathbb{R}^2 \to \mathbb{C}^1$ function $f(\boldsymbol{x}) = \cos x_1 + \mathrm{i} \sin x_2$ around $\boldsymbol{a} = (-\pi/2, \pi/2)$ to 6th order:

```julia
using GTPSA
d6 = Descriptor(2, 6)
Δx = vars(d6)
f(x) = cos(x[1]) + im*sin(x[2])
ft = f([-π/2, π/2] + Δx)

# Print imaginary part:
println(imag(ft)) # Output in following block
```

```
TPS64{Descriptor(NV=2, MO=6)}:
 Coefficient                 Order    Exponent
  1.0000000000000000e+00       0       0    0
 -5.0000000000000000e-01       2       0    2
  4.1666666666666664e-02       4       0    4
 -1.3888888888888887e-03       6       0    6
```

`GTPSA.jl` includes two types: `TPS64` and `ComplexTPS64`, which respectively represent 64-bit floats and complex numbers as two 64-bit floats. Promotion from regular numbers to `TPS`s, and from real to complex, is handled automatically. To define a `Descriptor` for custom truncation orders of the variables/parameters, see the documentation [59].

`GTPSA.jl` includes routines for `TPS` evaluation, composition, inversion, and translation. The syntax is natural:

```julia
gt = [ft, -im*ft] # New TPS vector function

```

```
gt([1, 2])    # Evaluation for Δx = [1,2]
ht = ft ∘ gt # Composition, equivalently ft(gt)
inv(ht)       # Inversion of Taylor map
translate(gt,[3,4]) # Translate expansion point
```

GTPSA.jl provides the following methods for getting/setting individual monomial coefficients in a TPS :

```
# 1) Flat index, sorted by order:
ft[0] # Scalar part
ft[1] # Coefficient of Δx₁
ft[2] # Coefficient of Δx₂

# 2) Monomial:
ft[[0,0]] # Scalar part
ft[[1,0]] # Coefficient of Δx₁
ft[[1,2]] # Coefficient of (Δx₁)(Δx₂)²

# 3) Sparse monomial:
ft[[1=>2, 2=>3]] # Coefficient of (Δx₁)²(Δx₂)³
```

For any of these methods, a colon (:) can be included to "slice" the TPS. For example, with monomial getting, ft[[1,:]] will return a new TPS including only the monomial coefficients from ft with Δx_1 at order 1, and all orders in Δx_2. This makes it easy to extract a particular polynomial from within the TPS. To extract a polynomial of a given order(s), the cutord and getord functions can be used. Finally, GTPSA.jl provides cycle! to easily cycle through all nonzero

coefficients; this is particularly useful for normal form algorithms, and is used extensively in the SciBmad normal form package `NonlinearNormalForm.jl` [61].

`GTPSA.jl` provides `jacobian`, `gradient`, and `hessian` functions to extract the corresponding derivatives. However, if you are only interested in these quantities, then we strongly recommend using `GTPSA.jl` with the popular, open-source `DifferentiationInterface.jl` package in Julia [17, 58]. This package enables users to plug-and-play different Julia AD backends with the same interface.

9.2.4 Integrating a GTPSA Map

`DifferentialEquations.jl` is an open source, massive suite of integrators [49]. It is impossible to highlight all of its features here, but of most interest to the accelerator physics community are probably its symplectic, Runge Kutta, Magnus, and stochastic integrators.

To enable integration of GTPSA maps using these integrators, bindings have been added to the base package `DiffEqBase.jl`. All one needs to do now is use `TPS`s as the initial conditions, and the result will be a GTPSA map. As an example, we compute a parametric 2nd order transport map through a paraxial quadrupole, where the strength is varied as a parameter. In this case, we define a `Descriptor` with 6 variables to 2nd order, and 1 parameter to 1st order. We use `params` to get a vector of the parameters Δk_i's. The 6th order Yoshida drift-kick-drift integrator [78] in `OrdinaryDiffEq.jl` is used:

```julia
using GTPSA, OrdinaryDiffEq
# 2nd order in 6 variables, 1st order parameter
d = Descriptor(6, 2, 1, 1)
Δx = vars(d)
Δk = params(d)

# Define EOM
pdot(p,q,K1,s) = -[K1*q[1], -K1*q[2], 0]
qdot(p,q,K1,s) = [p[1]/(1+p[3]), p[2]/(1+p[3]),
                  1/2*(p[1]^2+p[2]^2)/(1+p[3])^2]

# Quad strength (as TPS) and length:
K1 = 0.36 + Δk[1] # TPS
L = 0.5

#Initial conditions as TPSs:
p0 = Δx[1:3]; q0 = Δx[4:6]

prob = DynamicalODEProblem(
        pdot, qdot, p0, q0, (0, L), K1)

# sol contains the GTPSA map at each step
sol = solve(prob, Yoshida6(), dt=0.01)
```

9.2.5 Calling from Python

The `juliacall` package in Python makes it very easy to call any Julia code within Python [50]. For example:

```
from juliacall import Main as jl
jl.seval('import Pkg; Pkg.add("GTPSA")') # once
jl.seval("using GTPSA")
d6 = jl.Descriptor(2, 6)
x = jl.vars(d6)
ft = jl.cos(x[0]) + 1j*jl.sin(x[1])
```

9.2.6 `@FastGTPSA`/`@FastGTPSA!` Macros

Because `TPS`s are mutable, every operation with a `TPS` must dynamically-allocate a new `TPS`. This includes the temporaries computed during expression evaluation; for example if a, b, c, and d are `TPS`s, then the expression $(a+b)*(c+d)$ will allocate 3 `TPS`s: one for each sum, then one for the final product. Because Julia has garbage collection, the temporaries will be deallocated when Julia decides to. Nonetheless, dynamically-allocated memory and garbage collection can hinder performance.

To address this issue, a thread-safe buffer of `TPS`s for use by temporaries is preallocated in the `Descriptor`. In Julia the assignment operator cannot be overloaded. Therefore, to "tell" the code to use the pre-allocated buffer for temporaries, `GTPSA.jl` provides the `@FastGTPSA` macro which can be prepended to any expression, or block of code, that may include `TPS`s. By taking advantage

of multiple dispatch, the macro is also *completely transparent to all other types*, so it can be prepended to any existing code and *maintain universal polymorphism*. For example:

```
foo(a, b, c, d) = @FastGTPSA (a + b)*(c + d)
a, b, c, d = vars(Descriptor(4, 2))
r = foo(a, b, c, d) # Only 1 TPS allocated
r = foo(1, 2, 3, 4) # Transparent to non-TPSs
```

`GTPSA.jl` also provides the `@FastGTPSA!` macro, which is similarly transparent to all non-`TPS` types and can be used to write the result to pre-allocated `TPS`s for *zero* allocations:

```
r = zero(a) # Pre-allocates result
@FastGTPSA! r = (a + b)*(c + d) # Zero allocs
```

In our examples and tracking codes, we have seen a roughly 2x speedup by using these macros with `TPS`s.

9.2.7 Static vs. Dynamic Resolution

`GTPSA.jl` allows for multiple `Descriptor`s defined in the same program (though mixing `TPS`s with different `Descriptor`s is not allowed). This brings the question of whether a `Descriptor` should be stored explicitly in the `TPS` type itself (statically) or resolved from the `TPS` at runtime (dynamically).

GTPSA.jl allows users to decide between either; vars/params have the keyword argument dynamic, with default false. For dynamic resolution, if the Descriptor cannot be inferred at runtime, it can be specified with the use argument. use defaults to GTPSA.desc_current, a global variable always set to the last defined Descriptor:

```
d = Descriptor(1, 2)
# Promote 1.23 to a TPS:
x = TPS64{d}(1.23) # Static, as type parameter
y = TPS64{GTPSA.Dynamic}(1.23, use=d) # Dynamic
```

While static resolution may appear to be a better choice by storing all information in the type, the downside is that now new TPS methods must be JIT-compiled for every different Descriptor . This means bigger compiled binaries and also allows for type-instabilities between TPSs of different Descriptors.

9.2.8 Conclusions

Polymorphic codes that are differentiable with TPSA are essential to designing particle accelerators. The GTPSA library, written in C, has been shown to provide far better performance and flexibility than other well-known TPSA libraries. This full-featured interface package GTPSA.jl , written in Julia, brings the full-power of GTPSA to a much wider community, both inside and outside of accelerator physics. Julia-specific performance optimizations and features have been implemented, as well as bindings to widely-used Julia packages for

easy composability – this includes a generic autodifferentiation interface and a massive suite of polymorphic integrators. The new SciBmad accelerator physics code will use `GTPSA.jl` extensively.

9.3 `NonlinearNormalForm.jl`

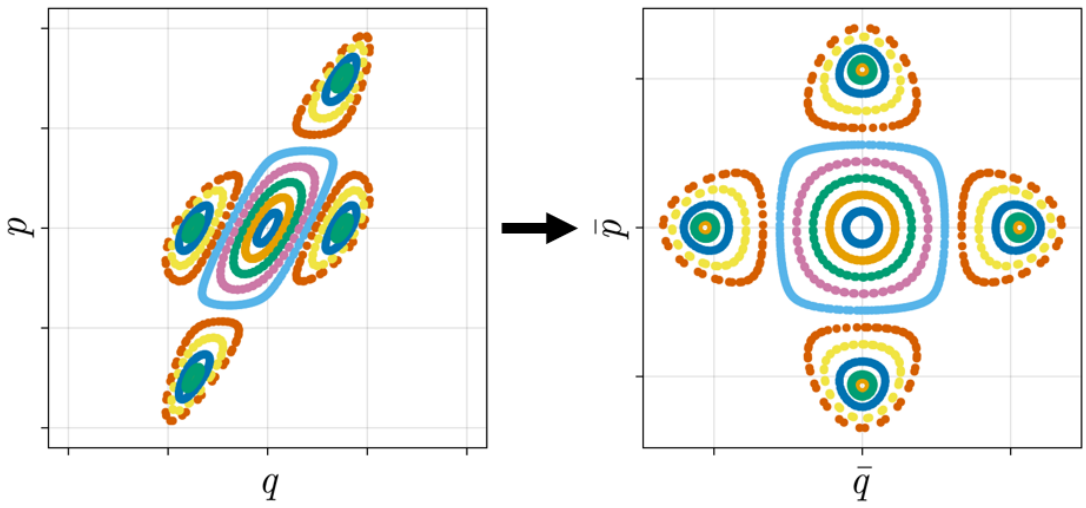

Figure 9.2: Phase space near a 1/4 resonance, before (left) and after (right) transforming to a 4th order single resonance normal form using the `NonlinearNormalForm.jl` package.

This package can be used for doing perturbation theory with nonlinear, parametric Hamiltonian maps using Lie algebraic methods. Maps with large damping can be handled. Given a map expressed as a truncated power series in small deviations of the variables and parameters, this package can be used to calculate and analyze the canonical transformation to the normal form – coordinates where the motion lies on action-dependent circles in phase space or contains a single resonance. This allows for easy calculation of all important (parameter-dependent) properties of the map. Furthermore, by extending the Lie algebra to

include a quaternion operator in the vector field, the spin normal form analysis can be performed in the same way as the orbital. This fully unifies spin and orbital one-resonance normal form calculations, without needing to learn two different theories, and allows for analysis of time-dependent Hamiltonians via Deprit-like algorithms. The package is used in the SciBmad accelerator physics ecosystem for all analysis, and may also be of interest in fields such as celestial mechanics, electronic circuits, electron microscopy, geometrical optics, and plasma physics.

Some features provided by this package include:

```
# DA map from orbital ray (v) and spin quaternion (q)
m = DAMap(v=v, q=q);

# Extract the linear part in orbital
m_lin = cutord(m, 2);

# Remove the linear part
m_nonlinear = inv(m_lin) ∘ m;

# Lie operator (including quaternion) generating nonlinear part
F = log(m_nonlinear);

# Reconstruct same map using Lie exponent and linear part
m = m_lin ∘ exp(F);

# Nonlinear (parametric) normalizing canonical transformation
a = normal(m);

```

```
# Nonlinear amplitude-dependent rotation
R_z = inv(a) ∘ m ∘ a;

# Transform to phasors basis √(J)*exp(±im*ϕ)
c = c_map(m);

# Nonlinear amplitude-dependent rotation in phasors basis
R_J = inv(c) ∘ R_z ∘ c;

# Spin part, nonlinear parameter-dependent fixed point, a1, a2
a_spin, a0, a1, a2 = factorize(a);

# Equilibrium sigma matrix with radiation
Σ = equilibrium_moments(m, a);

# Q_y - Q_spin one resonance normal form
a = normal(m, m=[0; 1], m_spin=[-1]);
```

All routines in this package have been tested against the Fully Polymorphic Package (FPP) [34].

9.4 `Beamlines.jl`

This package defines the `Beamline` and `LineElement` types, which can be used to define particle (or in the future, potentially x-ray) beamlines. The `LineElement` is fully extensible and polymorphic, and has been highly optimized for fast getting/setting of the beamline element parameters. High-order

automatic differentiation of parameters, e.g. magnet strengths or lengths, is easy using `Beamlines.jl`. Furthermore, all non-fundamental quantities computed from `LineElement`s are computed lazily as deferred expressions. There is no eager "bookkeeper". This both fully minimizes overhead from storing and computing quantities you don't need (especially impactful in optimization loops), and ensures that you don't need to rely on a bookkeeper to properly update all dependent variables, minimizing bugs and easing long term maintainence. Furthermore, the generic `DefExpr` type is provided as a general usage lazily-evaluated deferred expression for controlling potentially many parameters with only a single update.

The features of `Beamlines.jl` are best shown with an example:

```
using Beamlines, GTPSA

qf = Quadrupole(Kn1=0.36, L=0.5)
sf = Sextupole(Kn2=0.1, L=0.5)
d1 = Drift(L=0.6)
b1 = SBend(L=6.0, angle=pi/132)
d2 = Drift(L=1.0)
qd = Quadrupole(Kn1=-qf.Kn1, L=0.5)
sd = Sextupole(Kn2=-sf.Kn2, L=0.5)
d3 = Drift(L=0.6)
b2 = SBend(L=6.0, angle=pi/132)
d4 = Drift(L=1.0)

# We can access quantities like:
qf.L
```

```
qf.Kn1 # Normalized field strength

sol = Solenoid(Ksol=0.12, L=5.3)

# Up to 21st order multipoles allowed:
m21 = Multipole(Kn21=5.0, L=6)

# Integrated multipoles can also be specified:
m_thin = Multipole(Kn1L=0.16)
m_thick = Multipole(Kn1L=0.16, L=2.0)

m_thick.Kn1L == 0.16    # true
m_thick.Kn1 == 0.16/2.0 # true

# Whichever you enter first for a specific multipole
# - integrated/nonintegrated and normalized/unnormalized -
# sets that value to be the independent variable

# Misalignments are also supported:
bad_quad = Quadrupole(Kn1=0.36, L=0.5, x_offset=0.2e-3,
            tilt=0.5e-3, y_rot=-0.5e-3)

# All of these are really just one type, LineElement
# E.g. literally,
# Quadrupole(; kwargs) = LineElement("Quadrupole"; kwargs...)
# Feel free to define your own element "classes":
SkewQuadrupole(; kwargs...) = LineElement(;
        class="SkewQuadrupole", kwargs..., tilt1=pi/4)
sqf = SkewQuadrupole(Kn1=0.36, L=0.2)
```

```
45 # Alternatively and equivalently:
46 sqf = Quadrupole(Ks1=0.36, L=0.2)
47 # Note that tilt1 specifies a tilt to only the Kn1 multipole.
48
49 # Create a FODO beamline
50 bl = Beamline(
51             [qf, sf, d1, Bn1, d2, qd, sd, d3, b2, d4],
52             R_ref=60.0
53 )
54
55 # Now we can get the unnormalized field strengths:
56 qf.Bn1
57
58 # We can also reset quantities:
59 qf.Bn1 = 60.
60 qf.Kn1 = 0.36
61
62 # Set the tracking method of an element:
63 struct MyTrackingMethod end
64 qf.tracking_method = MyTrackingMethod()
65 # EVERYTHING is a deferred expression, there is no bookkeeper
66
67 # Easily get s, and s_downstream, as deferred expression:
68 qd.s
69 qd.s_downstream
70
71 # We can get all Quadrupoles for example in the line with:
72 quads = findall(t->t.class == "Quadrupole", bl.line)
73
```

```
# Or just the focusing quadrupoles with:
f_quads = findall(
            t->t.class == "Quadrupole" && t.Kn1 > 0.,
            bl.line
)

# And of course, EVERYTHING is fully
# polymorphic for differentiability.
# Let's make the length of the first drift a TPSA variable:
const D = Descriptor(2,1)
ΔL = vars(D)[1]

d1.L += ΔL

# Now we can see that s, s_downstream are TPSA variables:
qd.s
qd.s_downstream

# Even the reference energy of the Beamline can be set as
# a TPSA variable:
ΔR_ref = vars(D)[2]
bl.R_ref += ΔR_ref

# Now e.g. unnormalized field strengths will be TPSA:
qd.Bn1

# We can control elements together using the deferred
# expression type DefExpr. DefExpr uses closures to evaluate a
# parameter, and is always evaluated when *pulling* a value
```

```
# from a Beamline.

# Let's use DefExpr to set the Kn1 of qf and qd together

Kn1 = 0.36
qf.Kn1 = DefExpr(()->Kn1)
qd.Kn1 = DefExpr(()->-qf.Kn1)

# The quadrupole strengths are set to anonymous functions
# which "encloses" the value of Kn1 in its scope

# When getting a DefExpr parameter from a LineElement
# or parameter group, the deferred expression is evaluated:
qf.Kn1 == 0.36 # true
qd.Kn1 == -0.36 # true

Kn1 = 0.3 # update local variable
qf.Kn1 == 0.3 # true: closure evaluated upon *get*
qd.Kn1 == -0.3 # true: closure evaluated upon *get*

# We can improve the performance of deferred expressions by
# by passing type-stable functions:
g::Float64 = b1.g
b1.g = DefExpr(()->g) # Closure has inferrable return type
b1.BendParams # any gets from BendParams are now type stable


# Deferred expressions provide a "pull" way of controlling
# multiple elements together: in the above example, the
```

```
# DefExpr stored in qf.Kn1 is evaluated
# *at the time of getting*.

# An alternative way of controlling multiple elements together
# is with a "push" scheme, where when setting the control
# parameter, all dependent values are updated. Beamline.jl's
# Controller type provides a way to "push" values
# to LineElements, or other Controllers.

# Let's create a controller which sets the Bn1 of qf and qd:
c1 = Controller(
  (qf, :Kn1) => (ele; x) ->  x,
  (qd, :Kn1) => (ele; x) -> -x;
  vars = (; x = 0.0,)
)

# Now we can vary both simultaneously:
c1.x = 60.
qf.Kn1
qd.Kn1

# Controllers also include the element itself. This can
# be useful if the current elements' values should be
# used in the function:
c2 = Controller(
  (qf, :Kn1) => (ele; dKn1) ->  ele.Kn1 + dKn1,
  (qd, :Kn1) => (ele; dKn1) ->  ele.Kn1 - dKn1;
  vars = (; dKn1 = 0.0,)
)
```

```
161
162 c2.dKn1 = 20
163
164 qf.Kn1
165 qd.Kn1
166
167 # We can reset the values back to the most recently set state
168 # of a controller using set!
169 set!(c1)
170 qf.Kn1
171 qd.Kn1
172
173 # Controllers can also be used to control other controllers:
174 c3 = Controller(
175   (c1, :x) => (ele; dx) -> ele.x + dx;
176   vars = (; dx = 0.0,)
177 )
178
179 # And of course still fully polymorphic:
180 dx = vars(D)[1]
181 c3.dx = dx
182 qf.Kn1
183 qd.Kn1
184
185 # Beamlines.jl also provides functionality to convert the
186 # Beamline to a compressed, fully isbits type. This may be
187 # useful in cases where the Beamline is mostly static and you
188 # would like to put the entire line on a GPU, for example.
189 qf = Quadrupole(Kn1L=0.18, L=0.5)
```

```
d1 = Drift(L=1.6)
qd = Quadrupole(Kn1L=-qf.Kn1L, L=0.5)
d2 = Drift(L=1.6)

bl = Beamline([qf, d1, qd, d2])

# Fully immutable, isbits compressed type:
bbl = BitsBeamline(bl)

# A warning will be issued if the
# size is >64KB (CUDA constant memory)
sizeof(bbl)

# Convert back:
bl2 = Beamline(bbl)
all(bl.line .≈ bl2.line) # true

# Duplicate elements are allowed. In this case, the first
# element instance is used as the "parent", and all
# duplicates' parameters are pulled directly from the parent
qf = Quadrupole(Kn1=0.36, L=0.5)
d = Drift(L=1)
qd = Quadrupole(Kn1=-0.36, L=0.5)

fodo = Beamline([qf, d, qd, d, qf, d, qd, d])
bl.line[1] === qf # egality with first instance

# reset parent
qf.Kn1 = 0.1
```

```
219
220 # second instance
221 qf2 = fodo.line[5]
222 qf2.Kn1 == 0.1 # true
```

`Beamlines.jl` aims to provide the powerful lattice definitions enabled by classic Bmad [53] and the Particle Accelerator Lattice Standard (PALS) project [29]. The use of lazily-evaluated deferred expressions is inspired completely by MAD-NG [19]

9.5 `BeamTracking.jl`

This package provides universally polymorphic and portable, parallelizable integrators for simulating charged particle beams both on the CPU and, using `KernelAbstractions.jl` [16], various GPU backends including NVIDIA CUDA, Apple Metal, Intel oneAPI, and AMD ROCm. Explicit single instruction multiple data (SIMD) support has been implemented via `SIMD.jl`, `SIMDMathFunctions.jl`, and `SLEEFPirates.jl`.

At the time of this dissertation writing, the Yoshida's second, fourth, sixth, and eighth-order symplectic [78] methods for the following splits *including spin* have been implemented and tested against PTC [33]:

- Drift-kick
- Quadrupole-kick
- Solenoid-kick

- Bend-kick
- Patches

Patches and rectangular/elliptical apertures have also been implemented. Arbitrary time dependent parameters has been implemented too, and is fully GPU compatible. Any parameter could be made time-dependent

BIBLIOGRAPHY

[1] E. C. Aschenauer. Plans for Early Science. Electron-Ion Collider Machine Advisory Committee Meeting, 2025.

[2] V. N. Baier and V. M. Katkov. Quantum effects in magnetic bremsstrahlung. *Physics Letters A*, 25(7):492–493, 1967.

[3] V. N. Baier, V. M. Katkov, and V. M. Strakhovenko. Kinetics of radiative polarization. *Sov. Phys. JETP*, 31(5):908, 1970.

[4] D. P. Barber et al. High spin polarization at the HERA Electron Storage Ring. *Nucl. Instrum. Meth. A*, 338:166–184, 1994.

[5] D. P. Barber, H. Mais, G. Ripken, and R. Rossmanith. A General Harmonic Spin Matching Formalism for the Suppression of Depolarization Caused by Closed Orbit Distortions in Electron Storage Rings. *DESY-85-044*, 3 1985.

[6] D. P. Barber and G. Ripken. *Handbook of Accelerator Physics and Engineering (3rd Edition)*, chapter 2.6.6 - 2.6.8. World Scientific Publishing Company, 2023.

[7] V. Bargmann, L. Michel, and V. L. Telegdi. Precession of the polarization of particles moving in a homogeneous electromagnetic field. *Phys. Rev. Lett.*, 2:435–436, May 1959.

[8] M Bassetti and George A Erskine. Closed expression for the electrical field of a two-dimensional Gaussian charge. Technical report, CERN, Geneva, 1980.

[9] A. Bazzani, P. Mazzanti, G. Servizi, and G. Turchetti. Normal forms for hamiltonian maps and nonlinear effects in a particle accelerator. *Il Nuovo Cimento B (1971-1996)*, 102(1):51–80, Jul 1988.

[10] Armando Bazzani, G Servizi, Ezio Todesco, and G Turchetti. *A normal form approach to the theory of nonlinear betatronic motion*. CERN Yellow Reports: Monographs. CERN, Geneva, 1994.

[11] Gun Zara Mari Berglund. *Spin-Orbit Maps and Electron Spin Dynamics for the Luminosity Upgrade Project at HERA*. PhD thesis, Royal Institute of Technology, 01 2001.

[12] M Berz. *Modern Map Methods in Particle Beam Physics*. Academic Press, San Diego, 1999. Also available at `https://www.bmtdynamics.org/pub`.

[13] M Berz, E Forest, and J Irwin. Exact computation of derivatives with differential algebra and applications to beam dynamics. Technical report, Lawrence Berkeley Lab., CA (USA). SSC Central Design Group, 03 1988.

[14] M. Boge and T. Limberg. Calculations on depolarization in hera due to beam-beam effects. In *Proceedings Particle Accelerator Conference*, volume 5, pages 2901–2903 vol.5, 1995.

[15] A. W. Chao. Evaluation of radiative spin polarization in an electron storage ring. *Nucl. Inst. and Meth.*, 180(1):29–36, 1981.

[16] Valentin Churavy. KernelAbstractions.jl.

[17] Guillaume Dalle and Adrian Hill. A Common Interface for Automatic Differentiation, 2025.

[18] L. Deniau. Methodical Accelerator Design - Next Generation: Introduction to the Generalized Truncated Power Series Algebra. `https://indico.cern.ch/event/1513480/contributions/6368615/attachments/3036088/5368770/MADNG-GTPSA.pdf`,, March 2025.

[19] Laurent Deniau. Mad-ng, a standalone multiplatform tool for linear and non-linear optics design and optimisation, 2025.

[20] Laurent Deniau and Ciprian Tomoiagă. Generalised Truncated Power Series Algebra for Fast Particle Accelerator Transport Maps. In *6th International Particle Accelerator Conference*, page MOPJE039, 2015.

[21] André Deprit. Canonical transformations depending on a small parameter. *Celestial mechanics*, 1(1):12–30, 1969.

[22] Ya. S. Derbenev and A. M. Kondratenko. Polarization kinematics of particles in storage rings. *Sov. Phys. JETP*, 37:968–973, 1973.

[23] J. Devlin. private communication.

[24] A. J. Dragt. Lectures on nonlinear orbit dynamics. *AIP Conf. Proc.; (United States)*, 87:1, 07 1982.

[25] A. J. Dragt. *Lie Methods for Nonlinear Dynamics with Applications to Accelerator Physics*. University of Maryland DSAT Group, November 2020. Retrieved from `https://www.physics.umd.edu/dsat/`.

[26] A. J. Dragt and E. Forest. Computation of nonlinear behavior of hamiltonian systems using lie algebraic methods. *Journal of Mathematical Physics*, 24(12):2734–2744, 12 1983.

[27] Alex J Dragt and John M Finn. Lie series and invariant functions for analytic symplectic maps. *Journal of Mathematical Physics*, 17(12):2215–2227, 1976.

[28] Alex J. Dragt and John M. Finn. Lie series and invariant functions for analytic symplectic maps. *Journal of Mathematical Physics*, 17(12):2215–2227, 12 1976.

[29] A. Huebl et al. A community effort toward a particle accelerator lattice standard (pals). In *Proc. North American Particle Accelerator Conference (NAPAC2025)*, number 2025 in North American Particle Accelerator Conference, pages 350–353. JACoW Publishing, Geneva, Switzerland, 08 2025.

[30] E. Forest. *Beam Dynamics*. CRC Press, 1st edition, 1998.

[31] E. Forest. Geometric integration for particle accelerators. *Journal of Physics A: Mathematical and General*, 39(19):5321, apr 2006.

[32] E. Forest. *From Tracking Code to Analysis: Generalised Courant-Snyder Theory for Any Accelerator Model*. Physics and Astronomy. Springer Tokyo, Springer Japan, 1 edition, 2016.

[33] E. Forest, F. Schmidt, and E. McIntosh. Introduction to the polymorphic tracking code: Fibre bundles, polymorphic Taylor types and "Exact tracking". Technical Report CERN-SL-2002-044-AP, KEK-REPORT-2002-3, CERN, Geneva, 2002.

[34] Etienne Forest and Frank Schmidt. The "full polymorphic package" (fpp). *SIGPLAN Fortran Forum*, 20(3):12–17, December 2001.

[35] B. Ghojogh, F. Karray, and M. Crowley. Eigenvalue and generalized eigenvalue problems: Tutorial, 2023.

[36] Colwyn Gulliford and Adam Bartnik. Demonstration of cathode emittance

dominated high bunch charge beams in a dc bun-based photoinjector. *Applied Physics Letters*, 106:094101, 03 2015.

[37] G. H. Hoffstaetter. *High-Energy Polarized Proton Beams: A Modern View*, volume 218. 01 2006.

[38] G. H. Hoffstaetter. USPAS Accelerator Physics Lectures. 4, July 2025.

[39] G. H. Hoffstaetter, James Ellison, and H. Scott Dumas. Adiabatic invariance of spin-orbit motion in accelerators. *Physical Review Special Topics - Accelerators and Beams*, 9:014001, 01 2006.

[40] P.-V. Koseleff. Comparison between deprit and dragt-finn perturbation methods. *Celestial Mechanics and Dynamical Astronomy*, 58(1):17–36, Jan 1994.

[41] L.D. Landau and E.M. Lifshitz. *Mechanics*. Course of Theoretical Physics: Volume 1. Butterworth-Heinemann, Oxford, third edition edition, 1976.

[42] Vladimir N Litvinenko and A. A. Zholents. Compensating effect of solenoids with quadrupole lenses, 2018.

[43] D. Marx et al. Designing the EIC Electron Storage Ring Lattice for a Wide Energy Range. In *Proc. IPAC'22*, number 13 in International Particle Accelerator Conference, pages 1946–1949. JACoW Publishing, Geneva, Switzerland, 7 2022.

[44] D. Marx et al. Lattice design of the EIC electron storage ring for energies down to 5 GeV. In *Proc. IPAC'23*, number 14 in International Particle Accelerator Conference, pages 104–107. JACoW Publishing, Geneva, Switzerland, 9 2023.

[45] Daniel Marx, Yunhai Cai, Georg Hoffstaetter, Yongjun Li, Christoph Montag, Yuri Nosochkov, Steven Tepikian, Jonathan Unger, and Ferdinand Willeke. Dynamic Aperture Optimization in the EIC Electron Storage Ring with Two Interaction Points. In *12th International Particle Accelerator Conference* , 8 2021.

[46] Aaron Meurer, Christopher P. Smith, Mateusz Paprocki, Ondřej Čertík, Sergey B. Kirpichev, Matthew Rocklin, AMiT Kumar, Sergiu Ivanov, Jason K. Moore, Sartaj Singh, Thilina Rathnayake, Sean Vig, Brian E. Granger, Richard P. Muller, Francesco Bonazzi, Harsh Gupta, Shivam Vats, Fredrik

Johansson, Fabian Pedregosa, Matthew J. Curry, Andy R. Terrel, Štěpán Roučka, Ashutosh Saboo, Isuru Fernando, Sumith Kulal, Robert Cimrman, and Anthony Scopatz. Sympy: symbolic computing in python. *PeerJ Computer Science*, 3:e103, January 2017.

[47] Brian William St. Leger Montague. Linear Optics For Improved Chromaticity Correction. Technical report, CERN, Geneva, 1979.

[48] V. Ptitsyn. *Spin Matching*, pages 183–195. Springer International Publishing, Cham, 2023.

[49] Christopher Rackauckas and Qing Nie. DifferentialEquations.jl–a performant and feature-rich ecosystem for solving differential equations in Julia. *Journal of Open Research Software*, 5(1), 2017.

[50] Christopher Rowley. PythonCall.jl: Python and Julia in harmony, 2022.

[51] R. D. Ruth. Single-particle dynamics in circular accelerators. *AIP Conf. Proc.*, 153:150–235, 1987.

[52] D. Sagan. Bmad: A relativistic charged particle simulation library. *Nuclear Instruments and Methods in Physics Research Section A: Accelerators, Spectrometers, Detectors and Associated Equipment*, 558(1):356–359, 2006. Proceedings of the 8th International Computational Accelerator Physics Conference.

[53] D. Sagan. *The Bmad Manual*. New York, NY, 2022.

[54] D. Sagan. *Long Term Tracking Program*. Ithaca, NY, 2022.

[55] D. Sagan. *The Tao Manual*. Ithaca, NY, 2022.

[56] D. Sagan and D. Rubin. Linear analysis of coupled lattices. *Phys. Rev. ST Accel. Beams*, 2:074001, Jul 1999.

[57] M. Sands. The Physics of Electron Storage Rings: An Introduction. *Conf. Proc. C*, 6906161:257–411, 1969.

[58] Frank Schäfer, Mohamed Tarek, Lyndon White, and Chris Rackauckas. AbstractDifferentiation.jl: Backend-Agnostic Differentiable Programming in Julia, 2022.

[59] M. G. Signorelli. GTPSA.jl. https://github.com/bmad-sim/GTPSA.jl, 2023.

[60] M. G. Signorelli. Tao.jl. https://github.com/bmad-sim/Tao.jl, 2023.

[61] M. G. Signorelli. NonlinearNormalForm.jl. https://github.com/bmad-sim/NonlinearNormalForm.jl, 2024.

[62] M. G. Signorelli. *SODOM-2 Program Manual*. Ithaca, NY, 2024.

[63] M. G. Signorelli, Y. Cai, A. E. Connelly, G. H. Hoffstaetter, J. Kewisch, D. Marx, C. Montag, V. Ptitsyn, and S. Tepikian. Polarization preservation methods for the Electron Storage Ring of the EIC. *JACoW*, IPAC2024:MOPC83, 2024.

[64] M. G. Signorelli and G. H. Hoffstaetter. Different forms of first order spin-orbit motion and their utility in spin matching in electron storage rings, 2024.

[65] M. G. Signorelli, G. H. Hoffstaetter, J. Kewisch, and J. A. Crittenden. Spin Matching for the EIC's Electrons. In *Proc. IPAC'22*, number 13 in International Particle Accelerator Conference, pages 2369–2372. JACoW Publishing, Geneva, Switzerland, 7 2022.

[66] M. G. Signorelli, G. H. Hoffstaetter, and V. Ptitsyn. Electron polarization preservation in the EIC. *JACoW*, IPAC2023:MOPA052, 2023.

[67] M. G. Signorelli, G. H. Hoffstaetter, and D. Sagan. Nonlinear Coupling Resonances in the EIC Electron Storage Ring. presented at the 14th Int. Particle Accelerator Conf. (IPAC'23), Venice, Italy, May 2023, paper MOPA051, 5 2023.

[68] A. A. Sokolov and I. M. Ternov. On Polarization and Spin Effects in the Theory of Synchrotron Radiation. *Sov. Phys. Doklady*, 8:1203, June 1964.

[69] L. H. Thomas. I. the kinematics of an electron with an axis. *Phil. Mag.*, 3(13):1–22, 1927.

[70] L. H. Thomas. Recollections of the discovery of the Thomas precessional frequency. *AIP Conference Proceedings*, 95(1):4–12, 1983.

[71] S. T. Wang, V. Khachatryan, and P. Nishikawa. Lattice design and experimental studies of nonlinear resonance at the cornell electron storage ring. *Phys. Rev. Accel. Beams*, 26:104001, Oct 2023.

[72] Wikipedia. Automatic differentiation — Wikipedia, the free encyclopedia. `http://en.wikipedia.org/w/index.php?title=Automatic%20differentiation&oldid=1284647437`, 2025.

[73] Wikipedia contributors. Liouville's theorem (hamiltonian) — Wikipedia, the free encyclopedia, 2025. [Online; accessed 9-July-2025].

[74] F. Willeke and J. Beebe-Wang. Electron ion collider conceptual design report 2021. 2 2021.

[75] A. Wolski. Alternative approach to general coupled linear optics. *Phys. Rev. ST Accel. Beams*, 9:024001, Feb 2006.

[76] Derong Xu, Vasiliy S. Morozov, David Sagan, Yue Hao, and Yun Luo. Enhanced beam-beam modeling to include longitudinal variation during weak-strong simulation. *Phys. Rev. Accel. Beams*, 27:061002, Jun 2024.

[77] Kaoru Yokoya. An algorithm for calculating the spin tune in circular accelerators, 1999.

[78] Haruo Yoshida. Construction of higher order symplectic integrators. *Physics letters A*, 150(5-7):262–268, 1990.

[79] ZEUS Collaboration. Measurement of high-q2 charged current deep inelastic scattering cross sections with a longitudinally polarised positron beam at hera. *The European Physical Journal C*, 70(4):945–963, Dec 2010.